

Advanced Interferometry for Gravitational Wave Detection

Daniel Anthony Shaddock

B. Sc. (Hons), Australian National University , 1997.

A thesis submitted for the degree of
Doctor of Philosophy
at the Australian National University

Submitted
3rd November, 2000

To

Jan, Ann and Gran.

Declaration

This thesis is an account of research undertaken between March 1997 and September 2000 at *the Department of Physics, Faculty of Science, Australian National University, Canberra, Australia.*

Except where acknowledged in the customary manner, the material presented in this thesis is, to the best of my knowledge, original and has not been submitted in whole or part for a degree in any university.

Daniel Anthony Shaddock
November, 2000

Acknowledgements

I sincerely thank my supervisors Associate Professor David McClelland, Professor Hans Bachor and Dr Malcolm Gray for their support of the work presented here.

David has managed to strike the perfect balance between providing the group with strong leadership and direction, whilst allowing researchers the intellectual freedom to pursue new ideas. I have thoroughly enjoyed my time as a PhD student and much of the credit for this must go to David.

I also thank Hans Bachor, who has always remained approachable, despite his heavy work load as the Head of the Physics Department during a turbulent time. I do not envy him this thankless job. Hopefully, after submission of this thesis I will finally become eligible to play on his team during the annual staff vs. students cricket match.

The most thanks for the work in this thesis is owed to Malcolm Gray. Mal has contributed to many aspects of this work both theoretically and experimentally. I will forever be in awe of his breadth of knowledge, and his amazing personal library.

Throughout my time at ANU I have been privileged to work with many exceptional researchers. I thank Bram Slagmolen, Ben Buchler, Dr Ping Koy Lam, Conor Mow-Lowry, Karl Baigent, Warwick Bowen, Cameron Fletcher, Jessica Lye, Dr John Close and Dr Charles Harb for their help and friendship over the years. I am also grateful to researchers from the international gravitational wave community for their help and hospitality. I thank Jim Mason, Peter Beyersdorf, Mat Lawrence, Thomas Delker, Guido Mueller, David Ottaway, Chris Hollitt, Markus Bode, Sascha Brozek, Michael Peterseim, Volker Queschke, Andreas Frieze and Ken Strain for their generosity in sharing their knowledge, their offices, and their homes. The running and maintenance of a difficult experiment is often too much for an individual to handle alone. The word “we” used commonly throughout this thesis is more than mere convention. Specifically, I acknowledge the experimental aid of Conor Mow-Lowry in chapter 7, Bram Slagmolen and Malcolm Gray in section 10.1, Ping Koy Lam, Ben Buchler and Warwick Bowen in section 10.2, and David Ottaway, Malcolm Gray and Chris Hollitt in section 10.3.

As with any experimental work there are many people whose contributions often go unnoticed by the outside world. I take this opportunity to acknowledge Brett Brown, Chris Woodland, Paul MacNamara and Russel Koehne for work consistently of the highest quality, as well as Jenny Willcoxson and Zeta Hall for their friendly assistance with administration. I also thank Mal, David, Conor, Ping Koy, Jan, Mum and Dad for proof reading this thesis. Of course, any remaining errors are my responsibility :)

One of the most difficult things about the last year has been the amount of time that I have missed spending with my friends and family. I thank my parents, grandparents, and brothers for all they have done for Jan and I during an eventful four years. I also thank the entire Taylor family who have been wonderfully supportive from the beginning. I promise to come and visit more often now.

Finally, for her loving company, and enduring faith in me, I give the greatest thanks to my wife, Jan.

Abstract

In this thesis we investigate advanced techniques for the readout and control of various interferometers. In particular, we present experimental investigations of interferometer configurations and control techniques to be used in second generation interferometric gravitational wave detectors. We also present a new technique, tilt locking, for the readout and control of optical interferometers.

We report the first experimental demonstration of a Sagnac interferometer with resonant sideband extraction (RSE). We measure the frequency response to modulation of the length of the arms and demonstrate an increase in signal bandwidth of by a factor of 6.5 compared to the Sagnac with arm cavities only. We compare Sagnac interferometers based on optical cavities with cavity-based Michelson interferometers and find that the Sagnac configuration has little overall advantage in a cavity-based system.

A system for the control and signal extraction of a power recycled Michelson interferometer with RSE is presented. This control system employs a frontal modulation scheme requiring a phase modulated carrier field and a phase modulated subcarrier field. The system is capable of locking all 5 length degrees of freedom and allows the signal cavity to be detuned over the entire range of possibilities, in principle, whilst maintaining lock. We analytically investigate the modulation/demodulation techniques used to obtain these error signals, presenting an introductory explanation of single sideband modulation/demodulation and double demodulation.

This control system is implemented on a benchtop prototype interferometer. We discuss technical problems associated with production of the input beam modulation components and present several solutions. Operation of the interferometer is demonstrated for a wide range of detunings. The frequency response of the interferometer is measured for various detuned points and we observe good agreement with theoretical predictions. The ability of the control system to maintain lock as the interferometer is detuned is experimentally demonstrated.

Tilt locking, a new technique to obtain an error signal to lock a laser to an optical cavity, is presented. This technique produces an error signal by efficient measurement of the interference between the TEM_{00} and TEM_{10} modes. We perform experimental and theoretical comparisons with the widely used Pound-Drever-Hall (PDH) technique. We derive the quantum noise limit to the sensitivity of a measurement of the beam position, and using this result calculate the shot noise limited sensitivity of tilt locking. We show that tilt locking has a quantum efficiency of 80%, compared to 82% for the PDH technique. We present experimental demonstrations of tilt locking in several applications including frequency stabilisation, continuous-wave second harmonic generation, and injection locking of a Nd:YAG slab laser. In each of these cases, we demonstrate that the performance of tilt locking is not the limiting factor of the lock stability, and show that it achieves similar performance to the PDH based system.

Finally, we discuss how tilt locking can be effectively applied to two beam interferometers. We show experimentally how a two beam interferometer typically gives excellent isolation against errors arising from changes in the photodetector position, and exper-

imentally demonstrate the use of tilt locking as a signal readout system for a Sagnac interferometer.

Contents

Declaration	v
Acknowledgements	vii
Abstract	ix
1 Introduction	1
1.1 Overview of thesis structure	1
1.2 Publications	3
I Background	5
2 Gravitational waves and their detection	7
2.1 What are gravitational waves?	7
2.2 Why detect gravitational waves?	8
2.3 Detection of gravitational waves	9
2.3.1 Laser interferometric gravitational wave detectors	9
2.4 Factors affecting sensitivity	10
2.4.1 Shot noise	11
2.4.2 Radiation pressure noise	11
2.4.3 Thermal Noise	12
2.4.4 Seismic noise	12
2.4.5 Gravity gradient noise	13
2.5 Current status	13
2.6 Space-based detectors	13
2.7 Summary	14
3 Quantum noise	15
3.1 The Heisenberg Uncertainty Principle	15
3.2 Classical calculations of quantum noise	15
3.3 Quantum mechanical calculations	17
3.4 Model for a coherent state	18
3.5 Hermite-Gauss modes	19
3.6 Quantum limit of beam position noise	21
3.7 Summary	25
4 Modulation, demodulation and interferometer control	27
4.1 Phase and amplitude modulation	27
4.2 Interaction with an optical system	29
4.3 Demodulation	31
4.3.1 Photodetection	31

4.3.2	The mixer	32
4.4	Error signals for interferometers	33
4.4.1	Multiple beam interferometers	33
4.4.2	Two beam interferometers	36
4.5	Advanced modulation and demodulation	37
4.5.1	Single sideband modulation/demodulation	38
4.5.2	Double demodulation	42
4.6	Summary	44
II	Interferometer Configurations and Control	45
5	Gravitational wave detector configurations	47
5.1	Frequency response and the storage time limit	47
5.2	Arm cavities	48
5.3	Energy storage	48
5.4	Power recycling	49
5.5	A power recycled arm cavity Michelson interferometer	50
5.6	Signal recycling	50
5.7	Resonant sideband extraction	51
5.8	Frequency response of a Michelson interferometer with RSE	53
5.9	Autoalignment	57
5.10	Summary	57
6	Sagnac interferometers for gravitational wave detection	59
6.1	Sagnac interferometer basics	59
6.2	Delay line Sagnac interferometer	60
6.2.1	Summary	61
6.3	RSE in a Sagnac Interferometer	62
6.3.1	RSE Sagnac interferometer frequency response	63
6.4	Experimental Setup	65
6.5	Experimental Results	66
6.6	Discussion	69
6.6.1	Energy Storage	69
6.6.2	Beamsplitter Issues	70
6.6.3	Control	70
6.7	Conclusion	71
7	Power Recycled Michelson interferometer with resonant sideband extraction	73
7.1	Control System	73
7.1.1	Arm cavity common mode	76
7.1.2	Michelson common (Power cavity) mode	76
7.1.3	Michelson differential mode	77
7.1.4	Signal Cavity	78
7.1.5	Arm Cavity Differential Mode	79
7.1.6	Control summary	79
7.2	The experiment	80
7.2.1	Experimental layout	80
7.2.2	Input field preparation	82

7.2.3	Offset phase locking	82
7.2.4	Phase locking excess noise	84
7.3	Gain optimisation	87
7.4	Optimising demodulation phases	90
7.4.1	Arm cavity common mode demodulation phase	90
7.4.2	Michelson common mode demodulation phase	91
7.4.3	Signal cavity demodulation phase	91
7.4.4	Michelson differential mode phase	91
7.4.5	Arm cavity differential mode phase	91
7.4.6	Demodulation phase as a function of detuning	91
7.5	Lock acquisition	92
7.6	Locking performance	94
7.7	Frequency response measurement	94
7.8	Application to long base-line interferometers	99
7.9	Summary	102
III	Tilt Locking	103
8	Tilt locking	105
8.1	Frequency Locking techniques	105
8.2	Tilt locking	108
8.2.1	Hermite-Gauss modes	108
8.2.2	Obtaining an error signal from spatial mode interference	109
8.2.3	Other spatial mode interference techniques	112
8.3	The experiment	113
8.3.1	Frequency response and intensity noise immunity	114
8.4	Beam jitter and mechanical vibration	115
8.4.1	Double pass tilt locking	116
8.4.2	Impedance matching	118
8.4.3	TEM ₁₀ power and beam size	120
8.5	Tilt locking variations	121
8.6	Summary	121
9	Shot noise limited sensitivity of tilt locking	123
9.1	Tilt locking sensitivity	123
9.1.1	Tilt locking signal to noise ratio	127
9.1.2	Quantum efficiency	128
9.2	Pound-Drever-Hall locking sensitivity	129
9.2.1	Pound-Drever-Hall signal to noise ratio	130
9.2.2	Pound-Drever-Hall quantum efficiency	130
9.3	Summary	131
10	Applications of tilt locking	133
10.1	Laser frequency stabilisation	133
10.1.1	The experiment	135
10.1.2	Results	136
10.1.3	Summary	138
10.2	Second harmonic generator	138

10.2.1	The experiment	139
10.2.2	Error signals	140
10.2.3	Second harmonic output spectra	141
10.2.4	System stability	141
10.2.5	Summary	143
10.3	Injection locking	143
10.3.1	The experiment	144
10.3.2	Results	145
10.3.3	Future work	147
10.3.4	Summary	148
10.4	Conclusions	148
11	Tilt locking and two beam interferometers	149
11.1	Spatial modes in a nonresonant system	149
11.2	Tilt locking in a Mach-Zehnder interferometer	151
11.3	Sensitivity to mechanical vibrations	151
11.4	Sagnac interferometers	152
11.5	Summary	154
12	Conclusions	157
12.1	Summary of interferometer configurations work	157
12.2	Summary of tilt locking work	158
12.3	Further work	159
A	Construction of optical spectrum analysers	161
B	Circuit Diagrams	163
B.1	Split photodiode	163
B.2	PZT Servo	164
B.3	Laser Frequency Servo	164
C	Matlab files to model DC error signals	167
	Bibliography	173

List of Figures

1.1	Thesis structure.	2
2.1	Effect of a gravitational wave on a ring of test particles.	7
2.2	Basic layout of a Michelson interferometer.	10
3.1	Ball-on-stick representation of electric field.	16
3.2	Method for producing a coherent state with a perfect mode cleaner.	19
3.3	Electric field distributions of the Hermite-Gauss modes	21
3.4	Production of a coherent state in the multimode picture	22
3.5	The electric field of the flipped mode.	23
4.1	Phasor diagram of phase modulation of light.	28
4.2	Vector diagrams representing sine and cosine phase and amplitude modulation.	29
4.3	Vector diagram representing conversion of PM to in-phase AM	30
4.4	Vector diagram representing conversion of PM to quadrature AM	31
4.5	The electric fields of an optical cavity	34
4.6	Complex reflectivity of a cavity	35
4.7	Comparison of error signal and the imaginary component of the cavity reflectivity.	36
4.8	Examples of two beam interferometers	36
4.9	Vector diagram of Schnupp modulation	38
4.10	Mixer outputs for single sideband demodulation for an undercoupled cavity.	40
4.11	Mixer outputs for single sideband demodulation for an impedance matched cavity.	41
4.12	Double demodulation description.	42
5.1	A Michelson interferometer with Fabry-Perot cavities in the arms.	48
5.2	A power recycled Michelson interferometer	50
5.3	A signal recycled Michelson interferometer	51
5.4	A Michelson interferometer with resonant sideband extraction	52
5.5	Illustration of the arm cavity and electric fields	54
5.6	The fields of an arm cavity Michelson interferometer	55
5.7	The fields of a Michelson interferometer with resonant sideband extraction	56
6.1	Sagnac interferometer enclosing a net area of zero	60
6.2	Delay line Sagnac interferometer using polarisation based readout system	61
6.3	Measured frequency response of a 9.2 m delay line Sagnac interferometer.	62
6.4	Basic layout for resonant sideband extraction in a Sagnac interferometer.	63
6.5	Optical and electronic configuration for RSE Sagnac interferometer.	65
6.6	Measured and calculated signal response for a Sagnac interferometer with arm cavities.	67

6.7	A comparison of the frequency responses of an arm cavity Sagnac and the RSE Sagnac	68
6.8	Frequency response of an arm cavity Sagnac (no SEM), RSE Sagnac with SEM=50%, SEM=70% and SEM=90%.	68
6.9	Frequency response of detuned RSE Sagnac	69
7.1	Diagram of the power recycled Michelson with RSE showing length definitions and photodetector positions.	74
7.2	Input field modulation sidebands	75
7.3	Error signals for the arm cavity common mode and the power cavity . . .	77
7.4	Optical experimental layout for the RSE system.	81
7.5	Diagram of input field generation	82
7.6	Optical spectrum of the input field	85
7.7	Radio frequency spectrum of the phase locking detector photocurrent . .	86
7.8	Radio frequency spectrum of the phase locking beatnote	87
7.9	Alternative experimental techniques for producing the electronic local oscillator	88
7.10	Comparison of error signals obtained with different local oscillators. . . .	89
7.11	Optical spectra for a dual recycled Michelson	90
7.12	Power levels during lock acquisition for the power recycled Michelson with RSE.	92
7.13	Optical spectra for a power recycled Michelson with RSE	93
7.14	Measurement of interferometer power levels over a period of 500 seconds	95
7.15	Experimental layout used to measure the broadband frequency response of an arm cavity	95
7.16	Frequency response of the system measured by the use of a signal injection laser	96
7.17	Measured frequency response for RSE Michelson system	97
7.18	Measured and calculated frequency response	99
7.19	Arm cavities' transmitted powers during detuning of the signal cavity . .	100
7.20	Input optical spectra required for near RSE and near dual recycling	101
8.1	Hermite-Gauss modes	108
8.2	Addition of Hermite-Gauss modes	109
8.3	Plot of Gouy phase	110
8.4	Intensity distribution of Hermite-Gauss modes on the split photodiode . .	110
8.5	Vector summation of electric fields on photodiode halves	111
8.6	Interference between the Hermite-Gauss modes reflected from a resonator	112
8.7	Experimental arrangement for PDH locking and tilt locking	113
8.8	Power and error signal for PDH locking and tilt locking	115
8.9	Error signal frequency spectrum for PDH locking and single pass tilt locking	116
8.10	Experimental arrangement for double pass tilt locking and double pass PDH locking.	117
8.11	Power and error signal for single pass and double pass tilt locking	118
8.12	Difference in power detected on each side of the photodiode as a function of photodiode position	119
8.13	The derivative of the power difference with respect to photodiode position	120
9.1	Graphical representation of the approximation for small sidebands.	124

9.2	The electric fields incident and reflected from a cavity	125
10.1	The quadrant photodiode layout to detect the first higher order modes of the two lasers.	135
10.2	Experimental layout for tilt locking two lasers to one cavity.	136
10.3	The frequency spectrum of the amplitude of the beat note between the two lasers.	137
10.4	The Allan deviation of the beat note frequency	138
10.5	Experiment layout for external cavity second harmonic generation.	139
10.6	Power and error signals recorded as the SHG cavity length was scanned .	140
10.7	Second harmonic amplitude spectra from PDH and tilt locking.	141
10.8	Green output power fluctuations versus error signals	143
10.9	Experimental layout for injection locking experiment	144
10.10	Tilt locking and PDH error signals	145
10.11	Simultaneous measurement of the tilt locking error signal and the PDH error signal	146
10.12	Tilt locking and PDH error signal frequency spectrum	146
10.13	Experimental layout for new injection locking scheme	147
11.1	Vector diagram for the spatial mode interference of a two beam interferometer at a dark fringe.	150
11.2	Vector diagram for the spatial mode interference of a two beam interferometer with a phase shift in each arm.	150
11.3	Experimental layout for tilt locking in a Mach-Zehnder interferometer. . .	151
11.4	Power and error signal as the phase of the Mach-Zehnder is scanned . . .	152
11.5	Two dimensional intensity distribution of the light on the split photodiode	153
11.6	Two dimensional intensity distribution of the light at the bright fringe port	153
11.7	Power and error signals as the Mach-Zehnder phase is scanned.	154
11.8	Experimental layout for a 19.1 m Sagnac interferometer	155
11.9	Sagnac interferometer frequency response	155
A.1	Top down schematic view of the OSA.	161
A.2	Side-on schematic view of the OSA.	162
B.1	Circuit diagram used with the split photodiode.	163
B.2	165
B.3	Laser frequency servo circuit diagram.	166

List of Tables

7.1	Relationships between interferometer lengths and modulation frequencies	76
7.2	Look-up table for subcarrier offset frequency required for signal cavity de-tuning.	79
7.3	Measured intensity reflectivities, transmissivities and radii of curvature for the benchtop prototype mirrors.	81
10.1	Stability parameters of the second harmonic generator locked using both PDH and tilt locking.	142

Introduction

The opening decade of the new millennium should see the first direct detection of gravitational waves. The construction of long base-line interferometric gravitational wave detectors began several years ago and most detectors are expected to begin taking data in the next few years. Although it is hoped that these original detectors will produce the first direct detection of gravitational waves, it is expected that signals will be detected with insufficient regularity and signal to noise ratio to learn much about the sources of these waves.

Even before the first waves have been detected, there are plans to upgrade these interferometers to give vastly improved sensitivities. It is the development of techniques for these second generation detectors which is the focus of this thesis.

1.1 Overview of thesis structure

The work presented here falls into two general areas. The first is gravitational wave interferometer configurations. We report on various experimental investigations of different interferometric configurations performed at the ANU over the last few years. The second topic is a new technique for the readout and control of optical interferometers. This technique, tilt locking, was discovered due to the researchers exposure to frequency locking and autoalignment techniques used in gravitational wave detectors. Although useful for some purposes in gravitational wave detectors, tilt locking can be used in a range of applications outside this field.

This thesis is divided into three parts as shown in figure 1.1. Each part begins with a literature review and a motivation for the work presented. The first part of the thesis (chapters 2-4) is intended to equip the reader with the background knowledge required for the remainder of the thesis.

In chapter 2 we provide an overview of the field of gravitational wave detection. This chapter is intended to provide a basic understanding of gravitational wave detection and give the reader an impression of the current state of gravitational wave research. A more technical discussion of interferometer configuration is reserved for chapter 5.

Chapter 3 is concerned with quantum noise and its implications. We provide a calculation of the phase noise of an electric field based on a few simple assumptions. We present an experimentally relevant model of a single mode and multimode coherent state and use this to calculate the quantum fluctuations in the beam position.

Chapter 4 presents an introduction to modulation and demodulation schemes and their application to interferometer control. We introduce single sideband modulation and demodulation, and double demodulation, as methods for controlling interferometers.

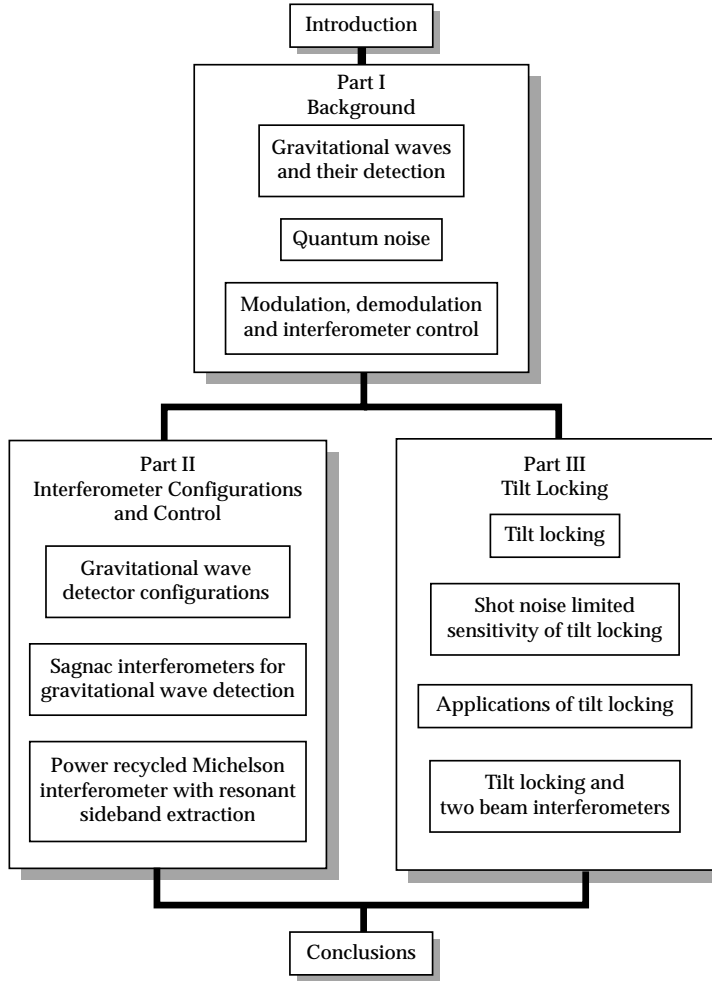


Figure 1.1: Thesis structure.

The second part of the thesis (chapters 5-7) gives an overview of interferometer configurations and presents the interferometer prototype experiments.

Chapter 5 provides a review of interferometric configurations. This discussion is motivated by energy storage and storage time considerations. The chapter includes a derivation of the frequency response of resonant sideband extraction.

In chapter 6 we present an investigation of Sagnac interferometers for gravitational wave detectors. In particular, we report the first demonstration of resonant sideband extraction in a Sagnac interferometer.

Chapter 7 contains the main work of this thesis. The first part of this chapter presents a control system for a power recycled Michelson interferometer with resonant sideband extraction. This control system is implemented in a benchtop prototype interferometer and its performance and features assessed in the latter part of the chapter.

The final part of this thesis (chapters 8-11) presents tilt locking, a technique used for obtaining an error signal for an interferometer.

In chapter 8 we provide a brief introduction to other frequency locking techniques before an introduction to tilt locking.

In chapter 9, using the results of chapter 3, we derive the shot noise limited perfor-

mance of tilt locking. For comparison the same derivation is carried out for the PDH technique.

Chapter 10 presents three experimental demonstrations of tilt locking in three applications: for laser frequency stabilisation, second harmonic generation, and injection locking of a medium power laser.

In chapter 11 we explain how tilt locking can be applied to two beam interferometers. We present experimental demonstrations of tilt locking in a Mach-Zehnder and a Sagnac interferometer.

Chapter 12 presents the conclusions of this thesis. Possible directions for further work are also discussed.

1.2 Publications

Much of the work presented here appears in international journals or conference proceedings. Below is a list of publications resulting from work in this thesis.

D. A. Shaddock, M. B. Gray, and D. E. McClelland, *Experimental demonstration of resonant sideband extraction in a Sagnac Interferometer*, Applied Optics **37**, 7995 (1998).

M. B. Gray, D. A. Shaddock, C. C. Harb, and H.-A. Bachor, *Photodetector designs for low noise, high power and broad band applications*, Rev. Sci. Instrum. **69**, 3755 (1998).

D. A. Shaddock, M. B. Gray, and D. E. McClelland, *Frequency locking a laser to an optical cavity by use of spatial mode interference*, Opt. Lett. **24**, 1499, (1999).

B. B. Buchler, D. A. Shaddock, T. C. Ralph, M. B. Gray, and D. E. McClelland, *Suppression of classic and quantum radiation pressure noise by electro-optic feedback*, Opt. Lett. **24**, 259 (1999).

M. B. Gray, D. A. Shaddock, and D. E. McClelland, *A power-recycled Michelson interferometer with resonant sideband extraction*, in Gravitational Waves: proceedings of the Third Edoardo Amaldi Conference 1999, Pasadena ed. S. Meshkov, 193 (2000).

D. E. McClelland *et. al.*, *Status of the Australian Consortium for Interferometric Gravitational Astronomy*, in Gravitational Waves: proceedings of the Third Edoardo Amaldi Conference 1999, Pasadena ed. S. Meshkov, 140 (2000).

D. A. Shaddock, B. C. Buchler, W. C. Bowen, M. B. Gray, and P. K. Lam *Modulation-free control of a continuous-wave second harmonic generator*, J. Opt. A: Pure & Appl. Opt. **2**, 400 (2000).

K. G. Baigent, D. A. Shaddock, M. B. Gray, and D. E. McClelland, *Laser intensity and frequency stabilisation for a measurement of thermal noise*, General Relativity and Gravitation **32**, 399 (2000).

D. A. Shaddock and M. B. Gray, *Frequency locking a laser to an optical cavity*, International Provisional Patent, Australian National University, June (2000).

D.E. McClelland, D.A. Shaddock and M.B. Gray, *RSE vs a power recycled, FP Michelson with injected squeezed vacuum*, in Gravitational Wave Detection II, Proc. of the Second TAMA Conference, ed. S. Kawamura and N. Mio, Universal Academic Press, 355 (2000).

D. Ottoway, M. B. Gray, D. A. Shaddock, C. Hollitt, P. J. Veitch, J. Munch and D. E. McClelland, *Stabilization of injection-locked lasers using spatial mode interference*, to appear in IEEE J. Quant. Electr. (2001).

Part I

Background

Gravitational waves and their detection

It was nearly a century ago that Einstein published his general theory of relativity [1]. One of the predictions of this theory was the existence of gravitational waves [2]. These waves propagate at the speed of light as perturbations in the curvature of space-time. Although many other predictions of general relativity have since been experimentally verified there has as yet been no direct detection of gravitational waves.

2.1 What are gravitational waves?

Gravitational waves can be understood by analogy to electro-magnetic waves [3]. Just as radio waves are produced due to the motion of a particle with an electric charge, so too are gravitational waves emitted due to the motion of a mass. Both are transverse waves that propagate at the speed of light. One important difference is that both positive and negative charges exist for electro-magnetic interactions, whereas the mass of a particle is always positive. As a consequence, the lowest mode of oscillation for a gravitational wave is quadrupole in nature [4] (compared to the dipole nature of electro-magnetic radiation).

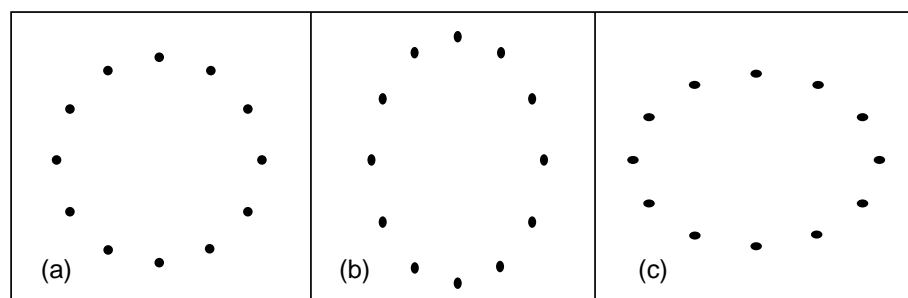


Figure 2.1: Effect of a gravitational wave on a ring of test particles, (a) before interaction, (b) during the first half of the gravitational wave period and (c) during the second half of the gravitational wave period.

To gain an understanding of gravitational waves it is instructive to consider the effects of a gravitational wave on the distance between objects. Consider a ring of particles floating in space as shown in figure 2.1(a). As a gravitational wave passes through these

particles it will perturb the distance between them. Due to its transverse nature, a gravitational wave propagating into the page will perturb the distances in the plane of the page. For the first half of the gravitational wave period the particles will be stretched apart in one axis (chosen here for convenience the vertical), and be brought closer together in the perpendicular (horizontal) axis, as shown in figure 2.1(b). During the second half of the gravitational wave period the distance between the test particles will contract in the vertical axis and expand in the horizontal direction, as illustrated in fig 2.1(c). This is an example of one polarisation of gravitational waves, normally referred to as (+) or \mathbf{h}_+ polarisation. An orthogonally polarised wave, denoted by (\times) or \mathbf{h}_\times , would have the axes of the distortions rotated by 45° .

The strength of a gravitational wave is measured by its strain, \mathbf{h} , which gives an indication of the fractional length change induced by the wave.

$$\frac{\Delta L}{L} = \frac{\mathbf{h}}{2} \quad (2.1)$$

The amount of distortion shown in figure 2.1 is grossly exaggerated. Gravitational waves which produce a fractional length change of the order of 10^{-21} to 10^{-22} are predicted to occur at the rate of only several events per year. If such a wave was to pass between the earth and the sun, their separation would change by less than the radius of a hydrogen atom. To detect the presence of a gravitational wave passing between two objects, we must be able to measure the changes in their separation with unprecedented accuracy.

There is already significant indirect evidence for the existence of gravitational radiation [5]. The Hulse-Taylor Binary Pulsar, PSR1913+16 [6], is a system of two neutron stars in an eccentric orbit. The two stars lose their energy by emitting gravitational wave radiation, which results in a gradual shrinking of the orbit, and a corresponding decrease in their orbital period. The timing of the pulsar can be used to determine the orbital parameters of the system including the masses of the stars. Based on these parameters, the orbital shrinking is predicted by the quadrupole formula of general relativity [3]. These predictions were compared with experimental observations made over several years, and were found to agree to within the experimental uncertainty [7–9].

2.2 Why detect gravitational waves?

The motivation for the direct detection of gravitational waves is two-fold. Initially, direct detection of gravitational waves will provide verification of the predictions of general relativity. It is expected that gravitational radiation will become an important theoretical tool for the understanding of relativistic systems. In addition, detailed measurements of gravitational waves may show a weak scalar component of gravity, which is predicted by various kinds of unified field theories [10].

The prime motivation for detecting gravitational waves is to perform gravitational wave astronomy. If signals can be detected with sufficient signal to noise ratio then careful analysis of the wave form can provide information about the sources of the waves. In many cases this information is not accessible by other forms of astronomy. For example, gravitational waves may provide the only direct observations of black holes. All other information about black holes is indirect, coming from their effects on gas and other objects in their immediate environments. Measurements of the polarisation of the gravitational waves should reveal more information about their sources, such as the orientation of the

orbit of a binary system relative to line of sight.

The difficulty of detection of gravitational waves is a consequence of their weak interaction with matter. One benefit of the faintness of this interaction is that they are not attenuated or scattered on their way to the detector. This means that they can reveal information about areas or processes that are ordinarily obscured, such as the interior of a supernova explosion.

Gravitational wave detection should complement existing forms of astronomy. Through accurate timing of the arrival of gravitational waves at different detectors around the Earth, the position of sources can be determined. Once the position is known, this information can be used to more closely examine the same region of space with traditional forms of astronomy. As both electro-magnetic and gravitational waves are expected to travel at the same speed, this should allow complementary observations of the same processes.

As the vast majority of our contact with the rest of the universe is through electro-magnetic radiation, it is difficult to predict everything that this new form of astronomy will deliver to us. Gravitational waves are emitted by the bulk motions of their sources and not by individual motions of atoms or electrons, thus they can be expected to carry a different kind of information about their sources. One thing that can be learnt from experiences with other “new” astronomies, such as x-ray astronomy and radio astronomy, is that gravitational wave astronomy may one day begin to discover entirely new and unexpected sources. This alone is perhaps the most compelling reason to pursue the detection of gravitational waves.

2.3 Detection of gravitational waves

The direct detection of gravitational waves remains one of the most challenging areas of experimental physics [11]. To achieve the target sensitivity requires pushing the limits of physics and engineering in a number of diverse areas such as seismic isolation, high Q suspensions, continuous-wave lasers, interferometry and materials science.

Efforts to detect gravitational waves were initiated by Joseph Weber in the 1960s [12]. This original type of detector consisted of a massive cylinder or “bar” of aluminium suspended around its circumference in a vacuum chamber. A bar detector’s interaction with a gravitational wave is similar to that of two masses joined by a spring. The passing of a gravitational wave induces vibrations which are measured by some form of transducer on the bar. These detectors exploit the narrow mechanical resonance of the bar to achieve high sensitivities over a bandwidth of a few hertz around the mechanical resonance (typically several hundred hertz). The field of bar detectors remains an active area of research with narrow band strain sensitivities approaching 10^{-19} [13].

2.3.1 Laser interferometric gravitational wave detectors

In the 1970s and 1980s, laser and mirror technologies were reaching the point where gravitational wave detectors based on laser interferometers were becoming a viable alternative to the bar detectors. By the early 1980s three prototype interferometers were operating in Glasgow, Garching, and at MIT, followed shortly after by a prototype at Caltech.

All currently planned long base-line interferometric gravitational wave detectors are based around a Michelson interferometer. A diagram of a Michelson interferometer is

shown in figure 2.2. The beamsplitter divides the incident light into two beams which each propagate down the arms of the interferometer where they are retro-reflected by the test masses. These end mirrors serve the same purpose as the test particles in figure 2.1. The beams are recombined at the same beamsplitter, where the interference is determined by the relative optical phase of the two beams. As the interference is only sensitive to differential changes in the length of the arms the Michelson interferometer is particularly suited to measure the quadrupole motion induced by a gravitational wave. If a gravitational wave of the correct polarisation passes through the Michelson interferometer, one arm of the Michelson will contract and the other arm will expand, resulting in a phase difference of the two beams when they are recombined at the beamsplitter. The Michelson interferometer is operated so that in the absence of a gravitational wave signal, the light from the two arms interferes destructively (produces a “dark fringe”) at the photodetector. When a gravitational wave perturbs the interference, some fraction of the light will be directed towards the photodetector. The sensitive measurement of this light will yield the gravitational wave signal.

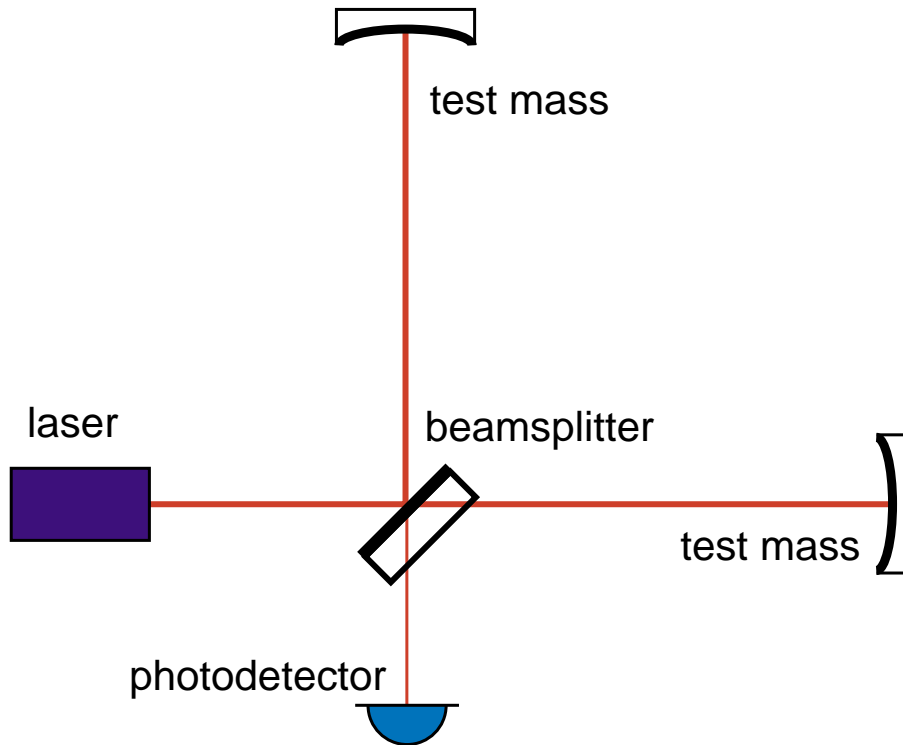


Figure 2.2: Basic layout of a Michelson interferometer.

2.4 Factors affecting sensitivity

The ultimate sensitivity of a gravitational wave detector is determined by the ratio of signal to noise in the final output, thus there are two avenues available to increase the sensitivity of a device. The first is to increase the size of the signal in the final output. A gravitational wave induces a fractional length change (see equation 2.1), however the phase change is proportional to the absolute length change ΔL . Thus the amount of

phase change at the beamsplitter for a given gravitational wave strength can be increased by making the interferometer arms very long. For this reason, gravitational wave detectors will use kilometre scale arms.

The size of the signal can also be increased by increasing the total power of the light in the interferometer arms. A given strength of gravitational wave couples some fraction of the light to the photodetector, so increasing the power in the arms will also increase the power at the dark fringe and consequently the signal. Increasing the signal in this way also increases the contribution of displacement noises, such as thermal noise or seismic noise (discussed below), to the final output by the same amount, and thus no advantage is achieved if these are the limiting noise sources. However one source of noise, shot noise, increases at a slower rate than the signal as the power is increased and thus a net increase in sensitivity can be achieved by increasing the power where this is the limiting noise source.

The sensitivity of a detector can also be improved by decreasing the noise in the final output. The final noise floor of a gravitational wave detector will originate from several different sources, each dominating the noise over different frequency ranges.

2.4.1 Shot noise

Shot noise is expected to be the dominant noise source at frequencies above a few hundred hertz. This noise is quantum mechanical in origin and is a consequence of the intrinsic randomness of light. Shot noise at the interferometer output arises from the fluctuations in phase of the beams in the interferometer arms. As described above, a Michelson responds to phase difference in the interferometer arms. If these beams have (uncorrelated) fluctuations in phase, they will pass through to the photodetector in the same way as the phase fluctuations induced by the gravitational waves. In chapter 3 we will provide a detailed calculation of the quantum mechanical phase fluctuations, showing that the level of these fluctuations is inversely proportional to the power. As a consequence, the shot noise limited sensitivity of a gravitational wave detector can be improved by increasing the optical power in the arms.

The effect of this noise source on the overall sensitivity of the device can be manipulated by the optical configuration of the detector. In chapter 5, we will discuss the use of optical cavities and recycling techniques to increase the power in the arms as well as manipulate the signal response.

2.4.2 Radiation pressure noise

In 1619 Johannes Kepler proposed that it was the pressure of sunlight that caused a comet's tail to always point away from the sun [14]. The pressure of light, or radiation pressure, is important in setting the limits of a gravitational wave detector. Radiation pressure refers to the force exerted on an object by light striking or reflecting from it. A photon carries a momentum of h/λ , where h is Planck's constant, and as this light is reflected it imparts a certain amount of momentum to the reflector. If the reflection is at normal incidence each photon will give the object a momentum kick of $2h/\lambda$ (the factor of two is present as the photon's direction is reversed). In a typical laser beam there are many billions of billions of photons and the combined force on a mirror can become considerable.

Radiation pressure in this form does not, in principle, introduce noise to the output

of a gravitational wave detector as the average power in each arm is equal and thus the radiation pressure is correlated. Radiation pressure *noise* arises from the uncorrelated fluctuations of the power of each arm. These fluctuations in power are also quantum mechanical in nature and originate from the random partitioning of photons into each arm of the detector by the beamsplitter.

Radiation pressure noise is expected to be too small to limit the sensitivity of first generation detectors. The intensity fluctuations, and thus the absolute force fluctuations on the mirror, increase with the power until eventually a limit will be reached where the interferometer will be equally sensitive to fluctuations of the photon number and fluctuations of the phase of the beam. This is known as the standard quantum limit [15, 16].

It is important to note that neither shot noise nor radiation pressure noise is effected by the phase or intensity noise of the input laser in an ideal interferometer. This is because these noise sources are proportional to the uncorrelated part of the fluctuations in the arms, and all phase and intensity fluctuations coming from the laser will be completely correlated.

2.4.3 Thermal Noise

Thermal noise [17] is expected to dominate the noise floor between a few tens of hertz and a few hundred hertz in first generation detectors. Thermal noise refers to the motion of the mirror due to thermal energy. It originates from three main areas: the pendulum modes of the suspension, the violin modes of the suspension wires, and the internal modes of the test mass. Each of these will exhibit resonances in different frequency ranges. Unlike bar detectors, interferometers will measure at frequencies away from mechanical resonances. For example, the pendulum modes are typically below and the internal mirror modes typically above the detection bandwidth. Only the violin modes lie inside the range of observational frequencies. Each mode of oscillation has a thermal energy of $k_B T$ at a temperature T , where this energy is distributed across a range of frequencies. To reduce the thermal noise within the measurement band, typically a very high quality factor Q is desired. By increasing the Q of the suspension system all of the thermal energy is condensed into a narrow region around the resonance, and thus the influence of the thermal noise outside this region is reduced. For an excellent review of this area see ref. [11].

2.4.4 Seismic noise

The motion of the mirrors due to seismic noise must be reduced to below the level induced by gravitational waves. The typical seismic noise in reasonably quiet areas is around $10^{-7}/f^2 \text{ m}/\sqrt{\text{Hz}}$ at frequencies above approximately 1 Hz. In order to achieve target strain sensitivities, seismic motion of the mirrors must be reduced by approximately 9 orders of magnitude, and even more at low frequencies. By suspending the mirrors on pendula, the vibrations are attenuated by a factor of f^2/f_0^2 , for frequencies above the resonant frequency f_0 . This alone does not provide the necessary isolation and it must be used with a combination of other techniques (both active and passive) to reduce the noise to the desired value. This noise will be the limiting noise source of first generation detectors at low frequencies.

2.4.5 Gravity gradient noise

Even if seismic noise could be completely removed there would still exist a lower frequency cut-off of the bandwidth of ground based detectors. This arises from gravity gradient noise, which is the direct gravitational coupling of the test masses to their outside environment. Gravity gradient noise on Earth is much larger than the amplitude of any expected waves from astronomical sources at frequencies below about 1 Hz [10].

2.5 Current status

Today there are many detectors nearing completion around the world. These include LIGO [18], which consists of a 4 km and 2 km detector in Hanford, Washington and a second 4 km detector in Livingston, Louisiana in the United States, VIRGO [19], a 3 km detector situated near Pisa, Italy, GEO600 [20], a 600 m detector outside of Hannover, Germany and TAMA300 [21], a 300 m detector in Tokyo, Japan. All of these detectors are due to become operational in the next few years, with target strain sensitivities of 10^{-22} to 10^{-23} .

In addition to these detectors, research and development continues for a future Australian gravitational wave detector [22]. The Australian Consortium for Interferometric Gravitational Astronomy (ACIGA) [23] is involved in several areas of research related to long base-line interferometers, including high power laser development, suspensions and isolation systems, data analysis and advanced interferometric techniques. Construction of an 80 m test facility near Perth in Western Australia began in 1998 and work is progressing well. This facility has the potential to be extended to a 4 km gravitational wave detector which would provide the global network of detectors with its first southern hemisphere component.

2.6 Space-based detectors

Looking further to the future, space-based gravitational wave detectors are essential for the full potential of gravitational wave astronomy to be realised. Gravity gradient noise will ultimately limit the minimum frequency at which gravitational waves can be measured on Earth. This noise source, however, is inversely proportional to the cube of the distance from Earth and so by moving the detector into space the noise can be substantially reduced. There are plans for a laser interferometer space antenna (LISA) [24] which will consist of three spacecraft each separated by 5×10^6 km, orbiting the sun. LISA will allow measurements of gravitational waves in the frequency band of 0.1 mHz to 0.1 Hz. Operating in the low frequency band, LISA's sensitivity will be complementary to the ground based detectors. LISA promises to provide signal to noise ratios of up to 10^3 for events such as the coalescence of massive black hole binaries [25]. Moreover, due to the much lower frequency range, these massive black hole binaries will be visible for many months before coalescence. The LISA project is currently being studied by both ESA and NASA with a view toward a collaborative mission around 2010.

2.7 Summary

The expected sensitivity of the first generation detectors is such that the first direct detection of gravitational waves may be achieved. However, to extend the detection of gravitational waves into a useful form of astronomy will require further improvements in the sensitivities and frequency responses of these devices. As we approach the end of the construction phase of the first generation detectors, research and development focus is shifting to meet the demands of second generation detectors. It is hoped that these second generation detectors, with their improved sensitivity and source detection rates, will herald the beginning of the new field of gravitational wave astronomy. These detectors will require significant improvements in almost every area, including suspension systems, mirrors, lasers and the interferometer configuration. It is this second generation of interferometers which is the main focus of the work presented here.

Quantum noise

Throughout this thesis we will be concerned with the fluctuations or *noise* of particular parameters, such as laser intensity, laser phase or beam position. In practice, fluctuations can be reduced or suppressed by the use of feedback systems. However, there exists a fundamental limit to the final noise level. This limit is set by quantum mechanics.

In this chapter we introduce some of the methods used to calculate the quantum noise level and perform a few key calculations, the results of which will be used in subsequent chapters. In the next section we discuss the Heisenberg Uncertainty Principle and its consequences. In section 3.2 we derive the quantum phase noise for a Poissonian distribution using classical techniques with a few basic assumptions. Section 3.3 introduces the linearised operator approach to calculating quantum noise. This approach is extended in section 3.6 to deal with multi-spatial modes to calculate the quantum limit of beam position noise.

3.1 The Heisenberg Uncertainty Principle

The Heisenberg Uncertainty Principle states that it is impossible to obtain simultaneous precise knowledge of two noncommuting variables. If two observables are related to each other via the commutator relation,

$$[\hat{O}_+, \hat{O}_-] = \epsilon \quad (3.1)$$

then the following uncertainty relation exists between the standard deviations of these observables,

$$\Delta\hat{O}_- \Delta\hat{O}_+ \geq \frac{1}{2}|\epsilon| \quad (3.2)$$

The best known form of the uncertainty principle is the position-momentum uncertainty relation. In this thesis we will be most concerned with the photon number-phase uncertainty relation for light,

$$\Delta n \Delta\phi \geq \frac{1}{2} \quad (3.3)$$

3.2 Classical calculations of quantum noise

In this section we will derive the level of quantum phase noise of a coherent state based on 2 assumptions: (i) the variance of the photon number of a coherent state is equal to the photon number and (ii) the fluctuations in the electric field are the same in all directions.

Consider a measurement of the number of photons, n , recorded over a detection interval of time τ . We can build up a probability distribution by plotting a histogram of n over many such detection intervals. For a coherent state this photon number distribution is well approximated by a Poissonian distribution. The distribution has the characteristic that the variance, $(\Delta n)^2$, is equal to the average photon number \bar{n} . Thus for a coherent state we have a standard deviation of $\Delta n = \sqrt{\bar{n}}$.

We now calculate the equivalent electric field standard deviation due to the photon number fluctuations. Given that $E^*E = P = h\nu n$, we can write,

$$|E| = \sqrt{h\nu n} \quad (3.4)$$

Using the relation,

$$\begin{aligned} \Delta|E| &= \frac{d|E|}{dn} \Delta n \\ &= \frac{1}{2} \sqrt{\frac{h\nu}{n}} \Delta n \\ &= \frac{\sqrt{h\nu}}{2} \end{aligned} \quad (3.5)$$

This is an interesting result as it shows that the variation in the magnitude of the electric field is a constant and thus independent of the photon number. In fact, even if the photon number were zero the fluctuations in the electric field would remain¹. This intrinsic variance is referred to as the *vacuum fluctuations* and is an important concept which will be dealt with later in this chapter.

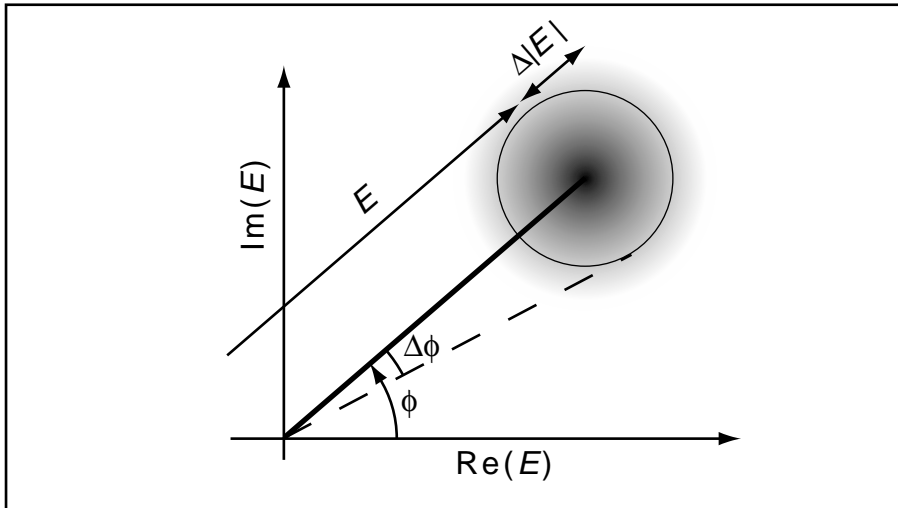


Figure 3.1: Ball-on-stick picture showing the coherent amplitude as the stick with quantum noise represented by the outline of the circle or “ball”. The shaded region represents the probability distribution of E where the circle is the standard deviation of this distribution.

Consider the ball-on-stick picture of figure 3.1. The stick represents the average value

¹Although this simple proof is not strictly valid for small photon numbers, the result still holds.

of the electric field and the ball represents the statistical deviation around this point. For a coherent state the ball is perfectly round, indicating that the fluctuations are isotropic. We can use this property to calculate the phase noise $\Delta\phi$ directly from $\Delta|E|$.

$$\begin{aligned}\Delta\phi &= \frac{\sqrt{h\nu}}{2} \cdot \frac{1}{\sqrt{h\nu\bar{n}}} \\ &= \frac{1}{2\sqrt{\bar{n}}}\end{aligned}\tag{3.6}$$

Note that together $\Delta n = \sqrt{\bar{n}}$ and equation 3.6 obey the uncertainty principle,

$$\Delta n \Delta\phi = \sqrt{\bar{n}} \frac{1}{2\sqrt{\bar{n}}} = \frac{1}{2}\tag{3.7}$$

The significance of the equality is that the variances are the minimum permitted by the uncertainty principle and such a state is a *minimum uncertainty state*.

3.3 Quantum mechanical calculations

If the fluctuations of an electromagnetic field are small compared to its steady state amplitude, we can represent the annihilation operator [26] by,

$$\hat{a}(t) = \alpha + \delta\hat{a}(t)\tag{3.8}$$

where all of the fluctuations are contained in the operator $\delta\hat{a}(t)$, and α is a complex number representing the classical steady state component. With reference to figure 3.1, $\delta\hat{a}(t)$ is analogous to the ball and α represents the stick (we assume that α is real for the calculations below). The fluctuating term has an average of zero, that is $\langle\delta\hat{a}(t)\rangle = 0$. We will refer to the annihilation operator as a function of time simply as \hat{a} and as a function of frequency as $\tilde{\hat{a}}$ (the Fourier transform of \hat{a}).

The photon number operator, \hat{n} is given by $\hat{a}^\dagger\hat{a}$ (the operator analogue of $P = E^*E$),

$$\hat{a}^\dagger\hat{a} = (\alpha + \delta\hat{a}^\dagger)(\alpha + \delta\hat{a})\tag{3.9}$$

$$= \alpha^2 + \alpha(\delta\hat{a} + \delta\hat{a}^\dagger) + \delta\hat{a}^\dagger\delta\hat{a}\tag{3.10}$$

In the linearised formalism [27, 28], $|\delta\hat{a}| \ll |\alpha|$, and we can neglect terms containing higher order products of the quantum fluctuations, $\delta\hat{a}$. Equation 3.10 becomes,

$$\hat{n} \approx \alpha^2 + \alpha(\delta\hat{a} + \delta\hat{a}^\dagger)\tag{3.11}$$

The average photon number can be found by taking the expectation value of equation 3.11. The second term in this equation contains terms that have a zero average, thus the expectation value of the photon number operator is equal to,

$$\langle\hat{n}\rangle = \alpha^2\tag{3.12}$$

The variance of the photon number is given by,

$$(\Delta\hat{n})^2 = \langle\hat{n}^2\rangle - \langle\hat{n}\rangle^2\tag{3.13}$$

$$= \langle(\hat{a}^\dagger\hat{a})^2\rangle - \langle\hat{a}^\dagger\hat{a}\rangle^2\tag{3.14}$$

$$= \alpha^2 (\delta\hat{a} + \delta\hat{a}^\dagger)^2 \quad (3.15)$$

$$= \alpha^2 \delta\hat{X}_a^{+2} \quad (3.16)$$

where $\delta\hat{X}_a^+ = (\delta\hat{a} + \delta\hat{a}^\dagger)$ is the amplitude quadrature fluctuations of the field. For a coherent state $\delta\hat{X}_a^+ = 1$, and the fluctuations in the photon number are characterised by,

$$(\Delta\hat{n})^2 = \alpha^2 \quad (3.17)$$

$$= \langle \hat{n} \rangle \quad (3.18)$$

This indicates that, for a coherent state, the variance of the photon number operator is equal to its expectation value. This is in agreement with the classical expression for the noise, $\Delta n = \sqrt{n}$ given in section 3.2.

The vacuum state is a special case of the coherent state which contains fluctuations but no coherent amplitude. As we will see in section 3.4 and 3.6, vacuum states can be used to model loss in an optical system. The annihilation operator for the vacuum, \hat{v} , can be represented by,

$$\hat{v} = \delta\hat{v} \quad (3.19)$$

However the amplitude quadrature fluctuations of the vacuum are the same as all coherent states.

$$\delta\hat{X}_v^+ = (\delta\hat{v} + \delta\hat{v}^\dagger) = 1 \quad (3.20)$$

3.4 Model for a coherent state

The quantum state most closely resembling a laser is the coherent state [29]. A coherent state can be expressed as an infinite sum of Fock states or number states. This expression may be somewhat unsatisfying for the experimentalist. When can it be assumed that a laser is a coherent state? How can a coherent state be produced experimentally? Figure 3.2 shows one possible scheme for production using a modecleaner cavity. The modecleaner is assumed to be perfect, in the sense that it has an infinite free spectral range (FSR), infinitesimal bandwidth, with 100% transmission exactly on resonance and 0% everywhere else.

Consider the linearised form of the input field annihilation operator,

$$\tilde{\hat{a}}(\omega) = \alpha\delta(0) + \delta\tilde{\hat{a}}(\omega) \quad (3.21)$$

where $\delta(0)$ is a delta function at $\omega = 0$. If we assume that the input field is on resonance with the modecleaner cavity then the only component of the input field which will make it to the output is α , and all of the fluctuations will be reflected off. The output field at all other frequencies will be that made up of the field incident on the empty port of the cavity, in this case the vacuum fluctuations. The output field annihilation operator will be given by,

$$\tilde{\hat{b}}(\omega) = \alpha\delta(0) + \delta\tilde{\hat{v}}(\omega) \quad (3.22)$$

This field has all the characteristics of a coherent state and will be used as a working model of a coherent state for subsequent discussions and calculations.

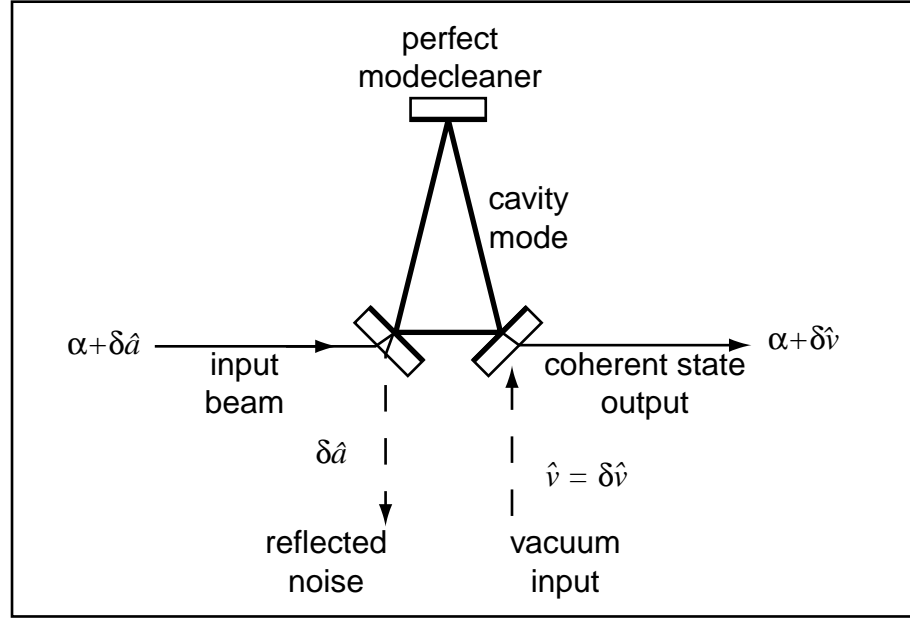


Figure 3.2: Method for producing a coherent state with a perfect mode cleaner.

3.5 Hermite-Gauss modes

A large part of this thesis is concerned with measuring the interference between different spatial modes. The aim of this section is to introduce the mathematical formalism used to describe these modes and their properties.

We choose the Hermite-Gauss modes [30, 31] as a basis for describing the transverse spatial beam profile. The Hermite-Gauss modes are made up of the Hermite polynomials multiplied by a Gaussian function. The first few Hermite polynomials are listed below.

$$\begin{aligned}
 H_0(x) &= 1 \\
 H_1(x) &= 2x \\
 H_2(x) &= 4x^2 - 2 \\
 H_3(x) &= 8x^3 - 12x
 \end{aligned} \tag{3.23}$$

Subsequent Hermite polynomials can be found using the recurrence relation,

$$H_{n+1}(x) = 2xH_n(x) - 2nH_{n-1}(x) \tag{3.24}$$

One important property of the Hermite polynomials is the orthogonality relation,

$$\int_{-\infty}^{\infty} H_n(x)H_m(x)e^{-x^2}dx = \sqrt{\pi}2^n n! \delta_{n,m} \tag{3.25}$$

where $\delta_{n,m}$ is the discrete delta function. Note that the integral only results in zero when the factor of e^{-x^2} is included in the integrand.

The Hermite-Gauss modes are obtained by multiplying the Hermite polynomials (with an argument $\sqrt{2}x$ instead of x) by a Gaussian function. We denote the n th Hermite-

Gauss mode by $u_n(x)$.

$$u_n(x) = H_n(\sqrt{2}x)e^{-x^2} \quad (3.26)$$

The orthogonality of the Hermite-Gauss modes follows directly from the orthogonality relation for the Hermite polynomials (equation (3.25))

$$\begin{aligned} \int_{-\infty}^{\infty} u_n(x)u_m(x)dx &= \int_{-\infty}^{\infty} H_n(\sqrt{2}x)e^{-x^2} H_m(\sqrt{2}x)e^{-x^2} dx \\ &= \int_{-\infty}^{\infty} H_n(\sqrt{2}x)H_m(\sqrt{2}x)e^{-2x^2} dx \end{aligned} \quad (3.27)$$

we now make the substitution $x' = \sqrt{2}x$ (and $dx' = \sqrt{2}dx$) and so equation (3.27) becomes,

$$\begin{aligned} \int_{-\infty}^{\infty} u_n(x)u_m(x)dx &= \frac{1}{\sqrt{2}} \int_{-\infty}^{\infty} H_n(x')H_m(x')e^{-x'^2} dx' \\ &= \frac{\sqrt{\pi}}{\sqrt{2}} 2^n n! \delta_{n,m} \end{aligned} \quad (3.28)$$

For convenience we choose to use the normalised versions of the Hermite-Gauss modes, which satisfy the orthonormality condition of equation (3.29).

$$\int_{-\infty}^{\infty} u_n(x)u_m(x)dx = \delta_{n,m} \quad (3.29)$$

In general the transverse electric field distribution is a two dimensional function of x and y . Different spatial modes can be present in each dimension and so the two dimensional electric field will be represented by $u_{mn}(x, y)$ where m and n denote the mode number in the x and y directions respectively. We will be primarily concerned with the first two Hermite-Gauss modes $u_{00}(x, y)$ and $u_{10}(x, y)$. If we assume that the entire beam is detected in the y direction we can use the one dimensional version of the modes $u_0(x)$ and $u_1(x)$ without loss of generality. These modes are related to the two dimensional version by,

$$u_0(x) = \int_{-\infty}^{\infty} u_{0m}(x, y)dy \quad (3.30)$$

$$u_1(x) = \int_{-\infty}^{\infty} u_{1n}(x, y)dy \quad (3.31)$$

Although this is true for all m and n , unless otherwise mentioned it should be assumed that $m = n = 0$ in equations 3.30 and 3.31.

The electric fields of the first two Hermite-Gauss modes, the TEM₀₀ and TEM₁₀ modes are displayed below.

$$u_0(x) = \left(\frac{2}{\pi}\right)^{\frac{1}{4}} \left(\frac{1}{w}\right)^{\frac{1}{2}} e^{-\left(\frac{x^2}{w^2}\right)} \quad (3.32)$$

$$u_1(x) = \left(\frac{2}{\pi}\right)^{\frac{1}{4}} \left(\frac{1}{w}\right)^{\frac{3}{2}} 2xe^{-\left(\frac{x^2}{w^2}\right)} \quad (3.33)$$

The beam radius, w , has been included in the expressions. The electric fields from equations 3.32 and 3.33 are plotted in figure 3.3.

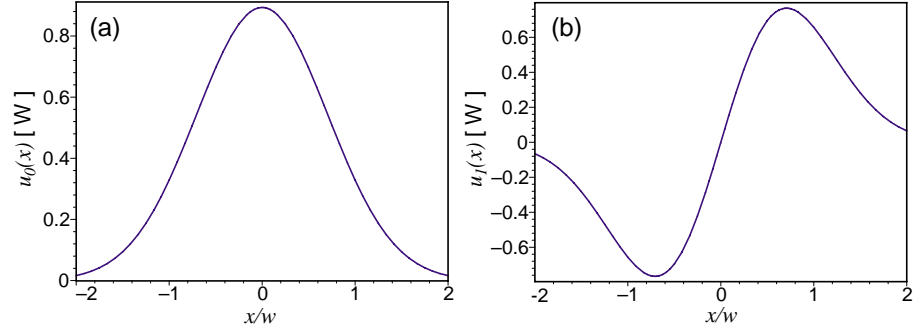


Figure 3.3: (a) TEM₀₀ and (b) TEM₁₀ as a function of x/w .

3.6 Quantum limit of beam position noise

In this section we show how the quantum noise of the higher order Hermite-Gauss modes leads to fluctuations of the beam position. A knowledge of this noise floor will be required to calculate the signal to noise ratio of tilt locking in chapter 9. In particular, we are interested in the difference in power measured by each element of a two element photodiode. First we need to expand our definition of a coherent state to incorporate spatial modes.

Consider the mode cleaner of figure 3.4. We again assume this to be a “perfect” mode cleaner, that is, it has a transmission of unity for the TEM₀₀ mode (on resonance) and is completely reflective for all other frequencies and higher order spatial modes. The operator for the $u_0(x)$ mode at the input will once again be given by,

$$\tilde{a}(\omega) = \alpha\delta(0) + \delta\tilde{a}(\omega) \quad (3.34)$$

This field at the input will contain other higher order spatial modes. However, these higher order modes are reflected from the cavity at the input, and thus they must necessarily have vacuum mode inputs at the output coupler. The annihilation operator for the field at the output of this modecleaner will be,

$$\hat{b} = \alpha u_0(x) + \sum_{i=0}^{\infty} \delta\hat{v}_i u_i(x) \quad (3.35)$$

We now consider the power detected on a two element split photodetector. We are interested in the difference n_D between the photon numbers on the left and right halves of the detector, n_L and n_R respectively.

$$\begin{aligned} n_D &= n_L - n_R \\ &= \int_{-\infty}^0 \hat{b}^\dagger \hat{b} dx - \int_0^{\infty} \hat{b}^\dagger \hat{b} dx \\ &= \int_{-\infty}^0 \alpha^2 u_0^2(x) + \sum_{i=1}^{\infty} (\alpha\delta\hat{v}_i + \delta\hat{v}_i^\dagger\alpha) u_0(x) u_i(x) + \sum_{i=1}^{\infty} \sum_{j=1}^{\infty} \delta\hat{v}_i^\dagger \delta\hat{v}_j u_i(x) u_j(x) dx \\ &\quad - \int_0^{\infty} \alpha^2 u_0^2(x) + \sum_{i=1}^{\infty} (\alpha\delta\hat{v}_i + \delta\hat{v}_i^\dagger\alpha) u_0(x) u_i(x) + \sum_{i=1}^{\infty} \sum_{j=1}^{\infty} \delta\hat{v}_i^\dagger \delta\hat{v}_j u_i(x) u_j(x) dx \end{aligned}$$

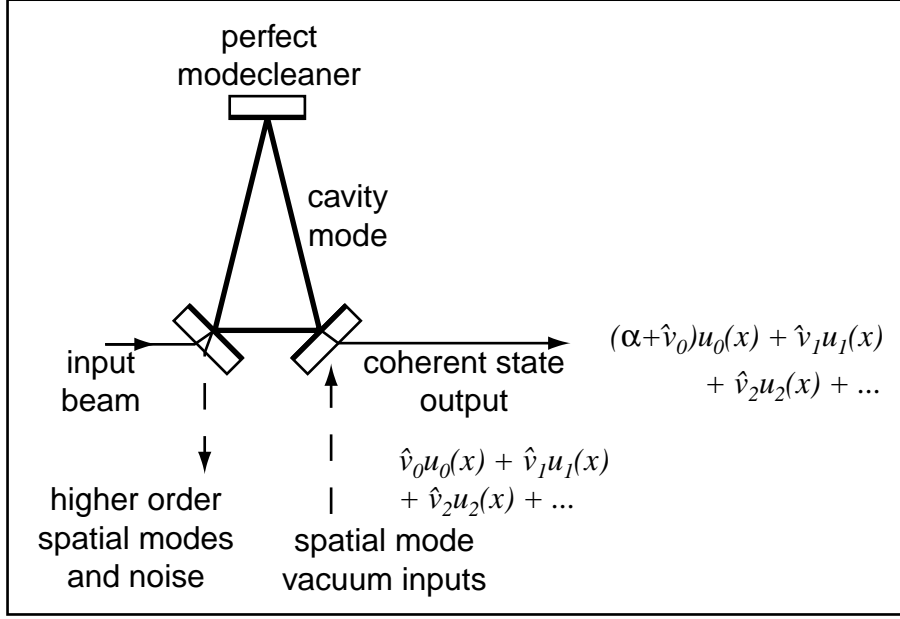


Figure 3.4: Production of a coherent state where higher order Hermite-Gauss modes are included.

(3.36)

Equation (3.36) shows the photon number on each side of the detector has three contributions. The first is the standard power term and is equal on both sides of the detector (due to the symmetry of the $u_0(x)$ mode) and thus will be cancelled by the subtraction. The second term is an interference term between the $u_0(x)$ input mode and the higher order modes. The third term arises from the powers of the vacuum modes and their interference. This term is of second order and can be neglected, which leaves us with the slightly simpler equation,

$$n_D = \int_{-\infty}^0 \sum_{i=1}^{\infty} (\alpha \delta \hat{v}_i + \delta \hat{v}_i^\dagger \alpha) u_0(x) u_i(x) dx - \int_0^{\infty} \sum_{i=1}^{\infty} (\alpha \delta \hat{v}_i + \delta \hat{v}_i^\dagger \alpha) u_0(x) u_i(x) dx \quad (3.37)$$

To aid the analysis we introduce a new mode², which we refer to as the *flipped* mode, denoted by $u_f(x)$ and defined as,

$$\begin{aligned} u_f(x) &= u_0(x) & \text{for } x \leq 0 \\ &= -u_0(x) & \text{for } x \geq 0 \end{aligned} \quad (3.38)$$

The flipped mode is just $u_0(x)$ with a phase flip at $x = 0$ and is pictured in figure 3.5.

Substituting $u_f(x)$ for $u_0(x)$ in equation (3.37) allows us to combine the two integrals into a single integral from $-\infty$ to ∞ . This is important as the orthogonality relationship

²Actually, $u_f(x)$ is an infinite sum of the odd modes.

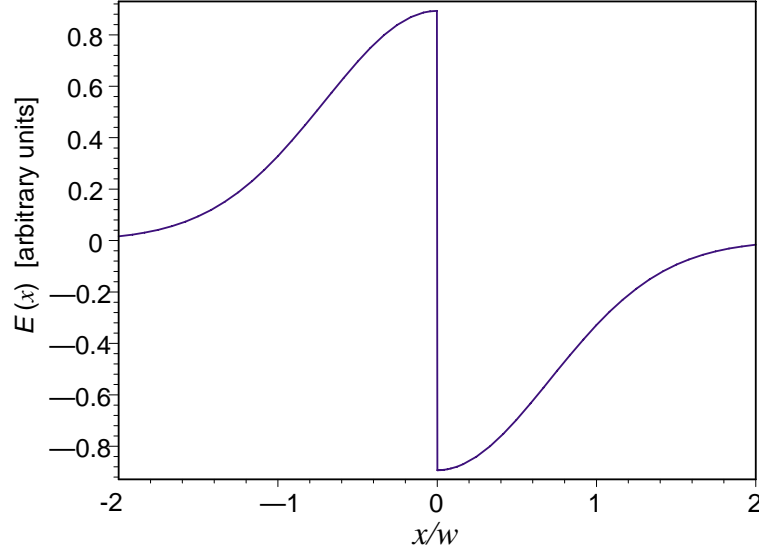


Figure 3.5: The electric field of the flipped mode is equal to the fundamental (gaussian) mode with a phase flip at $x = 0$.

only holds for an integral over all space.

$$n_D = \int_{-\infty}^{\infty} \sum_{i=1}^{\infty} (\alpha \delta \hat{v}_i + \delta \hat{v}_i^\dagger \alpha) u_f(x) u_{i0}(x) dx \quad (3.39)$$

We now decompose $u_f(x)$ into a sum of the orthonormal Hermite-Gauss modes,

$$u_f(x) = \sum_{i=1}^{\infty} c_i u_i(x) \quad (3.40)$$

where c_i is the coefficient of the $u_i(x)$ mode and can be determined in the usual way,

$$c_i = \int_{-\infty}^{\infty} u_f(x) u_i(x) dx \quad (3.41)$$

Making the substitution and bringing the operators outside of the integral gives,

$$n_D = \sum_{i=1}^{\infty} c_i (\alpha \delta \hat{v}_i + \delta \hat{v}_i^\dagger \alpha) \int_{-\infty}^{\infty} u_i^2(x) dx \quad (3.42)$$

$$= \alpha \sum_{i=1}^{\infty} c_i (\delta \hat{v}_i + \delta \hat{v}_i^\dagger) \quad (3.43)$$

The result of the integration is unity due to the normalised Hermite-Gauss basis. In addition, $(\delta \hat{v}_i + \delta \hat{v}_i^\dagger) = \delta \hat{X}_{v_i}^+$ from equation 3.20, and therefore the difference in the photon number on each side of the photodiode becomes,

$$n_D = \alpha \sum_{i=1}^{\infty} c_i \delta \hat{X}_{v_i}^+ \quad (3.44)$$

The variance of the photon number difference, $(\Delta n_D)^2$ is determined by the standard variance equation:

$$\begin{aligned}
 (\Delta n_D)^2 &= \langle n_D^2 \rangle - \langle n_D \rangle^2 \\
 &= \langle n_D^2 \rangle \\
 &= \alpha^2 \sum_{i=1}^{\infty} c_i^2 \langle (\delta \hat{X}_{v_i}^+)^2 \rangle + \alpha^2 \sum_{i=1}^{\infty} \sum_{j \neq i} c_i c_j \langle \delta \hat{X}_{v_i}^+ \delta \hat{X}_{v_j}^+ \rangle
 \end{aligned} \tag{3.45}$$

The second term contains the expectation value of the product of two uncorrelated vacuums, and so will yield zero. The first term contains the expectation value of the square of vacuum mode amplitude quadrature fluctuations which is equal to unity for each of the i vacuum modes.

$$(\Delta n_D)^2 = \alpha^2 \sum_{i=1}^{\infty} c_i^2 \tag{3.46}$$

To determine the sum of the coefficients, c_i^2 , we note that,

$$\begin{aligned}
 \int_{-\infty}^{\infty} \sum_{i=1}^{\infty} (c_i u_i(x))^2 dx &= \int_{-\infty}^{\infty} u_f^2(x) dx = \int_{-\infty}^{\infty} u_0^2(x) dx \\
 \sum_{i=1}^{\infty} c_i^2 \int_{-\infty}^{\infty} u_i^2(x) dx &= 1 \\
 \Rightarrow \sum_{i=1}^{\infty} c_i^2 &= 1
 \end{aligned} \tag{3.47}$$

Using this result and recalling that $\alpha^2 = \bar{n}$ (where \bar{n} is the total number of photons detected on both sides of the detector) gives the variance of the difference in the photon number measured on each half of the photodetector of,

$$(\Delta n_D)^2 = \bar{n} \tag{3.48}$$

which gives a standard deviation, Δn_D of,

$$\Delta n_D = \sqrt{\bar{n}} \tag{3.49}$$

This result is in agreement with the working assumption that shot noise is proportional to the square root of the power on the photodetector. Although the calculation performed here assumes that the only coherent amplitude is in the TEM₀₀ mode, we state here without proof that this relationship holds for any one of the spatial modes, and thus any combination of spatial modes, whose individual fluctuations can be expressed as uncorrelated vacuum modes.

In chapter 9, we will require the standard deviation of the power fluctuations due to quantum noise. To convert from photon number to power we can make the substitutions³ $\Delta n_D = \Delta P_D / h\nu$, and $\sqrt{\bar{n}} = \sqrt{\bar{P} / h\nu}$, so equation 3.49 becomes

$$\Delta P_D = \sqrt{\bar{P} h\nu} \tag{3.50}$$

³Where we define the measurement interval τ to be 1 second.

where \bar{P} is the total power on the detector.

3.7 Summary

Based on the assumption that the electric field fluctuations are isotropic, we have demonstrated that the presence of fluctuations in the photon number of $\Delta n = \sqrt{n}$ implies a phase fluctuation of $\Delta\phi = 1/(2\sqrt{n})$ radians. Thus as the power is increased the level of phase fluctuations is decreased. This has important consequences for a gravitational wave detector. Recall from section 2.4.1 that the phase noise of the beams in the arms is responsible for shot noise at the dark fringe. The larger the phase noise is the larger the phase shift due to the gravitational wave must be in order to be observed. Increasing the power of the laser will result in lower random phase fluctuations and the ability to measure a smaller gravitationally induced phase shift. This issue will be further discussed in chapter 5.

We have presented an experimentally based “definition” of a coherent state for single-spatial mode and multi-spatial mode beams. Using the linearised operator formalism we have shown that the standard deviation of the difference in photon numbers on each half of a beam is equal to the square root of the total photon number. This result will be used in chapter 8 for the calculation of the shot noise limited sensitivity of tilt locking.

Modulation, demodulation and interferometer control

Most types of interferometers require constant monitoring and feedback to maintain various parameters at their correct operating points. The first step towards achieving this is to obtain an error signal. An error signal is a signal which is proportional to the error between the current operating condition and the desired operating condition. This error signal can then be used in some form of feedback loop to actively control or lock a particular parameter to that desired value. Typical gravitational wave detectors will require many parameters to be locked simultaneously, including longitudinal and alignment degrees of freedom. In this thesis we will concentrate only on error signals for longitudinal degrees of freedom. To produce such an error signal we use techniques which require some form of optical modulation. This modulation is normally imposed on the field before it enters the interferometer (as modulator crystals inside the interferometer degrade performance by introducing extra losses and distortion). The light exiting the interferometer is detected and demodulated and the difference between the modulation imposed on the light and the modulation after interaction with the interferometer can be used to determine the interferometers operating condition in the form of an error signal. This chapter gives a basic introduction to modulation and demodulation and explains how they can be used to obtain an error signal for various types of interferometers.

4.1 Phase and amplitude modulation

Phase modulation can be produced by modulating the length of a beam's optical path. This is often as simple as varying the position of a mirror, however for high speed modulation the electro-optic effect of certain crystals (for example lithium niobate, LiNbO_3) is often utilised. Regardless of the method of production, the desired result is a time varying change in the phase of the field. Figure 4.1(a) shows a phasor diagram of a phase modulated laser beam with a modulation depth of δ [radians] and an angular frequency of ω_m [radians/second]. The dotted line represents the phase of the unmodulated field.

Mathematically, the phase modulated beam can be represented by,

$$E_0 e^{i(\omega t + \delta \sin(\omega_m t))} \quad (4.1)$$

where $E_0 e^{i\omega t}$ is the electric field prior to modulation. As shown in figure 4.1(b), for small modulation depth ($\delta \ll 1$) the field can be decomposed into the sum of two vectors, the original field before modulation (which is referred to as the carrier field), and a vector

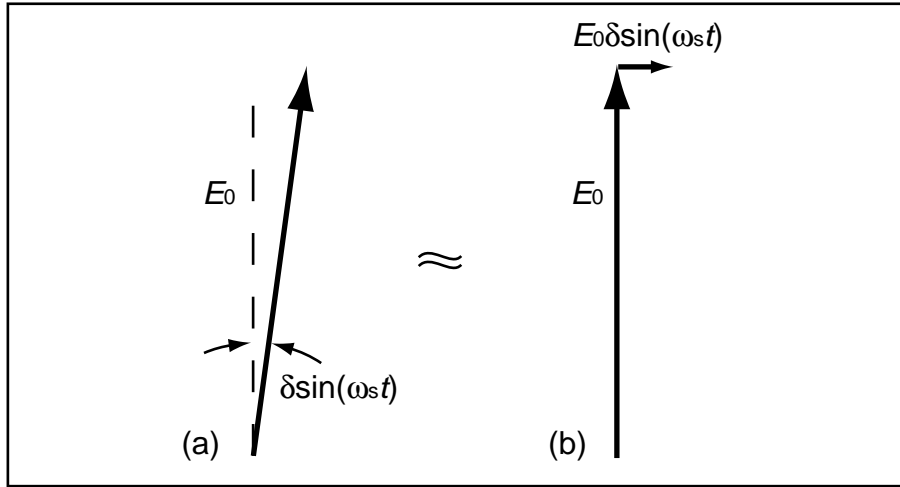


Figure 4.1: (a) Phasor diagram of phase modulation of light, and (b) the decomposition into a carrier and sidebands (assuming small modulation depth).

at 90° to the carrier with a magnitude oscillating at ω_m . This oscillating vector can be further decomposed into two single sidebands of constant magnitude each offset from the carrier in frequency by an amount $\pm\omega_m$.

$$E_0 e^{i\omega t} (1 + i\delta \sin(\omega_m t)) = E_0 e^{i\omega t} \left(1 + \frac{\delta}{2} e^{i\omega_m t} - \frac{\delta}{2} e^{-i\omega_m t} \right) \quad (4.2)$$

We have retained the assumption that $\delta \ll 1$. Equation 4.2 gives some useful physical insight into phase modulation, showing that three frequencies are present. Indeed if the phase modulated light were measured with an optical spectrum analyser, three peaks would be present, the carrier and two sidebands.

Equation 4.2 was derived assuming sinusoidal modulation. If the same analysis is carried out for cosine modulation the relative phase of the sidebands is different,

$$E_0 e^{i\omega t} \left(1 + i\frac{\delta}{2} e^{i\omega_m t} + i\frac{\delta}{2} e^{-i\omega_m t} \right) \quad (4.3)$$

Now each sideband has a $\pi/2$ phase shift with respect to the carrier. The vector pictures representing different types of modulation are shown in figure 4.2. The top section shows the vector diagrams for sine and cosine phase modulation. The longest vector represents the carrier, the two shorter ones the sidebands and the straight line is the frequency axis. The vector diagrams represent a snapshot in time. As the field evolves in time the sidebands spin around the axis at a frequency of ω_m relative to the carrier. The higher frequency sideband would rotate in one direction due to its accumulation of extra phase and the lower frequency sideband would rotate at the same rate, but in the other direction, due to its relative phase lag. Thus the cosine PM and sine PM differ only by a quarter of the modulation period of time evolution. This is expected as the definition of the type of signal applied to the phase is rather arbitrary, and depends on when we define $t = 0$.

Above we have assumed that the modulation depth δ is small. If this was not the case

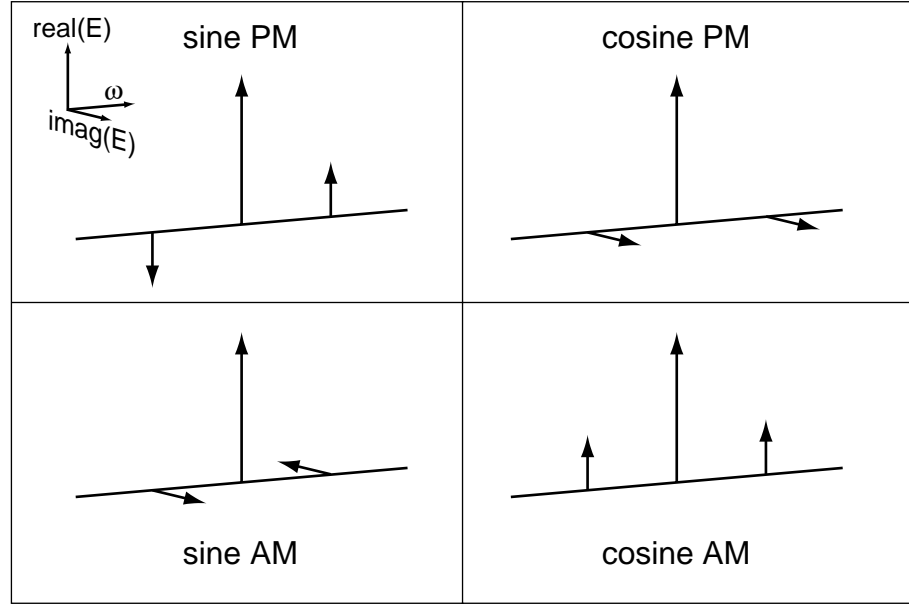


Figure 4.2: Vector diagrams representing sine and cosine phase and amplitude modulation.

then the modulation will introduce higher order sidebands at harmonics of ω_m given by,

$$E = E_0 e^{i\omega t} (J_0(\delta) + \sum_{l=1}^{\infty} i^l J_l(\delta) (e^{il\omega_m t} + e^{-il\omega_m t})) \quad (4.4)$$

Here $J_l(\delta)$ are the Bessel functions of the first kind. For simplicity we will neglect these higher order sidebands for the remainder of this discussion.

The bottom section of figure 4.2 depicts the two types of amplitude modulation. Amplitude modulation of a field is similar to (small) phase modulation in that the same sidebands are present, however these sidebands have a different phase relationship with the carrier. The equivalent expression to equation 4.2 for sine amplitude modulation is,

$$E_0 e^{i\omega t} (1 + \delta \sin(\omega_m t)) = E_0 e^{i\omega t} \left(1 - i \frac{\delta}{2} e^{i\omega_m t} + i \frac{\delta}{2} e^{-i\omega_m t} \right) \quad (4.5)$$

and for cosine amplitude modulation,

$$E_0 e^{i\omega t} (1 + \delta \cos(\omega_m t)) = E_0 e^{i\omega t} \left(1 + \frac{\delta}{2} e^{i\omega_m t} + \frac{\delta}{2} e^{-i\omega_m t} \right) \quad (4.6)$$

4.2 Interaction with an optical system

Let us now consider what happens to phase modulation as it passes through an optical system (for example, an interferometer). For the following examples we will use sine PM unless explicitly mentioned otherwise. Firstly we consider a system which introduces a

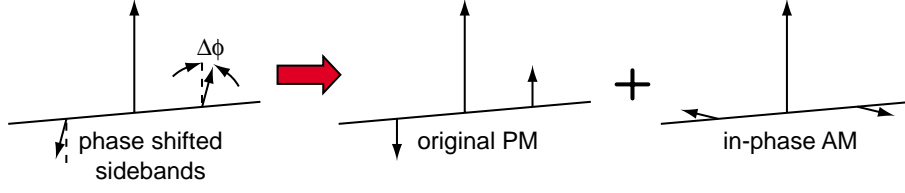


Figure 4.3: Vector diagram representing conversion of PM to in-phase AM by a phase shift.

phase shift, $\Delta\phi$ to each of the sidebands but not to the carrier.

$$E_0 e^{i\omega t} \left(1 + \frac{\delta}{2} e^{i(\omega_m t + \Delta\phi)} - \frac{\delta}{2} e^{-i(\omega_m t - \Delta\phi)} \right) \quad (4.7)$$

$$= E_0 e^{i\omega t} \left(1 + e^{i\Delta\phi} i\delta \sin(\omega_m t) \right) \quad (4.8)$$

$$= E_0 e^{i\omega t} (1 + (\cos \Delta\phi + i \sin \Delta\phi) i\delta \sin(\omega_m t)) \quad (4.9)$$

$$= E_0 e^{i\omega t} (1 + i\delta \sin(\omega_m t) \cos \Delta\phi - \delta \sin(\omega_m t) \sin \Delta\phi) \quad (4.10)$$

Equation 4.10 contains three terms, the carrier field, a term containing $\sin(\omega_m t)$ at 90° (perpendicular) to the carrier, and a $\sin(\omega_m t)$ out of phase with (but parallel to) the carrier. By comparison with equation 4.2 we can see that the first sine term has phase modulation symmetry with respect to the carrier. The second sine term has the same phase relationship as equation 4.5 (apart from a sign change) and so represents a component of amplitude modulation. As the AM and the original PM are both sine waves we refer to this as the *in-phase* component of AM. This process of producing AM from PM sidebands is described vectorially in figure 4.3. This result depends only on there being a relative phase shift between the carrier and sidebands thus in-phase AM is also produced when the carrier alone acquires a phase shift. The amplitude modulation component contains information about both the magnitude of the phase shift, and its direction. In some sense, we have managed to “encode” information about our signal, $\Delta\phi$, onto the high frequency sidebands.

We will now consider what happens as the phase modulation passes through an optical system where the sidebands are differentially attenuated. If the positive sideband magnitude is increased by a factor $(1 + \alpha)$ and the negative sideband is decreased by a factor of $(1 - \alpha)$ then the field becomes,

$$E_0 e^{i\omega t} \left(1 + \frac{\delta}{2} (1 + \alpha) e^{i\omega_m t} - \frac{\delta}{2} (1 - \alpha) e^{-i\omega_m t} \right) \quad (4.11)$$

$$= E_0 e^{i\omega t} \left(1 + \frac{\delta}{2} e^{i\omega_m t} - \frac{\delta}{2} e^{-i\omega_m t} + \alpha \left[\frac{\delta}{2} e^{i\omega_m t} + \frac{\delta}{2} e^{-i\omega_m t} \right] \right) \quad (4.12)$$

$$= E_0 e^{i\omega t} (1 + i\delta \sin(\omega_m t) + \alpha \cos(\omega_m t)) \quad (4.13)$$

Once again the result is the introduction of some component of amplitude modulation. In this case however, the modulation appears in the *quadrature* component (i.e., the PM was a sine wave and the AM is a cosine wave). Once again, the AM contains information about the magnitude and sign of the signal, in this case α . The vector picture for this process is given in figure 4.4.

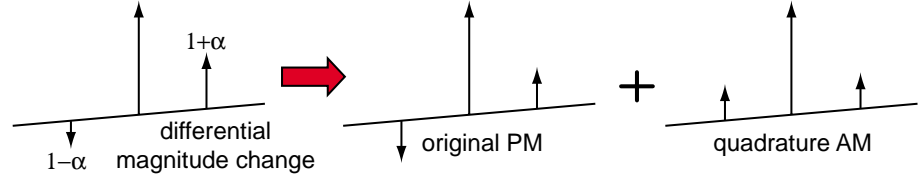


Figure 4.4: Vector diagram representing conversion of PM to quadrature AM by a differential change in the magnitude of the sidebands.

In both cases, the introduction of phase modulation has allowed us to impose information about the phase and amplitude response of an optical system onto the light. In the next section we discuss how to recover this information.

4.3 Demodulation

We have seen how phase modulation allows information about the phase and amplitude response of a system to be encoded on an optical beam. Demodulation represents the complementary decoding process where this information at high frequencies is mixed down to baseband. In this section we discuss several aspects of the recovery of the signal including the detection of the light, the electronic demodulation of the detected signal, and the filtering of the demodulated output.

4.3.1 Photodetection

Photodetection is the process of converting light into electric current. It can be described by the photoelectric effect, that is, the process whereby electrons are liberated from materials under the action of radiant energy. In our case, the material is an InGaAs photodiode specially designed for the purpose of photodetection. The number of liberated electrons is proportional to the number of photons in the beam detected. As a result, the photocurrent is a measure of the optical power of the detected beam. The photocurrent, I_{PD} will be given by,

$$I_{PD} = \eta_{QE} e \frac{P}{h\nu} \quad (4.14)$$

where e is the electronic charge, h is Planck's constant, ν [Hz] the optical frequency and P [Watts] the optical power. The symbol η_{QE} denotes the quantum efficiency of the photodiode and represents the fraction of photons which result in an electron in the photocurrent. Throughout this thesis we will neglect the intricacies of photodetection and assume that photocurrent is a measure of the optical power, ignoring quantum efficiency unless otherwise stated. The optical power is related to the electric field by,

$$P = E^* E \quad (4.15)$$

where E^* denotes the complex conjugate of E . By this definition, the power is always real and positive. Throughout this thesis we will assume that the units of electric field are $\sqrt{\text{Watts}}$ and so the constants normally associated with the Volts/metre definition of electric field are not required.

Consider a photodetection of a modulated field. For sinusoidal phase modulation, the electric field is defined by equation 4.1, and the detected power will be,

$$\begin{aligned}
 P &= E^* E \\
 &= E_0^* e^{-i(\omega t + \delta \sin(\omega_m t))} E_0 e^{i(\omega t + \delta \sin(\omega_m t))} \\
 &= E_0^* E_0 \\
 &= P_0
 \end{aligned} \tag{4.16}$$

This result shows that a measurement of the power does not give an indication of the instantaneous phase of the field. The situation is very different for the case of amplitude modulation (see equation 4.5), and photodetection yields,

$$\begin{aligned}
 P &= E^* E \\
 &= E_0^* e^{-i\omega t} (1 + \delta \sin(\omega_m t)) E_0 e^{i\omega t} (1 + \delta \sin(\omega_m t)) \\
 &= P_0 (1 + 2\delta \sin(\omega_m t) + \delta^2 \sin^2(\omega_m t))
 \end{aligned} \tag{4.17}$$

In this case the average power is the same as in the unmodulated case however a modulation at ω_m and $2\omega_m$ is present. The $2\omega_m$ component is smaller than the ω_m component and can be neglected if $\delta \ll 1$.

Detection of the fields containing sidebands with both AM and PM components will yield similar results. For example the measured power of the field in equation 4.10, produced by a relative phase shift between the carrier and sidebands will be,

$$\begin{aligned}
 P &= P_0 [1 - 2\delta \sin(\omega_m t) \sin \Delta\phi + \delta^2 \sin^2(\omega_m t) \cos^2 \Delta\phi \\
 &\quad + \delta^2 \sin^2(\omega_m t) \sin^2 \Delta\phi]
 \end{aligned} \tag{4.18}$$

The terms in δ^2 have been included for algebraic clarity only and we have previously assumed that $\delta \ll 1$. With this condition equation 4.18 simplifies to give,

$$P = P_0 [1 - 2\delta \sin(\omega_m t) \sin \Delta\phi] \tag{4.19}$$

Similarly, for the case where the phase modulation has been altered by a differential attenuation of the sidebands (see equation 4.13) the power is given by,

$$P = P_0 [1 + 2\alpha \cos(\omega_m t) + \delta^2 \sin^2(\omega_m t) + \alpha^2 \cos^2(\omega_m t)] \tag{4.20}$$

$$= P_0 [1 + 2\alpha \cos(\omega_m t)] \quad (\text{as } \delta \ll 1, \alpha \ll 1) \tag{4.21}$$

In both cases the signals of interest, α and $\Delta\phi$, appear at the modulation frequency. The terms that have been neglected due to small α and δ in equations 4.21 and 4.19 arise from beats among the sidebands themselves and so consist of a term at zero frequency (the power of each sideband) and a term at $2\omega_m$ (the upper sideband beating with the lower sideband). As we will see in the next section, this small modulation depth assumption is not necessary, as only signals at ω_m are mixed down to zero frequency, thus the terms at DC and $2\omega_m$ will not be present in the final filtered output.

4.3.2 The mixer

To recover the signal from high frequencies the photocurrent is multiplied by an electronic local oscillator. By the convolution theorem [32], a multiplication in the time do-

main is equivalent to a convolution in the frequency domain. For multiplication by a sine or cosine function oscillating at ω_m , this results in shifting all frequency components up and down by ω_m . As we are only interested in signals near baseband in the final output we need only consider the power fluctuations near $\pm\omega_m$. Demodulation of the photocurrent given in equation 4.19 (ignoring terms not at $\pm\omega_m$) can be represented by,

$$IPC = -2P_0\delta \sin(\omega_m t) \sin \Delta\phi \times \sin(\omega_m t) \quad (4.22)$$

$$= -2P_0\delta \sin \Delta\phi \left(\frac{1}{2} - \frac{\cos(2\omega_m t)}{2} \right) \quad (4.23)$$

A low pass filter with a cut off frequency less than ω_m is then used to remove higher frequency terms, giving a demodulated final output of,

$$IPC = -P_0\delta \sin \Delta\phi \quad (4.24)$$

$$\approx -P_0\delta \Delta\phi \quad (\text{for small } \Delta\phi) \quad (4.25)$$

The phase of the local oscillator determines which component of AM is present in the final output. In the example above we used a sine wave to demodulate the photocurrent as the signal of interest was embedded in a sine component of the photocurrent (thus the label *IPC* for in-phase component was used). Had we used a cosine wave, there would have been no DC component in the final output due to the orthogonality of sine and cosine.

Demodulating, equation 4.21 with a cosine local oscillator is represented by,

$$QC = 2P_0\alpha \cos(\omega_m t) \times \cos(\omega_m t) \quad (4.26)$$

$$= 2P_0\alpha \left(\frac{1}{2} + \frac{\cos(2\omega_m t)}{2} \right) \quad (4.27)$$

where *QC* denotes that the quadrature component is present at the output. This gives a final demodulated output after filtering,

$$QC = P_0\alpha \quad (4.28)$$

Equations 4.25 and 4.28 show that we have achieved our original goal of obtaining an output proportional to the original signals injected. As these signals contain information about the magnitude and direction of the signal they can be used to provide an error signal for controlling these parameters.

4.4 Error signals for interferometers

Throughout this thesis we will be discussing many different types of interferometers. All of these interferometers fall into one of two categories, multiple beam interferometers and two beam interferometers.

4.4.1 Multiple beam interferometers

The simplest form of multiple beam interferometer is the optical cavity, shown in figure 4.5. The fields of the optical cavity can be derived by using an infinite sum approach [14] or by solving a series of self consistent equations [31]. The circulating field E_{circ} , the

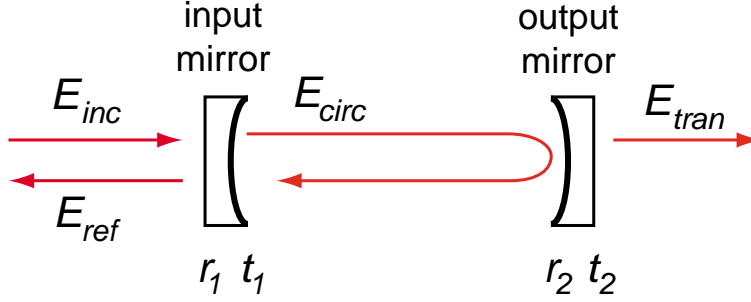


Figure 4.5: Diagram of an optical cavity showing the incident field, E_{inc} , the circulating field, E_{circ} , the reflected field, E_{ref} , and the transmitted field, E_{tran} . r_1 : amplitude reflectivity of input mirror, t_1 : amplitude transmissivity of input mirror, r_2 : amplitude reflectivity of output mirror, t_2 : amplitude transmissivity of output mirror.

reflected field E_{ref} and the transmitted field E_{tran} are related to the input field, E_{inc} and the single pass phase shift of the cavity, ϕ_{sp} , by the following expressions.

$$\frac{E_{circ}}{E_{inc}} = \frac{it_1}{1 - r_1 r_2 e^{i2\phi_{sp}}} \quad (4.29)$$

$$\frac{E_{ref}}{E_{inc}} = \frac{r_1 - (r_1^2 + t_1^2)r_2 e^{i2\phi_{sp}}}{1 - r_1 r_2 e^{i2\phi_{sp}}} \quad (4.30)$$

$$\frac{E_{tran}}{E_{inc}} = \frac{-t_1 t_2 e^{i\phi_{sp}}}{1 - r_1 r_2 e^{i2\phi_{sp}}} \quad (4.31)$$

The variables r_1 , t_1 , r_2 and t_2 represent the amplitude reflectivity and transmissivity of the input mirror and output mirror respectively. We have used the phase convention that there is no phase shift on reflection from a mirror and there is a $\pi/2$ phase shift on transmission. This will be the case throughout this thesis unless explicitly stated otherwise.

For the most part, we will be obtaining error signals from the field reflected from the cavity. The optical cavity can be thought of as a mirror with a frequency dependent, complex reflectivity $r_{cav}(\phi_{sp}) = E_{ref}/E_{inc}$. Figure 4.6 shows (a) the magnitude and (b) the phase of the r_{cav} as a function of the single pass phase, ϕ_{sp} . The cavity here is lossless and each mirror has a power reflectivity of 90%.

The real and imaginary components of the cavity reflectivity are plotted in figure 4.6(c) and (d). These are related to the magnitude, $|r_{cav}(\phi_{sp})|$, and the phase shift, $\Delta\phi_{cav} = \angle r_{cav}(\phi_{sp})$, of the cavity reflectivity by,

$$\text{Re}[r_{cav}(\phi_{sp})] = |r_{cav}(\phi_{sp})| \cos \Delta\phi_{cav} \quad (4.32)$$

$$\text{Im}[r_{cav}(\phi_{sp})] = |r_{cav}(\phi_{sp})| \sin \Delta\phi_{cav} \quad (4.33)$$

In many situations it is required that a cavity be held exactly on resonance. This occurs when the total round trip optical path is an integer number of wavelengths ($2\phi_{sp} = n \times 2\pi$). One way to obtain an error signal for locking the cavity on resonance is to phase modulate the input light. We will consider the case where the PM sidebands are well away from the resonance of the cavity (for this demonstration we have chosen them to be a quarter of a free spectral range away from the carrier). This means that the sidebands

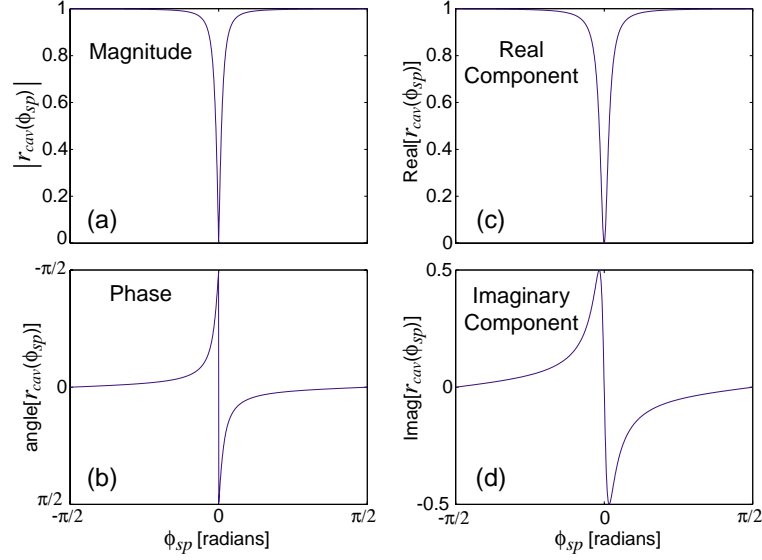


Figure 4.6: Complex reflectivity of a cavity as a function of single pass phase shift showing (a) magnitude, (b) phase, (c) real and (d) imaginary components. Parameters used: $r_1 = r_2 = \sqrt{0.9}$, $t_1 = t_2 = \sqrt{0.1}$

receive essentially no phase shift upon reflection from the cavity when the carrier field is near resonance. If the cavity is exactly on resonance it reflects off the cavity with no phase shift. When the cavity resonance drifts in one direction the carrier will acquire a phase shift, $\Delta\phi_{cav}$, while the phase of the sidebands remains unchanged. If the cavity resonance drifts in the other direction then the sign of the phase shift is different. The phase shift on reflection, $\Delta\phi_{cav}$, is equivalent to the phase shift introduced in section 4.2 (although in this case it corresponds to a phase shift of the carrier and not the sidebands). This phase shift affects the sideband symmetry in a similar manner to that depicted in figure 4.3 and thus produces the in-phase component of amplitude modulation. This amplitude modulation is demodulated by the original electronic signal to produce an error signal. Note that in equation 4.24 the signal is actually proportional to $\sin \Delta\phi$ rather than just $\Delta\phi$. This means that the error signal should closely approximate the imaginary part of the cavity reflectivity (see equation 4.33) rather than the phase of the cavity reflectivity.

We now calculate the error signal (i.e., the low pass filtered mixer output) as the cavity's single pass phase is varied from $-\pi/2$ to $\pi/2$. This can be accomplished either by substituting the cavity phase shift for $\Delta\phi$ in equation 4.24 or equivalently by substituting the imaginary part of the cavity reflectivity for $\sin \Delta\phi$ in the same equation. The error signal obtained when this is performed is shown in figure 4.7 with the imaginary part of the cavity reflectivity shown for comparison (the error signal has been scaled by a factor of 2). Around the cavity resonance the error signal is almost a perfect copy of the imaginary component of the cavity reflectivity. The difference away from $\phi = 0$ arises from the sidebands approaching resonance and acquiring their own phase shift, thus introducing an extra source of AM. This signal provides an excellent error signal for the control of the cavity resonance position.

The technique described above for obtaining an error signal is known as Pound-Drever-Hall (PDH) locking [33]. Over the last two decades it has become the standard

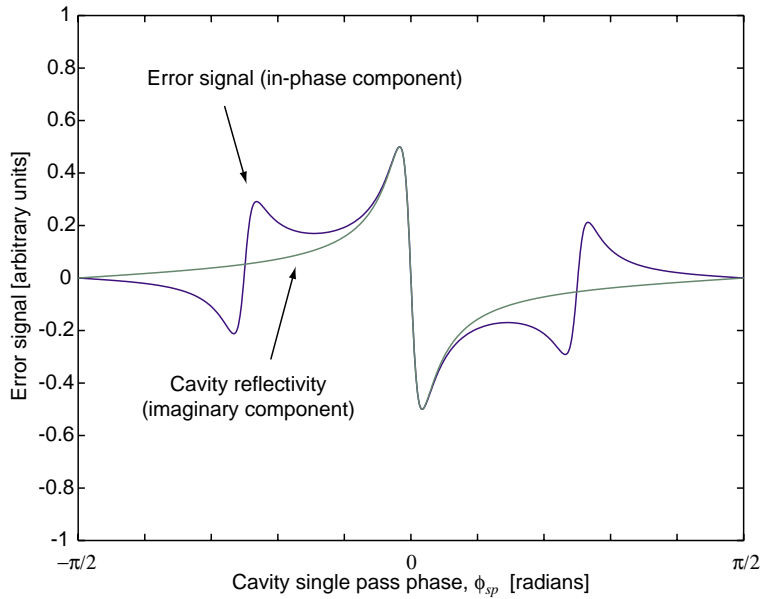


Figure 4.7: Comparison of error signal and the imaginary component of the cavity reflectivity. Parameters used: $r_1 = r_2 = \sqrt{0.9}$, $t_1 = t_2 = \sqrt{0.1}$

technique for high performance sensing and control of interferometers.

4.4.2 Two beam interferometers

The other class of interferometers considered in this thesis is the group of two beam interferometers. This includes the Michelson, the Sagnac and the Mach-Zehnder interferometers (see figure 4.8). These interferometers will be considered alone and coupled to optical cavities to build more sensitive or flexible interferometer configurations.

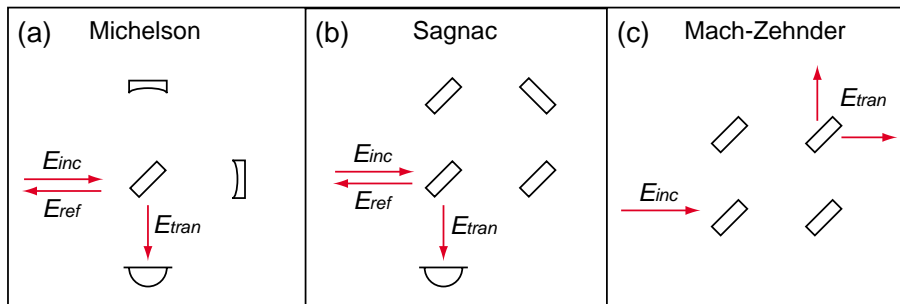


Figure 4.8: Examples of two beam interferometers: (a) Michelson interferometer, (b) Sagnac interferometer and (c) Mach-Zehnder interferometer.

Calculating the fields reflected and transmitted through a Michelson interferometer is simpler than for an optical cavity as the two beam interferometers are single pass devices, involving no optical feedback. In this thesis we will use the convention that the

Michelson arm lengths are $L - \Delta L$ and $L + \Delta L$. The transmitted field is given by,

$$\frac{E_{tran}}{E_{inc}} = it_{bs}r_{bs}(e^{i\frac{2\omega(L-\Delta L)}{c}} + e^{i(\frac{2\omega(L+\Delta L)}{c} + \pi)}) \quad (4.34)$$

$$= 2t_{bs}r_{bs} \sin(2\omega\Delta L/c) e^{i2\omega L/c} \quad (4.35)$$

where E_{inc} is the field incident on the interferometer and r_{bs} and t_{bs} are the amplitude reflectivity and transmissivity of the beamsplitter. In equation 4.35 we have assumed that the end mirrors reflect 100% of the light and have added a π phase shift to the beam in the longer arm so that the beams interfere destructively for $\omega = 0$. We can choose the carrier field to be at $\omega = 0$ so that ω represents the frequency offset of sidebands from the carrier. The electric fields in each arm can exactly cancel at the dark fringe regardless of the beamsplitter ratio, as each beam experiences one transmission and one reflection. The transfer function of equation 4.35 contains an exponential term which is a phase delay due to propagation over a distance $2L$, the average distance travelled through the device. Ignoring this propagation delay, the transmitted electric field has no imaginary component. Thus the in-phase component of detected photocurrent cannot be used to obtain an error signal for locking the Michelson interferometer.

The standard method for producing an error signal to lock a Michelson interferometer is Schnupp modulation [34]. It is to be used for all planned gravitational wave detectors. This technique uses phase modulation on the incident beam with detection and demodulation of either the reflected or transmitted beam. In this case we will consider the detection of the transmitted beam.

Figure 4.9 details the transfer of PM sidebands from the input field (a) to the dark fringe port (c) on the interferometer. We have used $\Delta L = 1$ for this demonstration. For maximum efficiency of transfer the modulation sidebands should be at the turning points of the electric field, $f_m = c/(8\Delta L) = 37.5$ MHz, however this is not essential. When the carrier is locked at a dark fringe the upper sideband is transmitted unchanged however the lower sideband is transmitted with a 180° phase change. If the interferometer drifts, the sine wave in (b) will shift sideways and introduce a small amount of carrier field, depicted by the dashed vector in (c). This carrier has AM symmetry with respect to the sidebands and thus will produce a signal at f_m in the photocurrent, which can be demodulated to produce the error signal. The further the interferometer drifts the more carrier present at the dark fringe and the larger the beat in the photocurrent. In addition the phase of the beat is proportional to the phase of the carrier, which changes by 180° across the desired lock point. As a consequence, the demodulated output contains information about both the size and direction of the interferometer offset from the dark fringe.

4.5 Advanced modulation and demodulation

For the central work of this thesis, it was necessary to employ more complicated, or at least, less common types of modulation and demodulation. These are briefly described in this section to prepare the reader for the control system presented in chapter 7. In particular we will discuss single sideband modulation and demodulation and double demodulation, highlighting the importance of demodulation phase in these systems.

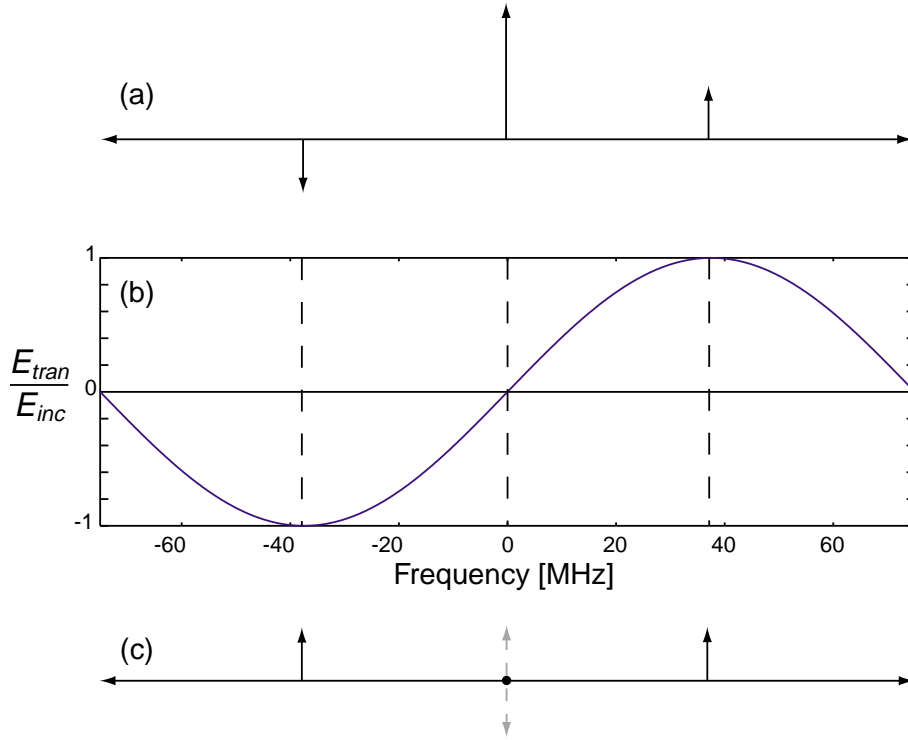


Figure 4.9: Vector diagram of Schnupp modulation showing (a) PM incident on the interferometer, (b) transfer function of the sidebands to the dark fringe and (c) fields present at the dark fringe port.

4.5.1 Single sideband modulation/demodulation

Single sideband modulation as the name suggests, has only one sideband, as opposed to the positive and negative sidebands that are present with standard phase or amplitude modulation. This single sideband, also referred to as a subcarrier, can be produced in several ways including using an acousto-optic modulator, a combination of amplitude and phase modulation, or by coherently combining two lasers operating at different frequencies. The principle of deriving an error signal for an optical cavity is similar to the PDH system, with the beat between the single sideband and the carrier used to map out the imaginary component of the electric field.

For this explanation we will consider a simple cavity, and we reserve the discussion of applying this technique to more complicated interferometers for chapter 7. Consider the electric field incident on a cavity consisting of a carrier and a lower power (electric field strength of γE_0) single sideband, offset in frequency by ω_{sc} ,

$$E_{inc} = E_0 e^{i\omega t} (1 + \gamma e^{i\omega_{sc} t}) \quad (4.36)$$

A measurement of the power will result in a photocurrent proportional to,

$$P_{inc} = P_0 (1 + \gamma e^{i\omega_{sc} t} + \gamma e^{-i\omega_{sc} t} + \gamma^2) \quad (4.37)$$

$$= P_0 (1 + \gamma^2 + 2\gamma \cos(\omega_{sc} t)) \quad (4.38)$$

The main difference for single sideband locking is that there is no optical cancellation of one sideband-carrier beat by the other sideband-carrier beat as is the case for pure phase modulation. As a result there is always a signal present in the photocurrent at ω_{sc} .

After reflection from an optical cavity, with complex reflectivity r_c and r_{sc} for the carrier and sidebands respectively (see equation 4.30), the electric field will be given by,

$$E_{ref} = E_0 e^{i\omega t} (r_c + r_{sc} \gamma e^{i\omega_{sc} t}) \quad (4.39)$$

$$= E_0 e^{i\omega t} (|r_c| e^{i\phi_c} + |r_{sc}| \gamma e^{i(\omega_{sc} t + \phi_{sc})}) \quad (4.40)$$

$$= E_0 e^{i\omega t} e^{i\phi_c} (|r_c| + |r_{sc}| \gamma e^{i(\omega_{sc} t + \Delta\phi)}) \quad (4.41)$$

Where ϕ_c and ϕ_{sc} are the phases of the cavity reflectivity for the carrier and subcarrier respectively¹ and $\Delta\phi = \phi_{sc} - \phi_c$. The detected power then becomes,

$$P_{ref} = P_0 (|r_c|^2 + |r_c| |r_{sc}| \gamma (e^{i(\omega_{sc} t + \Delta\phi)} + e^{-i(\omega_{sc} t + \Delta\phi)}) + |r_{sc}|^2 \gamma^2) \quad (4.42)$$

$$= P_0 (|r_c|^2 + |r_{sc}|^2 \gamma^2 + 2|r_c| |r_{sc}| \gamma \cos(\omega_{sc} t + \Delta\phi)) \quad (4.43)$$

Comparing equations 4.38 and 4.43 it is apparent that a change in relative phase of the carrier and sidebands, $\Delta\phi$ results in a change in phase of the beatnote. The problem of finding an error signal for the cavity resonance has been reduced to determining the phase of the beatnote. Once again we turn to demodulation by an electronic local oscillator. Our definition of in-phase and quadrature demodulation is relative to the phase of the original PM imposed on the beam. When only a single sideband is present this definition is no longer applicable. For single sideband demodulation we define the in-phase and quadrature demodulation relative to the beat between the single sideband and the carrier. From equation 4.38 it is clear that the beat note is a cosine wave, thus demodulation by cosine gives the in-phase component and demodulation by sine gives the quadrature component. The demodulation process to extract the quadrature component is described mathematically below, where only the term at ω_{sc} is considered.

$$QC = 2P_0 |r_c| |r_{sc}| \gamma \cos(\omega_{sc} t + \Delta\phi) \times \sin(\omega_{sc} t) \quad (4.44)$$

$$= P_0 |r_c| |r_{sc}| \gamma (\sin(2\omega_{sc} t + \Delta\phi) - \sin \Delta\phi) \quad (4.45)$$

After appropriate low pass filtering we obtain a signal at the mixer output of,

$$QC = -P_0 |r_c| |r_{sc}| \gamma \sin(\Delta\phi) \quad (4.46)$$

In essence this demodulation process compares the phase of the local oscillator to the phase of the beatnote. Figure 4.10(a) shows the mixer output for the sine demodulation as a function of the single pass phase shift of the cavity. If the sideband is well away from the cavity resonance then $r_{sc} = 1$ and equation 4.46 becomes,

$$QC = P_0 \gamma |r_c| \sin \phi_c \quad (4.47)$$

$$= P_0 \gamma \text{Im}[r_c] \quad (4.48)$$

As is the case for PDH locking, our error signal is proportional to the imaginary compo-

¹That is the angle of r_c and r_{sc} , not to be confused with the round trip phase shift of the cavity.

nent of the cavity reflectivity.

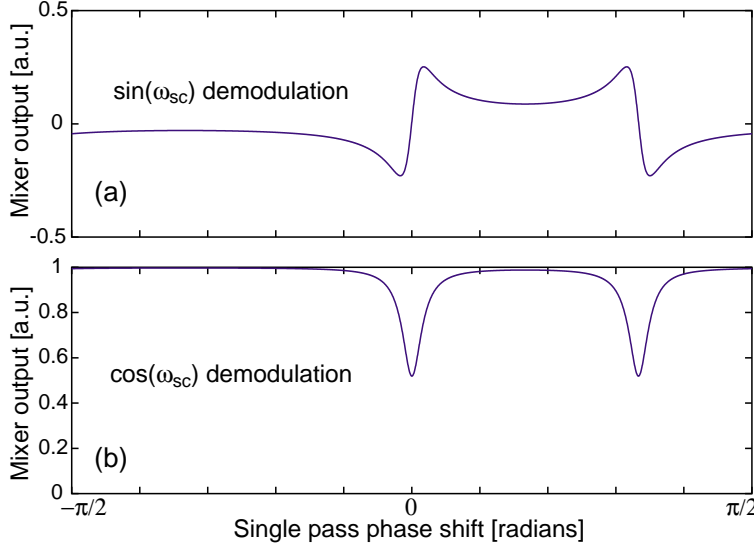


Figure 4.10: Mixer outputs for (a) sine and (b) cosine demodulation of the reflected field with single sideband demodulation. Carrier is resonant at $\phi = 0$ and subcarrier is resonant at $\phi = 2\pi/3$. Parameters used: $r_1 = \sqrt{0.95}$, $r_2 = \sqrt{0.85}$, $t_1 = \sqrt{0.05}$.

A demodulation of the in-phase component (assuming $r_{sc} = 1$) will give,

$$IPC = 2P_0\gamma|r_c| \cos(\omega_{sc}t + \Delta\phi) \times \cos(\omega_{sc}t) \quad (4.49)$$

$$= P_0\gamma|r_c| (\cos(2\omega_{sc}t + \Delta\phi) + \cos \Delta\phi) \quad (4.50)$$

After low pass filtering of the second harmonic the signal at the mixer output is,

$$IPC = P_0\gamma|r_c| \cos(\Delta\phi) \quad (4.51)$$

$$= P_0\gamma \text{Re}[r_c] \quad (4.52)$$

That is, the in-phase component is proportional to the real part of the cavity reflectivity. The real part of the cavity reflectivity on resonance is positive for an undercoupled cavity, negative for an overcoupled cavity and zero for an impedance matched cavity. Figure 4.10(b) shows the in-phase component for an undercoupled cavity.

The correct demodulation phase can be set by scanning the cavity and adjusting the demodulation phase until either the error signal is symmetric or the error signal far from resonance goes to zero. If the demodulation phase is set incorrectly by an amount ψ_{err} (i.e., the electronic local oscillator goes as $\sin(\omega_{sc}t + \psi_{err})$ instead of $\sin(\omega_{sc}t)$) then the in-phase component of the signal will be coupled into the measurement. When locking cavities using the PDH technique this is not a problem as the other component contains no signal, and the end result is merely a change in the slope of the error signal by a factor of $\cos \psi_{err}$. When using single sideband demodulation, errors in the demodulation phase are more detrimental as the in-phase component may be non zero.

To determine more quantitatively how an error in the phase of the local oscillator, ψ_{err} will corrupt the error signal, consider a demodulation of the reflected power by

$$\sin(\omega_{sc}t + \psi_{err})$$

$$\begin{aligned} QC(\psi_{err}) &= 2P_0\gamma|r_c|\cos(\omega_{sc}t - \phi_c) \times \sin(\omega_{sc}t + \psi_{err}) \\ &= P_0\gamma|r_c|(\sin(2\omega_{sc}t - \phi_{sc} + \psi_{err}) + \sin(\phi_{sc} - \psi_{err})) \end{aligned} \quad (4.53)$$

After filtering of the second harmonic term this becomes,

$$QC(\psi_{err}) = P_0\gamma|r_c|\sin(\phi_c - \psi_{err}) \quad (4.54)$$

$$= P_0\gamma(\text{Im}[r_c]\cos(\psi_{err}) - \text{Re}[r_c]\sin(\psi_{err})) \quad (4.55)$$

It is clear that any error in the demodulation phase can seriously influence the final error signal. The error ψ_{err} directly couples into the error signal in the same way as the cavity reflectivity phase ϕ_c , making the two indistinguishable. As mentioned earlier, the demodulation process compares the phase of the local oscillator to the phase of the beatnote, and so it seems reasonable that a change in the phase of the local oscillator would give the same result as a change in phase of the beatnote.

By impedance matching the cavity, the sensitivity to demodulation phase errors can be overcome. When the cavity is impedance matched the real part of the cavity reflectivity is zero near resonance, and it is clear from equation 4.55 that the cross coupling is eliminated. In the example of figure 4.10, the cavity is not impedance matched and thus the in-phase component contains a strong beat, even in the absence of a signal. By using an impedance matched cavity, the in-phase error signal goes to zero on resonance, as shown in figure 4.11.

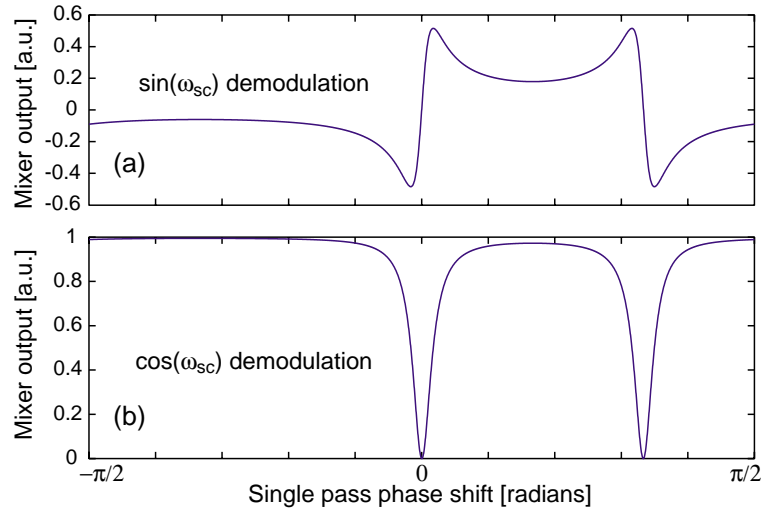


Figure 4.11: Mixer outputs for (a) sine and (b) cosine demodulation of the reflected field with single sideband demodulation. Carrier is resonant at $\phi = 0$ and subcarrier is resonant at $\phi = 2\pi/3$. The cavity is impedance matched with $r_1 = r_2 = \sqrt{0.9}$, $t_1 = \sqrt{0.1}$.

In summary, single sideband modulation/demodulation can be used to provide an error signal to lock an optical cavity to resonance. This error signal is proportional to the imaginary component of the cavity reflectivity. The single sideband modulation scheme is not as robust as the double sideband (PDH) scheme in the presence of errors in the demodulation phase. The sensitivity to demodulation phase error is dependent on the

impedance matching of the optical cavity. In the ideal case, where the system is perfectly impedance matched, an error in the demodulation phase produces a reduction in gain but introduces no offset. This is equivalent to the PDH system demodulation phase dependence.

4.5.2 Double demodulation

Double demodulation can be employed to obtain information which is carried by the beat between different sets of sidebands. In this instance, we will use the interference between phase modulation sidebands on the carrier and a subcarrier to provide an error signal for locking a Michelson interferometer to a dark fringe. Whereas Schnupp modulation uses the sidebands to sense the carrier presence at the dark fringe, this double demodulation scheme uses a subcarrier to sense the sidebands presence at the dark fringe.

Consider the electric field incident on the interferometer containing a carrier, (small) PM sidebands at ω_1 , and a subcarrier offset from the carrier by ω_{sc} .

$$E_{inc} = E_0 e^{i\omega t} (1 + i\delta \sin(\omega_1 t) + \gamma e^{i\omega_{sc} t}) \quad (4.56)$$

$$= E_0 e^{i\omega t} \left(1 + \frac{\delta}{2} e^{i\omega_1 t} - \frac{\delta}{2} e^{-i\omega_1 t} + \gamma e^{i\omega_{sc} t} \right) \quad (4.57)$$

In our system, we will have the PM sidebands at the point where they are completely reflected ($f_1 = \Delta L/4$) and the subcarrier near the point of maximum transmission. The positions of the sidebands relative to the Michelson transfer function (equation 4.35) is shown in figure 4.12.

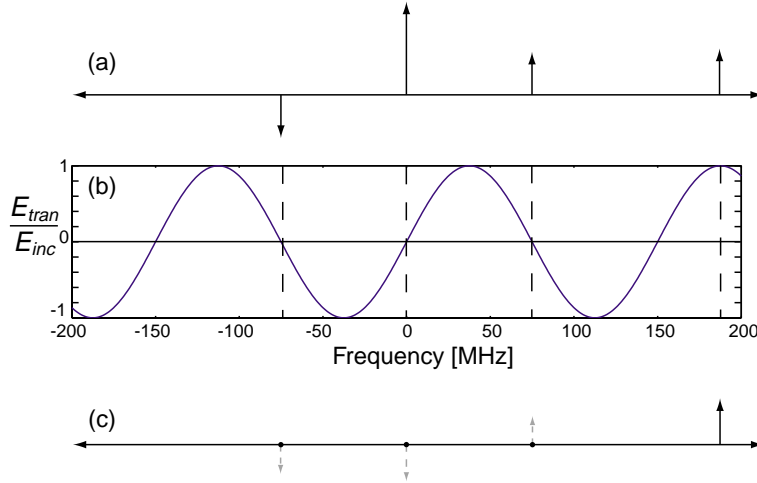


Figure 4.12: Double demodulation system showing (a) field incident on the interferometer, (b) transfer function from the incident field to the transmitted field and (c) field present at the dark fringe port.

To simplify the notation, we will assume that each sideband is transmitted with an efficiency of β , and the carrier with an efficiency of $-\beta$. Thus the aim of this exercise is to extract an error signal proportional to β . The subcarrier is near a turning point and we assume that it transmits to the dark fringe with an efficiency of 1. The field incident on

the photodetector at the transmitted port can be written as,

$$E_{tran} = E_0 e^{i\omega t} \left(-\beta + \frac{\beta\delta}{2} e^{i\omega_1 t} - \frac{\beta\delta}{2} e^{-i\omega_1 t} + \gamma e^{i\omega_{sc} t} \right) \quad (4.58)$$

The detected power, given by $E_{tran}^* E_{tran}$, will consist of many terms. We will only consider those at $\pm\omega_{sc} \pm \omega_1$, as these represent the interference between the sidebands and subcarrier. The components of the photocurrent at these frequencies will be proportional to,

$$P_{tran} = P_0 \frac{\beta\gamma\delta}{2} \left(e^{i\omega_{sc} t} e^{-i\omega_1 t} - e^{i\omega_{sc} t} e^{i\omega_1 t} + e^{-i\omega_{sc} t} e^{i\omega_1 t} - e^{-i\omega_{sc} t} e^{-i\omega_1 t} \right) \quad (4.59)$$

$$= P_0 \frac{\beta\gamma\delta}{2} (\cos((\omega_{sc} - \omega_1)t) - \cos((\omega_{sc} + \omega_1)t)) \quad (4.60)$$

Thus the photocurrent will contain information about β at the frequencies, $\omega_{sc} + \omega_1$, and $\omega_{sc} - \omega_1$. To recover this information we can demodulate at each of these frequencies, in parallel, and then add (or subtract) the result. A mathematically equivalent approach is to demodulate twice in series, first at ω_{sc} and then at ω_1 . This is simply a statement of the trigonometric identities,

$$\sin(\omega_{sc}) \sin(\omega_1) = \frac{1}{2} [\cos(\omega_{sc} - \omega_1) - \cos(\omega_{sc} + \omega_1)] \quad (4.61)$$

$$\sin(\omega_{sc}) \cos(\omega_1) = \frac{1}{2} [\sin(\omega_{sc} + \omega_1) + \sin(\omega_{sc} - \omega_1)] \quad (4.62)$$

$$\cos(\omega_{sc}) \sin(\omega_1) = \frac{1}{2} [\sin(\omega_{sc} + \omega_1) - \sin(\omega_{sc} - \omega_1)] \quad (4.63)$$

$$\cos(\omega_{sc}) \cos(\omega_1) = \frac{1}{2} [\cos(\omega_{sc} + \omega_1) + \cos(\omega_{sc} - \omega_1)] \quad (4.64)$$

These identities represent a basis for the possible demodulation phase combinations. Experimentally it is often easier to perform the demodulation in series, as the demodulation frequencies are more readily available. By comparing the right hand sides of equations 4.61-4.64 with equation 4.60, it is apparent that a sine-cosine or cosine-sine demodulation will have no DC component.

Cosine-cosine demodulation produces a signal at the mixer output given by,

$$CC = P_0 \frac{\beta\gamma\delta}{4} \left(\cos^2((\omega_{sc} - \omega_1)t) - \cos^2((\omega_{sc} + \omega_1)t) + \text{cross terms} \right) \quad (4.65)$$

$$= P_0 \frac{\beta\gamma\delta}{4} \left(\frac{1}{2} - \frac{1}{2} + \text{high frequency terms} \right) \quad (4.66)$$

$$(4.67)$$

which after low pass filtering gives zero. However, demodulating by sine-sine will yield,

$$SS = P_0 \frac{\beta\gamma\delta}{4} \left(\cos^2((\omega_{sc} - \omega_1)t) + \cos^2((\omega_{sc} + \omega_1)t) + \text{cross terms} \right) \quad (4.68)$$

$$= P_0 \frac{\beta\gamma\delta}{4} \left(\frac{1}{2} + \frac{1}{2} + \text{high frequency terms} \right) \quad (4.69)$$

which after low pass filtering will give,

$$SS = P_0 \frac{\beta\gamma\delta}{4} \quad (4.70)$$

Thus a series demodulation of the photocurrent by $\sin(\omega_{sc}t)$ and $\sin(\omega_1t)$ will give a signal proportional to the transmission of the sidebands, β , allowing the interferometer to be locked to a dark fringe. Furthermore, this technique has limited dependence on the demodulation phase as the other quadratures are all zero.

4.6 Summary

We have discussed how phase modulation can be used to determine certain properties of an interferometer. In particular we have shown how a change in the relative phase of the carrier and PM sidebands will result in a signal in one quadrature, while a differential attenuation will result in a signal in the other quadrature of the demodulated photocurrent.

In addition, we have analysed two techniques for controlling interferometers. We have shown how single sideband modulation can be used to obtain an error signal for an optical cavity. We have also introduced a technique, referred to here as double demodulation, which uses the beat between PM sidebands on the carrier and a subcarrier to lock a Michelson to a dark fringe. Both the single sideband technique and the double demodulation technique will be used in the control system introduced in chapter 7.

Part II

**Interferometer Configurations and
Control**

Gravitational wave detector configurations

This chapter gives a brief overview of the development of gravitational wave interferometry and, in particular, techniques collectively known as recycling [35]. These techniques include power recycling, signal recycling and resonant sideband extraction. The effects of storage time and power storage of the light are discussed as motivation for these techniques. Detailed quantitative comparisons of all of the configurations discussed here have been performed by Mizuno [36, 37] and will not be repeated here. Instead the aim is to give the reader a basic understanding of the advantages of the various configurations.

In the following discussion we will assume that shot noise is the dominant noise source. Of course, this is not true for all frequencies, but it is only in the frequency range where the interferometer is limited by optical noise sources that the type of configuration will influence the performance.

5.1 Frequency response and the storage time limit

To maximise the phase shift of the light due to interaction with a gravitational wave the interaction time must be optimised. The optimum interaction time is equal to $\tau_g/2$ where τ_g is the period of the gravitational wave. If the interaction time is longer than this time, then the length perturbation changes sign and begins to undo the phase shift imparted during the first half of the period. For a gravitational wave of frequency 500 Hz, the ideal interaction time is 1 ms. In 1 ms light travels a distance of 300 km, thus we would ideally like an arm length of around 150 km (after allowing for the return trip). This is much longer than is feasible for a ground based gravitational wave detector for practical reasons, and we must use other means to increase the storage time of the light.

One method to increase the effective arm length is to fold the interferometer arms [4]. Using delay lines with \mathcal{N} bounces, the effective arm length becomes $(\mathcal{N} + 1)L$, where L is the actual length of the interferometer arm. This results in a storage time increase of a factor of $(\mathcal{N} + 1)/2$ compared to the single bounce ($\mathcal{N} = 1$) case. One way to implement this in a long base-line interferometer is to use a Herriott delay line, where all of the reflections occur on two curved mirrors (one with a hole in it for the entrance and exit beams). One of the problems with using delay lines in a long base-line interferometer is that it is difficult to achieve the optimum number of bounces without the laser spots overlapping on the end mirrors. Any overlap can lead to scattering of light from one bounce interfering with the light from the next. Thus beams need to be kept sufficiently spatially separated on the end mirrors. A storage time of 1 ms with an interferometer

length of 3 km would require 50 spots on each mirror. Given the limits on beam sizes set by diffraction and the currently envisaged mirror sizes, it is difficult to achieve the required storage time using delay lines. For a detailed discussion of these issues see ref. [38].

5.2 Arm cavities

The standard way to achieve the required storage time is to use Fabry-Perot cavities in the arms of the interferometer, as shown in figure 5.1. Fabry-Perot cavities will produce diffraction-limited spot sizes on the mirrors, which minimises the size of the mirrors that can be used. In addition, the storage time of the arm cavity can be matched to the optimum storage time by adjusting the reflectivity of the input mirror. The bandwidth of such a device is now determined by the bandwidth of the arm cavities. Thus arm cavities improve the sensitivity but at the expense of a reduced detector bandwidth. As the carrier is resonant with the arm cavities the frequency response is centred around zero frequency.

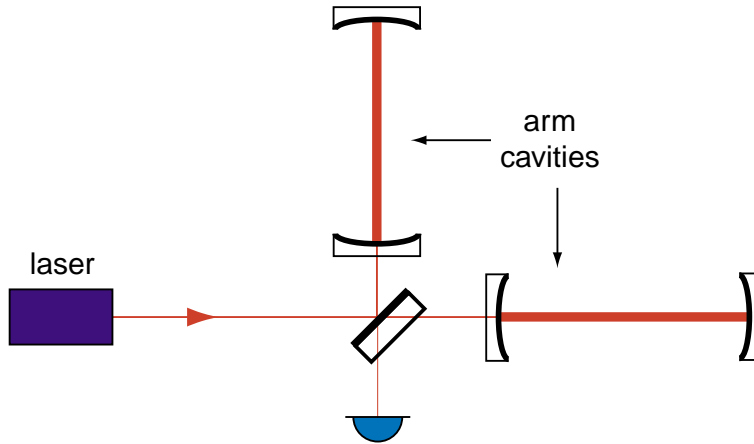


Figure 5.1: A Michelson interferometer with Fabry-Perot cavities in the arms.

Adding resonant cavities gives the optimum storage time although at the expense of considerable complexity. The interferometer now has three length degrees of freedom which must be controlled; the two arm cavities which must be held on resonance, and the Michelson interferometer which must be maintained at a dark fringe as before. As mentioned in chapter 2, the dark fringe only responds to the difference in the phase of the two beams in the arms and so only the differential part of the arm cavity error signals appear at the dark fringe. The bright fringe responds to changes in the average phase of the two beams in the arms and thus the common part of the arm cavity error signal is obtained here. The individual arm cavity resonances are controlled using this common and differential mode system.

5.3 Energy storage

The other major factor influencing shot noise limited sensitivity is the power in the interferometer arms. In chapter 3 we stated the standard deviation of the photon number

is equal to the square root of the average photon number. This gives rise to a standard deviation of the power given in equation 3.50.

$$\Delta P_D = \sqrt{\bar{P} h \nu} \quad (5.1)$$

In chapter 4, we derived the signal for different interferometers with various kinds of modulation based signal extraction schemes. In all of these examples the final signal at the demodulated output was proportional to P_0 , the power incident on the interferometer. Combining these two observations we can see that the signal to noise ratio of such a measurement will scale with the square root of the power.

$$S/N \propto P/\sqrt{P} \quad (5.2)$$

$$\propto \sqrt{P} \quad (5.3)$$

Thus, one way to improve the shot noise limited sensitivity of an instrument is to increase the optical power sensing the mirror test masses or equivalently the energy stored in each arm [39]. For this reason gravitational wave detectors will use the highest power lasers possible¹.

5.4 Power recycling

One method to achieve this power increase is to employ power recycling [40, 41]. As a Michelson interferometer is operated on a dark fringe, much of the incident power is reflected back towards the laser and is lost from the device. By placing a mirror between the laser and the interferometer this light can be reflected back into the interferometer. The light is effectively recycled and so this technique is referred to as *power recycling* with the mirror often called the *power recycling mirror*. This forms an optical cavity between the power recycling mirror and the Michelson interferometer as shown in figure 5.2. By choosing the reflectivity of this mirror so that the transmission is equal to the power recycling cavity's total round trip loss, the interferometer is impedance matched and the circulating power is maximised. The power hitting the main beamsplitter can be increased by factors of several hundred, with the increase proportional to the inverse of the total losses.

Power recycling was first reported by Maischberger *et al.* in 1987 [42], and shortly after, higher recycling powers were achieved by Man *et al.* [43]. In 1997, Schnier *et al.* [44] reported on a power enhancement of approximately 300 in the suspended 30 m prototype at Garching. Currently, the highest reported power increase due to power recycling has been achieved in the LIGO Phase Noise Interferometer situated at MIT where a recycling gain of approximately 450 was observed, corresponding to a power of 60 W at the beamsplitter [45].

Power recycling adds an extra length degree of freedom with the position of the power recycling mirror now requiring control to ensure that the power build up for the carrier is maximised. This extra complexity is justified in light of the improvement of the shot noise limited sensitivity of the device without a reduction in the instrument's bandwidth. Power recycling is to be used in all planned gravitational wave detectors.

¹There are of course other stringent requirements which will influence the choice of laser, such as, the laser's frequency and intensity noise, spatial quality and wavelength.

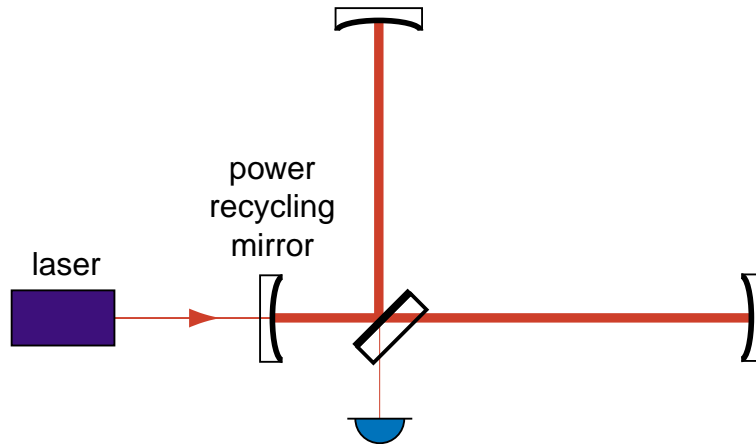


Figure 5.2: A power recycled Michelson interferometer. The thickness of the line gives an indication of the beam's power.

5.5 A power recycled arm cavity Michelson interferometer

By combining arm cavities with power recycling, both the storage time and the energy storage can be optimised. This is the configuration that will be used for LIGO, VIRGO and TAMA300. This interferometer requires the control of 4 degrees of freedom; the arm cavity common mode, arm cavity differential mode, the Michelson (differential) mode and the power cavity (or Michelson common mode).

This configuration was first experimentally demonstrated by Fritschel *et al.* in 1992 [46] using external modulation based signal extraction scheme. In 1995, Regehr *et al.* [47] experimentally demonstrated a control system with frontal modulation only. This scheme subsequently became the reference design for the LIGO control system. It used a single modulation frequency to obtain the four error signals by demodulation of the photocurrents at the transmitted port, the reflected port, and a tap off inside the power cavity. Regehr, demonstrated [48] that despite the power cavity degree of freedom not being dominant in any one output, stable operation of the interferometer could be obtained by the use of a gain hierarchy approach.

Since this time, a large amount of work has been performed by various groups [49–54] to improve the control system. This research has focussed on achieving better separation of the arm cavity common mode and power cavity error signals [50–53], and improving the stability of the modulation sidebands in the power cavity in the presence of thermal lensing [54].

5.6 Signal recycling

Power recycling does not effect the storage time of an interferometer because the gravitationally induced sidebands exit through the dark fringe port of the beamsplitter. These sidebands can also be recycled to optimise the bandwidth of the detector. This technique was developed by Meers in the late 1980s [41, 55] and is known as *signal recycling*. The *signal recycling mirror* is placed at the signal port and reflects the signal sidebands back into the interferometer as shown in figure 5.3. The typical signal recycling configuration has

no Fabry-Perot cavities in the arms, instead relying on the signal recycling mirror to optimise the storage time of the gravitationally induced signal sidebands. Signal recycling is also compatible with power recycling as the signal mirror and power mirror independently change the signal storage and the power storage respectively. The combination of signal and power recycling is referred to as *dual recycling*.

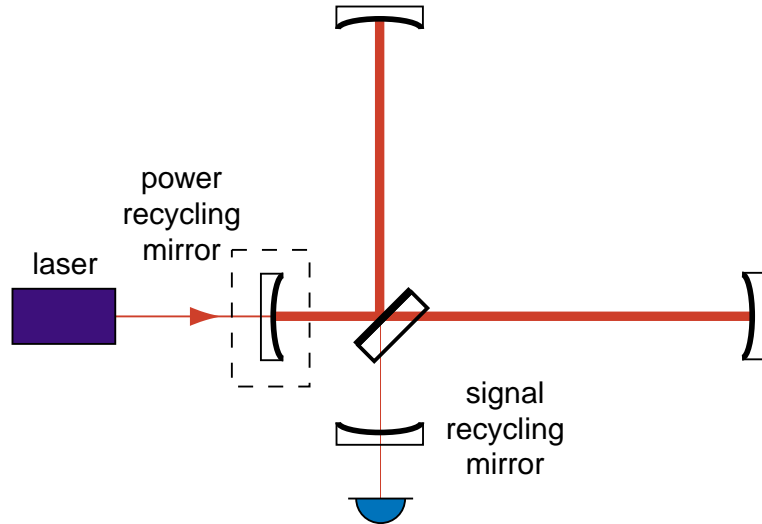


Figure 5.3: A signal recycled Michelson interferometer. The configuration is known as dual recycling when the optional power mirror is present.

One advantage of dual recycling over the power recycled arm cavity device is its ability to alter the frequency of its peak signal response. In broadband operation the signal cavity resonance is centred on the signal sidebands close to the carrier, corresponding to a maximum sensitivity to a gravitational wave with a frequency around zero hertz. However, if the signal mirror position is changed by a fraction of a wavelength, the resonant frequency of the signal cavity (and thus the peak signal frequency) is altered. The sensitivity theorem [36] states that the shot noise limited sensitivity of a detector is proportional to the square root of the energy stored divided by the bandwidth. Dual recycling allows a detector to be constructed which has a high sensitivity, narrow frequency response whose peak frequency can be adjusted to any desired value. By reducing the signal bandwidth it can achieve the same sensitivity as longer base-line detectors. GEO600 will be the only first generation detector capable of altering its peak signal frequency.

Dual recycling was first experimentally demonstrated in 1991 by Strain and Meers [56]. Since this time there have been several experimental investigations including a detailed measurement of the broadband and detuned frequency response [57] (signal recycling only) and an impressive demonstration of dual recycling in the suspended prototype in Garching by Heinzel *et al.* [58]. The control system from the Garching prototype will form the basis for the control system of GEO600.

5.7 Resonant sideband extraction

One problem with power recycling is that very large powers are transmitted through substrates such as the beamsplitter and the arm cavities' input couplers. Techniques

for thermally modelling interferometers [59] have shown that this can ultimately lead to a degradation of the sensitivity due to processes such as thermal lensing [60, 61] and thermally induced birefringence [62].

Resonant sideband extraction (RSE) is a technique which reduces these problems by allowing more optical power to be stored in the arm cavities. In addition to reducing thermal problems in the beamsplitter, this technique is in principle capable of yielding higher stored energy due to the lower loss of the arm cavities². Ordinarily, very high finesse arm cavities cannot be used due to the storage time limit discussed in section 5.1. Using resonant sideband extraction this storage time limit can be avoided.

Resonant sideband extraction was first proposed by Mizuno *et al.* [63] in 1993. The basic experimental layout of RSE is shown in figure 5.4. The principal of RSE is closely related to that of signal recycling in that a mirror placed at the signal port, referred to as the *signal extraction mirror* (SEM), can be used to manipulate the bandwidth and sensitivity of the interferometer. In contrast to signal recycling, the SEM is used to increase the signal bandwidth of an instrument. This is achieved by decreasing the storage time of the signal sidebands in the arm cavities.

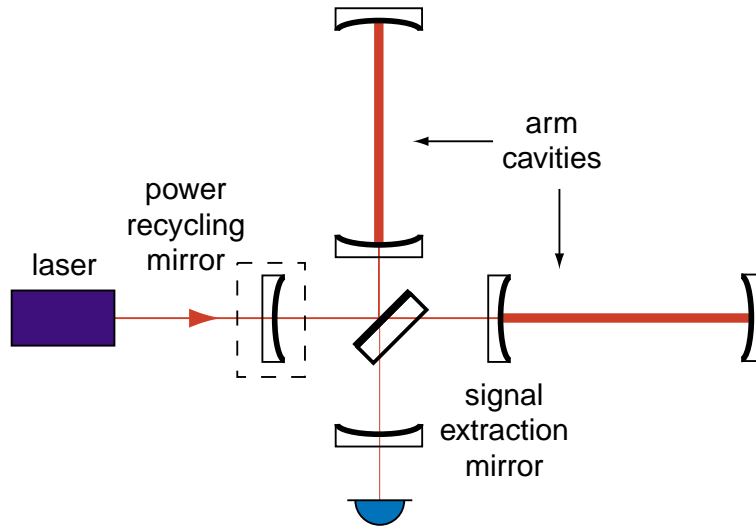


Figure 5.4: A Michelson interferometer with resonant sideband extraction. The power recycling mirror is optional.

In an ideal instrument, the carrier never reaches the dark fringe port and so the SEM has no effect on the stored power in the arm cavities. The signal sidebands, however, exit through the dark fringe port and so are influenced by the SEM. The SEM completes a coupled cavity system made up of the arm cavity and the signal extraction cavity with the inboard mirror common to both. A coupled cavity system is equivalent to a single cavity with a variable reflectivity or *compound* mirror (the signal extraction cavity). The reflectivity of this compound mirror can be changed by adjusting the SEM position by a fraction of a wavelength [64]. By tuning the signal extraction cavity to resonance, the effective reflectivity of the compound mirror is minimised. In this manner, the finesse

²The arm cavity contains only two surfaces, whereas the power cavity has at least 4 surfaces and the beamsplitter substrate.

of the coupled cavity, and thus the storage time of the signal sidebands, can be reduced thereby increasing the bandwidth of the instrument. Moreover, by detuning the signal extraction cavity from resonance, the signal bandwidth and peak signal frequency can be altered to obtain the desired frequency response.

Resonant sideband extraction was first experimentally demonstrated in a Michelson interferometer by Heinzl *et al.* [65]. Resonant sideband extraction in a Michelson interferometer has at least 4 degrees of freedom; the arm cavity common mode, arm cavity differential mode, Michelson differential mode and the signal cavity detuning. If power recycling is present then the power recycling mirror position must also be controlled. The original experimental demonstration [65] did not include power recycling and used a control system which was not suitable for a gravitational wave detector. For several years researchers at the Australian National University [66], Caltech [67] and the University of Florida [68] have been developing control systems for a power recycled Michelson interferometer with RSE. This year (2000), all three bench top experiments successfully demonstrated power recycled Michelson interferometers with resonant sideband extraction using different control systems. Now the focus of the experimental RSE work will move to the Glasgow prototype where power recycled RSE will be implemented in a suspended prototype [69].

As resonant sideband extraction is the main focus of this thesis, we now consider the signal response of this system.

5.8 Frequency response of a Michelson interferometer with RSE

In this section we derive the frequency response of a Michelson interferometer with resonant sideband extraction in the presence of phase modulation in the arms. This response [36, 63] is quite complicated and we will attempt to simplify the derivation by decomposing the total transfer function into the product of three simpler transfer functions:

- $\mathcal{A}(\omega_s)$, is the transfer function from the phase modulation inside the cavity to the field reflected from the front mirror of the arm cavity. It is normalised to the carrier field incident on the arm cavity.
- $\mathcal{M}(\omega_s)$, incorporates the response of the Michelson interferometer to antisymmetric sidebands. When multiplied by $\mathcal{A}(\omega_s)$, it will give the frequency response of an arm cavity Michelson interferometer.
- $\mathcal{E}(\omega_s)$, gives the enhancement of the signal sidebands due to the addition of a signal extraction mirror.

We begin by considering the production of signal sidebands in a single arm cavity. The fields associated with the cavity are shown in figure 5.5. Assuming that the carrier is on resonance with the arm cavity we will obtain a circulating field given by,

$$\frac{E_{circ}(0)}{E_{inc}(0)} = \frac{it_1}{1 - r_1 r_2} \quad (5.4)$$

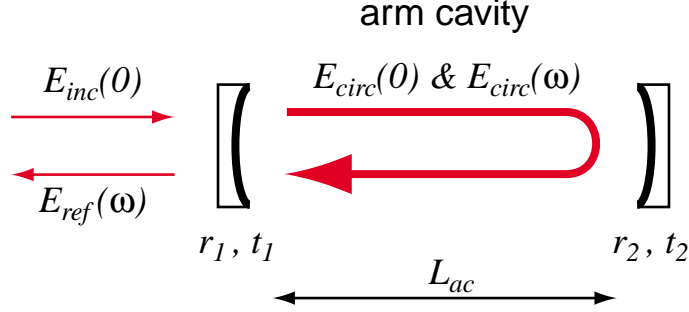


Figure 5.5: Illustration of the arm cavity and electric fields for the carrier and the signal sidebands.

where r_1 and t_1 are the electric field reflectivity and transmissivity of the input coupler, r_2 is the electric field reflectivity of the end mirror, $E_{circ}(0)$ represents the circulating field at the carrier frequency, $\omega_s = 0$, and $E_{inc}(0)$ is the carrier field incident on the cavity. Phase modulation of the light inside the cavity will result in sidebands at a frequency ω_s , given by $E_{pm}(\omega_s) = iJ_1(\delta)E_{circ}(0)$. Note that for the small signals considered here we have $\delta \ll 1$. The circulating signal field inside the cavity can be determined by adding $E_{pm}(\omega_s)$ to the circulating signal field from the previous round trip,

$$E_{circ}(\omega_s) = iJ_1(\delta)E_{circ}(0) + r_1r_2e^{i2\omega_sL_{ac}/c}E_{circ}(\omega_s) \quad (5.5)$$

$$= \frac{iJ_1(\delta)}{1 - r_1r_2e^{i2\omega_sL_{ac}/c}}E_{circ}(0) \quad (5.6)$$

where L_{ac} is the length of the arm cavity and c is the speed of light. The field reflected from the arm cavity is given by,

$$E_{ref}(\omega_s) = it_1r_2e^{i2\omega_sL_{ac}/c}E_{circ}(\omega_s) \quad (5.7)$$

$$= \frac{-t_1r_2e^{i2\omega_sL_{ac}/c}J_1(\delta)}{1 - r_1r_2e^{i2\omega_sL_{ac}/c}}E_{circ}(0) \quad (5.8)$$

Combining equations 5.4 and 5.8 gives us the transfer function, $\mathcal{A}(\omega_s)$, from the carrier field incident on the cavity, $E_{inc}(0)$, to the sideband field reflected from the cavity, $E_{ref}(\omega_s)$, due to the intra-cavity modulation.

$$\mathcal{A}(\omega_s) = \frac{-it_1^2r_2e^{i2\omega_sL_{ac}/c}J_1(\delta)}{(1 - r_1r_2)(1 - r_1r_2e^{i2\omega_sL_{ac}/c})} \quad (5.9)$$

We now consider the fields incident on the beamsplitter after reflection from the arm cavities. The fields associated with the arm cavity Michelson interferometer are shown in figure 5.6. For simplicity, we will assume the distances between the arm cavities and the beamsplitter are zero. Consider the fields in the in-line arm, $E_i(\omega_s)$, and perpendicular arm, $E_p(\omega_s)$, after reflection from the cavity with intra-cavity phase modulation. These fields are related to the carrier electric field incident on the Michelson interferometer,

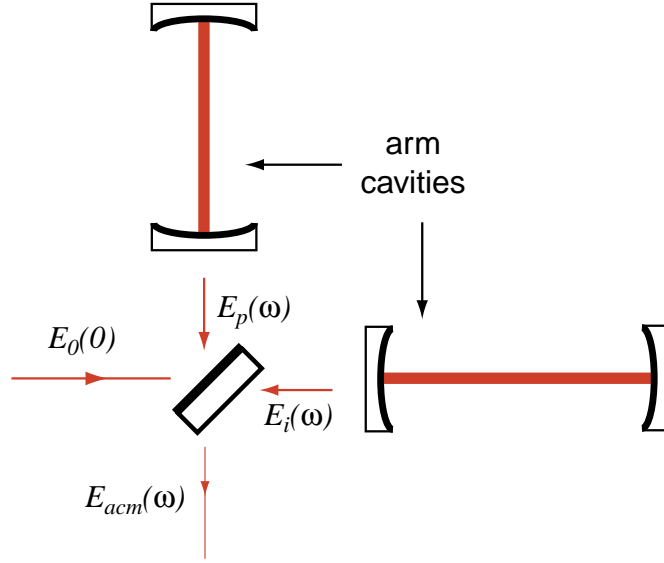


Figure 5.6: An arm cavity Michelson interferometer showing the electric fields required to calculate the signal response.

$E_0(0)$, by the expressions,

$$E_i(\omega_s) = it_{bs}E_0(0)\mathcal{A}(\omega_s) \quad (5.10)$$

$$E_p(\omega_s) = r_{bs}E_0(0)\mathcal{A}(\omega_s) \quad (5.11)$$

Ordinarily, one of these fields would be positive and the other negative due to the differential modulation of the gravitational wave. In this case, the sign change has been cancelled as one Michelson arm is shorter by $\lambda/2$ in order to hold the interferometer on a dark fringe for the carrier. At the beamsplitter the sidebands will interfere constructively towards the dark fringe. The field just after the beamsplitter at the dark fringe port is the response of an arm cavity Michelson, E_{acm} , and is equal to,

$$E_{acm}(\omega_s) = r_{bs}E_i(\omega_s) + it_{bs}E_p(\omega_s) \quad (5.12)$$

$$= 2it_{bs}r_{bs}\mathcal{A}(\omega_s)E_0(0) \quad (5.13)$$

$$= \mathcal{M}(\omega_s)\mathcal{A}(\omega_s)E_0(0) \quad (5.14)$$

where $\mathcal{M}(\omega_s)$ is the Michelson response and is equal to,

$$\mathcal{M}(\omega_s) = 2it_{bs}r_{bs} \quad (5.15)$$

Here $\mathcal{M}(\omega_s)$ is actually independent of the signal frequency due to our simplifying assumption that the Michelson arms are of length zero.

If we add a signal extraction mirror at the dark fringe, then $E_{acm}(\omega_s)$ will be the field injected into the signal cavity due to the gravitational wave. There will also be a contribution to the signal extraction cavity field from the previous round trip of the signal extraction cavity. The fields associated with the RSE Michelson interferometer are

shown in figure 5.7. The field inside the signal extraction cavity, $E_{sec}(\omega_s)$, will now be given by,

$$E_{sec}(\omega_s) = E_{acm}(\omega_s) + E_{sec}(\omega_s)r_s(r_{bs}^2 + t_{bs}^2)r_{cav}(\omega_s)e^{i(2\omega_s L_s/c + \phi_s)} \quad (5.16)$$

$$E_{sec}(\omega_s) = \frac{1}{1 - r_s(r_{bs}^2 + t_{bs}^2)r_{cav}(\omega_s)e^{i(2\omega_s L_s/c + \phi_s)}} E_{acm}(\omega_s) \quad (5.17)$$

where L_s is the length of the signal extraction cavity, r_s and t_s are the amplitude reflectivity and transmissivity of the signal mirror, and $r_{cav}(\omega_s)$ is the complex amplitude reflectivity of the arm cavity at the signal frequency (see for example equation 4.30). The variable ϕ_s represents the detuning of the signal cavity.

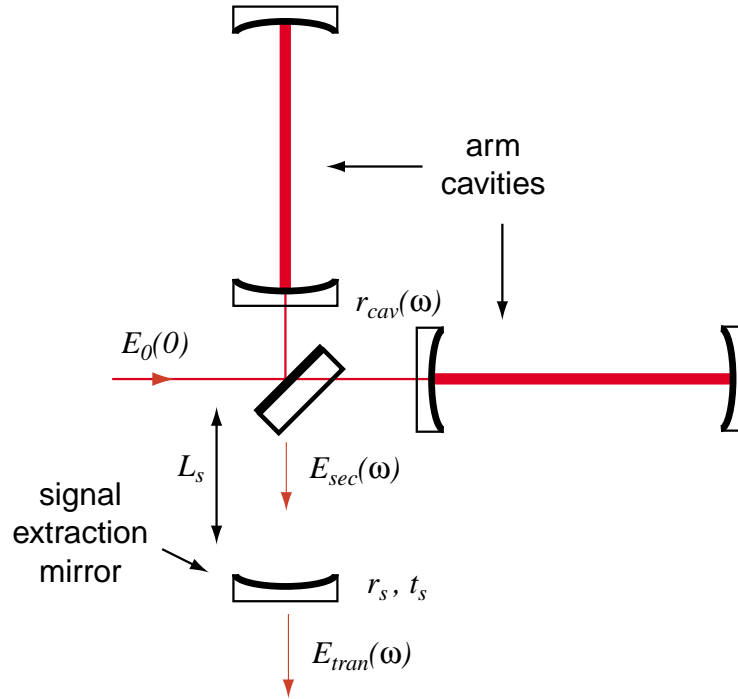


Figure 5.7: Michelson interferometer with resonant sideband extraction showing the field inside the signal extraction cavity

The signal at the dark fringe is related to the field inside the signal extraction cavity by $E_{tran} = E_{sec}it_s e^{i(\omega_s L_s/c + \phi_s/2)}$.

$$E_{tran}(\omega_s) = \frac{it_s e^{i(\omega_s L_s/c + \phi_s/2)}}{1 - r_s(r_{bs}^2 + t_{bs}^2)r_{cav}(\omega_s)e^{i(2\omega_s L_s/c + \phi_s)}} E_{acm}(\omega_s) \quad (5.18)$$

Substituting from equation 5.14 we obtain an expression for the total transfer function of the Michelson with resonant sideband extraction shown in equation 5.19.

$$\frac{E_{tran}(\omega_s)}{E_0(0)} = \mathcal{E}(\omega_s)\mathcal{M}(\omega_s)\mathcal{A}(\omega_s) \quad (5.19)$$

We have defined a new transfer function, \mathcal{E} , which is the signal enhancement due to the

signal extraction cavity. It is defined as,

$$\mathcal{E}(\omega_s) = \frac{it_s e^{i(\omega_s L_s/c + \phi_s/2)}}{1 - r_s(r_{bs}^2 + t_{bs}^2)r_{cav}(\omega_s)e^{i(2\omega_s L_s/c + \phi_s)}} \quad (5.20)$$

The frequency response of a Michelson interferometer with resonant sideband extraction is measured experimentally in chapter 7.

5.9 Autoalignment

The control systems discussed so far have been for the length degrees of freedom. In addition to these, suspended interferometers also require active control of the alignment degrees of freedom for optimum performance. Over the past decade, techniques have been developed based on the interference of the Hermite-Gauss modes [70, 71] to obtain a sensitive measure of the tilt and offset of a beam relative to an interferometer. Variants of the Ward technique [71] now form the basis for most interferometric alignment sensing systems. This technique, measures the interference between the TEM_{00} modes and the TEM_{10} and TEM_{01} modes using the modulation sidebands of PDH locking. Analysis and demonstrations of these technique applied to complicated coupled interferometers have since been performed by various groups [72–77]. An alignment sensing system is yet to be demonstrated for the resonant sideband extraction configuration. This thesis is only concerned with the length sensing degrees of freedom and the issue of alignment sensing in RSE systems is not considered here.

5.10 Summary

We have discussed the two main factors determining the shot noise limited sensitivity of a gravitational wave detector, energy storage and storage time. We have detailed the principle of operation of several configurations of gravitational wave detectors including arm cavity, dual recycled and RSE Michelson interferometers. We have also presented a simple derivation of the frequency response of RSE in a Michelson interferometer using a transfer function approach. In the next chapter we will examine yet another potential configuration for a gravitational wave detector, the Sagnac interferometer.

Sagnac interferometers for gravitational wave detection

In recent years there has been renewed interest in Sagnac interferometers [78] for use in gravitational wave detectors. Experimental investigations carried out on delay line systems [79–83] have found the Sagnac interferometer offers comparable sensitivity to the Michelson interferometer with several potential advantages. These advantages include a simplified control system, insensitivity to reflectivity imbalance in the arms and perhaps most importantly, insensitivity to laser frequency noise.

This chapter describes a brief experimental investigation of the Sagnac interferometer in various configurations. The purpose of this work was to determine experimentally if the Sagnac interferometer's advantages in a delay line system transfer to more complicated, cavity based, topologies. The chapter begins with a basic introduction to Sagnac interferometers before presenting an experimental demonstration of a delay line Sagnac in section 6.2. In this system we measure the frequency response of the interferometer using the polarisation signal extraction scheme developed by Sun *et al.* [80]. Section 6.3 presents the first experimental demonstration of a Sagnac interferometer with resonant sideband extraction. This experiment was performed to illuminate any practical difficulties or advantages associated with the configuration and should not be considered a thorough investigation of control or signal extraction issues.

6.1 Sagnac interferometer basics

In a Sagnac, the light is split into two beams which counter propagate through the instrument and interfere when recombined at the beam splitter. The optical paths of these beams are identical at zero frequency but differences can arise on time scales comparable to the travel time of the light. As a consequence, the control of a Sagnac is in general simpler than a Michelson. The common path length of the counter propagating beams ensures that the signal port of the Sagnac is always on a dark fringe. Losses due to absorption are also common to both beams and have no effect on the fringe visibility of the instrument. An unequal beamsplitter ratio however, can significantly degrade the fringe visibility and thus reduce instrument sensitivity. One beam experiences two reflections from the beamsplitter while the beam travelling in the opposite direction experiences two transmissions before detection at the signal port. Recently, the main beamsplitter has been replaced by a polarising beam splitter [82], which alleviates this problem by allowing each beam to once again experience one reflection and one transmission. Research into this type of polarisation Sagnac looks promising, and this configuration is

emerging as a viable alternative to the Michelson interferometer for future detectors [83]. Another potential disadvantage of the Sagnac interferometer is that mode distortions, due to imperfect mirror curvature within the interferometer, can have a greater effect in the Sagnac than in the Michelson system [84].

Historically, Sagnac interferometers have been used as rotation sensors. For a gravitational wave detector this sensitivity to rotation is undesirable, introducing an offset or noise source to the final output. By ensuring the Sagnac interferometer encloses a total area of zero this sensitivity to rotation can be eliminated. A zero area Sagnac is constructed by enclosing equal amounts of positive and negative area as shown in figure 6.1. Positive and negative areas are those enclosed by a beam travelling in a clockwise and anticlockwise direction respectively. For the benchtop Sagnac experiments discussed here we did not use zero area devices as the sensitivity to rotation for such a small interferometer was minimal, in addition to occurring at frequencies which are small compared to the signal bandwidth.

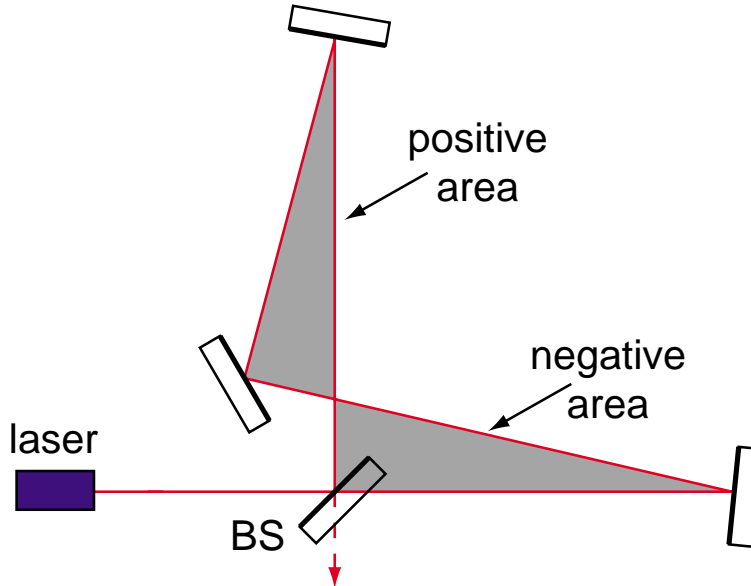


Figure 6.1: Sagnac interferometer enclosing a net area of zero, achieved by cancellation of positive and negative areas.

6.2 Delay line Sagnac interferometer

As discussed in chapter 5, a delay line can be used to increase the storage time of the signal sidebands. The result is a decrease in the bandwidth of a device. In this section, we measure the frequency response of a 9.3 m delay line Sagnac interferometer.

Figure 6.2 shows the experimental layout of the 9.3 m delay line Sagnac interferometer. Broadband phase modulators (Gsänger PM 25) were contained in the each arm of the interferometer, immediately after the beam splitter. These modulators were driven out of phase to simulate the gravitational wave signal and map out the frequency response of the instrument.

As a Sagnac interferometer contains no arm length mismatch, we cannot use frontal

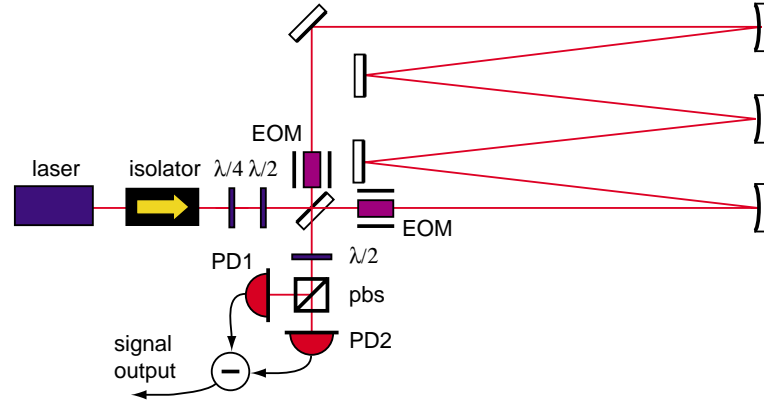


Figure 6.2: Delay line Sagnac interferometer using polarisation based readout system. EOM: electro-optic modulator, pbs: polarising beamsplitter, $\lambda/2$: half wave plate, $\lambda/4$: quarter wave plate, PD: photodetector.

modulation techniques such as Schnupp modulation [34] to provide a local oscillator at the dark fringe. One innovative solution [80] is to make use of the polarisation dependence of the beam splitter ratio to couple a fraction of the orthogonal polarisation (horizontal say) to the dark fringe. This horizontal polarisation can be used as a local oscillator for the vertically polarised signal. Analysis of the polarisation state of the output can provide a shot noise limited readout of the vibrations of the mirrors. In addition, the amount of local oscillator can be conveniently adjusted with a waveplate at the interferometer input. By using the subtraction of two detectors the intensity noise of the local oscillator can be removed. This technique can be thought of as the two beam interferometer equivalent of Hänsch-Couillaud locking [85] of optical cavities (see chapter 8) in the same way that Schnupp modulation can be thought of as the two beam equivalent of the Pound-Drever-Hall technique.

Figure 6.3 shows the measured broadband frequency response of the system when the phase modulators are driven out of phase. Notice that the response of the Sagnac drops to zero at DC and at multiples of c/L_c , where c is the speed of light and L_c , the characteristic length of the Sagnac, is the distance between the modulators. The signal null at DC is an inevitable consequence of the common optical paths of the interfering beams. The nulls at higher frequencies occur when the travel time of the light between the modulators is exactly equal to the signal period (or an integer number of signal periods). The maximum signal occurs at a frequency of $c/(2L_c)$, when each beam experiences exactly the opposite phase shift in each modulator, maximising the relative phase shift between the beams.

6.2.1 Summary

A 9.3 m delay line Sagnac was constructed and the signal response measured using a homodyne polarisation technique. One of the main drawbacks of such a delay line for a gravitational wave detector is that it is very hard to achieve the optimum storage time. The number of bounces required leads to a large overlap of spots on the mirrors surface which can cause problems with scattered light. In the next section we move our investigation to arm cavity based Sagnac interferometers to overcome the storage time problems.

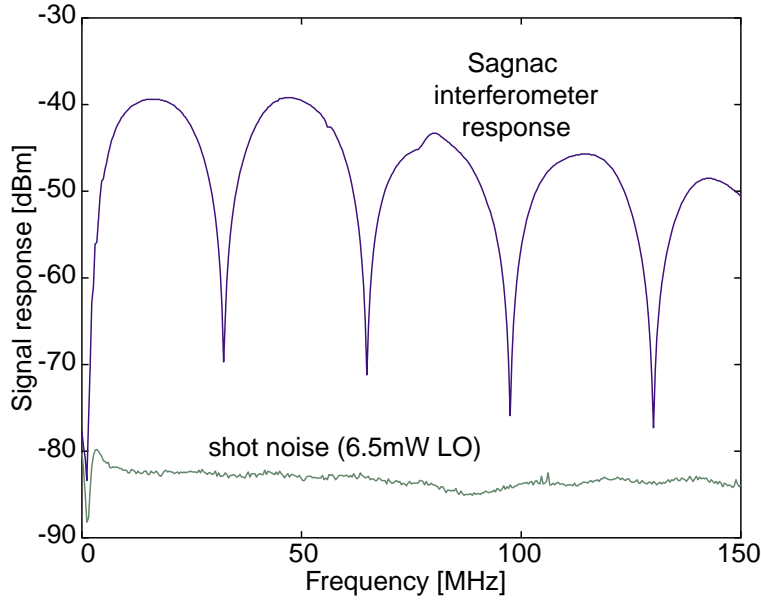


Figure 6.3: Experimentally measured frequency response of a 9.2 m delay line Sagnac interferometer.

6.3 RSE in a Sagnac Interferometer

Theoretical comparisons [37] of the frequency response of Sagnac and Michelson based systems have been carried out for several configurations. There has, however, been little experimental work performed on cavity based Sagnacs. One of the aims of the work presented in this section was to determine experimentally if the Sagnac's advantages over the Michelson in delay line systems transfer to cavity based configurations. In this section we will discuss an experimental investigation of a Sagnac interferometer with ring cavities in the arms and a Sagnac with resonant sideband extraction (RSE).

The RSE Sagnac interferometer is similar in principal to an RSE Michelson with several practical differences. Firstly, due to the ring nature of the Sagnac we require ring cavities instead of linear cavities in the interferometer arms. Note that the light passes through both cavities before returning to the beamsplitter ensuring counter propagating beams experience a common path. Another important difference is that the RSE Sagnac requires more optical components than an RSE Michelson interferometer and will therefore have a greater total optical loss (for both carrier power and signal). The basic layout for resonant sideband extraction in a Sagnac interferometer is shown in figure 6.4.

The Sagnac itself is made up of three mirrors and a beamsplitter. Two of these mirrors are the input couplers to the arm cavities. The third mirror can be used for Sagnac alignment and to extract error signals for control purposes. The Sagnac pictured here is not a zero area instrument and thus is sensitive to rotation. For a small benchtop device the effects of rotation are negligible due to the high frequency range of interest. For large scale instruments where rotation sensitivity is a concern, the RSE Sagnac can be made to encompass zero area in a similar way to that shown in figure 6.1.

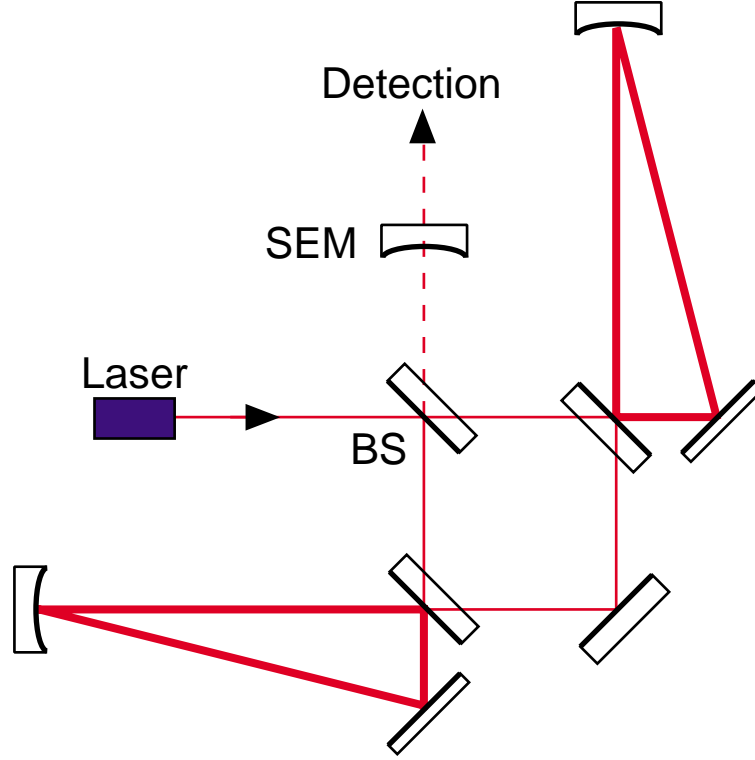


Figure 6.4: Basic layout for resonant sideband extraction in a Sagnac interferometer. Ring cavities are used to increase the stored power while the signal extraction mirror (SEM) optimises the storage time of the signal sidebands. BS: main beamsplitter

6.3.1 RSE Sagnac interferometer frequency response

To calculate the frequency response of an RSE Sagnac interferometer we will use the transfer function approach introduced in section 5.8. Experimentally, the gravitational wave signal is simulated with phase modulators in the arm cavities. A phase modulator inside an arm cavity produces sidebands on the reflected field at $\pm\omega_s$ each with an amplitude (normalised to the electric field incident on the cavity) given by,

$$\mathcal{A}(\omega_s) = \frac{-t_1^2 r_2 r_3 e^{i\omega_s p/c} J_1(\delta)}{(1 - r_1 r_2 r_3)(1 - r_1 r_2 r_3 e^{i\omega_s p/c})} \quad (6.1)$$

where ω_s is the modulation (or signal) frequency (rad/sec), r_1 , r_2 and r_3 are the electric field reflectivities of the cavity mirrors, t_1 the input coupler transmissivity, p is the cavity round trip distance and c is the speed of light. The sideband amplitude is proportional to the first order Bessel function of the first kind, $J_1(\delta)$ where δ is the modulation depth in radians. Note that for the small signals considered here we have $\delta \ll 1$. Equation 6.1, contains the product of three terms, the carrier field inside the cavity (on resonance), the efficiency of coupling from carrier to sidebands $J_1(\delta)$, and the leakage of these sidebands out of the cavity.

For an arm cavity Sagnac, the fields propagating in each direction (E_+ and E_-) after reflection from both arm cavities can be written as,

$$E_{s+}(\omega_s) = E_0 r_{bs}(\mathcal{A}(\omega_s) r_{cav}(\omega_s) e^{i\omega_s L_c/c} - \mathcal{A}(\omega_s) r_{cav}(0)) \quad (6.2)$$

$$E_{s-}(\omega_s) = E_0 i t_{bs}(-\mathcal{A}(\omega_s) r_{cav}(\omega_s) e^{i\omega_s L_c/c} + \mathcal{A}(\omega_s) r_{cav}(0)) \quad (6.3)$$

where $r_{cav}(\omega_s)$ is the reflectivity of the arm cavities at the sideband frequency ω_s , $r_{cav}(0)$ is the carrier reflectivity, r_{bs} and t_{bs} are the reflectivity and transmissivity of the beamsplitter, and E_0 is the electric field incident on the main beamsplitter. The distance L_c is the separation of the arm cavities and produces a relative phase shift for the signal sidebands produced in each cavity. The modulators are driven out of phase to simulate the quadrupole moment of a gravitational wave, which results in the subtraction between the two terms in each equation. In addition the beams experience the modulators in a different order which accounts for the sign reversal from equation 6.2 to equation 6.3. After recombination at the beamsplitter the field at the signal port of the arm cavity Sagnac is given by,

$$E_{acs}(\omega_s) = E_0 \mathcal{A}(\omega_s) (r_{bs}^2 + t_{bs}^2) [r_{cav}(\omega_s) e^{i\omega_s L_c/c} - r_{cav}(0)] \quad (6.4)$$

which can be rewritten as,

$$E_{acs}(\omega_s) = E_0 \mathcal{A}(\omega_s) \mathcal{S}(\omega_s) \quad (6.5)$$

where $\mathcal{S}(\omega_s)$ incorporates the response of the Sagnac to antisymmetric phase modulation and is given by,

$$\mathcal{S}(\omega_s) = (r_{bs}^2 + t_{bs}^2) [r_{cav}(\omega_s) e^{i\omega_s L_c/c} - r_{cav}(0)] \quad (6.6)$$

Note that $\mathcal{S}(\omega_s)$ approaches zero as $\omega_s \rightarrow 0$. This is markedly different from the Michelson response which has a maximum at zero frequency.

Once the response of the arm cavity Sagnac is obtained the RSE response can be determined by solving a self consistent equation for propagation in the signal extraction cavity similar to equation 5.16. From this we arrive at the signal enhancement factor, $\mathcal{E}(\omega_s)$, due to the addition of the signal extraction mirror.

$$\mathcal{E}(\omega_s) = \frac{it_s}{1 - 2ir_{bs}t_{bs}r_s r_{cav}(\omega_s)^2 e^{(i\omega_s p_s/c + \phi_s)}} \quad (6.7)$$

where r_s and t_s are the reflectivity and transmission of the signal extraction mirror, p_s is the round trip optical path of the signal extraction cavity and ϕ_s is the signal extraction cavity detuning. Finally, the total frequency response, $\mathcal{T}(\omega_s)$, of the RSE Sagnac is given by,

$$\mathcal{T}(\omega_s) = E_0 \mathcal{A}(\omega_s) \mathcal{S}(\omega_s) \mathcal{E}(\omega_s) \quad (6.8)$$

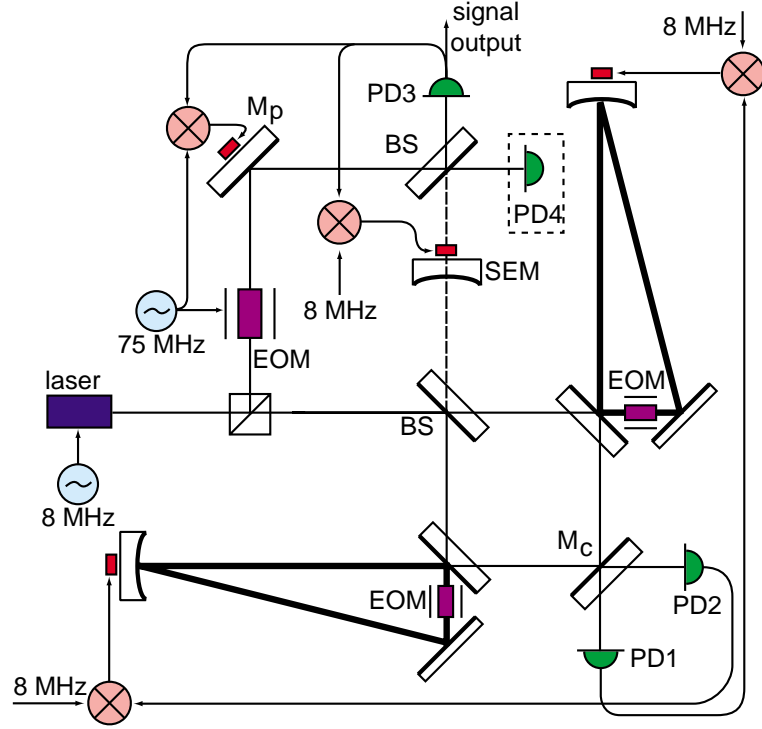


Figure 6.5: Optical and electronic configuration for RSE Sagnac interferometer. EOM: electro-optic modulator, PD: photodetector, BS: beamsplitter, SEM: signal extraction mirror.

6.4 Experimental Setup

It should be noted that due to the smaller scale and reduced finesse of this instrument the signal bandwidth stretches to several megahertz. For a large scale gravity wave detector the intended bandwidth would be approximately 40 Hz to 1 kHz.

The experimental setup is shown in figure 6.5. We use a 700 mW Nd:YAG non planar ring oscillator (NPRO) laser (Lightwave Electronics 126) operating in a single mode. Each arm cavity had a round trip of 4.0 m. The gravitational wave signal was simulated by broadband low loss modulators (Gsänger PM 25) within the arm cavities. Losses in these modulators restricted the arm cavity finesse to approximately 110. In order to maximise the circulating power, and thus the sensitivity, the arm cavities should be approximately impedance matched. In this experiment the cavities were slightly overcoupled with approximately 20 % of the incident power reflected on resonance.

The arm cavities were locked to the laser frequency using Pound-Drever-Hall reflection locking [33] using an 8 MHz phase modulation produced by directly modulating the laser crystal PZT. The locking signals were coupled out of the Sagnac through the mirror M_c , a 98% reflective coupling mirror between the arm cavities and fed back to PZTs on the end mirrors of the arm cavities. This produces two orthogonal error signals (in the absence of an RSE mirror) allowing the arm cavities to be independently locked. For identical cavities such as those used here, it is necessary that the beam waist is positioned at the centre of the Sagnac for symmetry reasons. The main beamsplitter power reflectivity was 54% which yielded a dark fringe of 7 mW with the arm cavities locked on resonance for an input power of 350 mW.

The signal extraction cavity had a round trip of approximately 1.9 m including the round trip of the Sagnac (0.57 m). The signal cavity was controlled with the error signal obtained from PD3 using a technique analogous to transmission locking. For this control system we utilise the imperfect beamsplitter ratio to couple some of the 8 Mhz modulation sidebands through to the signal port. The finesse of the signal cavity was extremely low due to the low reflectivities of the near impedance matched arm cavities. This means that the 8 Mhz sidebands are well inside the bandwidth of the signal extraction cavity and can be transmitted through to the signal port only slightly attenuated. In order to lock the signal cavity the arm cavities must be locked first with relatively high gain. This control system was not flexible enough to allow us to detune the signal extraction cavity. The results presented here for detuned points were obtained by manually tuning the SEM. This was made possible by the low finesse signal extraction cavity and was adequate for demonstration of the system's frequency response. Equations 6.9-6.11 summarise the origins of the 3 error signals, where Φ_{ac1} and Φ_{ac2} are the degrees of freedom of the arm cavities on the top right and bottom left of figure 6.5 respectively and ϕ_s is the signal cavity degree of freedom.

$$\Phi_{ac1} = \text{demodulate PD1 @ 8 MHz} \quad (6.9)$$

$$\Phi_{ac2} = \text{demodulate PD2 @ 8 MHz} \quad (6.10)$$

$$\phi_s = \text{demodulate PD3 @ 8 MHz} \quad (6.11)$$

The signal was obtained by recombining the light from the dark fringe of the interferometer with a 100 mW local oscillator derived from a tap off of the incident beam effectively forming a Mach-Zehnder interferometer. The combined beam was detected on a single high power detector, PD3 with a 3 dB bandwidth of approximately 65 MHz [86]. At the time of the experiment a second high power detector, PD4, was not available. A second detector would allow the subtraction of classical intensity noise of the local oscillator from the signal. The local oscillator was phase modulated at 75 MHz by an electro-optic modulator. This was for control purposes only and not for signal extraction. The relative phase of the local oscillator was controlled by feeding back to the PZT mounted on mirror M_p . For the RSE system, the optimum local oscillator phase is a function of SEM detuning and signal frequency. The Mach-Zehnder could be locked using either the 1st or 2nd harmonic. In principle, any arbitrary locking point can be obtained by using a linear combination of these two error signals. For the experimental data shown here the Mach-Zehnder phase was tuned manually.

The broadband modulators were driven with a swept frequency signal from a tracking generator, with the detected response recorded on a spectrum analyser (Hewlett-Packard 3589A). Frequency responses for the arm cavity Sagnac and RSE Sagnac with SEM power reflectivities of 50%, 70% and 90% were obtained.

6.5 Experimental Results

Figure 6.6 shows the measured and calculated frequency response of the arm cavity Sagnac interferometer. The theoretical curve was calculated from equation 6.5 using an independent calibration of all of the parameters including arm cavity response, modulation depths and detector efficiency and has been neither fitted nor scaled to the data.

The peaks at low frequency are due to the resonances of the phase modulators. As can

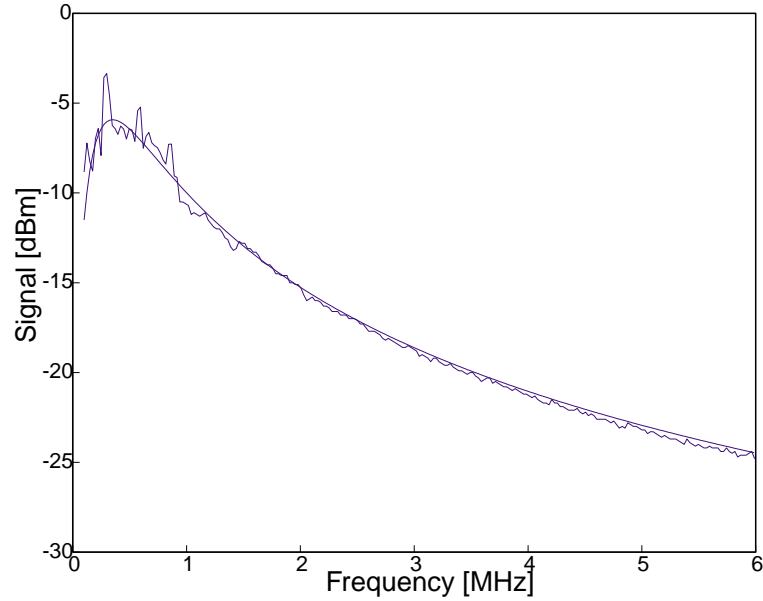


Figure 6.6: Measured and calculated signal response for a Sagnac interferometer with arm cavities.

be seen from equation 6.5 the frequency response is the product of the Sagnac frequency response with the arm cavities' response. The drop in signal to the left of the graph is due to the insensitivity of the Sagnac at low frequencies. The roll off at high frequencies is due to the response of the arm cavities. The same measurement was taken for the Sagnac for an SEM with a power reflectivity of 70% and is shown in figure 6.7.

The theoretical curve for the RSE case is based on equation 6.8. With the addition of the SEM mirror the signal bandwidth of the instrument was increased by a factor of 6.5 compared to the arm cavity Sagnac. Experimental results for 50% and 90% power reflectivity SEMs were also obtained and the results are shown in figure 6.8.

For this particular experiment the optimum SEM for high frequency signals is the 70% power reflectivity SEM. The 50% mirror increases the bandwidth of the instrument by a factor of 3.3. The 90% SEM has a lower signal response than the 70% SEM Sagnac at all frequencies. This is because the loss on reflection from the arm cavities dominates the total loss of the signal cavity when the signal mirror has low transmissivity. For the 90% SEM the circulating power in the arm cavities was observed to drop substantially as the signal extraction cavity was brought close to resonance. Possible causes of this power drop are discussed in section 6.6.

Figure 6.9 demonstrates the tuning capabilities of the Sagnac with RSE. Three frequency responses taken as the signal extraction mirror was tuned manually from resonance to antiresonance are shown. The calculated frequency responses, which are not shown here for clarity, can be fitted to show good agreement with the experimental curves by adjusting the signal extraction cavity detuning and Mach Zehnder phase.

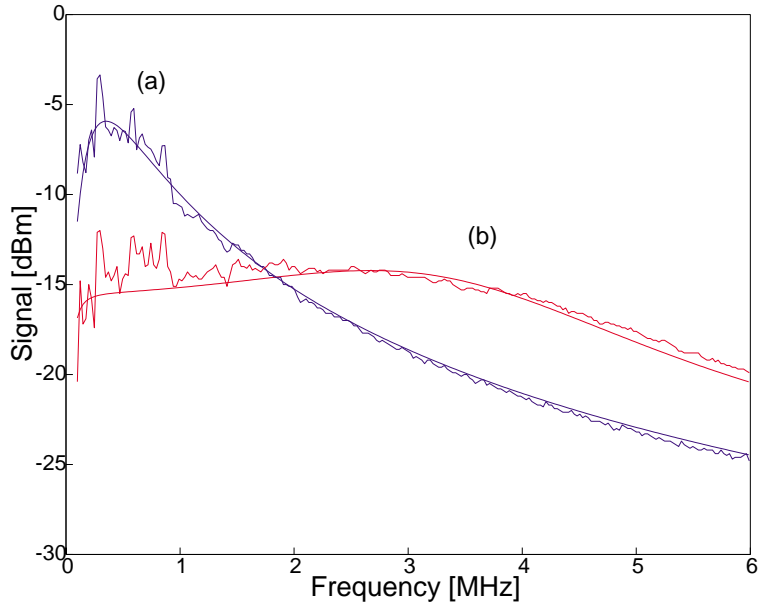


Figure 6.7: A comparison of the frequency responses of (a) arm cavity Sagnac (calculated and measured) to (b) RSE Sagnac (calculated and measured) with an SEM power reflectivity 70%.

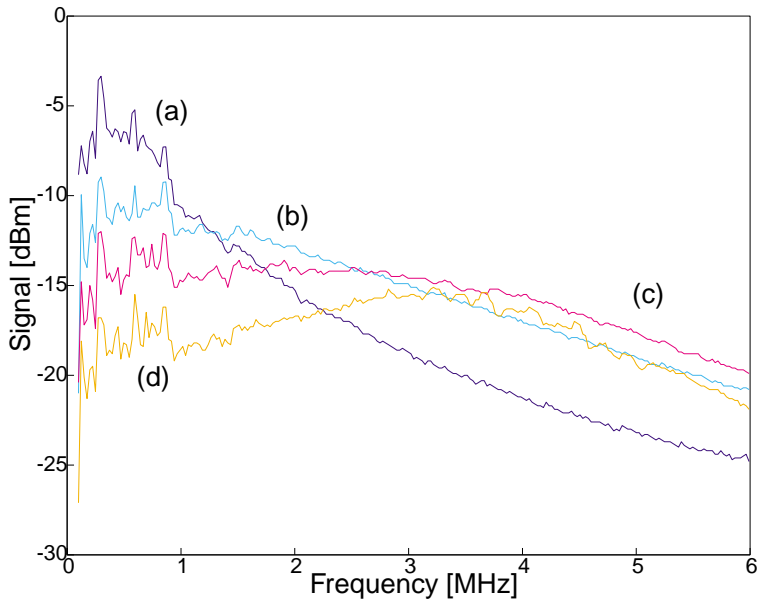


Figure 6.8: Frequency response of; (a) arm cavity Sagnac (no SEM), (b) RSE Sagnac with SEM=50%, (c) RSE Sagnac with SEM=70% (d) RSE Sagnac with SEM=90%.

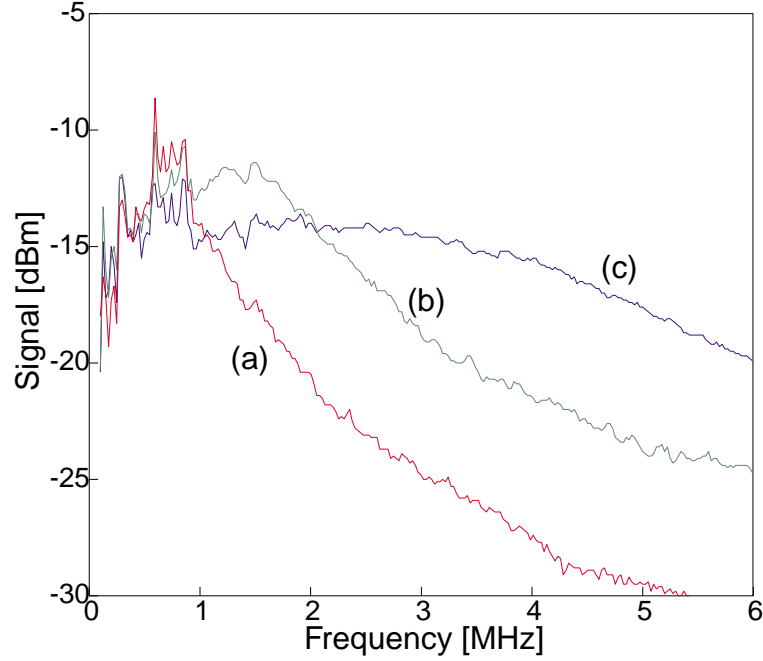


Figure 6.9: Frequency response of RSE Sagnac for SEM detuning (SEM reflectivity=50%). (a) signal recycling, (b) detuned point, and (c) resonant sideband extraction

6.6 Discussion

It can be seen from figures 6.6 and 6.7 that we have excellent agreement between the calculated and observed frequency responses. All parameters used in producing the theoretical curves were measured independently. For example, the properties of the arm cavities were measured by applying a scanning amplitude modulation to the input light and measuring the fraction of this amplitude modulation transmitted through the cavity as a function of frequency.

The main experimental difficulty encountered with this setup was the use of modulators in the arm cavities. With the arm cavities locked several watts of optical power were transmitted through the modulators. This caused distortions in the modulators leading to a slight misalignment of the cavities and consequently a misalignment of the entire system. This effect was more significant in the resonant sideband extraction case than the arm cavity case as the RSE system is more sensitive to alignment. For the purposes of this experiment, however, the modulators were necessary in order to obtain the broad frequency response of the system. In the following sections we will compare the features of the Sagnac and Michelson interferometers in three areas; energy storage, dependence on beamsplitter reflectivity and ease of control.

6.6.1 Energy Storage

The sensitivity theorem [36] relates the shot noise limited sensitivity to the stored optical energy. For large scale interferometers the stored optical energy will be limited by mirror loss. A three mirror ring cavity has an intrinsically higher loss than a linear cavity due to the extra mirror surface. As a consequence, an arm cavity Michelson device can attain

greater energy storage than an equivalent Sagnac. In addition, a loss dominated Sagnac is further disadvantaged due to the increased number of optical surfaces within the Sagnac itself. In an RSE device, the signal extraction cavity of a Sagnac has two more optical surfaces than the Michelson. As a consequence, the signal loss for an RSE Sagnac is greater than for its Michelson counterpart. Both power loss and signal loss translate directly into a reduction of the instrument sensitivity.

6.6.2 Beamsplitter Issues

As mentioned in section 6.1, the fringe visibility is dependent upon the beamsplitter ratio and is at a maximum for a 50:50 splitting ratio. For a Sagnac with resonant sideband extraction, the dependence on the beamsplitter ratio is increased. An imbalanced beamsplitter in an RSE Sagnac allows some of the carrier to be coupled into the signal extraction cavity. In this case, the signal mirror can decrease the storage time of the carrier in the same way that it does for the signal. This can result in a large drop in circulating power in the arm cavities which is detrimental to the total sensitivity of the instrument. This effect increases with SEM reflectivity.

A Sagnac's sensitivity to the main beamsplitter ratio is analogous to a Michelson's sensitivity to mismatched losses in the arms. The two problems both manifest themselves as a degradation of the fringe visibility. Conversely, the Sagnac is immune to imbalanced reflectivity in the arms and the Michelson is immune to beamsplitter ratio imbalance. It remains to be seen which will be the most significant factor in the fabrication of large scale optics for future detectors.

In order to obtain a control signal for the SEM using frontal modulation we used a marginally imbalanced beamsplitter with a power splitting ratio of 54:46. In the arm cavity Sagnac a slight increase in the dark fringe power was observed. In the RSE systems a significant drop in arm cavity circulating power was observed, which was particularly debilitating with the 90% SEM.

6.6.3 Control

The RSE Sagnac has fewer locking systems than the Michelson analogue. In a Michelson RSE system 4 separate locking signals are required: Michelson differential mode, signal extraction cavity and two arm cavities. In a Sagnac, we no longer have the need for a differential interferometer locking signal due to the internal common path length. A Sagnac RSE system requires no control of the inboard cavity mirror positions. On the negative side, modulation sidebands cannot be injected into the signal cavity using the standard technique of introducing an arm length mismatch. Other more complex methods must be employed to lock the signal extraction cavity such as using a beam injected into the signal cavity via the SEM [56] or using the orthogonally polarised light with a polarisation dependent beamsplitter.

Without the SEM in place the error signals for the arm cavities are completely independent. Once the signal mirror is added this is no longer true as each locking detector measures light reflected from both cavities. This effect is more pronounced for higher SEM reflectivities, a greater beamsplitter imbalance and when the signal extraction cavity is held close to resonance.

The system employed for control of the SEM is not intended for use in a high finesse instrument. The signal extraction cavity was locked using a technique similar to trans-

mission locking. The modulation sidebands pass into the signal cavity due to a combination of residual mode mismatch and a non 50/50 beamsplitter ratio. This system allowed the signal extraction cavity to be locked to the RSE position but was fairly inflexible for tuning the SEM position. To allow locking of the SEM to an arbitrary position a more versatile control system is required.

6.7 Conclusion

We have presented the first experimental demonstration of resonant sideband extraction in a Sagnac interferometer. The frequency response of the system was measured and found to be in excellent agreement with theoretical predictions.

The delay line Sagnac has many advantages over the delay line Michelson system. Common path lengths in the arms can be an enormous advantage if utilised properly. However, once the system is complicated with optical cavities many of the benefits of a Sagnac are lost. In general, the control systems for an RSE Sagnac are no simpler than its Michelson counterpart. The advantage of insensitivity to asymmetric losses in the arms is offset by the dependence on the beamsplitter ratio. The reduced ability of a resonant Sagnac device to store optical energy, due to intrinsically higher losses, ensures that the shot noise limited sensitivity of a Michelson interferometer will always be superior. For the purposes of our research, we are interested in an interferometric configuration which has a tunable signal bandwidth. For this application we believe that the Sagnac holds no advantage over the Michelson analogue.

Power Recycled Michelson interferometer with resonant sideband extraction

A power recycled Michelson interferometer with resonant sideband extraction has been chosen as the reference design for LIGO II [87], the first planned upgrade to LIGO due to take place in the middle of this decade. In this chapter we introduce a control system for the length degrees of freedom of such an interferometer. We report on an experimental implementation of this control system in a bench top prototype and present broadband measurements of the prototype's frequency responses for a range of signal cavity detunings.

7.1 Control System

This configuration of interferometer poses a difficult control problem. There are in total five degrees of freedom which must be controlled: the arm cavity common mode phase, Φ_+ , arm cavity differential mode phase, Φ_- , the Michelson common mode phase,¹ ϕ_+ , the Michelson differential mode phase, ϕ_- , and the signal cavity phase, ϕ_s . Our goal was to develop a flexible control system which could provide quasi-continuous detuning of the signal cavity as required, without the need for macroscopic changes of the interferometer parameters. To achieve this the first four degrees of freedom must be locked to a fixed position whilst the final degree of freedom is detuned to an arbitrary point. Ideally detuning should be performed without the interferometer dropping lock, thereby avoiding the need for lock reacquisition. The final criterion is that the system is able to be implemented in a long base-line interferometer. For this reason we have restricted the control system to frontal modulation only.

The requirement of tunability makes the control problem much more difficult. Two strategies can be employed to ensure the control signals for the other degrees of freedom are not influenced by the detuning of the signal cavity. The first is to calculate the offsets added due to the detuning of the signal mirror on all other control signals and then subtract these offsets to produce the error signals. This technique has the advantage that a relatively simple modulation scheme can be used; however, it relies on extremely accurate knowledge of interferometer parameters and may be difficult to implement for

¹The Michelson common mode degree of freedom, ϕ_+ , is also referred to as the power cavity degree of freedom.

arbitrary signal cavity detunings. The second approach is to use a modulation scheme which gives the maximum isolation against the signal cavity for all other degrees of freedom. This can be achieved by careful selection of interferometer lengths and modulation frequencies. For example, a modulation frequency that is completely reflected by the Michelson is immune to changes in the signal cavity as it never senses the signal mirror. One disadvantage is that this technique may require more modulation frequencies leading to a complex input beam preparation problem. We have chosen such a system, sacrificing a small amount of optical and modulation simplicity in return for flexibility of the detuning of the signal cavity and maximum orthogonality between error signals.

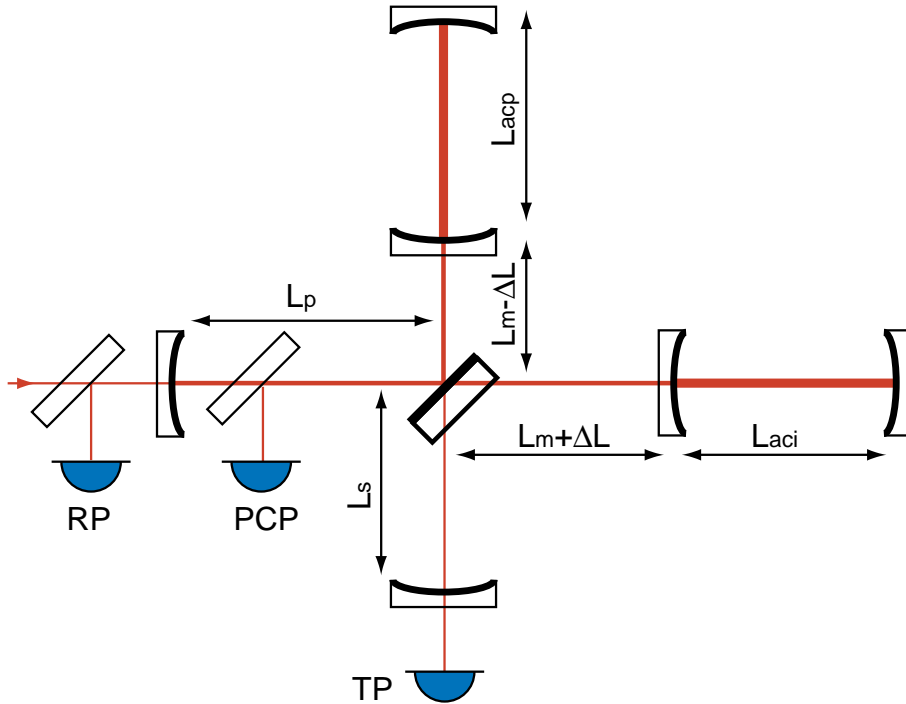


Figure 7.1: Diagram of the power recycled Michelson with RSE showing length definitions and photodetector positions. RP: reflected port, PCP: power cavity port, TP: transmission port.

Figure 7.1 shows the lengths used to describe the interferometer. The symbols L_p and L_s denote the distance from the beamsplitter to the power mirror and signal mirror respectively. The average Michelson arm length (distance from the beamsplitter to the arm cavities) is L_m with the difference between the two Michelson arms given by $2\Delta L$.

The control system was designed and modelled with MATLAB using the two m-files RSEcontrol.m and RSEinterf.m contained in appendix C. The first program calculates the 6 phase shifts experienced by a field (e.g. a sideband) in different parts of the interferometer (the power cavity, Michelson in-line arm, Michelson perpendicular arm, arm cavity in-line, arm cavity perpendicular and signal cavity). These phases are calculated from the 6 lengths (L_p , $L_m + \Delta L$, $L_m - \Delta L$, L_{aci} , L_{acp} and L_s) and the frequency offset of the field from the carrier. These phases are passed to a second m-file RSEinterf.m which uses these phases as an input to the equations for the fields at the reflected port (RP), power cavity port (PCP) and transmitted port (TP) (see figure 7.1). These complex fields are passed back to the main m-file, RSEcontrol.m. This process is repeated for each field present

in the interferometer. These fields are then demodulated and the results are plotted for examination. Typically we would like to know the demodulated output as a function of one of the interferometer degrees of freedom, in which case one or more of the six phases becomes a vector, and the program RSEinterf.m returns a vector for each of the fields. The demodulated outputs are calculated from these vectors and plotted as a function of the varied parameter.

The control system was designed around two initial ideas. The first was to use modulation sidebands which were completely reflected by the Michelson. This should ensure that any error signals obtained from these sidebands beating with the carrier are insensitive to the detuning of the signal mirror. The second idea was to use a subcarrier with a frequency tunable offset. It was hoped that if the signal cavity was locked to this subcarrier field then the instrument could be detuned by changing the offset frequency of the subcarrier.

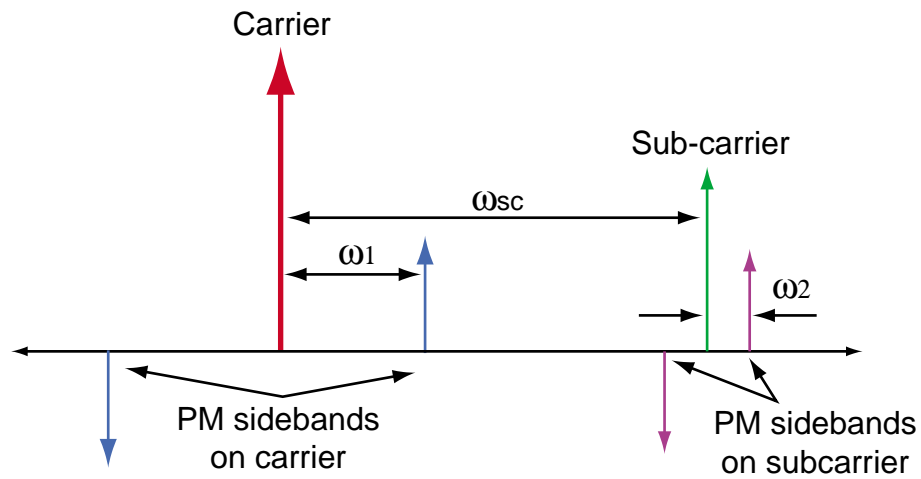


Figure 7.2: Modulation sidebands required on the input field for the power recycled RSE Michelson control system.

Our solution relies on the use of a subcarrier or single sideband offset from the carrier by a radial frequency of ω_{sc} . In addition to the subcarrier we have two modulation frequencies, one for phase modulation of the carrier (radial frequency ω_1), and the second for modulation of the subcarrier (radial frequency ω_2). These are shown diagrammatically in figure 7.2. When the interferometer is at the correct operating point only the carrier field is resonant in the arm cavities. The phase modulation sidebands at ω_1 are resonant in the power cavity, and are completely reflected by the Michelson interferometer. The single sideband is almost² completely transmitted by the Michelson interferometer and is resonant in the cavity formed by the signal mirror and the power mirror. The sidebands at ω_2 are nonresonant everywhere and are totally reflected at the power mirror. The relationships between the modulation frequencies and these lengths are summarised in table 7.1.

All error signals are derived by demodulation of the outputs of the three photodetectors at the RP, TP and PCP. In the following sections we discuss the details of the error

²As the single sideband frequency changes it is not always exactly at the point of maximum transmission.

Length	Relationship to modulation frequencies
ΔL	$c/(4\nu_1) \ \& \ \approx (n + \frac{1}{2})c/(4\nu_{sc})$
$L_p + L_m$	$n \times c/(2\nu_1)$
L_{aci}	free variable
L_{acp}	free variable
L_s	free variable (usually $\approx L_p$)

Table 7.1: Relationships between interferometer lengths and modulation frequencies (n represents an integer).

signals for each degree of freedom.

7.1.1 Arm cavity common mode

The arm cavities are the highest finesse cavities and thus will dominate many of the error signals which involve the carrier field. This important error signal is obtained from demodulation of the detected photocurrent at the power cavity port. As the ω_1 sidebands are nonresonant in the arm cavity, this is essentially the PDH technique applied to the arm cavity common mode.

In order to isolate the error signal from changes due to the detuning of the signal mirror, we set the Michelson arm length mismatch so that the interferometer is completely reflective at this frequency. The electric field transmissivity of a simple Michelson (held on a dark fringe for the carrier) is proportional to $\sin(2\omega_1\Delta L/c)$ (see equation 4.35). For zero transmission to the signal mirror a Michelson arm length mismatch of $\Delta L = c/(4\nu_1)$ is required. Using 75 MHz modulation a Michelson arm length mismatch of $\approx \pm 1$ m ensures any error signals derived from demodulating at 75 MHz are well isolated against detuning of the signal cavity.

7.1.2 Michelson common (Power cavity) mode

This error signal is obtained using the same sidebands at ω_1 except from demodulation of the photocurrent at the reflected port. The carrier and both sidebands are resonant in the power cavity. For a simple cavity with both the carrier and sidebands resonant the complex reflectivity of the cavity is the same for all three fields thus phase modulation symmetry is maintained. It follows that demodulation of the reflected port photocurrent will give no error signal. In the coupled interferometer considered here the carrier experiences a lower finesse power cavity than the sidebands due to the loss of the arm cavities. In this situation the carrier will receive less phase shift than the sidebands on reflection from the power cavity. This differential phase shift is responsible for producing the error signal as demonstrated in chapter 4 (see equation 4.25). This is similar to the system developed by Regehr *et. al.* [47], except that in our system the transmission of the sidebands to the dark fringe is zero.

This error signal responds to both the arm cavity common mode and the Michelson differential mode degrees of freedom. The error signal used for the arm cavity common mode also responds to both these degrees of freedom. The arm cavity common mode dominates both error signals because of its higher finesse. The demodulated outputs at the reflected port and power cavity port are shown in figure 7.3 as a function of Φ_+ and ϕ_+ . The slope of the each error signal due to motion of the arm cavities is positive, whilst the error signal slope due to changes in ϕ_+ is positive at the reflected port and negative at

the power cavity port. This sign change facilitates the extraction of the power cavity error signal. This can be achieved either with a hierarchical locking structure or by electronic processing of the error signals from both ports. For simplicity we chose a hierarchical locking arrangement.

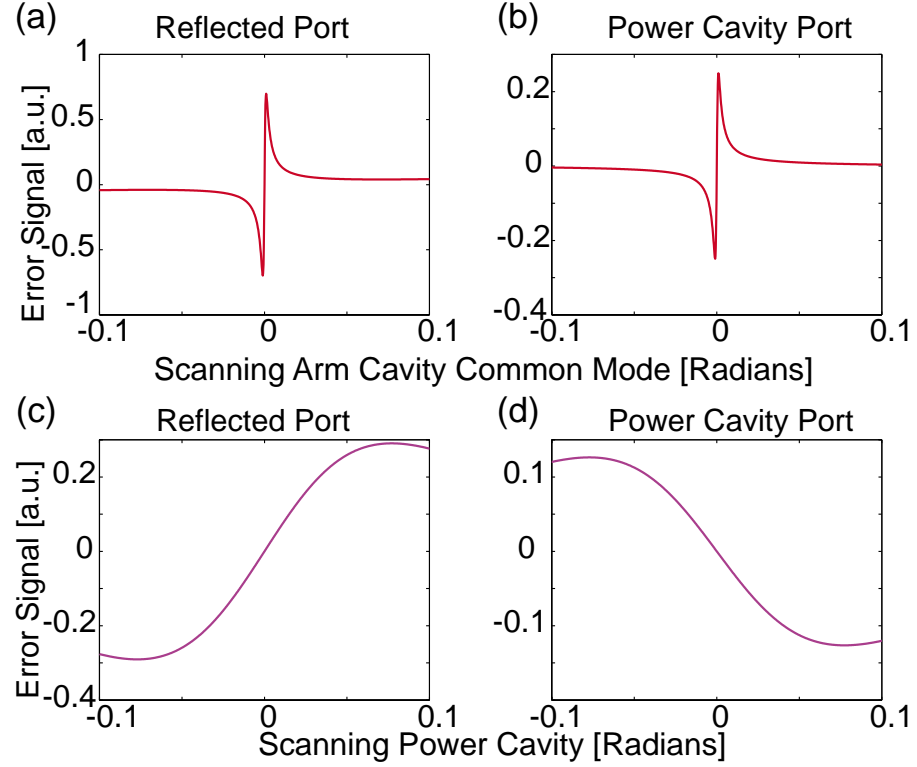


Figure 7.3: Error signals for the arm cavity common mode taken from (a) reflected port, (b) power cavity port and error signal for the power cavity from (c) reflected port and (d) power cavity port. [a.u.] = arbitrary units.

This error signal also has excellent isolation from the detuning of the signal cavity for the same reasons as the Φ_+ degree of freedom.

7.1.3 Michelson differential mode

The Michelson differential mode is the most difficult error signal to isolate from the effects of tuning the signal mirror. This is because in order to obtain an error signal for the Michelson we need some component of the field to be partially transmitted through the beamsplitter, hence we cannot use the isolation technique from the Φ_+ and ϕ_+ signals.

This error signal is obtained at the transmitted port using the double demodulation scheme, described in section 4.5.2. It uses the subcarrier to detect the presence of the ω_1 sidebands at the dark fringe by demodulating the photocurrent at the beat frequencies $\omega_{sc} \pm \omega_1$. When the Michelson is at a dark fringe the sidebands are completely reflected and there is no beat present in the transmitted port photocurrent. As the Michelson lock point changes, some of these sidebands are transmitted to the dark fringe. In addition, the phase of the ω_1 sidebands depends on the direction of the change in the lock point.

Although an error signal can be obtained by looking at just one of the beat frequencies (either $\omega_{sc} + \omega_1$ or $\omega_{sc} - \omega_1$), it is important to use the beat between the subcarrier and both sidebands, that is, the photocurrent at $\omega_{sc} \pm \omega_1$. If only one sideband is used this error signal will cross zero when the sideband transmission drops to zero, but this will only correspond to the desired lock point if ω_1 has been exactly matched to the arm length mismatch of the Michelson. When both beat frequencies are demodulated and the signals combined, any offsets (due to an error in the modulation frequency) will cancel and the desired lock point can be recovered.

We chose to use a double demodulation to produce this error signal (by first demodulating at ω_{sc} then at ω_1). This is mathematically equivalent to demodulating at $\omega_{sc} + \omega_1$ and at $\omega_{sc} - \omega_1$ and then combining the two signals. Experimentally it was more convenient as the demodulation frequencies were already present, and frequency adding and subtracting was not necessary.

This error signal is “well behaved” as the signal cavity is detuned, because the subcarrier is automatically held on resonance (and thus maximum transmission) by the signal cavity locking servo. In addition, we obtain excellent immunity to the Φ_+ and Φ_- degrees of freedom by using the beat between fields that are not resonant in the arm cavities.

7.1.4 Signal Cavity

An error signal for the signal cavity degree of freedom is produced by demodulating the reflected port at ω_2 (15 MHz). This measures the beat between the subcarrier and its own PM sidebands. As the Michelson is almost completely transmissive at the subcarrier frequency, the subcarrier effectively experiences a two mirror cavity made up of the power mirror and signal mirror. The ω_2 sidebands are non-resonant everywhere, and so are completely reflected by the power mirror. This error signal is equivalent to standard Pound-Drever-Hall locking of this combined power-signal cavity.

The signal cavity is detuned by changing the offset frequency of the subcarrier. Feedback to the signal mirror changes the combined power-signal cavity resonance to track the subcarrier and keep it on resonance. The subcarrier is transmitted to the dark fringe with maximum efficiency as the signal cavity is detuned. This is important as the subcarrier acts as a local oscillator for the extraction of the Φ_- degree of freedom (the gravitational wave signal). As we are using the beat between the subcarrier and its own 15 MHz sidebands, the optimum demodulation phase does not change as the signal cavity is detuned.

To determine the subcarrier offset frequency required for a particular detuning we constructed a look-up table using the program RSEcontrol.m. The values of the subcarrier offset frequency ω_{sc} , for a given signal cavity detuning are shown in table 7.2. We define the detuning angle to be 0° for (broadband) RSE and 90° for (narrowband) or dual recycled system. We have specified the subcarrier offset frequency to the nearest 10 kHz, however the precision required for this frequency will be determined by the required precision of the signal cavity detuning. If this frequency is set incorrectly, the signal cavity will simply be detuned to a different point, but the other control loops will experience no adverse effects.

The sub-carrier is close to anti-resonant in the arm cavities making this error signal immune to the arm cavity common and differential modes.

Detuning angle	$\omega_{sc}/(2\pi)$
5° (\approx RSE)	188.20 MHz
15°	186.45 MHz
30°	184.32 MHz
45°	182.50 MHz
60°	180.81 MHz
75°	179.12 MHz
88° (\approx DR)	177.04 MHz

Table 7.2: Look-up table for subcarrier offset frequency required for signal cavity detuning.

7.1.5 Arm Cavity Differential Mode

This control loop relies on the single sideband modulation/demodulation scheme introduced in section 4.5.2. By observing the beat between the carrier and sub-carrier on the transmission port, a strong error signal for the arm cavity differential mode is obtained. For locking a simple cavity, there is an increased sensitivity to errors in demodulation phase for single sideband locking compared to the usual double sideband (PDH) case. However, in section 4.5.2 we demonstrated that by using an impedance matched cavity the sensitivity to demodulation phase can be overcome. When single sideband locking is applied to locking the arm cavity differential mode in a Michelson interferometer, the fringe visibility of the Michelson interferometer also gives a degree of isolation against demodulation phase errors. For example, assuming a 100% Michelson fringe visibility, on resonance there is no carrier at the dark fringe and thus no beat note which ensures that a demodulation of any phase will not result in a DC offset. This issue will require a thorough quantitative analysis when considering this scheme for control and readout of a gravitational wave detector once realistic estimates for demodulation phase error and fringe visibility are available.

As single sideband demodulation also provides the extraction of the gravitational wave signal, the shot noise performance of the system must be considered. For the control system described above, only the single sideband is present on the TP photodetector. This ensures that there is no extraneous shot noise in the photocurrent due to other sidebands or the carrier field. Although the signal strength of single sideband modulation is reduced by a factor of 2 compared to the double sideband scheme (variation of PDH technique), the shot noise is reduced by a factor $\sqrt{3}$ [67] due to the lack of non-stationary shot noise in a single sideband system. The net result is a signal to noise ratio of $\sqrt{3}/2 \approx 87\%$ that of the double sideband case (i.e., a reduction of 13%).

As the single sideband is on resonance with the power-signal cavity, its transmission efficiency to the dark port is relatively unaffected by the signal mirror detuning. Thus the gain of the Φ_- degree of freedom will be minimally affected, apart from the desired change due to the frequency response of the RSE system to gravitational waves [36].

7.1.6 Control summary

We have designed a control system which is capable of locking the four degrees of freedom to a fixed point whilst the signal cavity is detuned to an arbitrary position. This system requires phase modulation sidebands on the carrier, and phase modulation sidebands on a frequency shifted subcarrier. Equations 7.1-7.5 summarise the origins of the five error signals.

$$\Phi_+ = \text{demodulate PCP @ } \omega_1 \quad (7.1)$$

$$\Phi_- = \text{demodulate TP @ } \omega_{sc} \quad (7.2)$$

$$\phi_+ = \text{demodulate RP @ } \omega_1 \quad (7.3)$$

$$\phi_- = \text{demodulate TP @ } \omega_{sc} \text{ \& } \omega_1 \quad (7.4)$$

$$\phi_s = \text{demodulate RP @ } \omega_2 \quad (7.5)$$

7.2 The experiment

In this experiment we first selected the modulation frequency of $\nu_1 = 75.9$ MHz as we had a resonant phase modulator available at this frequency. This defines a number of lengths of the interferometer (see table 7.1).

$$\begin{aligned} \Delta L &= \frac{c}{4\nu_1} = 0.9875 \text{ m} \\ L_p + L_m &= \frac{c}{2\nu_1} = 1.975 \text{ m} \end{aligned}$$

where $L_p + L_m$ is the effective length of the power cavity. These choices of lengths force the 75.9 MHz sidebands to be resonant in the power cavity when the carrier is resonant in the power cavity and the arm cavities. The phase flip of the carrier due to reflection from an overcoupled arm cavity is cancelled by the phase flip of the sidebands due to the Michelson reflectivity. Thus ν_1 must be an integer number of multiples of the FSR of the power cavity to be resonant in the power cavity.

The choice of lengths of the other parts of the interferometer is less critical and should be governed by the desired signal response and operating regime. For this experiment our choices were partly determined by mirror availability and modematching considerations. We chose the following interferometer parameters.

$$\begin{aligned} L_s &= L_p = 0.8 \text{ m} \\ L_{aci} &= L_{acp} = 0.175 \text{ m} \end{aligned}$$

The choice of $\nu_2 = 15$ MHz was made to utilise a second 15 MHz resonant phase modulator. These modulation sidebands must be nonresonant everywhere (i.e., they should be almost completely reflected at the power mirror).

7.2.1 Experimental layout

Figure 7.4 shows the full optical experimental setup used in this experiment. In total there were 9 photodetectors for locking or monitoring purposes.

In this experiment we used true common and differential mode feedback for the Michelson degrees of freedom, and there was no feedback to the power mirror position. The servos used contained a third order elliptic filter [88]. This filter was matched to the first mechanical resonance of the mirror-PZT, to ensure that maximum suppression is given at this frequency, whilst maintaining a small phase delay at frequencies down to an octave away. The circuit diagram is presented in appendix B.

7.2.2 Input field preparation

The lasers used in this experiment were diode pumped Nd:YAG NPRO lasers. For the carrier we used a 700 mW (Lightwave Electronics 126) and for the subcarrier a lower power 50 mW (Lightwave Electronics 120) was used.

Figure 7.5 shows a simplified diagram of the input beam preparation. The carrier was suitably isolated using a Faraday isolator and aligned into the 75.9 MHz resonant phase modulator (New Focus model 4003). Modulation depth was set to give approximately 10% of the carrier power in each sideband. Likewise the subcarrier was isolated and modulated at 15 MHz by a second resonant phase modulator (New Focus model 4003). The lasers were modematched to each other and combined on a 50:50 beamsplitter. The output of one of the beamsplitter ports was directed towards the main interferometer. The output of the second port was detected onto a high speed photodetector for the purpose of offset phase locking.

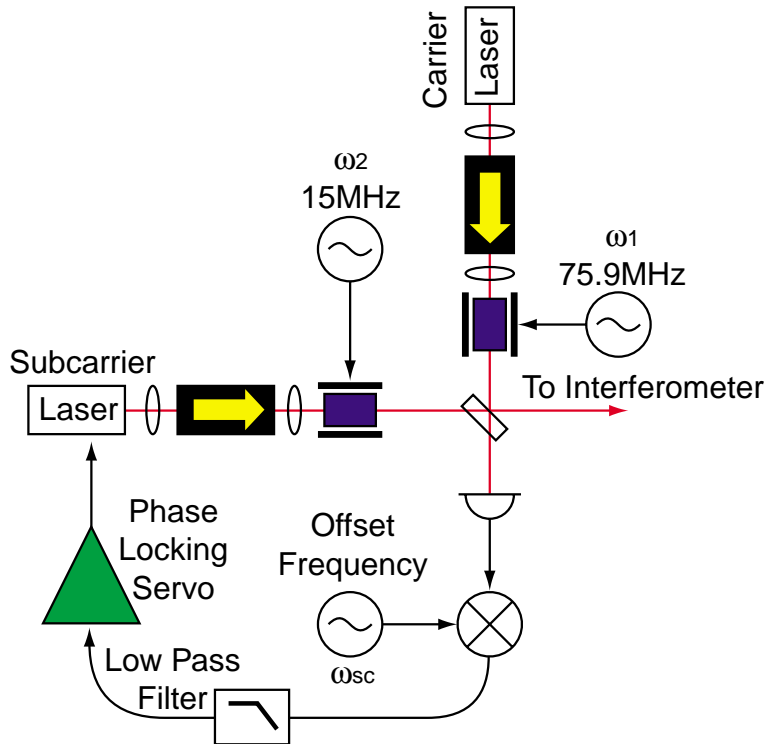


Figure 7.5: Diagram of input field generation by offset phase locking low power subcarrier to high power carrier after each laser is phase modulated.

7.2.3 Offset phase locking

In order to use the interference between the carrier and subcarrier for control and signal extraction we require a high degree of phase coherence between the two lasers. This can be achieved by a technique known as phase locking [89]. We will first consider the case of phase locking two lasers at the same frequency.

When two lasers of the same frequency (assumed to share the same spatial mode and polarisation) are combined on a 50:50 beamsplitter, interference will determine the

fraction of power at each output port of the beamsplitter. If the powers are equal on these two ports, then the lasers must be adding 90° out of phase. If the phase of one of the lasers changes then the power will increase at one port and decrease at the other. If the phase drifts in the other direction the power change will be reversed. By subtracting the outputs of photodetectors at these ports we can obtain a signal which is proportional to the phase difference between the two lasers. This signal can be used to feedback to a phase actuator on one of the lasers to maintain a consistent phase relationship, ϕ_0 , between them. For example, if the field of laser 1 can be represented by,

$$E_1 e^{i\omega t} \quad (7.6)$$

then when the lasers are phase locked the field of laser two will be given by,

$$E_2 e^{i(\omega t + \phi_0)} \quad (7.7)$$

where E_1 and E_2 are real.

Offset phase locking is very similar except that the phase relationship between the lasers has both a DC component, ϕ_0 , and a component which is changing linearly with time, $\omega_{sc}t$ say. We can see from equation 7.8 that this time varying phase offset, $\omega_{sc}t$ is equivalent to a frequency offset by an amount ω_{sc} .

$$E_2 e^{i(\omega t + \phi_0 + \omega_{sc}t)} = E_2 e^{i((\omega + \omega_{sc})t + \phi_0)} \quad (7.8)$$

A strong phase coherence between the two lasers operating at different frequencies is essential if the lasers are to be used as a readout system for the interferometer.

To obtain the error signal for offset phase locking we require a detector at only one of the output ports of the beamsplitter as shown in figure 7.5. In this experiment we require an offset frequency for the subcarrier, ω_{sc} of around 180 MHz. Offset phase locking is initiated by first tuning the subcarrier to approximately 180 MHz from the carrier. The photocurrent will exhibit a large beat note at the difference between the lasers frequency. To offset phase lock the two lasers, we must measure and control the phase (and in doing so, control the frequency) of this beat note. The photocurrent is then demodulated at the desired offset frequency, ω_{sc} , by the electronic local oscillator.

The field incident on the photodetector is given by,

$$E_{det} = it_{bs} E_1 e^{i\omega t} + r_{bs} E_2 e^{i((\omega + \omega_{sc})t + \Delta\phi)} \quad (7.9)$$

where $\Delta\phi$ is the error in the phases that we are trying to measure (we have assumed here that $\phi_0 = 0$). The photocurrent is proportional to the detected power,

$$P_{det} = E_{det}^* E_{det} \quad (7.10)$$

$$= t_{bs}^2 E_1^2 + r_{bs}^2 E_2^2 + t_{bs} r_{bs} E_1 E_2 \sin(\omega_{sc}t + \Delta\phi) \quad (7.11)$$

Equation 7.11 consists of three terms, the power of laser 1, the power of laser 2, and the interference between them. It is this high frequency interference term that we must use to extract the error signal. Demodulating the photocurrent at ω_{sc} gives a signal proportional

to,

$$\sin(\omega_{sc}t + \Delta\phi) \cos(\omega_{sc}t) = \frac{1}{2} \sin(\Delta\phi) + \frac{1}{2} \sin(2\omega_{sc}t + \Delta\phi) \quad (7.12)$$

The second term (an oscillation at $2\omega_{sc}$) can be removed by a low pass filter. For small errors in phase, $\sin(\Delta\phi) \approx \Delta\phi$ and thus we have a signal at the mixer output which is proportional to error in the phases. The lasers are offset phase locked by using this signal to feedback to the phase of the subcarrier.

In this experiment the subcarrier phase actuators were the laser crystal temperature at low frequencies (≤ 0.2 Hz) and to the PZT input of the laser at higher frequencies ($0.2 \text{ Hz} \leq f \leq 80 \text{ kHz}$). The phase locking servo was identical to a frequency locking servo except with the removal of a pole at high frequencies. To acquire phase lock the lasers must have approximately the correct frequency, so that the demodulated beat note lies well within the bandwidth of the phase locking servo. Once lock was acquired the servo held the offset frequency constant. We chose to feedback to the subcarrier due to the larger mode-hop-free tuning range of the lower power Lightwave 120 laser. Once the gains and crossover frequencies were optimised and lock acquired, phase locking lasted indefinitely (greater than 24 hours).

Figure 7.6 shows a measurement of the input field spectrum with the lasers phase locked with an offset frequency of 188.2 MHz and both modulations present. Several confocal cavities were purpose built for this experiment. These cavities were constructed with invar spacers 100 mm long with a finesse of 200 giving a resolution (FWHM) of 7.5 MHz. For more details on the optical spectrum analysers' construction, see appendix A. The 15 MHz sidebands on the subcarrier cannot be easily distinguished in figure 7.6 due to the combination of low cavity resolution and low sideband power (only 10% the height of the subcarrier). Resolving the 15 MHz sidebands was not important for the purposes of lock characterisation.

It was important to acquire phase lock before the modulations were turned on as it was possible to phase lock to the wrong beat note. The radio frequency spectrum of the photocurrent of the phase locking detector is shown in figure 7.7. The highest peak (at 188.2 MHz) was the beat between the carrier and the subcarrier. Notice that there were also signals at 188.2 ± 15 MHz on either side. These were the beat notes due to the carrier and 15 Mhz sidebands on the subcarrier. Likewise the signals at 188.2 ± 30 MHz were due to the interference of the carrier and second order modulation sidebands on the subcarrier. The same applied for the interference between other frequencies present on either laser. For example, the signal at approximately 360 MHz was actually due to the interference between the upper and lower 15 MHz sideband on the subcarrier beating with the lower and upper second harmonic of the 75 MHz sidebands on the carrier. Note that there was no beat at either 15 MHz or 75 MHz as phase modulation symmetry was maintained by these frequency sidebands.

7.2.4 Phase locking excess noise

Figure 7.8 shows a close up of the carrier-subcarrier beatnote at 188.2 MHz. Notice that the noise floor had quite a lot of structure, most probably due to mechanical resonances within the laser crystals. In addition, the noise inside the locking bandwidth (approximately 80 kHz on either side of the main peak) was higher than the background noise level, suggesting that we have insufficient gain in our feedback loop. Ideally, with infinite

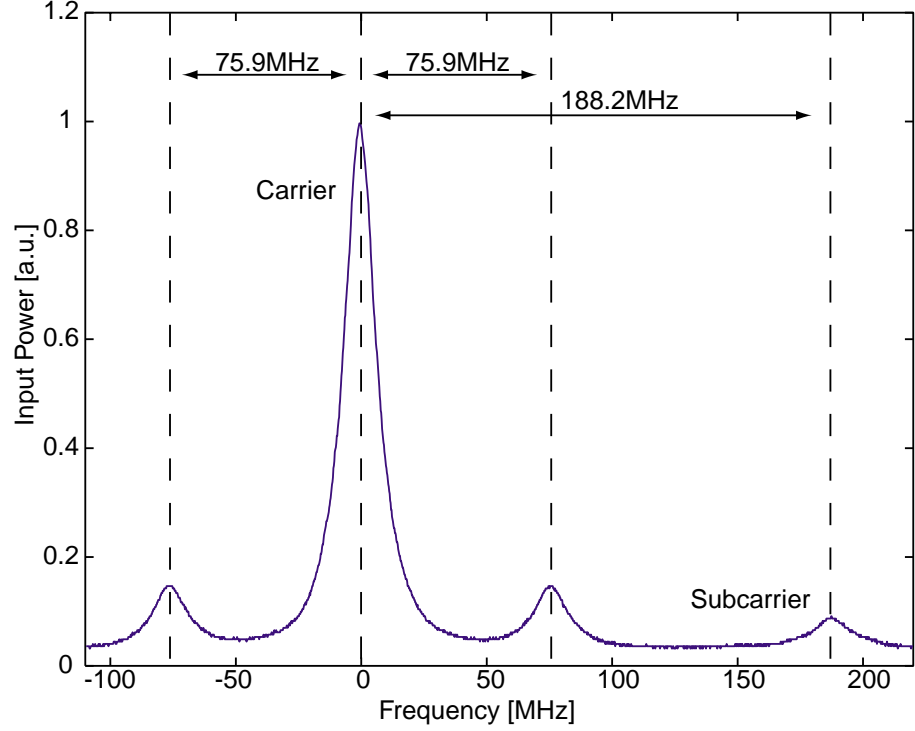


Figure 7.6: Optical spectrum of the input field measured with a 100 mm long scanning confocal resonator ($\mathcal{F} = 200$).

servo gain we could suppress the frequency noise of the in-loop photocurrent down to zero, and the in-loop photocurrent spectrum would be that of a perfect sinusoid³ giving a single narrow spike at 188.2 MHz.

This excess noise on the phase locking photodetector was potentially a large problem due to the nature of the single sideband interferometric readout system used here. As mentioned earlier the gravitational wave signal is read out by measuring the phase of the beat note between these two lasers. If the relative phase of the two lasers is not constant to begin with, then the gravitational wave signal will be corrupted. For example, assume that after phase locking, a small amount of residual phase noise, $\Delta\phi_r$, is present on the beatnote from equation 7.11. The AC component of the photocurrent can be represented by,

$$\sin(\omega_{sc}t + \Delta\phi_r) \quad (7.13)$$

After passing through the interferometer to the dark fringe the carrier will acquire an extra phase shift of ϕ_s due to a signal in the arm cavity differential mode (for example, a gravitational wave frequency). The AC component of the photocurrent measured by a photodetector at the dark fringe will be given by,

$$\sin(\omega_{sc}t + \Delta\phi_r + \phi_s) \quad (7.14)$$

³this is assuming that the local oscillator is a perfect sinusoid. The photocurrent spectrum should actually converge to that of the electronic local oscillator spectrum.

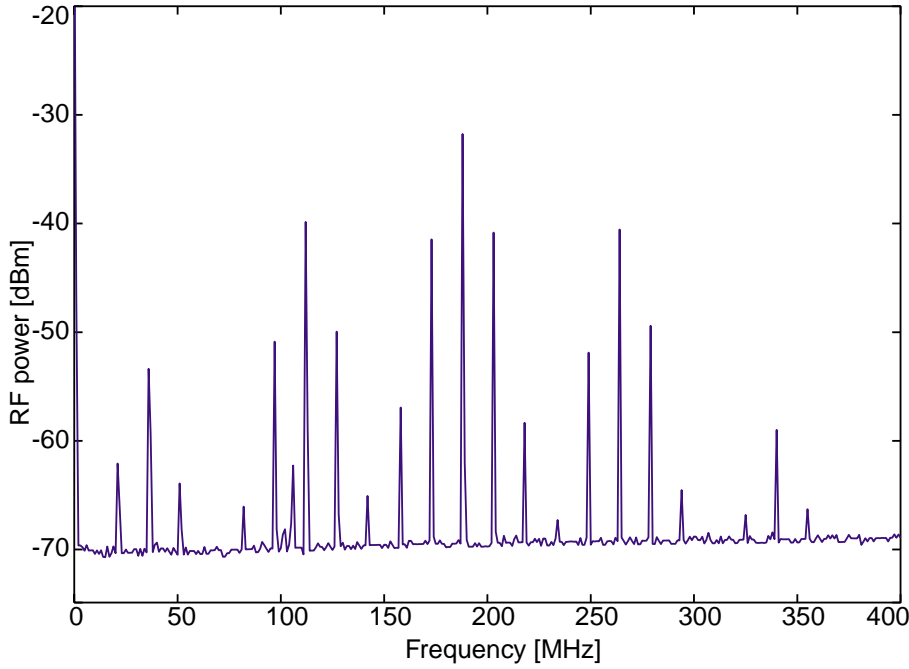


Figure 7.7: Radio frequency spectrum of the phase locking detector photocurrent with both modulation frequencies on and the subcarrier offset phase locked at 188.2 MHz.

This photocurrent is demodulated by multiplying by the electronic local oscillator,

$$\sin(\omega_{sc}t + \Delta\phi_r + \phi_s) \cos(\omega_{sc}) = \frac{1}{2} \sin(\Delta\phi_r + \phi_s) \quad (7.15)$$

where we have neglected the term at $2\omega_{sc}$. Equation 7.15 shows that the residual phase locking error directly couples into the signal readout, becoming indistinguishable from a gravitational wave signal.

One innovative solution, suggested by Guido Mueller [90], is to replace the electronic local oscillator for the final signal demodulation by the photocurrent of the phase locking detector, as illustrated in figure 7.9. The final demodulation is now represented by,

$$\sin(\omega_{sc}t + \Delta\phi_r + \phi_s) \cos(\omega_{sc} + \Delta\phi_r) = \frac{1}{2} \sin(\phi_s) \quad (7.16)$$

where we have again neglected the second harmonic term. Notice now that the output is completely free from any spurious signal related to the residual phase noise in the phase locking loop. The cancellation of noise on the phase locking was shown to be crucial in order to lock even a simple arm cavity stably.

Figure 7.10 shows a comparison of the error signals obtained using each of these techniques. The error signals were measured using one arm cavity only, in order to simplify the experimental demonstration of the noise cancellation principle. The diagram on the left shows the mixer outputs as the arm cavity was scanned through resonance. The upper trace was obtained using the signal generator as the electronic local oscillator. Two zero crossing points were present; one appeared when the carrier passed through resonance and another as the subcarrier passed through resonance. Notice the large amounts

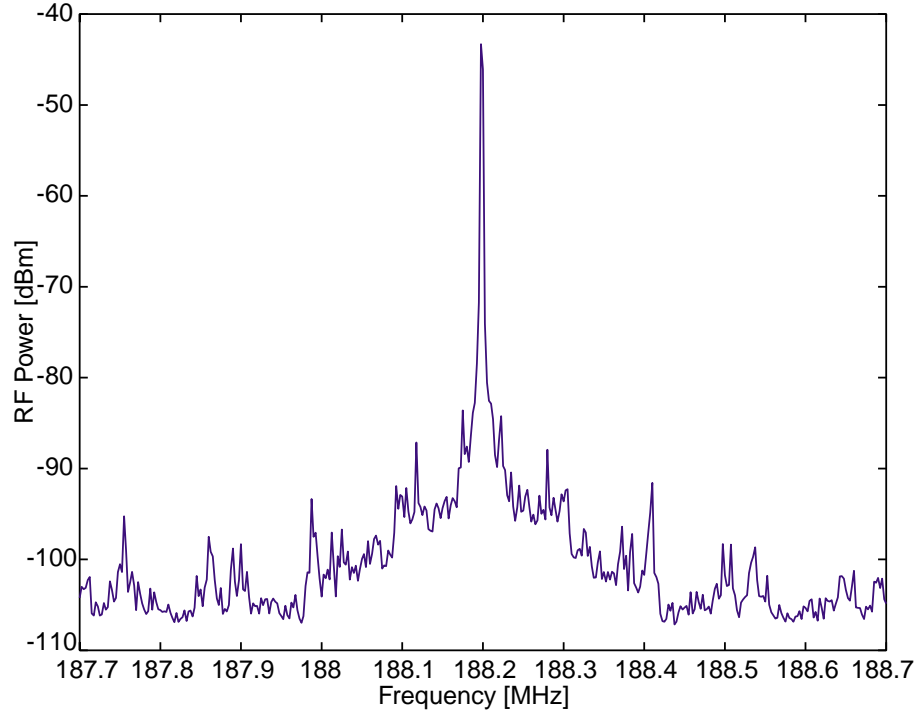


Figure 7.8: Radio frequency spectrum of the phase locking detector photocurrent near the subcarrier-carrier beatnote frequency.

of background noise and the inconsistency in the absolute height of the error signal between FSRs. The lower trace shows the same measurement when the photocurrent of the phase locking detector was used (suitably amplified and filtered) for the demodulation.

A more quantitative estimate of the improvement in locking performance can be obtained by locking the cavity and recording the fast Fourier transform (FFT) of the error signal. Figure 7.10(b) shows the FFT from 0 to 100 kHz measured with a dynamic signal analyser (Hewlett-Packard model 3561A). The upper trace shows the error signal spectrum obtained using the signal generator as a local oscillator while the bottom trace was obtained using the measured beat as the local oscillator. Note that the beat note technique produces consistently lower noise by about 30-35 dB across the entire measurement range an improvement of approximately a factor of 40. These results convinced us that it was essential to use this technique in our control system.

An alternative approach, suggested by Alain Brillet [91] to improve the phase locking performance is to injection lock the subcarrier laser with an acousto-optically frequency shifted tap off of the carrier laser. This would ensure that the frequency noise of the two lasers was highly correlated over a very large bandwidth, and would substantially reduce the gain requirements of the phase locking servo.

7.3 Gain optimisation

It was found to be essential to preset the servo gains to approximately the correct levels for the interferometer to acquire lock, especially in the case of the arm cavity signals Φ_+ and Φ_- . Initially a trial and error approach was attempted; however, after many days of

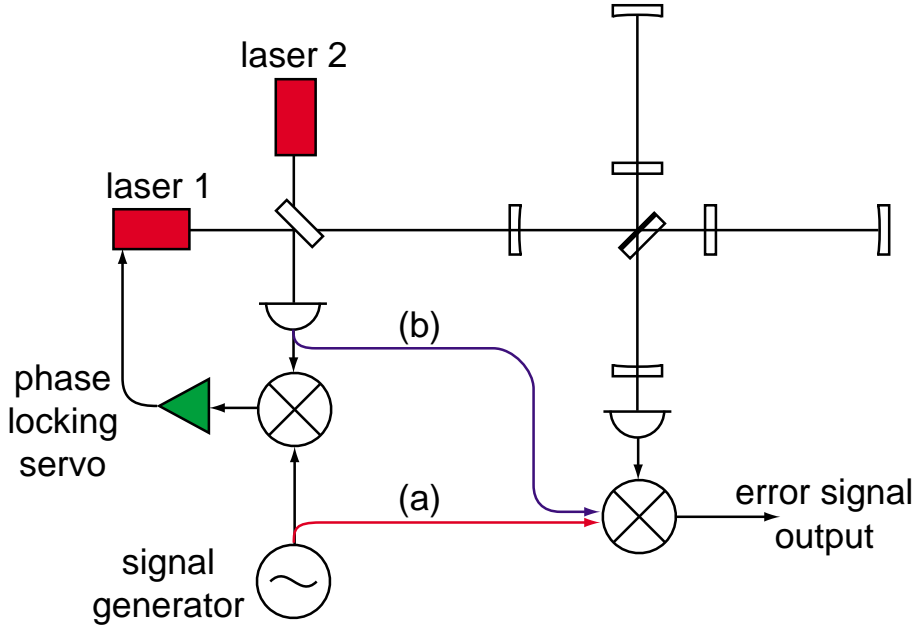


Figure 7.9: Alternative experimental techniques for producing the electronic local oscillator for the Φ_- and ϕ_- degrees of freedom. Either use (a) the signal generator used to phase lock the two lasers or (b) the beat note measured on the phase locking photodetector.

frustration a procedure was devised to determine and implement the approximate gain required. Firstly, a simple subconfiguration was locked and the gain optimised. For example, the in-line arm cavity was locked using the Φ_+ error signal with the power mirror and signal mirror severely misaligned and a beam dump in front of the other arm cavity. A network analyser was used to measure the servo gain (from the mixer output to the high voltage amplifier input) at a frequency of 100 Hz. We then used the matlab program RSEcontrol.m (see appendix C) to calculate the slope of the error signal for this subconfiguration and compare this to the calculated slope for the full RSE system. Finally, while monitoring with the network analyser, the servo gain was increased or decreased as required to compensate for the change in slope of the error signal. The advantage of this method is that it gives a quantitative prediction of the gain without requiring any knowledge of parameters such as laser power, detector efficiency/gain, PZT responsivity etc. The technique still relies on reasonably accurate knowledge of the interferometer itself but even this requirement can be alleviated somewhat by making the subconfigurations gradually more complicated until the full interferometer is constructed. For example, the calculation could be performed to determine the change in slope when going from simple arm cavity locking as described above, to predict the gain for a combined power mirror single arm cavity system. Once the gain is experimentally optimised for this set up, a second arm cavity could be added and the procedure repeated until the arm cavity gain for the full RSE system is obtained.

The final intermediate subconfiguration to be locked was a dual recycled Michelson (no arm cavities). This configuration was useful for final optimisation of a number of the servo gains, in particular the Michelson differential mode phase, ϕ_- , the signal cavity phase, ϕ_s , and to a lesser extent the Michelson common mode phase, ϕ_+ . The dual recy-

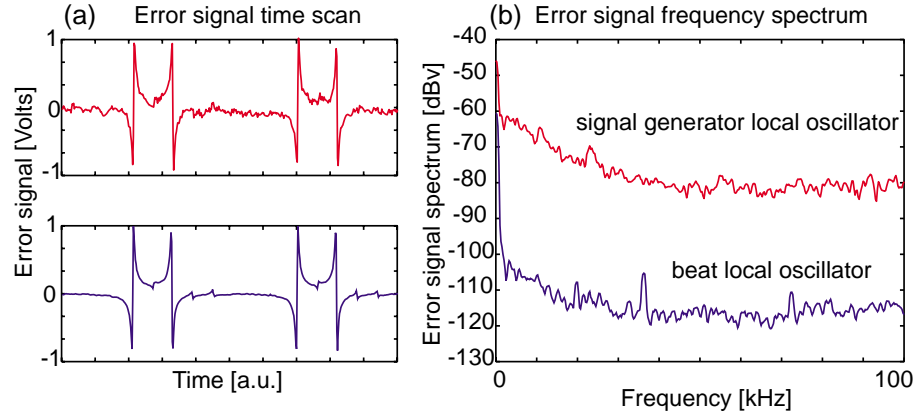


Figure 7.10: Comparison of error signals obtained with different local oscillators. (a) shows the mixer output as one arm cavity is scanned (upper trace: signal generator LO, lower trace: beat note LO). (b) shows an FFT of the mixer output when one arm cavity is locked.

cled Michelson was locked so that the 75.9 MHz sidebands were resonant in the power cavity. The absence of the overcoupled arm cavities meant that the carrier was in fact antiresonant in the power cavity and was almost completely reflected at the power mirror. Figure 7.11 shows the optical spectra associated with this subconfiguration.

The top trace shows the input field with a subcarrier offset at 188.2 MHz. The middle trace shows the field at the power cavity port, which was a direct measure of the field circulating inside the power cavity. Notice that the 75.9 MHz sidebands were the dominant field with the carrier strongly suppressed. The carrier was still present despite it being exactly antiresonant because of the low finesse of the power cavity (power mirror reflectivity 68.2%, Michelson reflectivity $\approx 100\%$). The subcarrier experienced an even lower finesse cavity (power mirror reflectivity 68.2%, signal mirror reflectivity 68.8%) and so its power enhancement was slightly less.

As neither the ϕ_- nor ϕ_s error signals were derived from interference with the carrier, and the carrier was the only field resonant in the arm cavities, these error signals were basically identical to those for the full RSE system. In addition, these error signals were identical for all values of signal mirror detuning. Building a dual recycled Michelson with no arm cavities was an excellent way to test, debug and optimise these control loops.

The error signal for ϕ_+ was also only slightly altered by the presence of the arm cavities. To understand why, we must examine more closely just how the ϕ_+ error signal arises in both cases. For the case of dual recycling (with no arm cavities) we had a system akin to anti-Pound-Drever-Hall locking, where both 75.9 MHz sidebands are resonant and the carrier exactly anti-resonant in the power cavity. In this case, the error signal arose because the sidebands acquired a phase shift as the power cavity resonance changed. This altered the symmetry of the modulation, introducing some component of amplitude modulation (at 75.9 MHz) which was demodulated to produce the error signal. When the arm cavities were added, the sidebands acquired the same phase shift as before but now the carrier also received a phase shift as it too was resonant in the power cavity. The carrier, however, experienced a lower finesse power cavity (due to the loss on reflection from the arm cavities) and thus received a smaller phase shift. The error signal was proportional to the difference between the phase shift of the sidebands and the car-

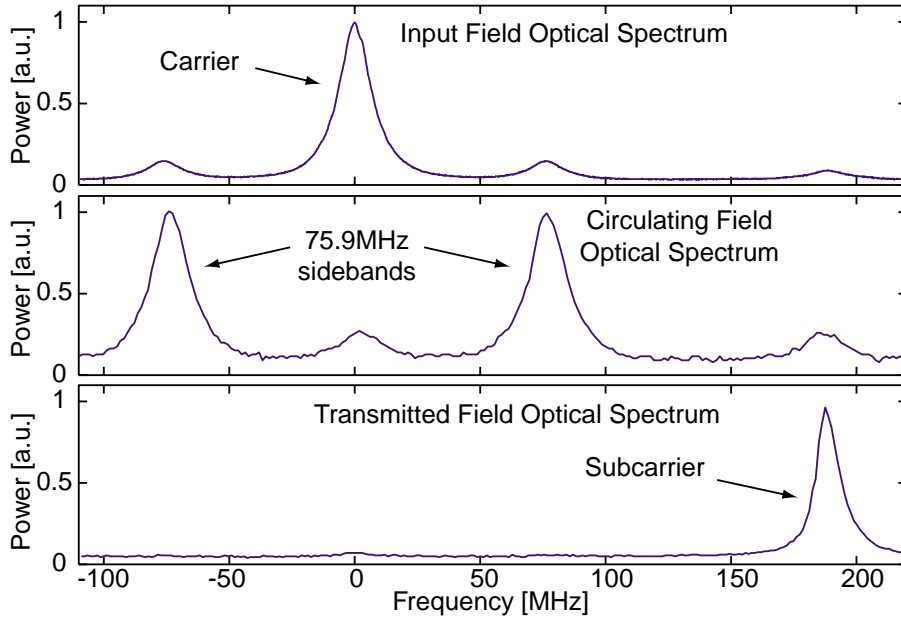


Figure 7.11: Optical spectra for a dual recycled Michelson (no arm cavities) showing the field at the input (upper trace), at the power cavity port (middle trace) and at the transmitted port (lower trace)

rier. The carrier now had some amount of phase shift in common with the sidebands and thus the error signal was slightly reduced. For our system, the loss of the arm cavities was very high (mostly due to transmission), and we required an increase in the servo gain of only 4 dB to compensate for the reduced slope of the error signal when the arm cavities were added. The polarity of the error signal did not change as the phase shift of the sidebands is dominant in both cases.

7.4 Optimising demodulation phases

As discussed previously, careful adjustment of the demodulation phase was necessary to ensure optimum locking performance. In our experiment the demodulation phases were continuously adjustable with phase shifters (Synergy Microwave Corporation) acting on the electronic local oscillator. These phase shifters were capable of producing phase shifts from 0° to 90° at both 75.9 MHz and subcarrier frequencies. Below we describe the procedures used to optimise each of the demodulation phases.

7.4.1 Arm cavity common mode demodulation phase

The demodulation phase required for the full RSE system was the same as for either one of the arm cavities alone. We optimised this demodulation phase by blocking one arm of the Michelson, misaligning the power and signal mirrors and scanning the arm cavity. A typical PDH error signal was observed at the PCP and could be optimised by adjusting the phase shifters to maximise the size of the central peak. As this error signal used a double sideband (PDH) scheme the demodulation phase only affected the gain and did not produce an offset.

7.4.2 Michelson common mode demodulation phase

As the arm cavity common mode signal appeared in the same quadrature and on the same output as the Michelson common mode output, optimising the phase for the arm cavity common mode signal automatically optimised the phase for the Michelson common mode signal. We set this demodulation phase at the RP using the procedure described in section 7.4.1.

7.4.3 Signal cavity demodulation phase

The demodulation phase was optimised by scanning the signal mirror with one arm of the Michelson blocked, with the power and signal mirrors properly aligned. Again, this system used a double sideband scheme and thus demodulation phase was not as important as it was for Φ_- .

7.4.4 Michelson differential mode phase

The Michelson differential mode phase was optimised, with the power and signal mirrors misaligned and the arm cavities blocked, by scanning the Michelson differential mode phase. As this error signal was obtained by a double demodulation it was necessary to adjust both phases to obtain the correct error signal. This was a relatively simple task as each phase could be individually adjusted to maximise the final error signal output. This provided the correct demodulation phases without any need for iterative adjustment.

7.4.5 Arm cavity differential mode phase

This was the most important demodulation phase. It was also potentially difficult to optimise, as the final error signal could only be observed by scanning both arm cavities “symmetrically” out of phase with the Michelson locked. If only one cavity was scanned then the absolute propagation length of the laser changed, which changed the correct demodulation phase for that cavity.

The method we chose was to block both arm cavities and misalign the signal mirror, thus forming a simple Michelson with the two input couplers of the arm cavities. By scanning the Michelson, an error signal appears at the Φ_- output. The height of this error signal was maximised by adjusting the demodulation phase. This was found to provide the correct demodulation phase for Φ_- in the full RSE system.

7.4.6 Demodulation phase as a function of detuning

In principle the demodulation phases do not change as the subcarrier and signal cavity are detuned. In practice this will only be true if the absolute delay of the electronic local oscillator and the optical modulation from a common point (the signal generator, say) are closely matched. Commonly, these delays are only matched down to an integer number of periods of the modulation source. Thus when the subcarrier offset frequency changes, time delays which were an integral number of the original period will no longer be integral number of the new period, and thus the demodulation phase changes. As a consequence, the demodulation phase was readjusted for each detuning point. This only applied to those error signals that utilised a beat between the subcarrier and either

the carrier or its sidebands, namely, the arm cavity differential mode and the Michelson differential mode.

This can, of course, be overcome by carefully matching the absolute delay of the optical modulation and electronic local oscillator, allowing continuous tuning without demodulation phase adjustment. This was deemed unnecessary for this benchtop demonstration and the demodulation phase was optimised as described above for each detuning point.

7.5 Lock acquisition

Once the gains and polarities were correctly set, lock acquisition was a relatively simple process. The DC power levels were monitored at the reflected port, the power cavity port and the transmitted port. In addition, the power transmitted through each arm cavity was also recorded. Figure 7.12 shows these DC power levels during a typical lock acquisition. All of the results presented in this section were recorded for a subcarrier offset frequency $\omega_{sc}=182.2$ MHz. This corresponds to a detuning of the signal cavity of approximately 5° from broadband RSE.

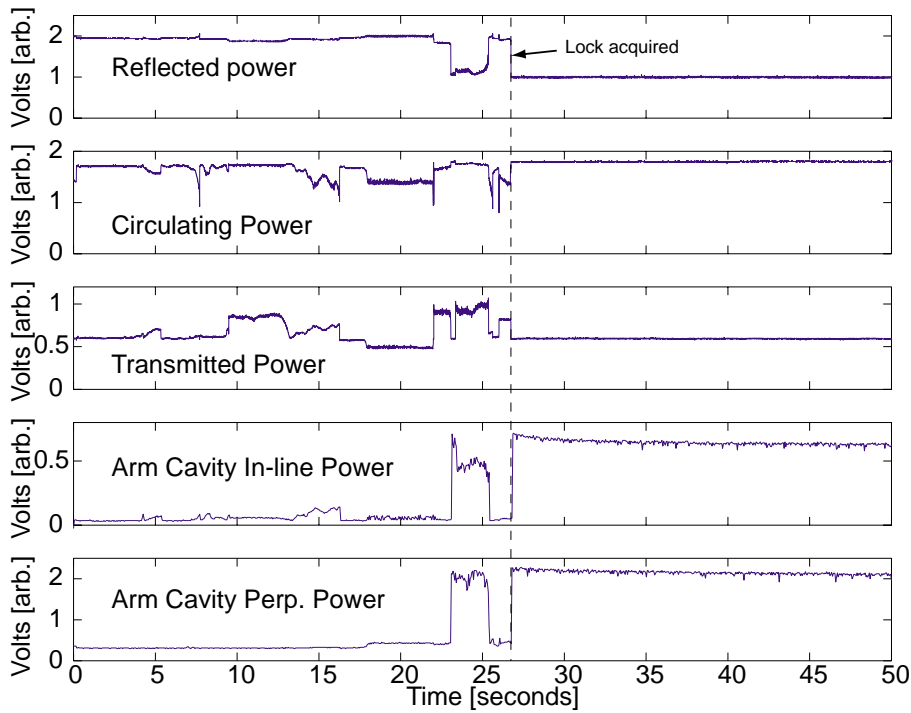


Figure 7.12: Power levels during lock acquisition for the power recycled Michelson with RSE. DC levels shown (from top to bottom): reflected port, power cavity port, transmitted port, AC in-line transmitted and AC perpendicular transmitted power.

With the arm cavities off resonance the interferometer acquired lock almost instantly for the other three degrees of freedom (ϕ_+ , ϕ_- and ϕ_s). The integrators on these servos were turned on just before the one second mark. For the next 22 seconds one or other of the arm cavities was drifting towards resonance. When only one arm cavity drifts near resonance, the mismatch of the losses on reflection from the arm cavity means that the

Michelson locking loop can no longer maintain a good quality dark fringe. Consequently, all of the error signals become more strongly coupled. At around the 23 second mark both arm cavities jump into lock; however, the locking is unstable as the signal mirror PZT had reached the end of its range and was no longer tracking the subcarrier correctly. This slightly corrupted the Φ_- error signal as evidenced by the variation in the arm cavities transmitted power. Shortly after the 25 second mark, the signal mirror servo integrator was turned off and then on again allowing the servo to recapture lock one fringe away at around the 26 second mark. The interferometer was now operating at the desired lock point and remained so for the rest of the trace. Both arm cavities seemed to exhibit a near exponential decay of the transmitted power from the time of lock acquisition to a near constant level at the end of the trace. This was due to heating effects in the neutral density filters used in front of the monitor photodetectors and is not related to the interferometer locking performance.

The power levels shown in figure 7.12 are slightly ambiguous for determining if the interferometer is operating at the correct lock position. The DC power levels give no information about the source of this power, and this source is important for lock to be unequivocally established. For example, the power at the transmitted port was slightly higher once lock was achieved than it was at the 20 second mark. From figure 7.12 we had no simple way of telling if this power increase was due to the subcarrier coming on resonance as expected, or if it was actually the carrier field, present due to some imperfection in the Michelson or arm cavity differential mode locking. A measurement of the optical spectrum of the field at the transmitted port and the power cavity port provided us with the information to unambiguously determine if the interferometer was at the desired operating point.

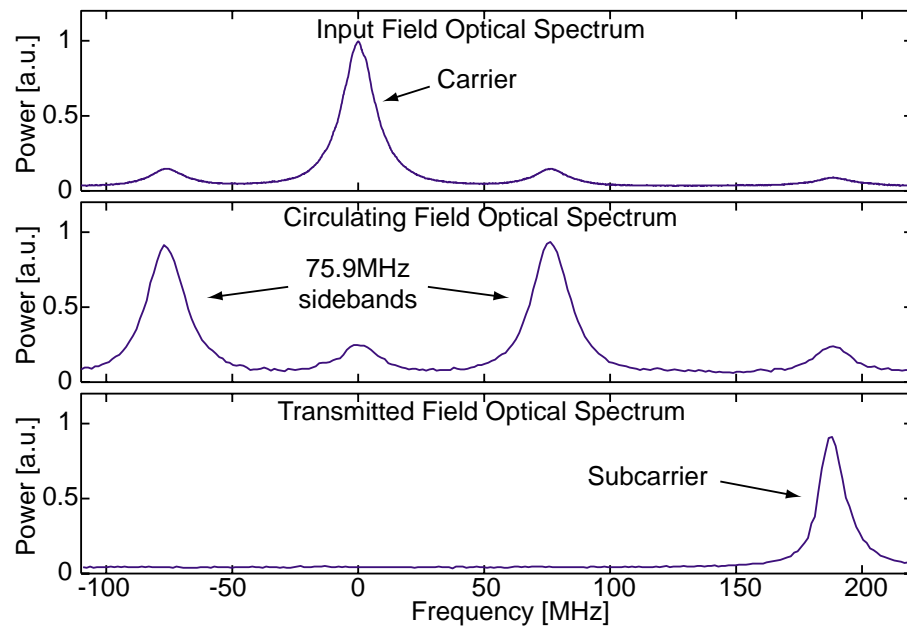


Figure 7.13: Optical spectra for a power recycled Michelson with RSE showing the field at the input (upper trace), at the power cavity port (middle trace) and at the transmitted port (lower trace).

Figure 7.13 shows the optical spectra for the fields at the input (top trace), power cavity port (middle trace), and transmitted port (bottom trace). The carrier, subcarrier and 75.9 MHz sidebands were all resonant in the power cavity and so all three fields were present at the power cavity port. The power of each of these fields was enhanced by a different amount, as each experienced a different version of the power cavity. We expected the 75.9 MHz sidebands to have the highest power build up as they experienced a power cavity made up of the power mirror (68% reflectivity) and the Michelson ($\approx 100\%$ reflectivity) giving a power enhancement of just over a factor of 10 compared to the incident field. The subcarrier experienced a cavity formed by the power mirror and the signal mirror (69% reflectivity) forming a nearly impedance matched cavity with a predicted power enhancement of approximately 3. The carrier experienced a very under-coupled cavity made up of the power mirror and the arm cavities (average reflectivity of 26.5%) giving only a 0.96 power enhancement factor (i.e. a slight attenuation). This was a consequence of our choice of mirror reflectivities⁴ only and it is not a restriction of the control system. Ideally the power mirror would be chosen to impedance match the interferometer for the carrier.

The optical spectrum of the field at the transmitted port was also important for determining if the interferometer was correctly locked. The power-signal cavity was almost impedance matched for the subcarrier, ensuring high transmission to the transmitted port. Both the carrier and 75.9 MHz sidebands should be absent from this port if the Michelson is properly held at a dark fringe. The measured spectra in figure 7.13 are in good agreement with these predictions, indicating that the interferometer was locked to the correct operating point.

7.6 Locking performance

The interferometer lock was found to be very robust, with the servos maintaining the interferometer at the correct operating point for periods of several hours. Figure 7.14 shows the DC power levels for a measurement period of 500 seconds (the maximum measurement time of our Yokogawa 4 channel oscilloscope). When the system did drop lock it was usually because one of the PZTs had reached the end of its range, and lock was often reacquired automatically. Once again, these results were taken with a subcarrier offset frequency of $\omega_{sc}=188.2$ MHz corresponding to a signal cavity detuning of approximately 5° from broadband RSE.

7.7 Frequency response measurement

As one of the prime motivations for constructing the RSE Michelson was the ability to alter the signal response, we went to considerable effort to devise a method to accurately measure the broadband signal response of our instrument. The peak response of our system when operating at the RSE point was expected to be greater than 5 MHz. This was well outside the linear frequency range of our PZTs (typically only about 20 kHz). Using methods based on averaging and normalising the broadband response of the PZTs can still provide a signal response at these frequencies, however the signal to noise ratio is

⁴The arm cavity mirrors were changed midway through the experiment to give higher transmission however this degraded the impedance matching of the carrier. The power cavity mirror was not altered.

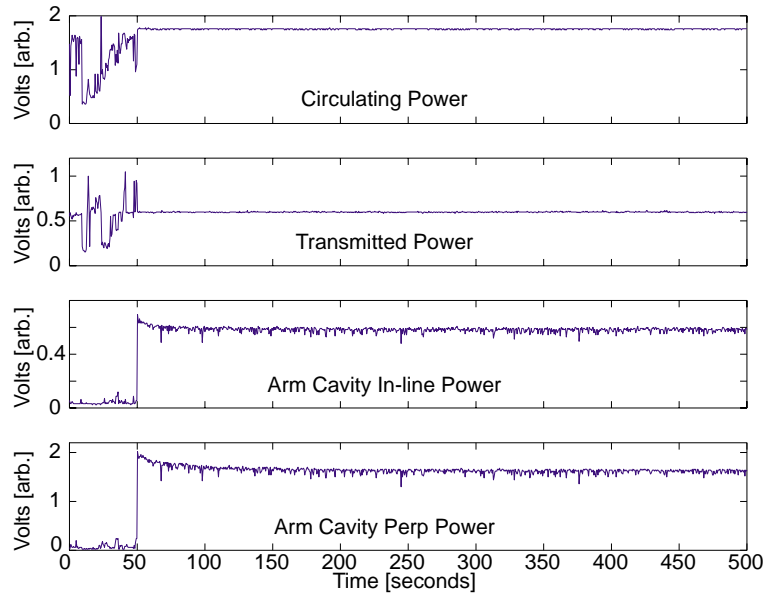


Figure 7.14: Measurement of interferometer power levels over a period of 500 seconds at the a) Power cavity port, b) transmitted port, c) arm cavity in line transmitted port and d) arm cavity perpendicular transmitted port.

typically quite low. Another method is to use broadband phase modulation at the input of the interferometer, and then calculate the transfer function between this and a signal injected into the arm cavities. This is a rather convoluted way to test the signal response of the interferometer. Injecting a signal with broadband modulators inside the arm cavities was avoided for reasons of loss and thermal distortions mentioned in chapter 6.

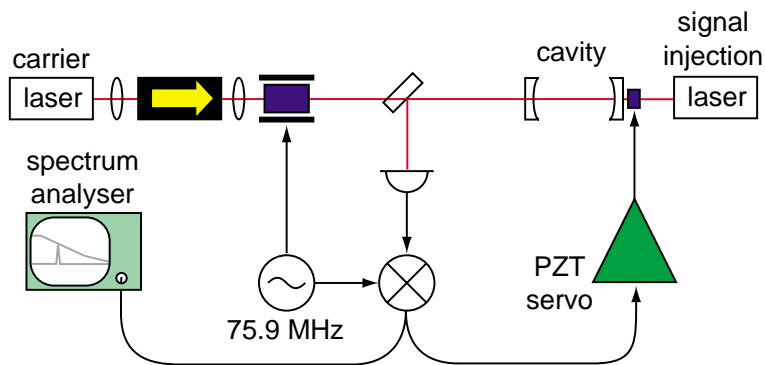


Figure 7.15: Experimental layout used to measure the broadband frequency response of an arm cavity

The method we used to map out the signal response was to inject a third Nd:YAG laser (Lightwave Electronics 122) through the far mirror of one of the arm cavities. The advantage of this technique is that its bandwidth is limited only by the photodetection/demodulation electronics and so can very easily cover the signal frequencies of interest (0-20 MHz). The technique also allows the positive and negative signal frequency

responses to be independently measured. This was an advantage when measuring the response of the detuned interferometer. This is not possible using techniques based on phase modulation (produced either piezo-electrically or electro-optically) without altering the demodulation frequency.

We first demonstrate how this technique can be applied to a simple cavity using standard Pound-Drever-Hall locking. Figure 7.15 shows the experimental layout used to measure the signal response of one of the arm cavities. The cavity was locked and the error signal observed on a spectrum analyser. In this case the error signal was the 75.9 MHz demodulated output at the reflected port. The signal injection laser was tuned to have nearly the same frequency as the carrier laser. We ensured that the difference frequency was greater than the servo bandwidth so that the lock was not disrupted in any way. A peak was observed, arising from the interference between the signal injection laser and the 75.9 MHz sidebands. It is important to note that this was not the beat between the signal injection laser and the carrier as we are observing the demodulated output.

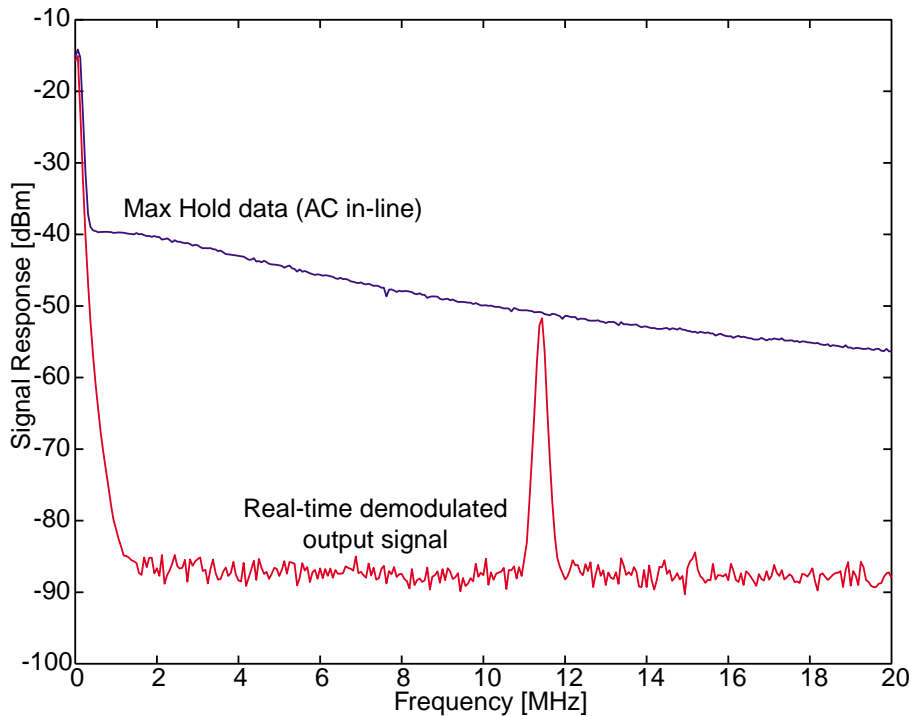


Figure 7.16: Spectrum analyser traces illustrating how the frequency response of the system is measured by the use of a signal injection laser. Lower trace: real time signal (beatnote) after demodulation. Upper trace: broadband frequency response obtained using MAX HOLD function on RF spectrum analyser as the frequency of the signal injection laser is manually changed.

As the signal injection laser frequency was manually tuned the frequency of the beat note changed accordingly. By using the MAX HOLD feature on the spectrum analyser the signal response of the cavity was mapped out. The spectrum analyser measures only the RF power of the error signal as a function of frequency and so unfortunately this technique does not retain any of the phase information of the signal transfer function. Phase information could be obtained if the signal injection laser was phase locked to the carrier with an offset determined by the source of a network analyser. This was not performed

firstly as the amplitude response was adequate to demonstrate successful detuning and secondly due to the considerable complexity of such a system.

The situation was slightly different when measuring the response of the RSE system (refer to figure 7.4 for the detailed experimental set up). As we were injecting a sideband in only one of the arm cavities this effectively added both a common and differential mode signal in equal amounts. The common mode signal, however, never reached the detector at the transmitted port and so the signal response was identical to that produced if we were injecting a truly differential mode signal⁵. The other difference when measuring the signal response of the entire interferometer is that we observed the frequency spectrum of the error signal by measuring the Φ_- degree of freedom error signal, namely the transmitted port photocurrent demodulated at ω_{sc} .

Figure 7.17 shows the measured frequency responses of the power recycled RSE Michelson interferometer for various detunings of the signal cavity. Both positive and negative signal frequencies are presented, clearly showing the asymmetry of the signal response for detuned cases. Of course when the signals reached the spectrum analyser the positive and negative frequencies were indistinguishable. The positive and negative frequency responses of figure 7.17 were recorded separately and combined during plotting.

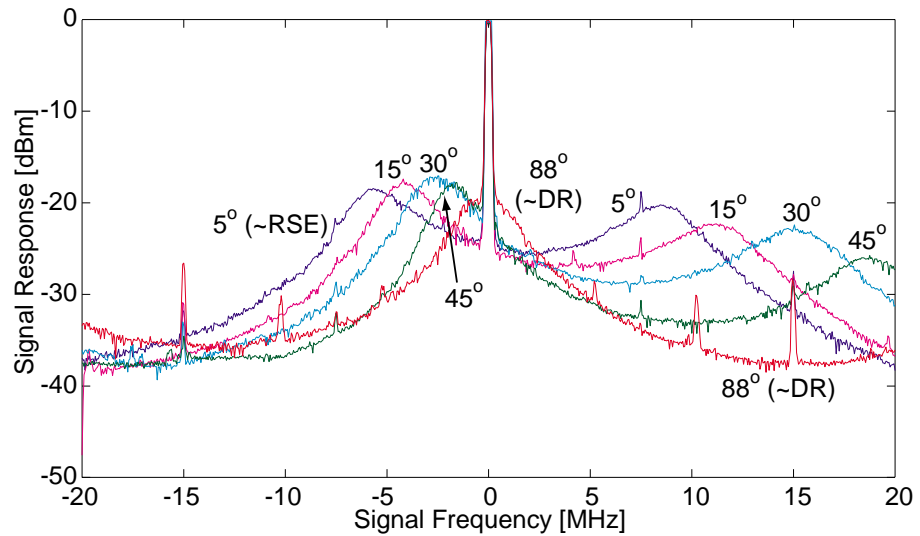


Figure 7.17: Measured frequency response (both positive and negative frequencies) of the signal transfer from one arm cavity to the Φ_- error signal for RSE Michelson system. The signal cavity detunings are indicated on the responses.

The number in degrees on each of the curves represents the detuning of the signal cavity where 0° is broadband RSE and 90° corresponds to dual recycling. The signal cavity was detuned by changing the offset frequency to the value corresponding to the desired detuning in the look-up table (table 7.2). Between each different signal scan the interferometer locking was stopped (including phase locking), the signal generator frequency changed to its new value, phase lock of the subcarrier and carrier reacquired and the demodulation phases reoptimised for the new subcarrier frequency. Our system could

⁵This is assuming that the arm cavities are identical.

not be configured to lock the interferometer at exactly the RSE point or the dual recycling point. When the subcarrier was tuned to the required frequency for these lock points, intermodulation products of sidebands and their harmonics produced large beat signals near DC at the mixer outputs. Although these were not strictly within the locking bandwidth, their presence made optimisation of the demodulation phase more difficult and so these regions of detuning were avoided. This is not a fundamental flaw in the control system but rather a consequence of our choice of modulation frequencies and lengths for the benchtop interferometer. In particular, our choice of making the signal cavity exactly the same length as the power cavity ensured that an intermodulation product is mixed down to DC when the subcarrier frequency is set to 0° detuning (broadband RSE).

Unfortunately, this control system cannot easily be configured to lock the system without the signal mirror, and so a direct comparison with the frequency response of a power recycled Michelson with arm cavities was not possible. However, the signal response of one of the arm cavities alone, presented in figure 7.16, gives an indication of the expected bandwidth of the interferometer without a signal mirror.

Figure 7.18(a) shows a subset of the responses of figure 7.17 plotted on a linear scale. The signal enhancement near the broadband RSE detuning can be clearly seen compared to the dual recycled response, particularly around 7 MHz. Due to the excessive loss of the arm cavities the peak of the near dual recycled response was actually slightly lower than the peak of the 30° response.

The theoretically predicted frequency responses are shown in figure 7.18b. These responses were calculated using the measured mirror parameters given in tables 7.3. The only fitted parameter is the scale of the vertical axis which has been scaled to allow easy comparison with the experimental data. We can see that the qualitative agreement between theory and experiment is quite good. The peaks of the frequency responses were as predicted, as were the relative heights of the peaks. The peaks in the experimental response were slightly wider than calculated, which may indicate that there is extra loss in the signal cavity that is not accounted by the mirror reflectivities alone. The most likely source of this loss is a mode mismatch between the signal cavity and the arm cavity mode, or a higher than expected loss in the arm cavities.

As a demonstration of the continuous tuning properties of this control system, figure 7.19 shows the power transmitted through the arm cavities as the interferometer was detuned from 30° to 15° without dropping lock (apart from two glitches at 200 seconds and 460 seconds⁶). This was achieved by slowly changing the subcarrier offset frequency (from 184.315 MHz to 186.445 MHz) at a rate which allows the signal cavity mirror to dynamically track the subcarrier frequency to keep it on resonance. The frequency generator we used changed frequency in discrete steps up to 4 times a second. The largest step rate which allowed reliable interferometer locking was 1 kHz, providing a tuning rate of 4 kHz per second. At this rate the arm cavity transmitted power was quite noisy, but the system remained in lock. The phase locking system could actually handle discrete steps of 10 kHz without dropping lock; however, the transients introduced into the relative phase of the carrier and subcarrier were detrimental to the main interferometer lock, causing it to sporadically drop lock over a time scales of a few seconds using these larger steps. With careful design of the phase locking loop, and genuinely continuous tuning of the offset frequency, it should be possible to detune from RSE to DR in a matter of seconds.

⁶Lock was automatically and almost instantaneously reacquired.

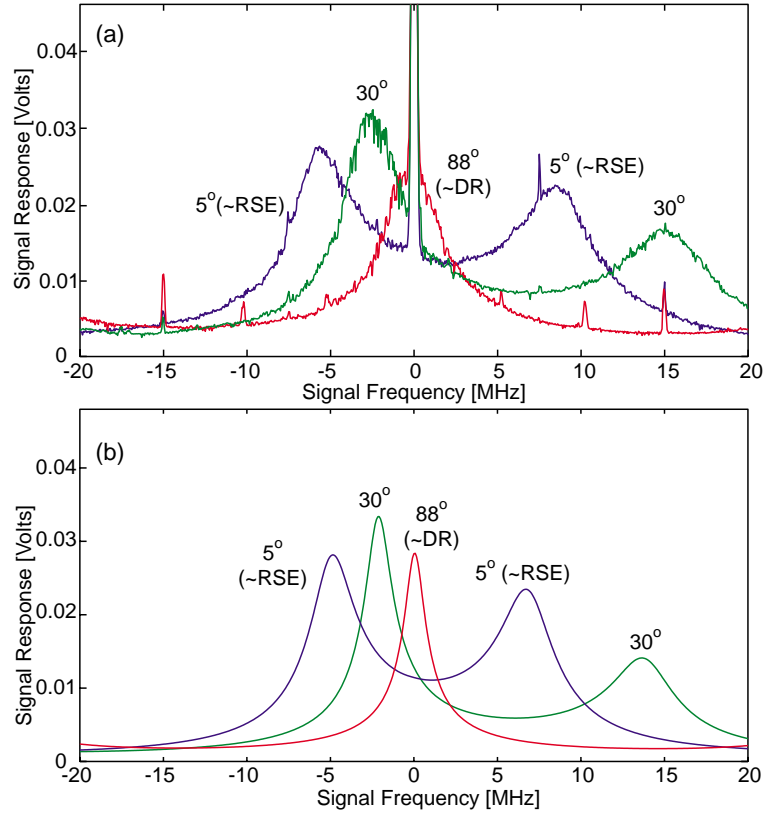


Figure 7.18: (a) Measured and (b) calculated signal transfer from AC in-line to Φ_- error signal for signal cavity detunings of 5° , 30° and 88° from RSE with a linear vertical scale. Vertical scale of (b) has been adjusted to roughly correspond to experimental data, measured values have been used for all other parameters.

As mentioned earlier, in our benchtop system the demodulation phases should be reset for each subcarrier frequency. Whilst tuning over the range shown in figure 7.19 the demodulation phase shifted by about 5° from the optimum for the Φ_- error signal. However, the interferometer remained locked. This demonstrated that at least the interferometer locking was stable in the presence of small demodulation phase errors.

7.8 Application to long base-line interferometers

There are a few key differences in the application of this control system to a long base-line gravitational wave detector. Firstly, on the bench top system the subcarrier could be tuned continuously over the entire range without coming into contact with an arm cavity resonance. This was possible due to the small ratio of lengths of the arm cavity to the signal cavity, $L_{ac}/(L_s + L_m) \approx 0.1$. In a long base-line detector this ratio increases to approximately 200, ensuring that as the subcarrier frequency is detuned it will encounter each arm cavity resonance approximately every 40 kHz. To avoid these resonances the subcarrier frequency could be moved in discrete steps of the arm cavity FSR. In this way the subcarrier could be kept anti-resonant with the arms yet still provide an adequate number of detuning points for the signal cavity.

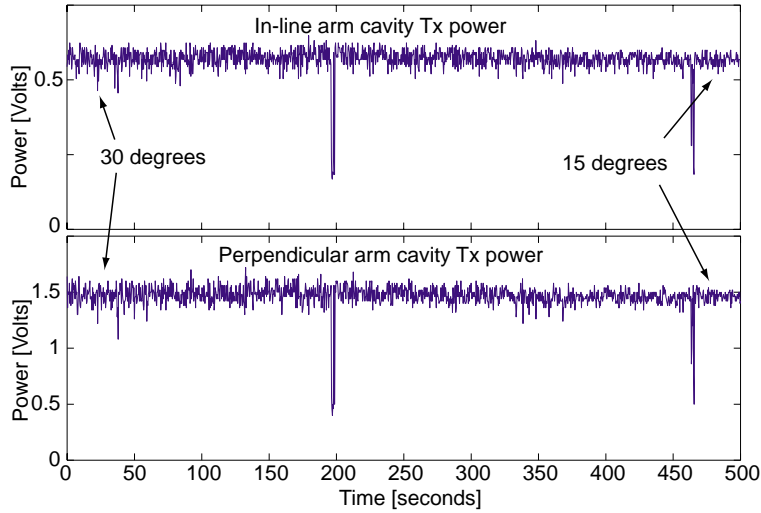


Figure 7.19: Arm cavities' transmitted powers during detuning of the signal cavity from 30° (184.315 MHz subcarrier offset) to 15° (186.445 MHz subcarrier offset), at a rate of approximately 4 kHz per second.

Secondly, in a long base-line interferometer the signal cavity will be much longer. As a consequence, it is possible that the entire range of detuning could be accessed by changing the subcarrier frequency by 1 MHz or less. In this case the subcarrier offset frequency could be reduced to approximately half the frequency of the ω_1 sidebands as intermodulation products would be easier to avoid. This frequency ($\omega_{sc} \approx 40$ MHz) will be more convenient for detection and signal extraction purposes.

Finally, it may be possible to extract the ϕ_s degree of freedom using a double demodulation of the beat between ω_1 sidebands and the ω_{sc} subcarrier at the reflected port. In this case the ω_2 sidebands on the subcarrier would no longer be needed, simplifying the input field to a set of PM sidebands on the carrier, and a tunable offset frequency subcarrier. This possibility is yet to be fully analysed and requires further investigation.

Figure 7.20 shows a comparison of the input fields required to lock the interferometer to the 5° detuned point and the 88° detuned point. The subcarrier frequency has changed by about 10 MHz to achieve this. This is equivalent to a fractional offset frequency change of around 6%. This amount of tunability can be easily dealt with by the electronic systems such as photodetectors, mixers and even modulators; however, it is a very awkward frequency shift to deal with in the input optics. In particular, it will be very difficult to pass all of the optical frequencies through a single mode cleaner of moderate length (several metres, say).

There are several potential solutions to this problem. The most flexible from a control point of view, would be to have individual suspended mode cleaners for the carrier and subcarrier. These two modecleaners could be of fixed (but different) lengths, locked on resonance to the carrier and subcarrier respectively, and each pass the single pair of modulation sidebands n free spectral ranges away.

Another solution is to use a very long modecleaner. The subcarrier frequency offset could be tuned discretely between adjacent FSRs. The number of tuning points of the signal cavity is proportional to the ratio of the lengths of the modecleaner to the signal

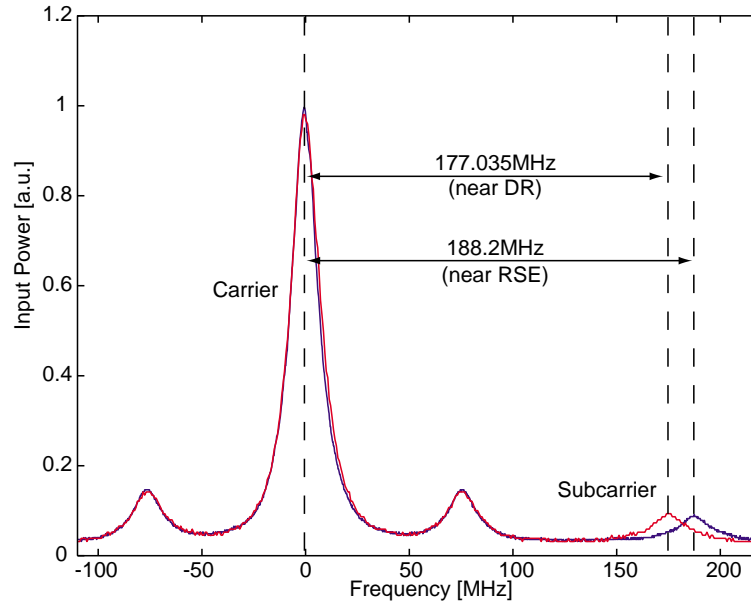


Figure 7.20: Input optical spectra required for near RSE (188.2 MHz subcarrier offset) and for near DR (177.035 MHz subcarrier offset), illustrating the amount of subcarrier offset tuning required.

cavity, thus having a short signal cavity may help as well. This solution could be suitable for the VIRGO interferometer as it uses a 160 m modecleaner.

To justify the extra complication of the input modecleaners, this control system should be applied to an interferometer which is required to be detuned either often or quickly. Such an interferometer may be operated in a reasonably narrow band mode, perhaps to complement the broadband responses of other detectors. The 2 km LIGO interferometer is one candidate for reasonably narrow band operation, which could potentially benefit from such a control system.

If the detuning point of the signal cavity will be basically fixed, much of the flexibility benefits of this control system are not necessary. However, in this mode of operation, the subcarrier frequency is also fixed, and thus all fields could be passed through the same modecleaner, removing one of the biggest obstacles to the simple implementation of this technique. In addition, if occasional detuning is required, this could be achieved by a macroscopic movement of the signal mirror, in the mode of operation suggested by Mason [67].

One of the biggest unknowns in this experiment is the ability of single sideband modulation to be used as an effective signal extraction technique for the gravitational wave signal. An investigation of techniques for minimising demodulation phase errors would be useful, for example, there may be a way to actively stabilise the demodulation phase to suppress such errors. Detailed analysis of the coupling of demodulation phase error into the signal output is required as well as realistic estimates of the size of the probable demodulation phase error.

7.9 Summary

We have designed and implemented a length sensing control system for a power recycled Michelson interferometer with resonant sideband extraction. This control system relies on frontal modulation only, and extracts the error signals of the 5 degrees of freedom from the reflected, transmitted and power cavity ports. We have experimentally operated a benchtop prototype over almost the entire range of the signal cavity detuning. In addition we have demonstrated that the interferometer can be continuously detuned without dropping lock. Finally, the signal response of the interferometer was measured (for both positive and negative frequencies) at these detuned points and was found to be in good agreement with theoretical predictions.

Part III

Tilt Locking

Tilt locking

So far this thesis has been concerned with precision control and readout of the main interferometer of a gravitational wave detector. There are many other optical cavities which must be frequency locked such as the (pre)modecleaner [92], output modecleaner and injection locking systems [93]. The frequency locking of lasers to optical cavities is also required for a wide range of other scientific applications including frequency stabilisation [94], continuous wave second harmonic generation [95] and optical frequency standards [96]. The remainder of this thesis is devoted to a new technique for the readout and control of optical interferometers. This technique, tilt locking [97], utilises a high sensitivity measurement of the interference between two spatial modes of a cavity to produce an error signal.

8.1 Frequency Locking techniques

Frequency locking involves obtaining an error signal which is proportional to the difference between the laser frequency and the cavity resonance¹. This error signal is usually utilised in a closed loop feedback system to actuate either the laser frequency or the cavity length to the desired value. The actuator for cavity length control for the experiments described in this thesis was a PZT attached to one of the cavity mirrors. For the Nd:YAG lasers used here, the frequency actuators are the laser crystal temperature and a PZT attached to the laser crystal. More recently, feedback to the current of the pump diode lasers has been found to produce effective frequency stabilisation [98]. This coupling from the pump intensity to output frequency is due to thermally induced changes in the optical path length of the laser crystal [99]. Unity gain frequencies of 80 kHz have been demonstrated with this system with the added benefit that the free running laser intensity noise is also suppressed.

Several methods for obtaining an error signal have been used over the last several decades including fringe side locking [100], transmission locking [101], Hänsch-Couillaud locking [85] and Pound-Drever-Hall locking [33]. We will give a brief overview of these techniques, highlighting their advantages and disadvantages.

Fringe side locking

Fringe side locking [100] is a commonly used technique which involves locking the laser halfway up the side of the cavity resonance. The basic idea is that as the laser frequency

¹The condition of proportionality need only be satisfied when the laser is sufficiently close to resonance.

drifts with respect to the cavity resonance, the fraction of the power transmitted through the cavity will be changed. If the cavity drifts closer to resonance the transmitted power will increase, and as it drifts away from resonance the power will decrease. By subtracting an offset from a measurement of the transmitted power a zero crossing error signal can be obtained. This error signal will not lock the laser to resonance but part way up the side of the fringe. The technique has the advantage that it is simple to use and it requires no additional components to be added to the beam path. It is inherently a DC technique, and thus low speed photodetectors and electronics can be used. In addition the processing of the photocurrent to produce an error signal is very straightforward.

The main shortcoming of the technique in this simple form is that it is sensitive to amplitude noise of the laser. For example, if the power on the transmitted detector increases it is impossible to distinguish whether this was due to a change in the frequency of the laser or an increase in the laser intensity. This problem can be overcome by detecting both the transmitted and reflected beams and subtracting the two photocurrents. As the intensity noise is correlated on these two detectors it will be removed by the subtraction². The photocurrents will be anticorrelated with respect to frequency measurement and so the subtraction will result in an increase of the signal. To approach the same sensitivity as other techniques all of the power needs to be detected. This can be a problem if high powers are involved, or the beam is to be used later in the experiment.

Transmission locking

Transmission locking [101] involves dithering either the laser frequency or the cavity length and monitoring the transmitted power to obtain an error signal. The photocurrent is demodulated at the dither frequency typically by a lock in amplifier. The frequency of the dither must be kept to approximately the cavity bandwidth or lower otherwise no error signal is obtained. As a consequence, the bandwidth of this system is fairly small (less than half the dither frequency to prevent aliasing problems). As this technique uses the transmitted field, it also suffers from a time delay due to passage through the cavity. This method can be useful to control complicated coupled interferometers as different components can be dithered at different frequencies to isolate the error signals from cross coupling.

One of the disadvantages of this technique is that the laser frequency dither will be present on the output beams which may interfere with subsequent measurements [102]. The alternative of mechanically dithering the cavity may be undesirable or impossible in high sensitivity applications, for example, a rigid or suspended cavity, potentially in vacuum.

Hänsch-Couillaud locking

Hänsch-Couillaud locking [85] is a conceptually elegant method to produce an error signal for birefringent cavities. If the polarisation of the field incident on the birefringent cavity differs from the polarisation eigenmodes of the cavity (typically s and p polarisations) the cavity will decompose this into a resonant (s say) polarisation mode and a non resonant (p say) polarisation mode. When the s mode sweeps through resonance it will receive a phase shift, which will alter the polarisation state of the light reflected from the

²This is not the case at frequencies large compared to the cavity linewidth where the filtering of the cavity reduces the transfer of the intensity noise to the dark fringe

cavity. By analysing this polarisation, an error signal for the cavity resonance position can be obtained.

A cavity can be made birefringent by inserting a polarising element inside; however, this will add extra loss, limiting the feasibility of this technique for high finesse cavities. A ring cavity exhibits birefringence due to different phase shifts obtained by each polarisation upon reflection from a tilted mirror, and so is a natural candidate for Hänsch-Couillaud locking. The technique could also be applied to cavities containing non-linear birefringent materials such as second harmonic generators and optical parametric oscillators.

Hänsch-Couillaud locking exhibits the best shot noise limited sensitivity of all techniques. In fact it is the only technique which is, in principle, capable of measuring a signal at the quantum noise level. Unfortunately, technical factors often limit the performance well before this limit. The main disadvantage of the Hänsch-Couillaud technique is the complexity and stability of the polarisation analysis system. The polarisation analysis requires the alignment and optimisation of several components including two photodetectors, waveplates and a polarising beamsplitter. To reach the shot noise limit, the wave plates must firstly be optimised to give equal power on the two photodetectors. This is not sufficient to guarantee maximum sensitivity and the change in power on the detectors for any given phase shift must be maximised by careful adjustment of the waveplates. A major drawback for high precision applications is the temperature sensitivity of the polarisation optics. This can severely degrade the DC accuracy of this technique.

Pound-Drever-Hall locking

Currently the most widely used method for high performance applications is the Pound-Drever-Hall (PDH) technique [33]. As discussed earlier, the PDH technique utilises the beat between the carrier field and non-resonant phase modulation sidebands. The sidebands provide a reference for the phase of the carrier field reflected from the cavity. As will be demonstrated in section 9.2, by making a measurement of the phase of the reflected field, a high sensitivity, quantum noise limited measurement of the cavity is possible. Remarkably, this technique can achieve this sensitivity with only a small fraction of the total power on the photodetector. The PDH technique also has an excellent frequency response as it is a reflection based technique and it is insensitive to low frequency amplitude noise.

As PDH measures the component of the phase modulation sidebands converted to amplitude modulation it is sensitive to any excess amplitude noise at the modulation frequency. To avoid this the modulation frequency is normally chosen to be in a region where the laser is shot noise limited, typically above 5 to 10 MHz depending on the laser. A problem arises if the phase modulation is not pure and has some component of amplitude modulation. In practice, electro-optic modulators will produce some component of AM which is usually temperature dependent. If this is a problem, it can be overcome by measuring the AM directly, and servoing it to zero [103], although this variation is only required in ultrahigh performance systems and is seldom used.

Other disadvantages of the PDH technique are its complexity and expense. It typically requires a signal generator, electro-optic modulator, high speed photodetector and RF electronics for processing the signal. One other technical problem which is becoming a concern for gravitational wave detectors, is associated with passing high optical powers through electro-optic phase modulators. Despite these minor shortcomings, the PDH

technique continues to be the preferred system for high performance applications.

8.2 Tilt locking

The technique presented here, tilt locking [97], also utilises interference between the carrier field and a directly reflected phase reference. In this case the phase reference is a non-resonant higher order spatial mode. Instead of electro-optic encoding and electronic decoding of frequency sidebands, tilt locking uses optical encoding and decoding of spatial modes. The nature of the spatial modes and their interference is crucial to understanding tilt locking.

8.2.1 Hermite-Gauss modes

An optical cavity decomposes an input field into a set of spatial transverse electromagnetic (TEM) modes, which can be approximated by the Hermite-Gauss functions [31] (see section 3.5). Higher order Hermite-Gauss modes can be excited by incorrect mode matching or alignment of the laser to the fundamental Gaussian mode of the cavity. Tilt locking relies on the fundamental TEM_{00} mode and the TEM_{10} mode interference to obtain an error signal. Figure 8.1(a) shows the cross section of the real and imaginary parts of the fundamental mode electric field. We are only concerned with the electric field distribution in the x -axis and we assume that all modes considered here have a Gaussian distribution in the y -axis. Note that the fundamental beam has the same phase across the entire cross section. Figure 8.1(b) shows the same information for the TEM_{10} mode. Note that the electric field has a phase flip of 180° at $x = 0$. For modal interference the phase difference between the two modes is crucially important. Figure 8.1(c) shows a TEM_{10} shifted by $\pi/2$ radians, that is, $\pm\pi/2$ out of phase with the carrier field.

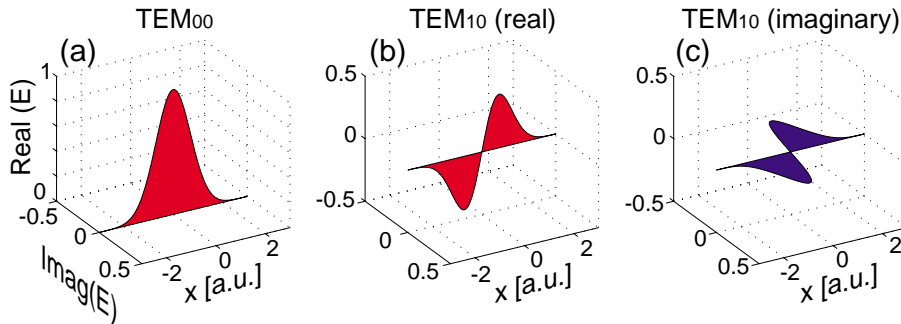


Figure 8.1: (a) Fundamental mode, (b) TEM_{10} mode (in-phase), (c) TEM_{10} mode ($\pi/2$ phase shift)

We now consider interference of these two modes[104]. If we add the TEM_{00} field with a small fraction of the TEM_{10} (in-phase) mode, the electric fields will add constructively on the right hand side and subtract on the left hand side of the beam. The result, as shown in figure 8.2(a) is that the beam position will be offset by a small amount to the right, thus we refer to the in-phase TEM_{10} mode as the offset mode. If we add a small fraction of the TEM_{10} mode with a $\pi/2$ phase shift to the TEM_{00} mode, the beam adds in quadrature on both sides of the beam. The resultant electric field is shown in figure 8.2(b). Note that the magnitude of the beam remains approximately unchanged; however, the

phase now changes nearly linearly with x . This is equivalent to a tilted wave front, and so we call the $\pi/2$ phase shifted TEM_{10} mode the tilt mode. Conversely, the TEM_{10} modes can be excited in an optical cavity by the misaligning the input beam with respect to the cavity. For example, the TEM_{10} tilt mode ($\pi/2$ out of phase) can be produced at the input from a TEM_{00} mode by tilting the input beam with respect to the cavity input mirror. In general, the amount of tilt and offset will determine the magnitude and phase of the TEM_{10} produced.

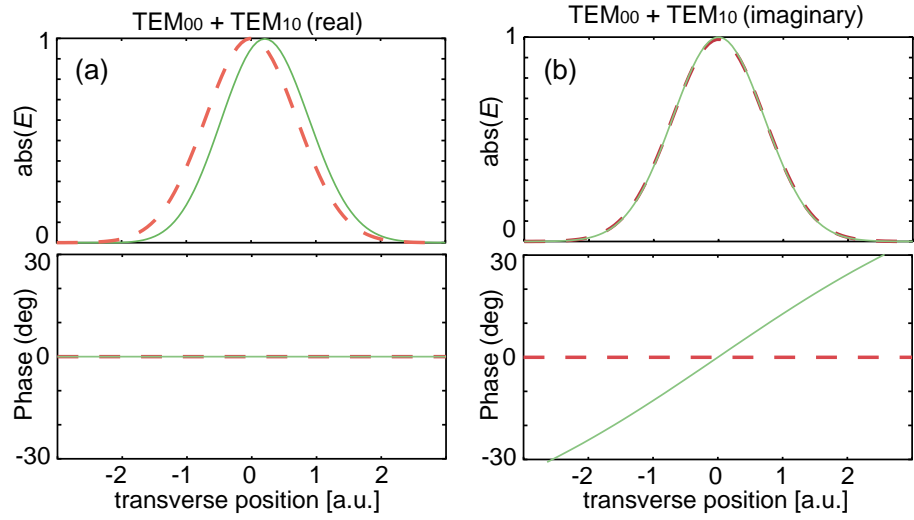


Figure 8.2: Effect on the magnitude and phase of the field of adding a small amount of the TEM_{10} mode to the TEM_{00} mode (a) in-phase and (b) $\pi/2$ out of phase.

Different Hermite-Gauss modes accumulate different phase shifts as they propagate through space. In an optical cavity, the position and curvature of the mirrors will determine the extra round trip phase shift each mode will receive. This is known as the Gouy phase shift [31], and it is plotted for the TEM_{00} and TEM_{10} modes in figure 8.3. One consequence of the Gouy phase shift is that the TEM_{00} and TEM_{10} modes of the cavity will have a different round trip phase shift and thus a different resonant frequency. Exceptions to this are the cases on the border of stability for flat-flat or concentric cavity geometries where the round trip relative phase shift is 0 and 2π respectively. Tilt locking requires a cavity where the TEM_{10} mode is non-resonant when the TEM_{00} mode is near resonance. This condition is satisfied for most stable cavities of reasonable finesse.

8.2.2 Obtaining an error signal from spatial mode interference

In its standard form, tilt locking uses a nonresonant TEM_{10} mode as a phase reference for the resonant TEM_{00} mode (the carrier). The transverse electric field distribution for the TEM_{00} mode and a TEM_{10} (offset) mode is shown in figure 8.4(a). The detected signal is proportional to the magnitude of the interference between these two spatial modes, and is given by the overlap integral [31]. For Hermite-Gauss modes where the entire beam is detected, no interference can be measured with the overlap integral given by,

$$I_{0,1} = \left| \int_{-\infty}^{\infty} \int_{-\infty}^{\infty} u_{00}^*(x, y) u_{10}(x, y) dx dy \right| = 0 \quad (8.1)$$

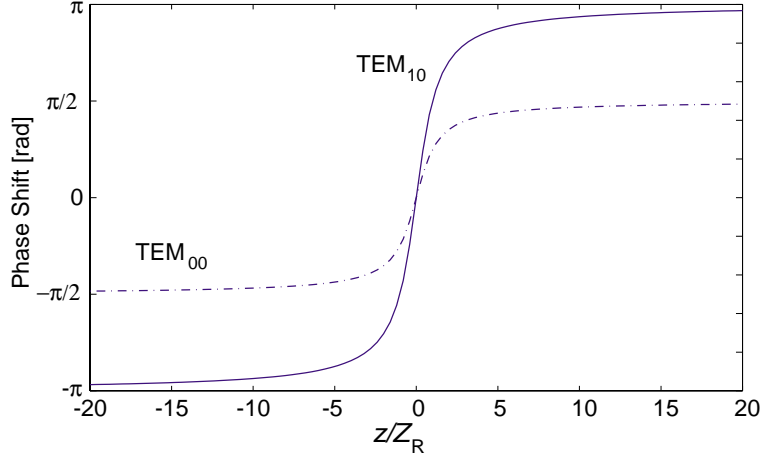


Figure 8.3: Plot of Gouy phase for the TEM_{00} and TEM_{10} modes as a function of propagation distance, z , normalised to the Rayleigh range, Z_R . The waist is at $z = 0$ for both modes.

where $u_{00}(x, y)$ and $u_{10}(x, y)$ are the electric field distributions for the normalised TEM_{00} and TEM_{10} modes respectively. The integral is zero due to the orthogonality of the Hermite-Gauss modes. No interference is detected and thus no error signal is obtained.

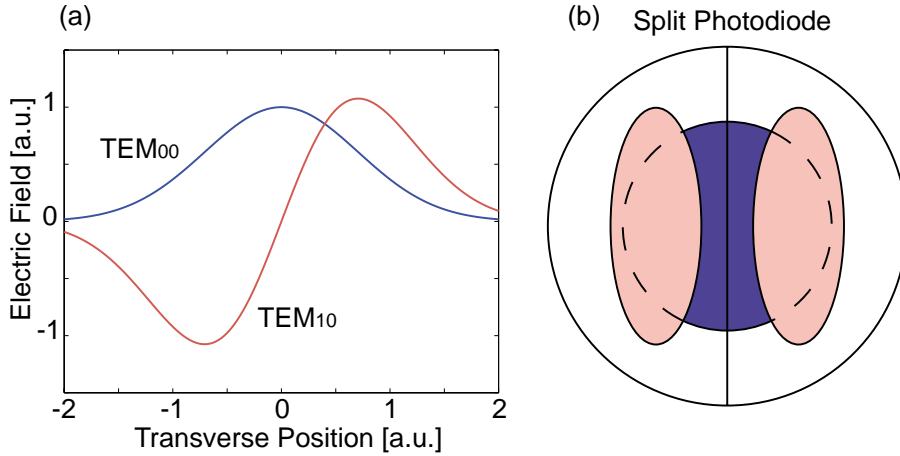


Figure 8.4: (a) TEM_{00} and TEM_{10} transverse electric field amplitude and (b) diagram of intensity distribution of TEM_{00} (dark circle) and TEM_{10} (light ellipses) on the split photodiode.

To measure the interference between the two spatial modes efficiently, we use a method similar to that used in auto-alignment systems [70, 71]. The reflected beam is detected on a two element split photodiode, as shown in figure 8.4(b), in such a way that each lobe of the TEM_{10} mode falls in a separate half of the photodiode. The error signal is given by subtraction of the photocurrents from each photodiode half. The interference measured by this split detection is given by,

$$I_{0,1} = \left| \int_{-\infty}^{\infty} \int_{-\infty}^0 u_{00}^*(x, y) u_{10}(x, y) dx dy \right| - \left| \int_{-\infty}^{\infty} \int_0^{\infty} u_{00}^*(x, y) u_{10}(x, y) dx dy \right| \quad (8.2)$$

As the $u_{00}(x, y)u_{10}(x, y)$ product is antisymmetric, breaking the overlap integral at the origin maximises the error signal.

As mentioned earlier, TEM_{10} mode arises from two types of misalignment - beam displacement and beam tilt. For tilt locking, the input beam is aligned and mode matched to give only the TEM_{00} mode and a TEM_{10} mode with a relative phase of $\pm\pi/2$ at the plane of the photodetector³. Figure 8.5 shows a simplified electric field vector diagram of the TEM_{00} and TEM_{10} (tilt) modes on the two halves of the photodiode where a single vector is used to represent the phase and average amplitude of the field on each side. Figure 8.5(a) shows the interference when there is no phase shift added by the cavity. This occurs when the TEM_{00} mode is exactly resonant with the cavity and the TEM_{10} is non-resonant. On the left half, the TEM_{10} adds to the TEM_{00} mode with $\pi/2$ phase while on the right half, the TEM_{10} adds with $-\pi/2$ phase. The power, proportional to the square of the resultant vector, is equal on each half. Thus the error signal, obtained by subtracting the photocurrents from the two halves of the photodiode, is zero. As the carrier drifts slightly away from resonance, the TEM_{00} mode acquires an equal phase shift in both photodiode halves while the non-resonant TEM_{10} mode remains unchanged as shown in figure 8.5(b). This causes the power in each photodiode half to increase and decrease respectively. The electronically subtracted photocurrent is no longer zero and gives an error signal proportional to the imaginary component of the cavity reflectivity for the carrier.

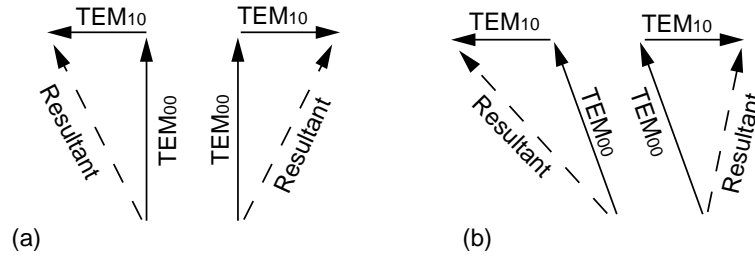


Figure 8.5: Vector summation of electric fields on each photodiode half with TEM_{00} (a) on resonance and (b) slightly off resonance.

An alternative explanation of the process is that a split photodetector performs a measurement of beam position. When the cavity is on resonance, the relative phase of the TEM_{10} and TEM_{00} modes, and thus the tilt symmetry, is preserved. A measurement will find the beam position unchanged. Reflection from an off-resonant cavity adds a phase shift between the two modes, converting the TEM_{10} mode from tilt mode symmetry to offset mode symmetry. A sensitive measurement will find that the average position of the beam has been altered.

The vector pictures presented above are instructive; however, they do not give a complete picture of the interference over the entire beam. Figure 8.6 shows the power on the split photodetector as the carrier phase shift changes from $-\pi/1500$ to $\pi/1500$. In this case we have assumed that the cavity is impedance matched. The power clearly shifts from right to left as the cavity drifts through resonance.

³The relative phase of the TEM_{00} and TEM_{10} modes changes depending on the separation of the detector and cavity. The phase difference is only important at the photodetector where the interference is measured.

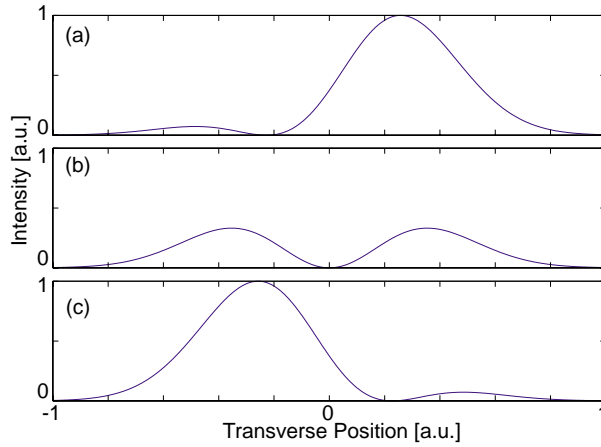


Figure 8.6: Interference between the TEM_{00} and $\pi/2$ phase advanced TEM_{10} Hermite-Gaussian modes reflected from an impedance matched resonator for a TEM_{00} mode with a phase change of (a) $-\pi/1500$, (b) 0, and (c) $\pi/1500$ rad in one resonator cycle.

8.2.3 Other spatial mode interference techniques

An earlier system developed by Wieman and Gilbert [105] also uses spatial mode interference. The beam reflected from the cavity is divided into two on a beamsplitter. An error signal is obtained with an apertured detector sampling a small section of one of the reflected beams. Interference between spatial modes will change the amount of power passing through the aperture and thus give some form of error signal with a large DC offset. The entire profile of the second beam is measured by a detector with a variable attenuator to correct for this offset. In addition to being a little more complicated than tilt locking, this scheme suffers from low efficiency due to inefficient measurement of the interference and losses introduced by the aperture. It can also be limited by the accuracy of the offset compensation. Another technique developed by Schnier and Madej [106] also uses spatial mode interference to control an interferometer. In this case it is to control the phase of optical feedback for a diode laser but it could also be applied to locking optical cavities. This system, however, requires a cavity which has close to degenerate spatial modes as the modal interference is measured on the transmitted beam, again with the use of apertures. This suffers from the same efficiency problems associated with the scheme of Wieman and Gilbert in addition to being restricted to cavities with particular geometries.

Tilt locking has more in common with Hänsch-Couillaud and PDH locking in that it is a reflection based technique which uses a non-resonant field as a phase reference or local oscillator for the carrier field. The three techniques utilise three different ways to produce a non-resonant field: spatial mode non-degeneracy, polarisation mode non-degeneracy and frequency mode non-degeneracy. As all three techniques are based upon the same physical principle they all share approximately the same fundamental limits. This will be examined more thoroughly in Chapter 9.

8.3 The experiment

In this thesis, we will often compare the performance of tilt locking to that of PDH locking as this is the current “state of the art”. We wish to demonstrate that tilt locking can potentially achieve the same performance as PDH locking; however, in a much simpler manner. Figure 8.7 shows the experimental layout of a standard PDH and tilt locking experiment. A ring cavity is used for simplicity however tilt locking works equally well

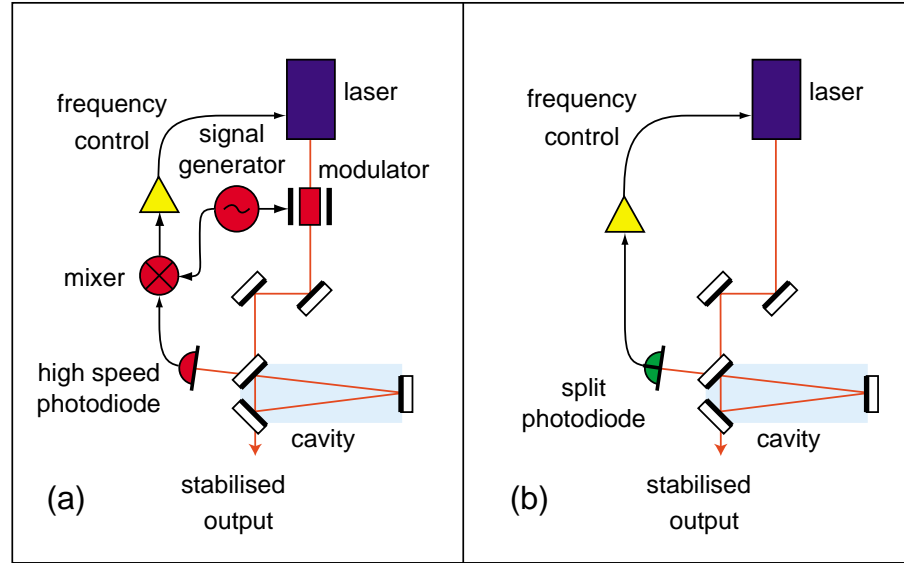


Figure 8.7: Experimental arrangement for (a) PDH locking and (b) tilt locking.

on a linear cavity. In figure 8.7(a) the beam passes through an electro-optic modulator and the reflected light is detected on a high speed photodetector. The photocurrent is then demodulated with the original driving signal to produce an error signal. In the tilt locking scheme of figure 8.7(b) the beam is aligned onto the cavity and the reflected beam detected on a two element split photodetector. The signal generator, electro-optic modulator, high speed photodetector and mixer have been replaced by a split photodiode and a subtraction circuit (not shown here). The split photodetector built for this experiment uses a commercial quadrant photodiode (EG&G C30843E) with the two quarters of each side added together (for details of the photodetector see appendix B). This forms a vertically split two element detector requiring a horizontal tilt to extract the error signal. The photodetector has sum and difference outputs allowing both the power and error signal to be monitored.

Careful alignment of the laser beam with respect to both the cavity and the tilt detector is necessary. Initially we align the laser beam to the cavity with no offset or tilt, in the standard way by scanning the cavity length and minimising the TEM_{10} mode power. We then position the split photodetector at the centre of the reflected beam by zeroing the subtracted output. By introducing a small misalignment with one of the input mirrors an error signal is generated which is slightly offset from zero. A second input mirror is adjusted to zero the error signal in a region of the scan far from resonance. Instead of adjusting the second mirror to zero the error signal it is possible to displace the tilt detector to recentre the beam. The technique will still work reliably, however the shot

noise performance of the system will be slightly reduced⁴. This procedure ensures that the TEM_{10} is $\pi/2$ out of phase with the carrier field as required. Any offset present in the final alignment is apparent by the asymmetry of the resulting error signal and can be readily removed thus ensuring the error signal is zero crossing at cavity line centre.

Figure 8.8 shows experimental results as the cavity length is scanned using a PZT attached to one of the cavity mirrors. Figure 8.8(a) shows the transmitted power and error signal obtained using the PDH scheme as the cavity is scanned through a complete free spectral range (FSR). The error signal was taken at the output of the level 7 mixer and a $\times 3$ amplifier and produced an error signal of approximately 0.5 Vp-p. Figure 8.8(b) shows the sum (total reflected power) and difference (error signal) outputs of the two element split detector for the tilt locking system again after $\times 3$ amplification. A large error signal (5 Vp-p) was obtained even with a small misalignment ($\text{TEM}_{10}/\text{TEM}_{00} \sim 1\%$) due to the larger front end gain of the tilt locking detector. It should be noted that the size of the tilt locking error signal in figure 8.8 was deliberately reduced to allow the use of the same frequency servo designed for PDH locking. Tilt locking error signals of 25 Vp-p could be readily achieved by increasing the beam tilt or photodetector transimpedance gain. The size of the error signal for PDH was ultimately limited by the type of mixer used and the RF power of the local oscillator. A large error signal may be an advantage if the electronic noise of the servo is close to the shot noise level in the error signal.

In figure 8.8(b) an error signal also appeared (at approximately 8 ms) as the small TEM_{10} mode passed through resonance with the fundamental now acting as a phase reference. As both these error signals resulted from TEM_{00} - TEM_{10} interference they were the same size, even though the TEM_{10} error signal occurred with negligible light inside the cavity. This was in contrast to the PDH system where the error signals for the sidebands were smaller than the carrier error signal as only one sideband contributed to the error signal at a time.

8.3.1 Frequency response and intensity noise immunity

Tilt locking and PDH locking have identical frequency responses as both schemes sample the optical field reflected from the cavity. Figure 8.9(a) shows the frequency spectrum of the error signals of both PDH and single pass tilt locking. The noise features present are typical of our 50 mW Nd:YAG laser (Lightwave Electronics120) and show the mechanical resonances of the laser crystal. The difference between the two spectra shown here was due to the 400 kHz roll off of the photodetector because of the R-C time constant of the quadrant detector and the limited bandwidth of the audio op-amps used⁵ (AD708). As noted earlier, the tilt locking error signal was much larger than the PDH error signal and the tilt locking data in figure 8.9 has been scaled to allow a simple comparison at low frequencies.

A well known feature of the PDH technique is its immunity to low frequency laser intensity noise. The intensity noise spectrum of our laser, shown in figure 8.9(b), had a large single feature at 430 kHz; the laser relaxation oscillation. This feature was absent from the PDH error signal as expected, and from the tilt locking error signal.

⁴The in-phase component of the nonresonant TEM_{10} mode does not contribute to the error signal.

⁵This particular photodetector was designed for a feedback system with a bandwidth of a few kHz only, and thus was not optimised for measurements in the MHz range. The quadrant photodiodes can have a bandwidth of many tens of MHz.

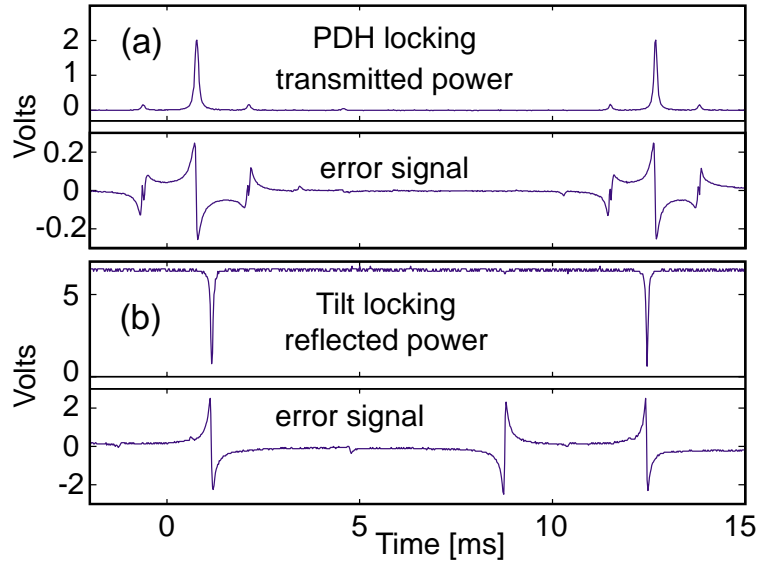


Figure 8.8: Power and error signal for (a) PDH locking, and (b) tilt locking for a cavity with a finesse of 200. Note power in (a) is transmitted intensity while (b) is the reflected intensity.

Tilt locking relies on balanced power in the two photodiode halves to obtain this intensity noise immunity. If the power is perfectly balanced then the intensity noise is subtracted down to the quantum noise limit. In practice, however, the balancing of the power on the photodiodes, and thus the intensity noise immunity, will be determined by the DC gain of the locking servo. For the servo used in this demonstration we expect approximately 100 dB isolation from laser intensity noise.

8.4 Beam jitter and mechanical vibration

Every locking scheme is sensitive to at least one noise source, if only the fluctuations in the quantity measured to infer the frequency noise. In the PDH technique, the measured quantity is the amplitude modulation at the modulation frequency, and thus the technique will be sensitive to amplitude or intensity noise at this frequency. In Hänsch-Couillaud locking an analysis of the polarisation of the reflected field is carried out and thus it is sensitive to fluctuations in the polarisation of the light incident on the cavity. Tilt locking essentially performs a measurement of the position of the beam reflected by an interferometer, and so fluctuations of the input beam position will couple into the error signal, mimicking fluctuations in frequency. This is the primary source of noise in tilt locking, indeed as we will demonstrate in chapter 9, the quantum mechanical fluctuations in the beam position (derived in section 3.6) are responsible for the *shot noise limit* of the tilt locking system. For this reason tilt locking is not ideally suited for use on suspended cavities.

It is reasonably straightforward to see how beam position fluctuations create a false error signal. As the beam moves the power on each side of the detector changes and thus the subtracted output will contain a false signal. In terms of spatial modes, beam position fluctuations arise from fluctuations in the TEM_{10} mode. The interference of the TEM_{00}

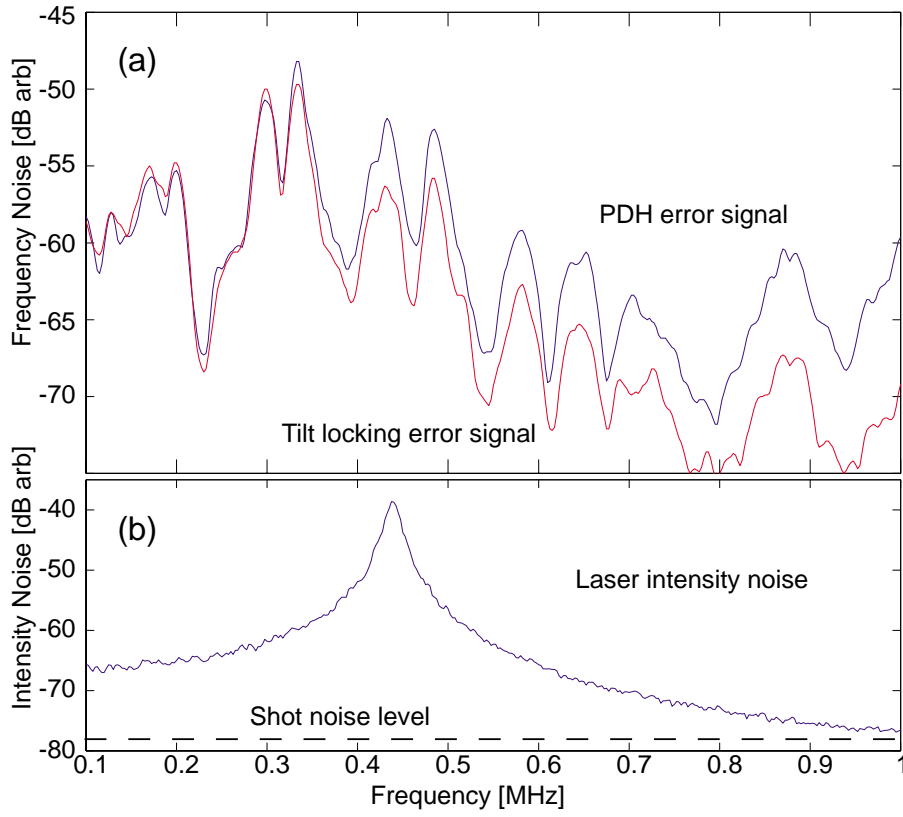


Figure 8.9: (a) Error signal frequency spectrum for PDH locking (top trace) and single pass tilt locking (lower trace) for a cavity with a finesse of 4000. (b) Laser intensity noise over the same frequency range.

mode with this noisy TEM_{10} mode induces beam position fluctuations in a manner similar to that depicted in figure 8.5.

8.4.1 Double pass tilt locking

There are several ways to minimise the effects of beam jitter. Perhaps an obvious solution to a person familiar with gravitational wave detectors is to use a modecleaner cavity to spatially filter the beam before it is directed onto the cavity. This solution involves the control of yet another cavity, a task equal in difficulty to the original problem to be solved. One elegant method to overcome the extra complexity is a scheme we refer to as double pass tilt locking, where the light is passed twice through the same cavity. The cavity is used as a spatial mode cleaner on the first pass and as a frequency reference on the second pass. Figure 8.10(a) shows the experimental layout of double pass tilt locking, where the light passes through the cavity once and is then retro-reflected, with a slight tilt, back through the cavity. It is important to note that the two passes through the cavity do not interfere as they are propagating in opposite directions⁶. The beam reflected on the second pass is used to obtain the error signal. Assuming that the filtering of the cavity

⁶In a linear cavity the second pass must be made orthogonally polarised to the first pass beam by adding a $\lambda/4$ plate before the retro-reflecting mirror.

is adequate, the beam jitter as seen by the photodetector only depends on the relative mechanical stability of the retro-reflecting mirror, optical cavity and the photodetector. Careful engineering of these components can ensure that the excess beam jitter is kept to a minimum. For example in section 10.1, the retro-reflecting mirror and photodetector are contained in a single invar block which is directly bolted to the cavity spacer.

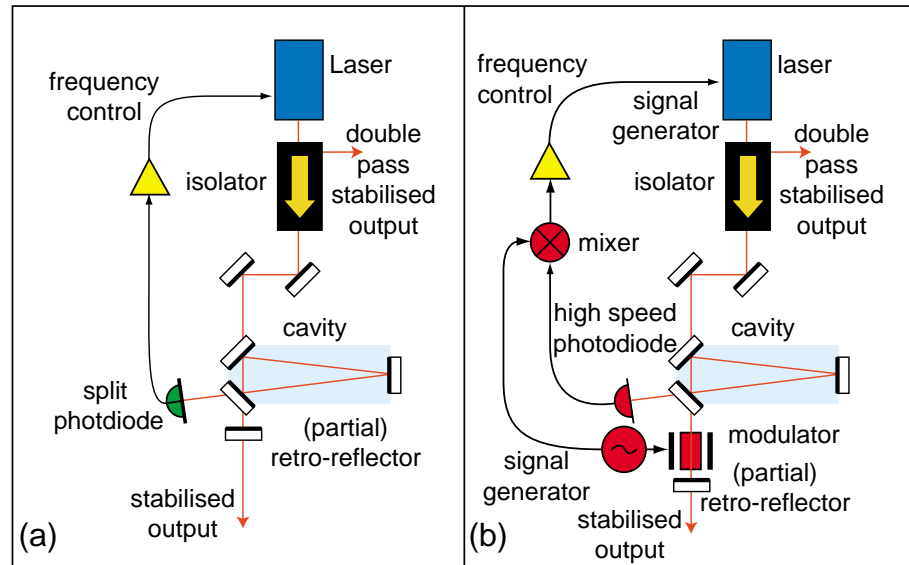


Figure 8.10: Experimental arrangement for (a) double pass tilt locking and (b) double pass PDH locking.

Double pass locking is not restricted to tilt locking systems. Figure 8.10(b) shows the equivalent experimental layout for a PDH locking system. This is similar to the double pass tilt configuration except note that the phase modulation must be introduced between the first and second passes. The advantages of using double pass PDH locking are two fold. Firstly when used in a modecleaner configuration, the two passes through the cavity give twice the filtering of intensity, frequency and spatial modes as a single pass through the mode cleaner. The filtering will be equivalent to two identical yet individual modecleaners in series but is achieved with only one control loop. A second benefit is in the amount of power that can be safely detected by a photodetector. Consider an impedance matched, near lossless cavity operating in a standard (single pass) PDH locking configuration (see figure 8.7(a)). Ideally, the photodetector would be optimised for the small amount of power reflected when the cavity is on resonance. When the laser drops lock nearly 100% of the light is incident on the photodiode, which could result in serious damage or necessitate the use of high speed attenuation. In the double pass configuration of figure 8.10(b), when the laser is on resonance nearly all of the power is transmitted through the cavity on the first pass, and then again on the second pass, so that the power on the photodetector is very small. When the laser drops lock, the amount of power on the photodetector remains small as the light is totally reflected by the first pass through the cavity. The maximum amount of power which can strike the photodetector is one quarter the input power, and this is only instantaneously as the laser either acquires or drops lock and the transmission and reflection equals 50%.

Figure 8.11 shows a comparison of the error signals obtained experimentally with

(single pass) tilt locking and the double pass tilt locking scheme. Note that due to the mode cleaner action of the first cavity pass, there is no error signal at the TEM_{10} resonance. In addition, the error signal drops to zero away from resonance somewhat faster than the single pass case due to the filtering effect of the first cavity pass.

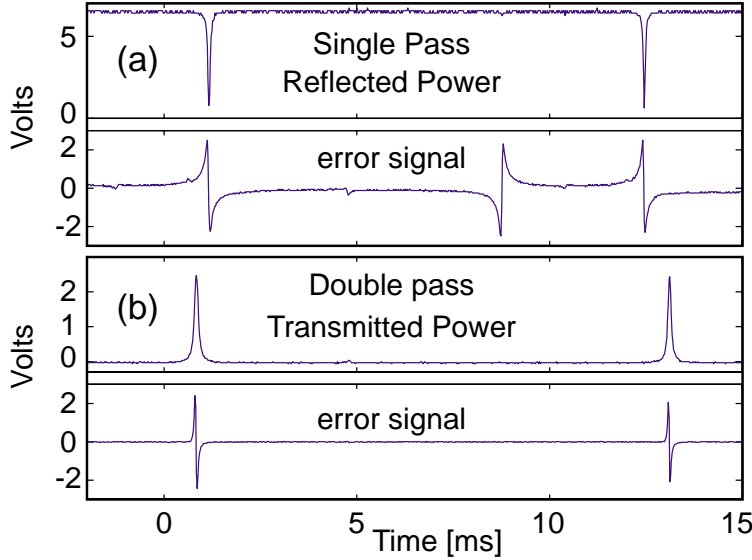


Figure 8.11: Power and error signal for (a) single pass tilt locking, and (b) double pass tilt locking for a cavity with a finesse of 200. Note power in (a) is reflected intensity while (b) is the intensity transmitted through the cavity.

One potential concern with double pass tilt locking is that the error signal is obtained after a single pass through the cavity, and so the locking loop suffers a delay associated with the cavity transmission. If this is a problem, a high speed frequency actuator (an electro-optic modulator, for instance) can be added between the retro-reflector and the cavity, which will effectively remove the delay for the high frequency component of the locking loop. The low frequency actuators (typically the laser crystal temperature and PZT) can still be operated before the first pass and will only be minimally effected by this delay.

For ultra-high precision experiments the double pass configuration of tilt locking will provide the best results. However, there are other simple measures that can be taken to ensure that the effects of beam jitter are minimised. Impedance matching, beam size and TEM_{10} mode power are three optical parameters which strongly influence lock stability for a given mechanical stability of the detector.

8.4.2 Impedance matching

If the cavity is close to impedance matched, very little TEM_{00} mode power will be reflected on resonance. Any jitter on the input light produces a TEM_{10} mode on reflection from the cavity. In the absence of TEM_{00} light, this mode's power is equally balanced across the photodiode halves and so does not contribute to the error signal. Similarly, the result of any mechanical motion of the photodetector is also reduced for an impedance matched cavity. As the TEM_{10} has negligible power near the center of the beam, any

small motion of the photodetector does not change the amount of power on each half of the photodiode. Thus tilt locking on an impedance matched system is, to first order, insensitive to mechanical vibrations of the photodetector.

This can be demonstrated mathematically by considering a photodetection of a TEM_{10} mode with a transverse electric field distribution given by,

$$u_1(x) = \left(\frac{2}{\pi}\right)^{\frac{1}{4}} 2xe^{-x^2} \quad (8.3)$$

where $u_1(x)$ is normalised to a total power of

$$P_T = \int_{-\infty}^{\infty} u_1^2(x) dx = 1 \quad (8.4)$$

The power detected by the left side of the photodiode will be given by

$$P_L = \int_{-\infty}^a u_1^2(x) dx \quad (8.5)$$

and on the right side by,

$$P_R = \int_{-a}^{\infty} u_1^2(x) dx \quad (8.6)$$

where a is the position of the centre of the photodetector ($a = 0$ corresponds to the centre of the beam).

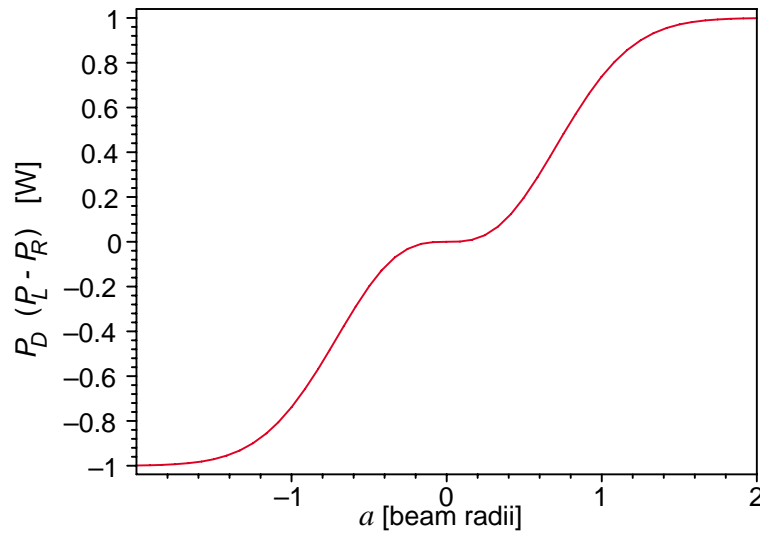


Figure 8.12: Difference in power detected on each side of the photodiode as a function of photodiode position, a , for the TEM_{10} mode.

We are interested in how the power difference, P_D changes as a function of photodetector position a .

$$P_D = P_L - P_R \quad (8.7)$$

$$= \int_{-\infty}^a u_1^2(x) dx - \int_a^{\infty} u_1^2(x) dx \quad (8.8)$$

$$= 2 \int_0^a u_1^2(x) dx \quad (8.9)$$

$$= \frac{(-2a\sqrt{2} + \sqrt{\pi} \operatorname{erf}(a\sqrt{2}) e^{(2a^2)}) e^{(-2a^2)}}{\sqrt{\pi}} \quad (8.10)$$

The result is plotted in figure 8.12 as a function of a . The most important feature of this graph is the point of inflection at $a = 0$. If the photodetector position was to change slightly around the centre of the beam, the subtracted output of the photodetector would be unchanged.

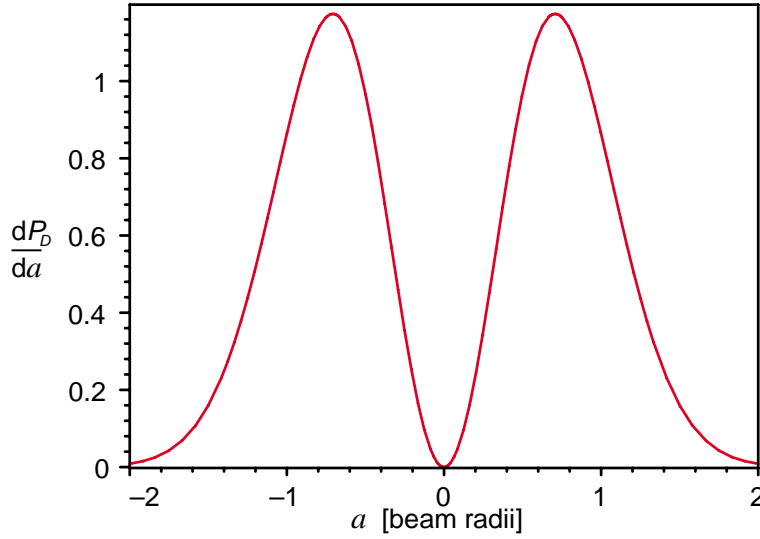


Figure 8.13: The derivative of the power difference P_D with respect to the photodiode position a indicating the strength of coupling from mechanical motion to error signal as a function of a .

The strength of the coupling from mechanical motion of the photodetector to the difference in the power will be given by the derivative of equation 8.10, dP_D/da . This is plotted in figure 8.13. Notice that as long as the beam is near the origin there is almost no transfer of the displacement da to the error signal output P_D . This is also true for large a but here there is no signal as the beam is completely on one side of the photodiode.

8.4.3 TEM₁₀ power and beam size

In situations where mechanical noise is the limiting noise source of the tilt locking system, the accuracy of the error signal can be increased by coupling more power into the TEM₁₀ mode. By increasing the power of the TEM₁₀ mode relative to the TEM₀₀ mode, the effective offset of the reflected beam becomes greater for any given phase shift. The extra power in the TEM₁₀ mode degrades the shot noise performance of the system, but if the system is limited by mechanical noise this is of no consequence. This is analogous to increasing the modulation depth in Pound-Drever-Hall locking to overcome electronic noise.

Another way the lock stability can be increased is to ensure the beam diameter is large at the detector surface. For a given phase signal, the beam position will move by some fraction of the beam diameter, so the absolute distance the beam moves is proportional to

the beam diameter. Thus, maximising the beam diameter at the detector surface reduces the phase shift required to overcome any displacement noise.

8.5 Tilt locking variations

This method can also be used with other higher order spatial modes with different types of multi-element photodiodes. For example, TEM_{11} mode interference can be measured using a bullseye photodiode to make a measurement of beam size. By making a measurement of beam size, the technique can be made insensitive to laser beam jitter⁷. This technique was briefly investigated experimentally; however, we found it was more difficult to optimise the interference. The technique is also less promising due to the inefficiency of the interference between the TEM_{00} and TEM_{11} modes.

8.6 Summary

We have developed a new technique, tilt locking, which relies on spatial mode interference to derive an error signal for an optical cavity. Tilt locking is an inexpensive system which replaces a signal generator, electro-optic modulator, high speed photodetector and mixer by a quadrant photodiode and several low frequency op-amps. The total cost of these items was less than \$100. In addition, tilt locking can be used with servos designed for PDH locking schemes with no modifications other than a reduction in gain. The technique is immune to intensity noise of the laser, and methods have been developed to minimise sensitivity to beam jitter. This combination of low cost, simplicity, and high sensitivity should facilitate the use of tilt locking in a broad range of applications.

⁷However, this technique is now influenced by changes in the size of the laser mode

Shot noise limited sensitivity of tilt locking

In this chapter we derive the performance limits of tilt locking. The derivation assumes that the performance is limited by shot noise. Other factors may limit the performance of tilt locking well before the shot noise limit is reached; however, these noise sources are usually technical in nature and can, in principle, be overcome by careful engineering of the experiment.

Section 9.1.1 deals with determining the error signal frequency response and signal to noise ratio for a measurement of phase modulation sidebands. In section 9.1.2 the quantum efficiency is calculated, allowing transparent comparison with other phase measurement techniques. In section 9.2 the same calculations are carried out for the PDH system.

9.1 Tilt locking sensitivity

Here we derive the sensitivity of the tilt locking discriminator to broadband phase modulation sidebands on the input field. We assume that the carrier is always exactly resonant with the cavity and that the phase modulation is small. The field incident on the cavity is given by,

$$E_{inc} = E_0 e^{i\omega_0 t} e^{i\alpha \cos(\omega_s t)} \quad (9.1)$$

where E_0 is the square root of the input power, ω_0 is the carrier angular frequency, and the carrier has phase modulation sidebands at an angular frequency ω_s , and a modulation depth α radians. As illustrated in the phasor diagram of figure 9.1, for small modulation depth ($\alpha \ll 1$) we can approximate equation 9.1 by,

$$E_{inc} = E_0 e^{i\omega_0 t} (1 + i\alpha \cos(\omega_s t)) \quad (9.2)$$

As tilt locking relies on spatial mode interference to obtain an error signal we now decompose the field into spatial modes which can be approximated by the normalised Hermite-Gauss modes. We consider only the interference between the TEM_{00} mode and TEM_{10} (with electric fields denoted by $u_0(x)$ and $u_1(x)$ respectively) as these are the only modes with appreciable amplitude for small amounts of tilt.

$$u_0(x) = \left(\frac{2}{\pi}\right)^{\frac{1}{4}} \left(\frac{1}{w}\right)^{\frac{1}{2}} e^{-\left(\frac{x^2}{w^2}\right)} \quad (9.3)$$

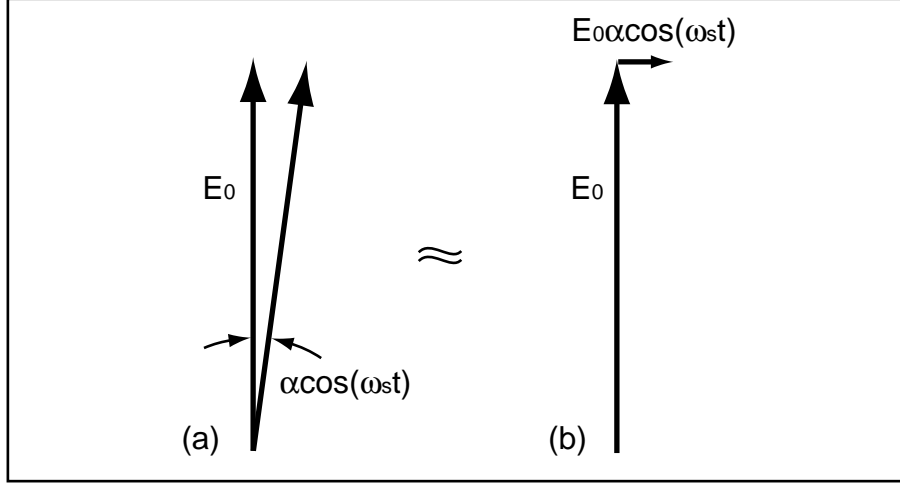


Figure 9.1: Graphical representation of the approximation for small sidebands. (a) Phase modulated field as represented in equation 9.1, and (b) the approximation for small sidebands as shown in equation (9.2). Approximation holds in the regime where $\alpha \approx \tan \alpha$.

$$u_1(x) = \left(\frac{2}{\pi}\right)^{\frac{1}{4}} \left(\frac{1}{w}\right)^{\frac{3}{2}} 2xe^{-\left(\frac{x^2}{w^2}\right)} \quad (9.4)$$

where w is the beam radius and x is the transverse coordinate. We are using the power normalised Hermite-Gauss modes, each satisfying the condition,

$$\int_{-\infty}^{\infty} u_m^2(x) dx = 1 \quad (9.5)$$

If the beam incident on the cavity is tilted around the plane of the photodetector, we add a TEM_{10} mode with a phase shift of $\pi/2$ radians relative to the carrier TEM_{00} mode. The input field is now a function of the transverse direction, x and can be represented by,

$$E_{inc}(x) = E_0 e^{i\omega_0 t} \left(a_0 u_0(x) + i a_1 u_1(x) \right) \left(1 + i \alpha \cos(\omega_s t) \right) \quad (9.6)$$

where the coefficients a_0 and a_1 are real and satisfy $a_0^2 + a_1^2 \approx 1$. The ratio of these coefficients determines the degree of tilt at the photodetector. The incident field as written in equation (9.6) consists of four fields: the TEM_{00} carrier field, the TEM_{00} phase modulation sidebands, the TEM_{10} carrier field and the TEM_{10} phase modulation sidebands. These fields are illustrated vectorially in figure 9.2(a).

Reflection from a cavity multiplies the input field by the complex reflectivity of the cavity $r_{cav}(\omega_s)$, where we write $r_{cav}(0) \equiv r_{cav}(\omega_s = 0)$ explicitly for the reflectivity of the TEM_{00} carrier field. This complex reflectivity is given by,

$$r_{cav}(\omega_s) = \frac{r_1 - (r_1^2 + t_1^2) r_2 e^{i2\omega_s L/c}}{1 - r_1 r_2 e^{i2\omega_s L/c}} \quad (9.7)$$

At this stage it is necessary to express the $u_0(x)$ -cosine product from equation 9.6 as a sum of positive and negative exponentials as these upper and lower sidebands experience different reflectivities of $r_{cav}(\omega_s)$ and $r_{cav}(-\omega_s) = r_{cav}^*(\omega_s)$ respectively. We also

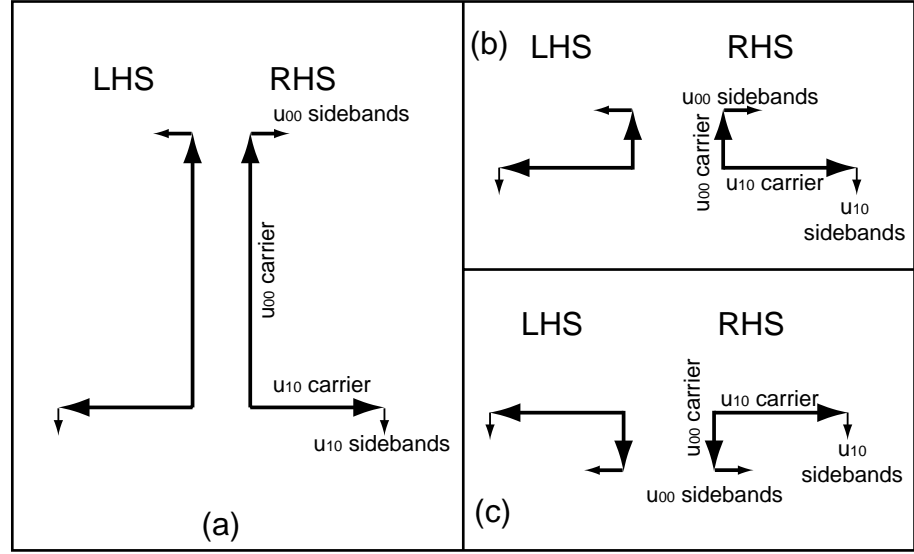


Figure 9.2: (a) The electric fields incident on the cavity consist of four components: the $u_0(x)$ mode and phase noise sidebands, and the $u_1(x)$ mode and its corresponding phase noise sidebands. The same electric fields after reflection from (b) an undercoupled cavity and (c) an overcoupled cavity. Note the $u_0(x)$ mode is attenuated by the cavity loss whilst the $u_1(x)$ mode remains unchanged.

assume that the TEM_{10} mode reflects off the cavity with no phase change and unity efficiency. This will be a good approximation for a stable cavity with reasonable finesse. The reflected electric field can thus be written,

$$E_{ref}(x) = E_0 e^{i\omega_0 t} \left[a_0 u_0(x) r_{cav}(0) + \frac{a_0 u_0(x) i\alpha}{2} (r_{cav}(\omega_s) e^{i\omega_s t} + r_{cav}^*(\omega_s) e^{-i\omega_s t}) + i a_1 u_1(x) (1 + i\alpha \cos(\omega_s t)) \right] \quad (9.8)$$

$$= E_0 e^{i\omega_0 t} \left[a_0 u_0(x) (r_{cav}(0) + i\alpha \text{Re}[r_{cav}(\omega_s) e^{i\omega_s t}]) + i a_1 u_1(x) (1 + i\alpha \cos(\omega_s t)) \right] \quad (9.9)$$

The vector components of the reflected field are shown in the phasor diagram of figure 9.2(b) and (c) for an undercoupled and overcoupled cavity respectively. The side bands attenuation and phase shift will depend upon their frequency. In figure 9.2 the vectors are drawn for sidebands well outside the cavity linewidth (i.e. they receive no attenuation or phase shift on reflection from the cavity).

To determine the error signal we need to calculate the power reflected from the cavity, $P_{ref}(x)$, which is obtained by evaluating $E_{ref}^*(x) E_{ref}(x)$.

$$P_{ref}(x) = E_0^* E_0 \left[a_0^2 u_{00}^2(x) r_{cav}^2(0) + a_0^2 u_{00}^2(x) \alpha^2 \text{Re}[r_{cav}(\omega_s) e^{i\omega_s t}]^2 + a_1^2 u_{10}^2(x) + a_1^2 u_{10}^2(x) \alpha^2 \cos^2(\omega_s t) + 2 a_0 u_0(x) a_1 u_1(x) \alpha (\text{Re}[r_{cav}(\omega_s) e^{i\omega_s t}] - r_{cav}(0) \cos(\omega_s t)) \right] \quad (9.10)$$

The first line of equation (9.10) gives the average power on the detector due to the TEM₀₀ mode and its sidebands. The second line gives the power due to the TEM₁₀ which, due to an artefact of the first order approximation in figure (9.2), now appears as the sum of two terms. Recalling that this is just a phase modulated field, it is apparent that the actual power in the TEM₁₀ mode is exactly equal to $a_1^2 u_{10}^2(x)$. Equation (9.10) can be further simplified by noting $\text{Re}[r_{cav}(\omega_s)e^{i\omega_s t}] = |r_{cav}(\omega_s)| \cos(\omega_s t + \phi(\omega_s))$, where $\phi(\omega_s)$ is the phase shift on reflection from the cavity and is related to $r_{cav}(\omega_s)$ by,

$$\tan \phi(\omega_s) = \frac{\text{Im}[r_{cav}(\omega_s)]}{\text{Re}[r_{cav}(\omega_s)]} \quad (9.11)$$

After making these substitutions the reflected power becomes,

$$\begin{aligned} P_{ref}(x) = & P_0 \left[a_0^2 u_{00}^2(x) \left(r_{cav}^2(0) + \alpha^2 |r_{cav}^2(\omega_s)| \cos^2(\omega_s t + \phi(\omega_s)) \right) \right. \\ & + a_1^2 u_{10}^2(x) \\ & \left. + 2a_0 u_0(x) a_1 u_1(x) \alpha \left(|r_{cav}(\omega_s)| \cos(\omega_s t + \phi(\omega_s)) - r_{cav}(0) \cos(\omega_s t) \right) \right] \end{aligned} \quad (9.12)$$

The tilt locking error signal is proportional to the power difference on each half of the split photodetector. For these calculations we assume that the detector halves extend from $-\infty$ to zero and from zero to ∞ . This approximation is valid provided that the detector is large enough to sample the entire beam and that the gap between the two halves is negligible compared to the beam radius. The power on the left half of the detector is given by,

$$P_L = \int_{-\infty}^0 P_{ref}(x) dx \quad (9.13)$$

$$\begin{aligned} = & P_0 \left[a_0^2 \left(r_{cav}^2(0) + \alpha^2 |r_{cav}^2(\omega_s)| \cos^2(\omega_s t + \phi(\omega_s)) \right) \int_{-\infty}^0 u_{00}^2(x) dx \right. \\ & + a_1^2 \int_{-\infty}^0 u_{10}^2(x) dx \\ & \left. + 2a_0 a_1 \alpha \left(|r_{cav}(\omega_s)| \cos(\omega_s t + \phi(\omega_s)) - r_{cav}(0) \cos(\omega_s t) \right) \int_{-\infty}^0 u_0(x) u_1(x) dx \right] \end{aligned} \quad (9.14)$$

Due to the symmetry of the Hermite-Gauss modes, it follows from equation (9.5) that the first two integrals are equal to a half. The integral of the product of the two modes is equal to $-1/\sqrt{2\pi}$ which gives,

$$\begin{aligned} P_L = & P_0 \left[\frac{1}{2} a_0^2 \left(r_{cav}^2(0) + \alpha^2 |r_{cav}^2(\omega_s)| \cos^2(\omega_s t + \phi(\omega_s)) \right) + \frac{1}{2} a_1^2 \right. \\ & \left. + \sqrt{\frac{2}{\pi}} a_0 a_1 \alpha \left(|r_{cav}(\omega_s)| \cos(\omega_s t + \phi(\omega_s)) - r_{cav}(0) \cos(\omega_s t) \right) \right] \end{aligned} \quad (9.15)$$

and similarly, the power on the right half is given by,

$$\begin{aligned} P_R = & \int_0^{\infty} P_{ref}(x) dx \\ = & P_0 \left[\frac{1}{2} a_0^2 \left(r_{cav}^2(0) + \alpha^2 |r_{cav}^2(\omega_s)| \cos^2(\omega_s t + \phi(\omega_s)) \right) + \frac{1}{2} a_1^2 \right] \end{aligned} \quad (9.16)$$

$$-\sqrt{\frac{2}{\pi}}a_0a_1\alpha\left(|r_{cav}(\omega_s)|\cos(\omega_s t + \phi(\omega_s)) - r_{cav}(0)\cos(\omega_s t)\right)\Big]$$

Note that the average power is equal in equations (9.15) and (9.16) and the interference is the same but with a sign flip in the second instance. Differencing the powers on each side of the photodetector cancels the average component giving a remaining error signal of,

$$\begin{aligned} P_L - P_R &= \int_{-\infty}^0 P_{ref} dx - \int_0^{\infty} P_{ref} dx \\ &= P_0 \frac{2\sqrt{2}}{\sqrt{\pi}} a_0 a_1 \alpha \left(|r_{cav}(\omega_s)| \cos(\omega_s t + \phi(\omega_s)) - r_{cav}(0) \cos(\omega_s t) \right) \end{aligned} \quad (9.17)$$

Note that the error signal slope is proportional to P_0 . In addition, well outside the cavity bandwidth $\phi(\omega_s) \rightarrow 0$ and the error signal is proportional to the difference between the sideband reflectivity and the carrier reflectivity. Upon closer inspection of equation 9.17 it is apparent that one effect of $r_{cav}(0)$ is to reduce the signal for an undercoupled cavity ($r_{cav}(0) > 0$) and enhance it for an overcoupled cavity ($r_{cav}(0) < 0$).

9.1.1 Tilt locking signal to noise ratio

To get the signal to noise ratio where shot noise is the dominant noise source we divide equation (9.17) by the power fluctuations due to shot noise, ΔP_D given in equation 3.50.

$$\begin{aligned} \Delta P_D &= \sqrt{(P_L + P_R)h\nu} \\ &= \sqrt{P_0 h\nu} \sqrt{a_0^2 r_{cav}(0)^2 + a_1^2} \end{aligned} \quad (9.18)$$

where we have ignored the power terms due to the sidebands in equations (9.15) and (9.16). This gives the signal to noise ratio shown in equation (9.19).

$$S/N_{TL} = \frac{2\sqrt{2P_0}a_0a_1\alpha\left(|r_{cav}(\omega_s)|\cos(\omega_s t + \phi(\omega_s)) - r_{cav}(0)\cos(\omega_s t)\right)}{\sqrt{h\nu\pi}\sqrt{a_0^2 r_{cav}(0)^2 + a_1^2}} \quad (9.19)$$

Upon inspection of equation (9.19) the second effect of $r_{cav}(0)$ is apparent. The $r_{cav}(0)$ in the denominator contributes to the shot noise. The best signal to noise ratio will be obtained when the cavity is impedance matched, that is when $r_{cav}(0) = 0$. Assuming the cavity is impedance matched and also that $a_0 \approx 1$ (small amount of tilt), equation (9.19) reduces to,

$$S/N_{TL} = \sqrt{\frac{2}{\pi}} \sqrt{\frac{P_0}{h\nu}} 2\alpha |r_{cav}(\omega_s)| \cos(\omega_s t + \phi(\omega_s)) \quad (9.20)$$

Equation 9.20 shows that the signal to noise ratio of tilt locking is proportional to the magnitude of the cavity reflectivity for the sidebands. It makes sense that if the sidebands are attenuated (due to loss or transmission in the cavity) they cannot be as efficiently read out. It is only the magnitude of the sideband reflectivity which determines the signal level as any phase shift will be equal and opposite for the positive and negative sidebands. This ensures that phase modulation symmetry is maintained. The net result is a phase shift of the measured signal by an amount $\phi(\omega_s)$. One important conclusion is that to

measure quantum phase noise down to very low frequencies a low corner frequency of the cavity reflectivity is needed. The corner frequency can be reduced by increasing either the finesse or the length of the cavity. Conversely, for phase signals at frequencies large compared to the cavity linewidth, increasing the cavity finesse provides no advantage, as the shot noise limit has already been reached.

9.1.2 Quantum efficiency

We now consider the signal to noise ratio with which we can measure a signal at the quantum noise level, namely quantum phase noise. We will only treat the impedance matched case here. In section 3.2, we showed that for a coherent state with n photons, the level of frequency independent phase fluctuations is given by,

$$\Delta\phi_{QNL} = \frac{1}{2\sqrt{n}} \quad (9.21)$$

If we make the substitution $\alpha \cos(\omega_s t) = \Delta\phi_{QNL}$ into equation 9.1 and repeat the above analysis equation (9.20) becomes,

$$S/N_{TL} = \sqrt{\frac{2}{\pi}} \sqrt{\frac{P_0}{h\nu}} \frac{1}{\sqrt{n}} |r_{cav}(\omega_s)| \quad (9.22)$$

where we have ignored the phase shift, ϕ , as this does not effect the magnitude of the signal. Realising that $P_0/h\nu = n$, the signal to noise ratio with which we can measure quantum phase noise is,

$$S/N_{TL} = \sqrt{\frac{2}{\pi}} |r_{cav}(\omega_s)| \quad (9.23)$$

Recall that for frequencies large compared to the cavity linewidth $r_{cav}(\omega_s) \rightarrow 1$, and so in principle, tilt locking is able to measure quantum noise limited signals with a signal to noise ratio of $\sqrt{2/\pi}$, or approximately 80%.

Intuitively, we might expect the system to be 100% efficient at measuring quantum phase noise. The source of inefficiency is the imperfect interference between the TEM_{00} and TEM_{10} modes, which introduces the factor of $\sqrt{2/\pi}$.

$$\int_{-\infty}^{\infty} u_{00}^2(x) u_{10}^2(x) dx = \frac{2}{\pi} \quad (9.24)$$

Although the efficiency of the signal is not perfect, the interference of the noise is, as each spatial mode contains its own noise. In order to increase the efficiency of the interference we need to use the special *flipped* mode (see figure 3.5 and equation 3.38), which is a field that is equal in magnitude to the TEM_{00} but with a sign flip at $x = 0$. This mode, or sum of modes, interferes with the TEM_{00} mode with unit efficiency as measured by a split photodiode. Thus the signal to noise ratio is degraded slightly. This flipped mode is difficult to produce in practice, and difficult to use due to the dispersion of the higher order modes.

9.2 Pound-Drever-Hall locking sensitivity

For comparison we perform the same calculation for the Pound-Drever-Hall locking technique. This derivation is similar to that performed by Day *et al.* [107] except that we include nonstationary (or cyclo-stationary) shot noise [108] in the analysis.

Once again we begin with an input field with broadband phase modulation sidebands (see equation (9.1)). This field passes through a phase modulator which adds modulation sidebands at frequency ω_m [radians/second] with a modulation depth of δ [radians].

$$\begin{aligned} E_{inc} &= E_0 e^{i\omega_0 t} e^{i\alpha \cos(\omega_s t)} e^{i\delta \cos(\omega_m t)} \\ &= E_0 e^{i\omega_0 t} (1 + i\alpha \cos(\omega_s t)) (1 + i\delta \cos(\omega_m t)) \end{aligned} \quad (9.25)$$

We multiply the incident field by the complex reflectivity of the cavity. We assume that the modulation frequency is much larger than the cavity linewidth which means that these sidebands reflect off the cavity unchanged.

$$E_{ref} = E_0 e^{i\omega_0 t} \left(r_{cav}(0) + i\alpha |r_{cav}(\omega_s)| \cos(\omega_s t + \phi(\omega_s)) + i\delta \cos(\omega_m t) - \alpha\delta \cos(\omega_s t) \cos(\omega_m t) \right) \quad (9.26)$$

The total power detected is again given by $E_{ref}^* E_{ref}$. For simplicity, we assume that we have an impedance matched cavity ($r_{cav}(0) = 0$).

$$\begin{aligned} P_{ref} &= P_0 \left[\alpha^2 |r_{cav}(\omega_s)|^2 \cos^2(\omega_s t + \phi(\omega_s)) + \delta^2 \cos^2(\omega_m t) - \alpha^2 \delta^2 \cos^2(\omega_s t) \cos^2(\omega_m t) \right. \\ &\quad \left. + 2\alpha\delta |r_{cav}(\omega_s)| \cos(\omega_s t + \phi(\omega_s)) \cos(\omega_m t) \right] \end{aligned} \quad (9.27)$$

The terms in the top line are the power of the individual sidebands. The first and last terms of this line can be neglected as the phase signal (at ω_s) is much smaller than our imposed modulation at ω_m . Thus $\alpha \ll \delta$ and equation (9.27) becomes,

$$P_{ref} = P_0 \left[\delta^2 \cos^2(\omega_m t) + 2\alpha\delta |r_{cav}(\omega_s)| \cos(\omega_s t + \phi(\omega_s)) \cos(\omega_m t) \right] \quad (9.28)$$

The first term is the power of the modulation sidebands and the second term is the interference containing our signal. The detected power is now mixed down by multiplying by $\cos(\omega_m t)$. In calculating the signal at the mixer output, S we only consider terms near ω_m as only these will be mixed down to baseband.

$$\begin{aligned} S &= P_{ref} \times \cos(\omega_m t) \\ &= P_0 2\alpha\delta |r_{cav}(\omega_s)| \cos(\omega_s t + \phi(\omega_s)) \cos^2(\omega_m t) \end{aligned} \quad (9.29)$$

But $\cos^2(\omega_m t) = 1/2 + 1/2 \cos(2\omega_m t)$ so we can rewrite equation (9.29) as,

$$S = P_0 \delta |r_{cav}(\omega_s)| \alpha \cos(\omega_s t + \phi(\omega_s)) + \text{higher frequency terms} \quad (9.30)$$

The mixer output is typically low pass filtered to remove the higher frequency terms.

9.2.1 Pound-Drever-Hall signal to noise ratio

Calculating the true noise floor for the Pound-Drever-Hall system is a little more complicated as the detected power (and thus shot noise) is fluctuating at $2\omega_m$ due to beating of the phase modulation sidebands. This beating is sampled by the demodulation in such a way that it is over represented at the output of the mixer.

In the absence of a signal ($\alpha = 0$) the reflected power is,

$$P_{ref} = P_0 \delta^2 \cos^2(\omega_m t) \quad (9.31)$$

To calculate the shot noise due to this power we will work in terms of noise variances. The variance of the power $(\Delta P)^2$ for a coherent state is equal to $\langle h\nu P \rangle$, thus

$$(\Delta P_{ref})^2 = \langle h\nu P_0 \delta^2 \cos^2(\omega_m t) \rangle \quad (9.32)$$

The variance of the mixer output can be determined by,

$$\begin{aligned} (\Delta S)^2 &= \langle h\nu P_0 \delta^2 \cos^2(\omega_m t) \times \cos^2(\omega_m t) \rangle \\ &= \langle h\nu P_0 \delta^2 \cos^4(\omega_m t) \rangle \\ &= h\nu P_0 \delta^2 \left\langle \left(\frac{1}{2} + \frac{1}{2} \cos(2\omega_m t) \right) \left(\frac{1}{2} + \frac{1}{2} \cos(2\omega_m t) \right) \right\rangle \\ &= \frac{h\nu P_0 \delta^2}{4} \left\langle \left(1 + \frac{1}{2} + 2 \cos(2\omega_m t) + \frac{1}{2} \cos(4\omega_m t) \right) \right\rangle \\ &= \frac{h\nu P_0 \delta^2}{4} \left(\frac{3}{2} + 2 \langle \cos(2\omega_m t) \rangle + \frac{1}{2} \langle \cos(4\omega_m t) \rangle \right) \\ (\Delta S)^2 &= \frac{3h\nu P_0 \delta^2}{8} \end{aligned} \quad (9.33)$$

$$\Rightarrow \Delta S = \frac{\sqrt{3}}{2\sqrt{2}} \delta \sqrt{h\nu P_0} \quad (9.34)$$

Thus the signal to noise with which our phase signal can be measured is,

$$S/N_{PDH} = \sqrt{\frac{2}{3}} \sqrt{\frac{P_0}{h\nu}} 2|r_{cav}(\omega_s)| \alpha \cos(\omega_s t + \phi(\omega_s)) \quad (9.35)$$

This should be compared to equation 9.20 for the tilt locking case.

9.2.2 Pound-Drever-Hall quantum efficiency

The quantum efficiency of the Pound-Drever-Hall locking can be calculated by substituting $\Delta\phi_{QNL}$ (see equation 9.21) for $\alpha \cos(\omega_s t)$. After making this substitution, and again ignoring the phase shift, $\phi(\omega_s)$, we arrive at the signal to noise with which we can measure shot noise,

$$S/N_{PDH} = \sqrt{\frac{2}{3}} |r_{cav}(\omega_s)| \quad (9.36)$$

The source of the inefficiency here is the nonstationary shot noise. This can be overcome to some extent by using more complicated modulation; however, doing so is often impractical as phase modulators have a finite bandwidth and are often unable to produce the required higher harmonics.

Comparing equation (9.36) with the same expression for tilt locking in equation (9.23)

we can see that they are of the same form except that tilt locking is a factor of $\sqrt{\frac{3}{\pi}} \approx 0.98$ lower in quantum efficiency than the Pound-Drever-Hall technique corresponding to an absolute difference of only 2%.

9.3 Summary

We have calculated the shot noise limited sensitivity of tilt locking for a measurement of broadband phase sidebands. Tilt locking is comparable to PDH in this regard with a difference in sensitivity between the two techniques of approximately 2%. Both techniques are able to measure a signal at the quantum noise level with a signal to noise ratio of approximately 0.8. In the case of the PDH technique this inefficiency arises from nonstationary shot noise, whereas tilt locking suffers from inefficient interference of the TEM_{00} and TEM_{10} modes.

Applications of tilt locking

This chapter describes three experiments which investigate the performance of tilt locking in three different applications: laser frequency stabilisation, control of a continuous-wave second harmonic generator and control of an injection locked laser.

10.1 Laser frequency stabilisation

Aside from gravitational wave detection, laser frequency stabilisation is required for a wide range of scientific applications from high-resolution spectroscopy [109] to fundamental tests of special relativity [110]. Increasingly, short term frequency stability is important in commercial applications, for example, in coherent lidar systems [111].

The aim of this experiment was to determine the performance limits of tilt locking for the purpose of locking a laser to an optical cavity. One approach would be to have two independent systems (i.e. two lasers stabilised independently to respective optical cavities), interfere the lasers and measure the stability of the beat note (see for example Sampas *et. al.* [112]). The problem with such an approach is that cavity length fluctuations may limit the stability thus revealing nothing about the performance of tilt locking. With two independent systems it is difficult to distinguish between beat frequency fluctuations due to the locking system and frequency fluctuations originating from changes in the cavity length. For example if one of the cavities changes in length by an amount ΔL , the beat frequency, ν_B will change by,

$$\Delta\nu_B = \frac{\Delta L}{L}\nu \quad (10.1)$$

where L is the cavity length, and ν is the optical frequency of the laser. If a laser frequency stability of 10 Hz is required, then we must ensure that the cavity's fractional length fluctuations are kept below a level of 3×10^{-14} (assuming $\lambda = 1 \mu\text{m}$). This is a very difficult task, particularly over long time scales even with the use of ultra low expansion (ULE) glass ceramic or cryogenic sapphire cavities [113, 114]. To maintain this degree of length stability over shorter times requires placing the cavity in vacuum for acoustic isolation, and usually some form of vibration isolation.

By locking two lasers to the same cavity [107, 115] the sensitivity to cavity length variations can be substantially reduced. For example, if we lock two lasers at optical frequencies ν_1 and ν_2 , any length change ΔL in the cavity will induce a change in the

optical frequencies of

$$\Delta\nu_1 = \frac{\Delta L}{L}\nu_1 \quad (10.2)$$

$$\Delta\nu_2 = \frac{\Delta L}{L}\nu_2 \quad (10.3)$$

The change in the beat frequency will be given by,

$$\Delta\nu_B = \Delta\nu_1 - \Delta\nu_2 \quad (10.4)$$

$$= \frac{\Delta L}{L}\nu_1 - \frac{\Delta L}{L}\nu_2 \quad (10.5)$$

$$= \frac{\Delta L}{L}\nu_B \quad (10.6)$$

Comparing equations 10.1 and 10.6 it is clear that by locking both lasers to the same cavity the fluctuations in the beat frequency originating from cavity length variations have been suppressed by a factor of ν_B/ν . For a beat frequency of 500 MHz this reduces the requirements on optical cavity length stability down to a fractional length fluctuation of 2×10^{-8} in order to achieve a beat frequency stability of 10 Hz (an improvement by a factor of $\approx 10^6$).

In order to simultaneously lock two lasers to one cavity it is necessary to produce two error signals that are somewhat independent. With modulation techniques this can be achieved by using a different modulation/demodulation frequency for each laser. One approach which can be employed with tilt locking is to use a horizontal tilt on the first laser and a vertical tilt on the second. Using a quadrant photodiode, the TEM_{01} and TEM_{10} interference can be distinguished by observing the horizontally subtracted and vertically subtracted detector outputs respectively, as illustrated in figure 10.1

As discussed in section 8.4, double pass tilt locking can be employed to minimise the effects of beam jitter on the locking stability. The basic form of double pass tilt locking cannot be used to selectively provide horizontal and vertical tilt respectively to the two lasers as both beams reflect off the same retro-reflector and thus receive the same tilt. However, just as tilting a TEM_{00} excites a TEM_{10} mode, so too does tilting a TEM_{10} mode excite a TEM_{00} . To distinguish between the error signals we locked one laser to the TEM_{10} mode and the other to the TEM_{01} mode resonance. We aligned the input beams so that the power in the TEM_{10} mode was maximised for the first laser and the TEM_{01} was maximised for the second. The retro-reflector was tilted in both the vertical and horizontal directions. As seen by one laser, the horizontal tilt excited a small component of the TEM_{00} , whilst the vertical tilt caused a small amount of the TEM_{11} mode to be present. For the second laser the horizontal tilt excited a component of the TEM_{11} whilst the vertical tilt excited the fundamental TEM_{00} mode. Neither TEM_{00} mode was resonant and so they were reflected from the cavity on the second pass, serving as a local oscillators for their respective resonant TEM_{10} or TEM_{01} modes. There was a small amount of cross coupling between the error signals¹ due to the interference of the resonant modes and higher order spatial modes, but the effect did not substantially degrade the locking performance. Because we were using a ring cavity, the TEM_{10} and TEM_{01} modes were not degenerate (i.e. did not have different resonant frequencies) which allowed us to lock the

¹That is the vertical output contained a small error signal for laser 1 and the horizontal output contained a small error signal for laser 2.

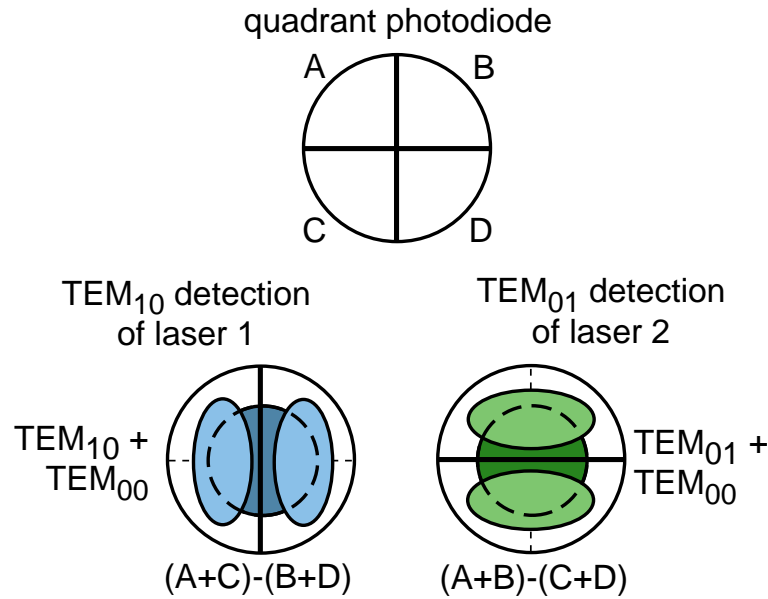


Figure 10.1: The quadrant photodiode layout to detect the first higher order modes of the two lasers. The photodetector has three outputs, a sum output $(A+B+C+D)$, a horizontal error signal output $(A+C)-(B+D)$ and a vertical error signal output $(A+B)-(C+D)$.

two lasers with a frequency separation of less than the free spectral range. This ensured that the ratio, ν_B/ν was kept to a minimum and in doing so gave maximum isolation against cavity length changes.

The dominant technical noise source associated with tilt locking is thought to be mechanical vibrations of the cavity and photodetector. This raises the concern that by locking the lasers to the same cavity with the same detector the error due to vibrations will also be correlated. If this is the case then an analysis of the beat note stability will give an overly optimistic estimate of the stability of the tilt locking system. This is unlikely to occur in this system as the two error signals are obtained from perpendicular axes and therefore any mechanical vibrations will be uncorrelated.

10.1.1 The experiment

The experimental set up for the beat note measurement is shown in figure 10.2. Laser 1 had an output power of 400 mW (InnoLight Mephisto 400), and laser 2 had an output power of 200 mW (Lightwave Electronics 122). Each laser passed through a Faraday isolator and a waveplate with a polarising beamsplitter to control the power incident on the cavity. The optical cavity was a ring cavity with a finesse of 4100 for s-polarised light (200 for p-polarised light). The waveplate in front of the ring cavity was used to control the input polarisation thereby allowing operation of the experiment with either finesse. The free spectral range of the cavity was approximately 700 MHz with a difference in frequency between the TEM₁₀ and TEM₀₁ modes of 356 MHz. The 356 MHz beat note was detected before the optical cavity on a high speed photodetector [86] at the unused port of the beamsplitter which combined the two lasers. This beat note was sent to a frequency counter (Stanford Research Systems 620) connected to a data logging computer

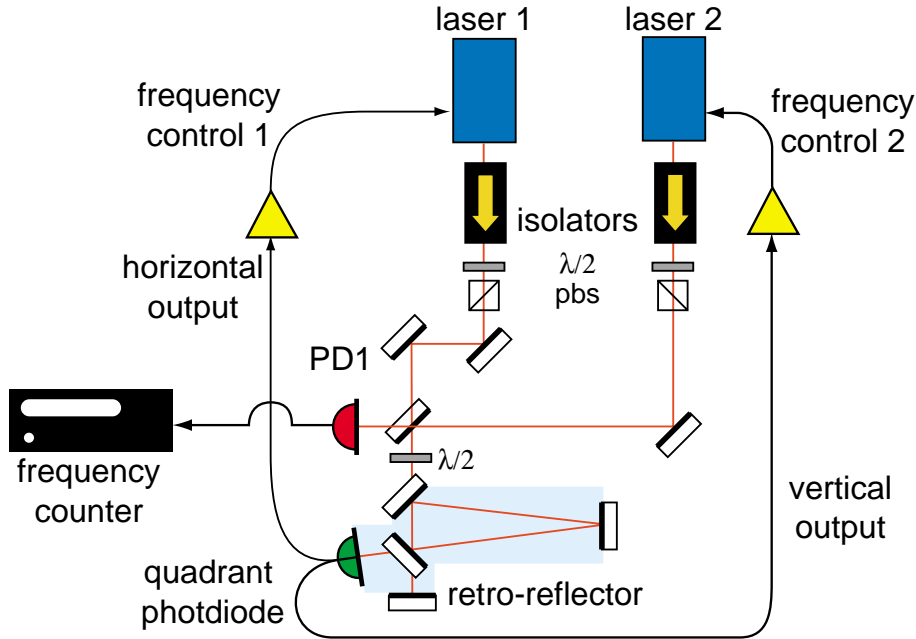


Figure 10.2: Experimental layout for tilt locking two lasers to one cavity. The beat note is monitored on PD1. Subtraction circuits are not shown for simplicity.

or to an RF spectrum analyser (Hewlett-Packard 8568B).

To minimise the effects of laboratory temperature changes the cavity mirrors were clamped to a triangular invar spacer. The retro-reflecting mirror and quadrant photodiode were housed in another invar block which was bolted directly to the cavity spacer. The four quadrants of the photodiode were individually amplified and the horizontally subtracted and vertically subtracted outputs were obtained for feedback along with the sum output for monitoring.

10.1.2 Results

Figure 10.3 shows the beat note measured on the spectrum analyser. The 3 dB linewidth of the beat note was found to be 13 Hz with the spectrum analyser set to its minimum resolution bandwidth of 10 Hz. If we assume that the RBW filter and the linewidth are both Gaussian, then we can calculate the actual beatnote linewidth from equation 10.7 [32].

$$a = \sqrt{b^2 - c^2} \quad (10.7)$$

where a is the linewidth of the beatnote, b is the measured beatnote linewidth, and c is the RBW. This gives a beatnote linewidth of approximately 8.3 Hz. Ignoring the common mode noise of the two lasers and assuming that both lasers contribute equally to the linewidth of the beatnote, this gives an individual laser linewidth of 5.9 Hz.

To quantify the frequency stability over longer time scales we use the Allan deviation [116, 117]. The Allan deviation is a statistical measure of the variation of a parameter, typically frequency, as a function of the time scale of the fluctuations. It has the advantage that as the measurement time increases the Allan deviation converges whereas the standard deviation may diverge for many practical oscillators.

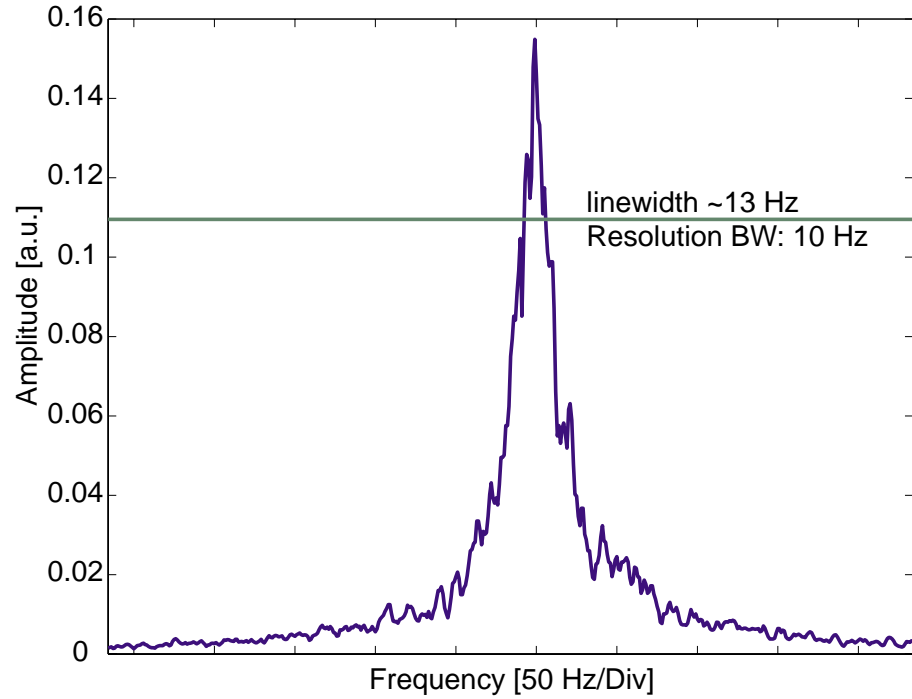


Figure 10.3: The frequency spectrum of the amplitude of the beat note between the two lasers.

Consider a measurement where the frequency of the beat note, f , is recorded M times at regular intervals of τ_0 . From this data we can calculate the Allan deviation at times $\tau = n\tau_0$ where n is an integer number² and $n \leq (M - 1)$. This provides us with a discrete set of frequency measurements, $f_1, f_2, f_3 \dots$. From this data we can calculate the Allan deviation, $\sigma_f(\tau)$, from equation 10.8.

$$\sigma_f(\tau) = \sqrt{\frac{1}{2(M-1)} \sum_{i=1}^{M-1} (f_{i+1} - f_i)^2} \quad (10.8)$$

It is customary for the Allan variance to be dimensionless as it is calculated using the fractional frequency change. The units of σ_f in equation 10.8 will be in Hertz as we have used the absolute frequency change. This was deliberate as we are not interested in the fractional beat note stability, but in the fractional stability of the tilt locking system. To infer this we need to divide the absolute Allan deviation (in Hertz) by the optical frequency of the lasers. If instead, we had used the fractional frequency change in equation 10.8, the factor of ν_B/ν mentioned earlier would be ignored.

Figure 10.4 shows the results of two separate measurements of the beat note with $\tau_0 = 2$ seconds and $\tau_0 = 100$ milliseconds. Sampling times of less than 100 ms were not possible due to limitations of the data acquisition system. An Allan deviation of less than 4 Hz was achieved for a time scale of 100 ms. Ignoring common mode changes in the laser frequencies, this is equivalent to a fractional Allan deviation of approximately 1.3×10^{-14} . The stability of the beat note decreases for longer time scales, to give an Allan

²In practice, $n \ll M$ to ensure that enough data points are taken for the Allan deviation to converge.

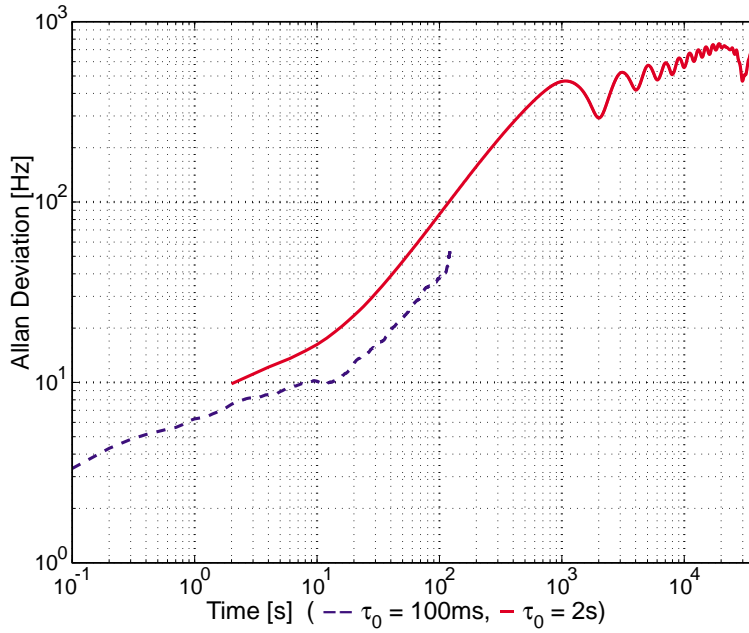


Figure 10.4: The Allan deviation of the absolute frequency change of the beat note.

deviation of 2×10^{-12} over 10000 seconds.

Despite locking both lasers to the same cavity, the cavity length fluctuations still remain the dominant source of error. Subsequent measurements of the temperature of the laboratory confirm thermal expansion of the cavity as the main source of noise over time scales of a few seconds and longer. We believe that the stability over shorter time scales is limited by acoustically or mechanically induced length changes. Recall that this experiment was performed in air with no temperature stabilisation or acoustic isolation whatsoever. In the near future the system will be put into vacuum on a suspension system. This should dramatically reduce geometric fluctuations in the cavity and further increase stability.

10.1.3 Summary

Double pass tilt locking has been used to lock two independent lasers to separate spatial modes of a ring cavity. The technique was found to produce a beatnote linewidth of approximately 8 Hz, with an Allan deviation of 3.3 Hz at 100 ms. Ignoring common mode errors between the lasers, this gives a laser linewidth of less than 6 Hz and an Allan deviation of 1.3×10^{-14} at 100 ms. Moreover, the frequency stability of the beat note is limited by the fluctuations in the length of the cavity and not the performance of tilt locking.

10.2 Second harmonic generator

Second harmonic generation provides powerful coherent radiation at wavelengths other than those of laser transitions. It relies on the $\chi^{(2)}$ nonlinearity of a medium which is in

general very small, thus very high fundamental intensities are required to obtain reasonable conversion efficiencies. In continuous-wave second harmonic generation this high intensity can be obtained by placing the nonlinear medium inside an optical resonator [118]. In order to successfully control the cavity resonance, an error signal must be produced which is proportional to the difference between the laser frequency and the cavity resonance. In this section, we present successful second harmonic generation by the use of tilt locking and compare the performance with that of the PDH technique. In particular we investigate the maximum power, stability and spectral purity of the 532 nm second harmonic of 1064 nm light from a Nd:YAG laser.

10.2.1 The experiment

Our experimental set up is shown in figure 10.5. The second harmonic generator (SHG) was a hemilithic cavity consisting of a $5 \times 7.5 \times 2.5$ mm MgO:LiNbO₃ nonlinear crystal and an output coupler with 94%/4% reflectivity at 1064/532 nm. The back surface of the crystal had a ROC of 10 mm and was harmonically coated for high reflectance ($R > 99.96\%$) for both wavelengths and the front crystal surface was polished flat and AR coated at both wavelengths ($R < 0.1\%$). The output coupler had a radius of curvature of 25 mm. It was placed 23.1 mm from the front surface of the crystal, forming a $27 \mu\text{m}$ waist for the 1064 nm light within the crystal. This nonlinear crystal was pumped with a LZH continuous-wave Nd:YAG laser with a maximum output power of 700 mW at 1064 nm. The combination of a half and a quarter wave plate controlled the polarisation of the fundamental beam and a Faraday isolator prevented retro-reflection back to the laser. A small fraction of the fundamental power was monitored on a photodetector. The remaining fundamental beam was focussed into the SHG with a combination of two lenses and aligned with a beam steerer.

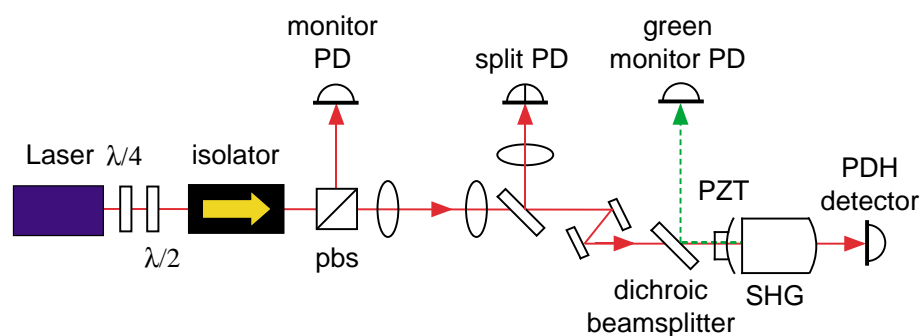


Figure 10.5: Experiment layout for external cavity second harmonic generation.

For tilt locking, a small amount of tilt was introduced to the pump beam using the beam steerer just before the SHG cavity. Note that this does not affect the SHG output direction as this is determined by the SHG cavity mode only. For the purpose of PDH locking, we made use of the electro-optic properties of the MgO:LiNbO₃ crystal to produce phase modulated sidebands on the fundamental beam. The transmitted fundamental beam was detected and demodulated to produce the necessary error signal. Although this is strictly speaking a transmission locking system, the differences between detecting the beam on reflection and transmission in this particular set up are unimportant and we

will refer to the system as PDH locking. In order to obtain an error signal for tilt locking, a pellicle was used to removed a small amount of the reflected fundamental radiation which was detected and analysed by the split photodiode. The second harmonic light was extracted from the reflected beam by a dichroic mirror with high reflection at 532 nm placed immediately in front of the nonlinear crystal and detected by the green monitor photodiode.

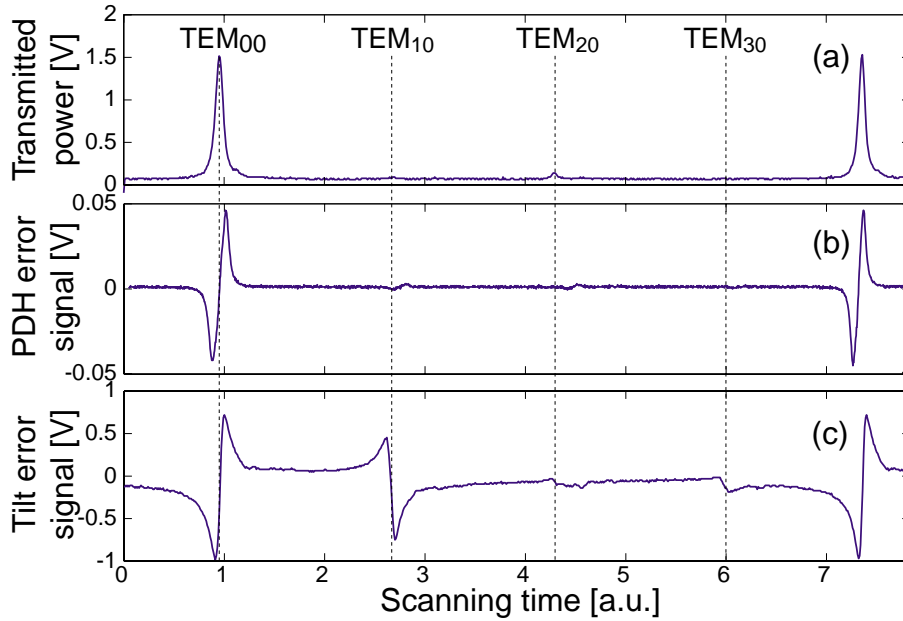


Figure 10.6: Power and error signals recorded as the SHG cavity length was scanned, showing (a) transmitted fundamental power, (b) PDH error signal and (c) tilt locking error signal.

10.2.2 Error signals

Fig. 10.6(a) shows the transmitted intensity of the fundamental beam, (b) the PDH error signal and (c) the tilt locking error signal as the SHG cavity was scanned using the input coupler PZT. Note that the error signals were not recorded simultaneously; there was no modulation during the tilt locking measurement and no deliberate tilt during the PDH measurement. We note that an extremely small amount (just visible in figure 10.6(a)) of the TEM₁₀ mode is sufficient to generate a large error signal and to facilitate tilt locking. The TEM₂₀ mode, however, is present only due to the imperfect mode-matching of our frequency doubler. Whilst in PDH locking a useful error signal is only produced from the TEM₀₀ mode, tilt locking generates large error signals for both the TEM₀₀ and TEM₁₀ modes as well as a smaller error signal for TEM₃₀. We observe that the error signal for tilt locking is much broader than that for PDH locking. This increases the capture range of the locking system. Furthermore, the tilt locking error signal is well over an order of magnitude larger than that obtained using PDH locking. This can be an advantage if electronic noise in the servo systems is significant.

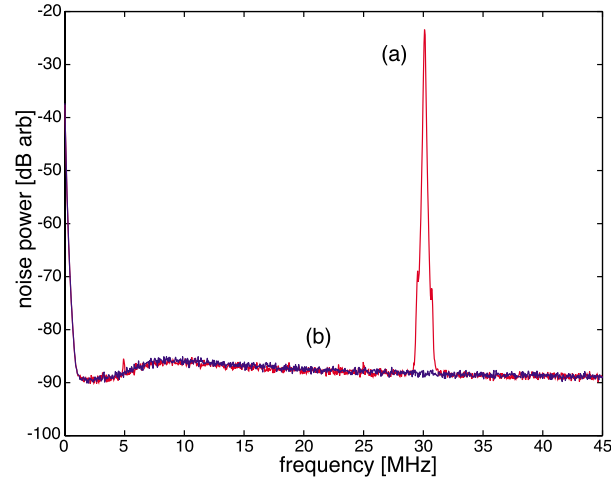


Figure 10.7: Second harmonic amplitude spectra from (a) PDH and (b) tilt locking.

10.2.3 Second harmonic output spectra

Figure 10.7 shows the second harmonic amplitude spectra obtained from PDH and tilt locking. The low frequency features are due to the roll off of the photodetector electronics and the noise of the pump laser. The >60 dB spike at 30 MHz observable in the PDH locking spectrum is a direct result of the modulation of the crystal required to obtain an error signal and is believed to be due to sum frequency generation between the carrier and the sidebands. The tilt locking spectra exhibits no such noise spikes. Aside from the noise features associated with the modulation the two spectra are indistinguishable. Thus tilt locking is preferable for applications that rely on high spectral purity such as spectroscopy [119–122] and precision interferometry.

10.2.4 System stability

We used several measures to quantify the stability of the PDH and tilt locking techniques in our system. Table 10.1 gives a comparison of some PDH and tilt locking parameters for a measurement period of 100 minutes.

The average second harmonic power \bar{P}_G and standard deviation σ_{P_G} are often the most critical parameters in many applications. In our set up, we obtained identical average second harmonic output power for the two techniques, with 420 mW produced from 650 mW of IR. The standard deviation of the power is also very similar at 1.05% and 1.06% for PDH and tilt locking, respectively. The majority of the fluctuations can be directly attributed to the long term fluctuations in the IR pump power ($\sigma_{P_{IR}} = 1.05\%$ and 1.10% for PDH and tilt locking runs respectively), mostly due to a 12 minute cycle of the laboratory air conditioning. After normalising to the long term drift of the pump power, the standard deviation of the green power, $\sigma_{P_{G'}}$ produced using PDH and tilt locking was inferred to be 0.65% and 0.7%, respectively. Another significant factor contributing to this fluctuation was the temperature stability of the nonlinear crystal. In our experiment, the crystal oven was controlled at $\approx 108^\circ\text{C}$ (for phase matching) with an accuracy inferred from a thermistor readout of $\pm 0.002^\circ\text{C}$. However, this does not guarantee a similar temperature stability at the crystal core. Crystal core temperature fluctuations alter

<i>Parameters</i>	<i>PDH-locked</i>	<i>Tilt-locked</i>
P_{IR} (mW)	650 ± 5	650 ± 5
$\sigma_{P_{\text{IR}}} (\%)$	1.05 ± 0.05	1.10 ± 0.05
P_{G} (mW)	420 ± 5	420 ± 5
$\sigma_{P_{\text{G}}} (\%)$	1.05 ± 0.05	1.06 ± 0.05
$\sigma_{P_{\text{G}'}} (\%)$	0.65 ± 0.05	0.70 ± 0.05
$\bar{\varepsilon} (\%)$	0.21 ± 0.02	0.25 ± 0.02
$\sigma_{\varepsilon} (\%)$	0.74 ± 0.05	0.80 ± 0.05
Locking stability (mrad)	0.61 ± 0.05	0.67 ± 0.05
$r_{\text{cav}}(P_{\text{G}} : \varepsilon^2)$	-0.06 ± 0.03	-0.15 ± 0.03

Table 10.1: Stability parameters of the second harmonic generator locked using both PDH and tilt locking.

the phase matching conditions and this results in corresponding fluctuations in second harmonic power.

A more direct measure of locking stability can be obtained from the analyses of the error signals of the two techniques. One error signal is used to lock the SHG cavity (referred to as the locking error signal) and the other error signal is used to monitor the performance (referred to as the monitor error signal). If we observe the monitor error we can determine the difference between the two techniques and also check for any correlations with the second harmonic power. For the remaining results in table 10.1 measurements are presented for the monitor error signal.

The mean of the unused error signal, $\bar{\varepsilon}$, gives an indication of the relative long term performance of the two techniques. A value of 100% represents a whole peak-to-peak error (see Fig. 10.6) corresponding to the cavity full width half maximum (FWHM). The average error signal is found to be +0.21% and +0.25% of the FWHM for PDH and tilt locking respectively. This suggests that both techniques agree quite well as to the position of the cavity resonance. Ideally, we would expect the mean of the PDH to be the negative of the mean of the tilt locking error signal. The fact that they are the same sign and approximately the same size suggests that the non-zero mean arises not from the error signal generation but from an offset in the frequency locking servo.

The standard deviation of the two error signals was found to be 0.74% and 0.80% of the peak to peak error signal value for PDH and tilt locking, respectively. As the peak values of the error signal occur at the cavity linewidth, multiplying by the hot cavity linewidth (≈ 100 MHz) converts this to an absolute locking stability of 740 kHz for PDH and 800 kHz for tilt locking. These may appear large, however they are a consequence of the relatively low finesse (≈ 37) and large free spectral range (3.80 GHz) of the SHG cavity. The locking stability in terms of round trip cavity phase was 0.61 mrad and 0.67 mrad, respectively.

The last parameters investigated are the correlation coefficients between the error signals and the second harmonic output power. Correlation existing between these quantities would indicate poor locking quality of the scheme under interrogation. For example, if the system is tilt locked and the PDH error signal shows strong correlations with the second harmonic output power, then it could be concluded that the PDH error signal represents a better error measure of the resonance of the SHG cavity.

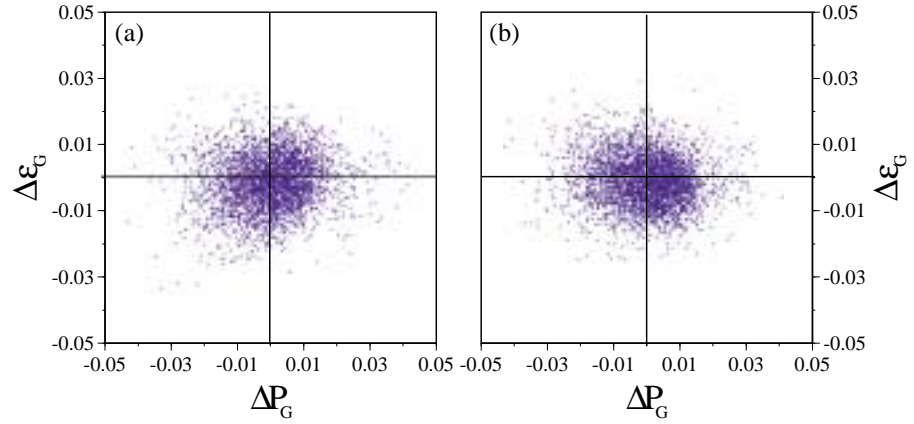


Figure 10.8: Green output power fluctuations versus error signals (a) Tilt-locked PDH signal and (b) PDH-locked Tilt signal.

The cavity transmission peak of the second harmonic output is a Lorentzian which can be approximated by a quadratic function near resonance. The error signals, however, are linear near resonance as shown in figure 10.6. Thus we compare the transmitted second harmonic power P_G with the square of the unused error signal, ε^2 . This results in a linear correlation between the two quantities, where a small correlation coefficient implies good locking performance.

The correlation coefficients of the output green power with the square of the error signal are -0.06 and -0.15, respectively for PDH and tilt locked runs. As expected, the correlations are negative as the error signals are minimised when the green power is at a maximum. Although the PDH system shows a slightly smaller correlation than the tilt locking system, we believe that for most practical applications the difference is negligible.

If the cavity were locked substantially away from resonance there would be a linear correlation between the monitor error signal, ε , and the second harmonic power fluctuations, ΔP_G . Figure 10.8 shows scatter diagrams for fluctuating green power and error signals. Neither locking scheme exhibits any measurable correlation between the monitor error signal and the second harmonic output power.

10.2.5 Summary

Tilt locking was shown to provide performance comparable to that of PDH locking for the control of continuous-wave second harmonic generation. The average second harmonic power and standard deviation produced by the two techniques were identical to within the experimental errors. One major advantage of the tilt locking technique is the absence of the modulation peak in the RF spectrum of the second harmonic output.

10.3 Injection locking

In this section we describe an experiment carried out with researchers at the University of Adelaide to injection lock a medium power slave laser with the use of tilt locking. Injection locking [93, 123] is a commonly used technique to transfer the frequency stability

of a stable, single mode, low power laser (the master), to a medium or high power laser (the slave) [124]. By injection locking the slave laser can be made uni-directional, and to oscillate in a single spatial and longitudinal mode. Injection locking requires the master laser to be resonant with the slave laser cavity, which generally involves obtaining a Pound-Drever-Hall type error signal and feeding back to a length actuator on the slave laser cavity. In this experiment, we demonstrate the use of tilt locking to lock the slave laser cavity to the master laser and compare its performance to that achieved with the PDH technique.

10.3.1 The experiment

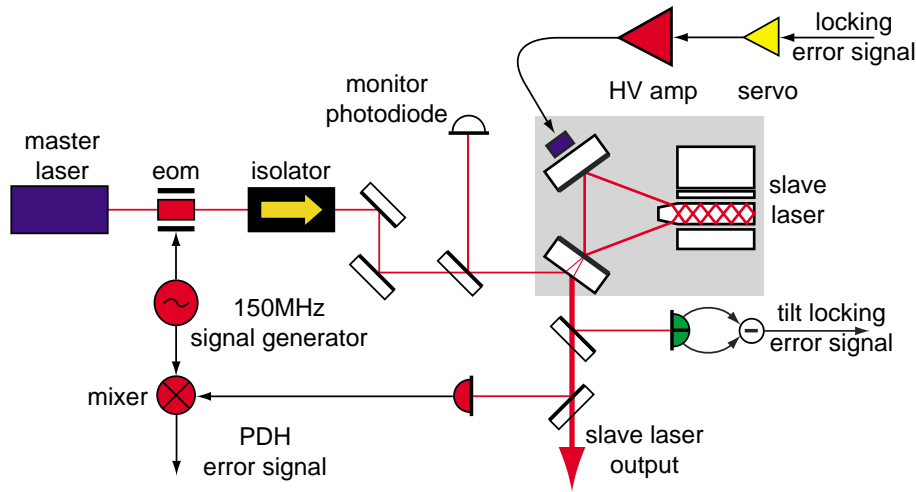


Figure 10.9: Experimental layout for injection locking experiment showing apparatus to simultaneously obtain both tilt locking and PDH error signals. Either error signal can be used to lock the slave laser cavity to the master laser.

The experiment was set up so that the tilt locking and PDH error signals could be produced simultaneously as shown in figure 10.9. The master laser is a LZH model 450 NPRO. The slave laser has a free spectral range of approximately 2 GHz, and is capable of producing 5 W of diffraction-limited TEM₀₀ output when pumped with a single 20 W laser diode array. For more details regarding the slave laser see Ottaway *et al.* [123]. For this experiment we chose to operate the slave laser at an output power of 3 W. Although injection locking is used to enforce uni-directional operation of the slave laser, a high power isolator is still necessary to protect both the electro-optic modulator and the master laser from optical damage when the slave laser is free running. The injection locking system was operated with 100 mW incident on the slave laser cavity. The monitor photodiode senses the power in the reverse direction of the slave laser cavity. This power drops to zero when the slave laser is injection locked.

The PDH system uses a modulation frequency of 150 MHz with a high speed photodetector at a tap off on the slave laser output. The tilt locking error signal was produced by slightly tilting the master in the vertical axis due to the lower levels of slave laser beam jitter exhibited in this axis. A quadrant photodiode situated at a second tap off was used to produce the tilt locking error signal.

To provide the most robust servo and minimise noise the zero-crossing of the error signal should correspond to the center of the injection locking range of the slave laser. Thus the alignment of the master laser beam, slave laser resonator and detector must be carefully adjusted. We do this by initially aligning the master laser beam and the beam from the free running slave laser and then ensuring that the quadrant photodetector is centred on the output of the injection locked laser. The master laser beam is then tilted and its position (height) adjusted until the error signal is symmetric.

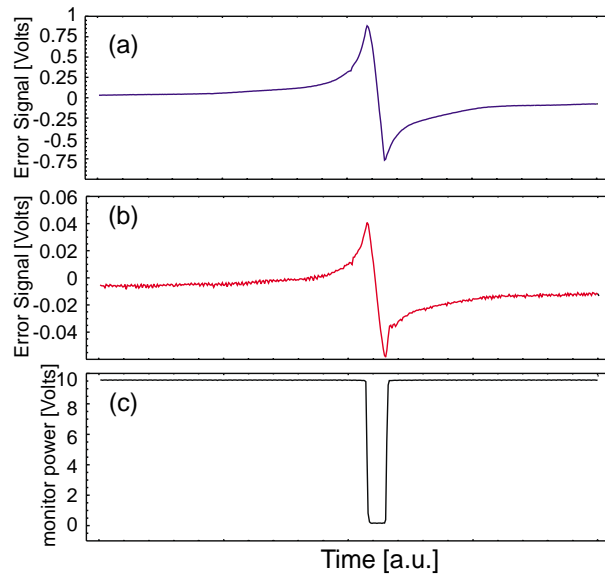


Figure 10.10: (a) Tilt locking error signal, (b) PDH error signal and (c) reverse power on the monitor photodetector.

10.3.2 Results

The shape of the error signals were recorded by slowly scanning the length of the slave laser cavity with a PZT. Figure 10.10 shows the tilt locking error signal, the PDH error signal and the reverse power monitor photodetector. Note that the reverse power drops to zero as the cavity resonance sweeps through the master laser frequency, indicating that injection locking was temporarily achieved. Again, the tilt locking error signal is much larger than the PDH error signal due to the larger front end gain of the transimpedance photodetector.

The closed loop error signals will contain residual fluctuations due to finite bandwidth and gain of the servo. If both techniques are properly reading out the resonance of the slave laser resonance we would expect the residual error signals to be strongly correlated³. For the experimental results presented below the tilt locking error signal is used to maintain injection locking and the PDH error signal is used only for monitoring purposes.

³This is assuming that the residual error is much larger than shot noise. The shot noise on each of the error signals will be uncorrelated

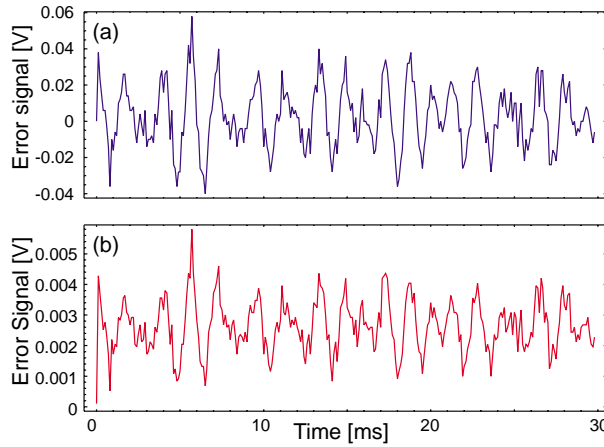


Figure 10.11: Simultaneous measurement of (a) the tilt locking error signal and (b) the PDH error signal whilst the cavity was locked using tilt locking.

Figure 10.11 shows a time domain measurement of the simultaneously recorded error signals for a duration of 30 ms. It is clear that the error signals are strongly correlated indicating that the injection locking performance is not limited by the choice of readout system.

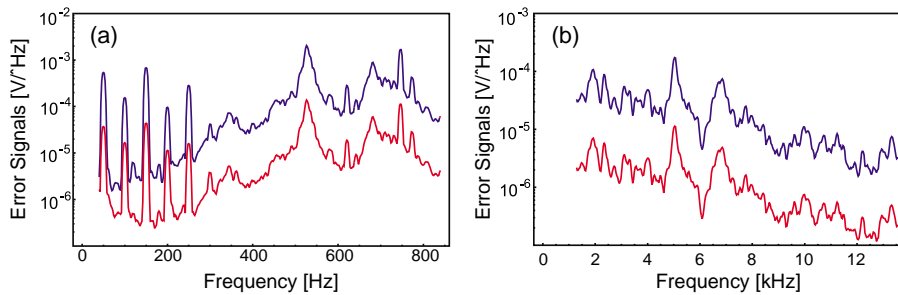


Figure 10.12: Tilt locking and PDH error signal frequency spectrum from (a) 30 Hz to 800 Hz and (b) 1 kHz to 13 kHz whilst the cavity was locked using tilt locking. In both plots tilt locking is the upper spectrum.

Further proof of correlations can be found by comparing the frequency spectra of the error signals. Figure 10.12 shows the frequency spectra of the tilt locking (upper trace) and PDH (lower trace) spectra over two different frequency ranges. These spectra, recorded on a dynamic signal analyser or FFT machine (Hewlett-Packard 3561A), exhibit excellent correlations even at frequencies where electronic pickup dominates the error signal, suggesting that the pickup occurs down stream from the error signal production.

One of the potential advantages of using tilt locking over PDH locking is that the slave laser output is free from modulation sidebands [125]. This may be particularly important for gravitational wave detectors as these sidebands can interfere with locking loops further downstream.

10.3.3 Future work

As discussed in chapter 8, the performance of tilt locking in the presence of mechanical vibration and beam jitter dramatically improves as the cavity approaches the impedance matching condition. Unfortunately, it is impossible to reach this point with a standard injection locking configuration. The slave laser output will always be larger than the master input and thus there will always be a large TEM_{00} mode on the photodetector.

One idea yet to be tested experimentally, is to inject the master laser through a different mirror of the slave laser cavity (i.e., not the main output coupling mirror). Consider the diagram of figure 10.13(a). The slave laser's main output coupler, mirror M2, has the same value as in the traditional injection locking case (in the traditional case M2 serves as both the input coupler for the master and the output coupler for the slave). Mirror M1, however, has a much higher reflectivity than M2 so that in the free running case only around 100 mW leaks out of this port. In the traditional scheme M1 has zero transmission. The master laser is incident on M1, and its power adjusted using the half wave plate and polarising beam splitter to also give 100 mW. By careful adjustment of the master power it may be possible to impedance match the interferometer by cancelling the slave leakage field with the reflected master field and thus decrease the amount of TEM_{00} light on the quadrant photodetector to an arbitrarily small amount. This should ensure that the tilt locking error signal is immune to beam jitter and mechanical vibration.

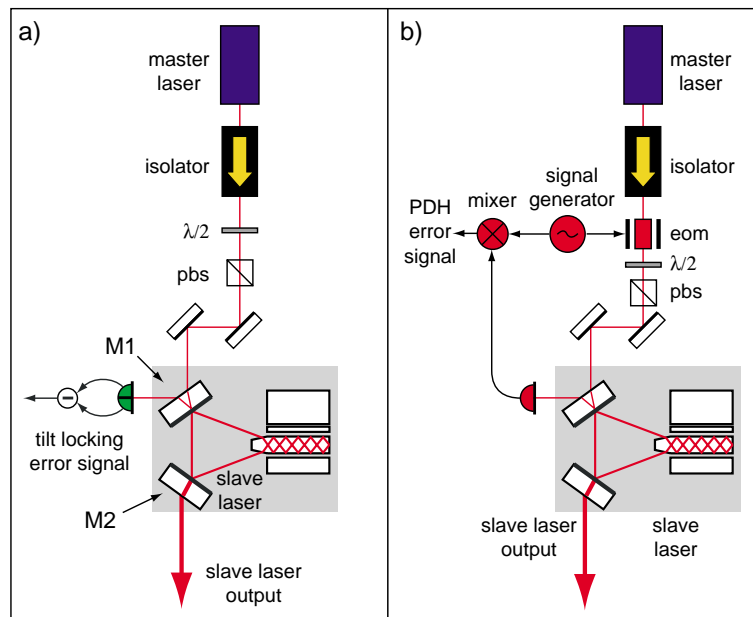


Figure 10.13: Experimental layout for new injection locking scheme with (a) tilt locking and (b) PDH locking.

The scheme should be equally applicable to PDH locking as shown in figure 10.13(b). PDH shares the benefits of impedance matching in that it becomes immune to residual amplitude modulation as impedance matching is approached. The scheme has other potential benefits such as filtering of master laser amplitude and phase noise at frequencies which are large compared to the slave cavity linewidth. The injection locking bandwidth (or alternately power scaling factor) should be maximised as effectively all of the avail-

able master power enters the slave laser cavity. Further theoretical and experimental investigations are required to clarify such issues. The technique has several practical advantages over traditional techniques. For example, a high power isolator is no longer required to protect the master laser from the reverse circulating field of the free running laser. The largest power that can leak out of the slave laser cavity back to the master is approximately equal to the master power and so ordinary Faraday isolators should suffice. Finally, there is no need for any optics in the output of the slave laser which may be important once very high slave powers are reached.

10.3.4 Summary

We have demonstrated successful control of an injection locked laser by the use of tilt locking. The error signals obtained using tilt locking and the PDH technique are highly correlated, indicating that the method used to obtain the error signal is not the limiting factor in locking performance.

We have also presented a new configuration for injection locking of lasers which could provide advantages under certain conditions. This system is yet to be fully analysed or experimentally tested.

10.4 Conclusions

We have reported on the successful use of tilt locking for laser frequency stabilisation, control of a continuous-wave second harmonic generator, and control of an injection locked slave laser. In all three cases the sensitivity and stability of tilt locking was adequate to ensure that these systems' performances were limited by other noise sources, thus there are no performance advantages to be gained by using a different locking technique. Practical considerations, however, could make tilt locking more desirable for use in such a system. Aside from the complexity, cost and size advantages mentioned in chapter 8, it produces an output which is free from modulation. This can be important in many applications.

Tilt locking and two beam interferometers

Until now we have discussed tilt locking in the context of a readout system for optical cavities. However, tilt locking can also be used effectively for the readout and control of two beam interferometers, such as, Michelson, Mach-Zehnder and Sagnac interferometers. In this chapter we give a brief explanation of tilt locking in a nonresonant system. We experimentally demonstrate tilt locking's insensitivity to photodetector displacements in a Mach-Zehnder interferometer and use tilt locking to measure the frequency response of a Sagnac interferometer.

11.1 Spatial modes in a nonresonant system

The explanation of tilt locking an optical cavity presented in chapter 8, involved the interference of resonant and nonresonant spatial modes. Although a two beam interferometer is a nonresonant system, we will continue to use the Hermite-Gauss modes as a basis for describing the interference.

In section 8.2.1, we demonstrated that adding a small TEM_{10} mode $\pi/2$ out of phase with a TEM_{00} mode results in a TEM_{00} mode with a tilted phase front (see figure 8.2). Conversely, if two TEM_{00} modes, slightly tilted with respect to each other, are subtracted the result is a TEM_{10} mode $\pi/2$ out of phase with the original beams. In a two beam interferometer, a subtraction can occur between the electric fields of the two beams when they are recombined (with opposite phase) at the beam splitter. If the two beams are slightly tilted before recombination, the field present at the dark fringe will be the TEM_{10} mode.

This small amount of TEM_{10} light can be used as a local oscillator for any carrier or signal sidebands present at the dark fringe. Once again, to measure the interference efficiently we use a split photodiode. Figure 11.1 shows the vector diagram representing the electric fields at the dark fringe on the left and right sides of the photodiode. The two beams interfering at the beamsplitter have been decomposed into a TEM_{00} component and a TEM_{10} component (where the Hermite-Gauss mode basis is defined with respect to the untilted beam in each arm). Exactly on a dark fringe, the TEM_{00} modes interfere destructively and do not appear at the photodiode. The TEM_{10} modes, however, interfere constructively as the beams have been tilted in opposite directions in each arm of the interferometer. The power on each half of the photodiode is equal, and thus the error signal, again given by subtracting the photocurrents of each half, is zero.

As the interferometer drifts slightly away from the dark fringe, the interference is

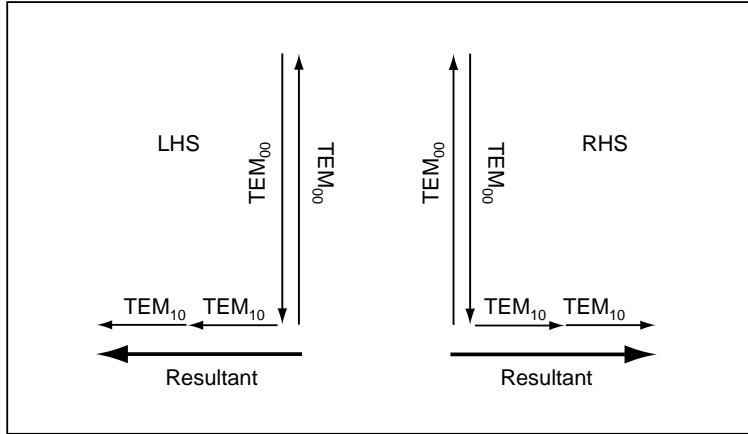


Figure 11.1: Vector diagram for the spatial mode interference of a two beam interferometer at a dark fringe.

altered as shown in figure 11.2. In a two beam interferometer both the TEM_{00} carrier and the TEM_{10} local oscillator will receive a phase shift, in contrast to an optical cavity where only the resonant mode receives the phase shift. For small phase shifts, the amount of TEM_{10} mode present does not change appreciably (the TEM_{10} is effectively at a bright fringe which is a turning point). The carrier field at the dark fringe will be approximately $\pi/2$ out of phase with each of the carriers in the arms and thus will add to the TEM_{10} field on one side and subtract on the other. The resultant vector, and thus the power, increases on one side of the photodiode and decreases on the other, resulting in a non-zero subtraction. This provides an error signal to lock the interferometer to a dark fringe.

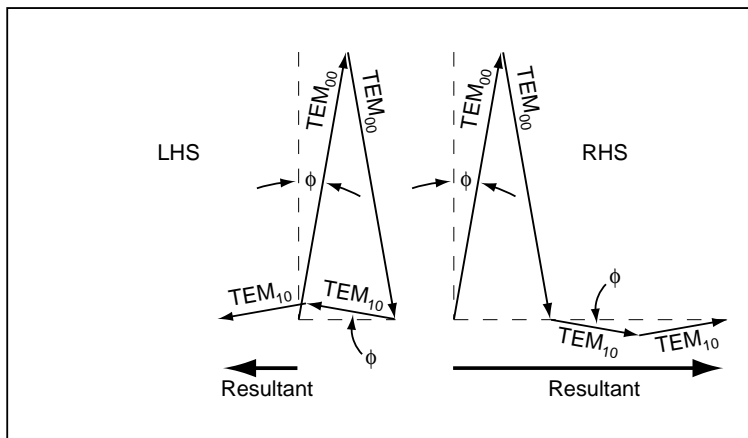


Figure 11.2: Vector diagram for the spatial mode interference of a two beam interferometer with a $\phi = 10^\circ$ phase shift in each arm.

11.2 Tilt locking in a Mach-Zehnder interferometer

We have chosen a Mach-Zehnder interferometer to demonstrate tilt locking as we can individually misalign the beams in each arm. The amount of tilt required is much less than the amount required to produce fringes. Typically, tilt locking requires only a few degrees phase difference across the entire beam. As long as the interferometer is kept reasonably small, then tilting the mirrors introduces predominantly tilt with very little offset. If significant offset is produced this can be compensated by adjusting the alignment of the beamsplitters. Figure 11.3 shows the basic layout of this experiment.

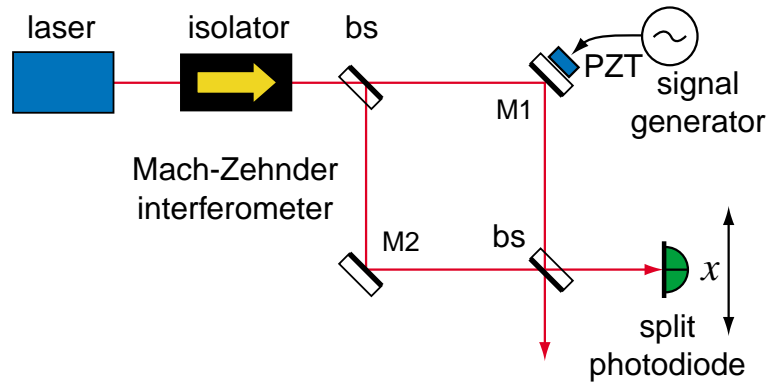


Figure 11.3: Experimental layout for tilt locking in a Mach-Zehnder interferometer. Mirrors M1 and M2 are slightly tilted to produce a TEM_{10} beam at the photodetector in the absence of a carrier.

The interferometer phase is scanned by driving a PZT mounted to mirror M1. The sum (total power) and the difference (error signal) outputs of the photodetector are plotted in figure 11.4. As is the case for Schnupp modulation [34], the tilt locking error signal is a sinusoid which is 90° out of phase with the power. The error signal crosses zero when the power is minimised.

By feeding back the subtracted output via a servo and HV amp to the PZT on M2, the interferometer was locked to a dark fringe. A fraction of the light was tapped off before the split photodetector and measured with a Beamscan. Figure 11.5 shows the two dimensional intensity distribution of the beam at the dark fringe. The intensity profile has a double hump in the x direction, as expected for the TEM_{10} beam. In the y direction the intensity profile has a roughly Gaussian distribution.

The intensity distribution of the bright fringe was also measured using the Beamscan. The beam at the bright fringe should closely approximate the mode of the input field, and show no irregularities due to the tilt introduced by the interferometer. The results of figure 11.6 show that the output is a clean TEM_{00} field with no significant higher order structure.

11.3 Sensitivity to mechanical vibrations

The most promising aspect of tilt locking applied to two beam interferometers is its immunity to beam jitter. In section 8.4 we showed that for an impedance matched cavity

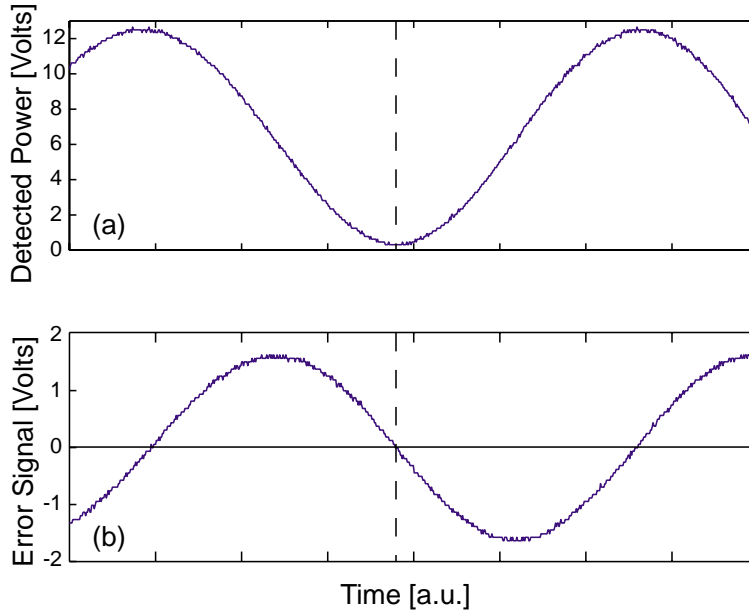


Figure 11.4: (a) Power and (b) error signal as the phase of the Mach-Zehnder is scanned

tilt locking is, to first order, immune to mechanical motion of the photodetector. Unfortunately, in practice it is difficult to approach impedance matching for high finesse cavities due to the sensitive dependence on the mirror reflectivities and losses. In contrast, two beam interferometers exhibit very high fringe visibilities, routinely over 99%. In the context of tilt locking, this ensures that the amount of residual TEM_{00} light at the dark fringe is kept to a minimum, and the regime described in section 8.4 can be approached.

To examine this experimentally, we scanned the Mach-Zehnder interferometer and recorded the error signals as the photodiode was moved across the beam. These results are plotted in figure 11.7. Although the form of the error signal changes as the photodiode is moved through the beam, the position of the zero crossing point does not. In addition, the slope of the error signal is not significantly altered ensuring that the closed loop performance of such an interferometer is unchanged.

The photodetector position can be calibrated by comparing the sum and difference outputs when the power on the photodiode is at a maximum. For example, for the highest error signal of figure 11.7, the subtracted output is approximately 5 V when the total power is 12 V. Simple algebra shows that there is 70% of the beam on one side of the detector and 30% on the other. Assuming the beam is a simple Gaussian at this bright fringe (see figure 11.6), we calculate that the detector has been moved by 0.23 of the beam radius. This is in agreement with the theoretical predictions of figure 8.12.

11.4 Sagnac interferometers

Sagnac interferometers have found widespread commercial use for applications such as fibre optic gyroscopes [126] and more recently in fibre optic current sensors [127]. Due to the common optical path length experienced by the counter propagating beams the Sagnac interferometer is naturally on a dark fringe. In traditional gyroscope systems the

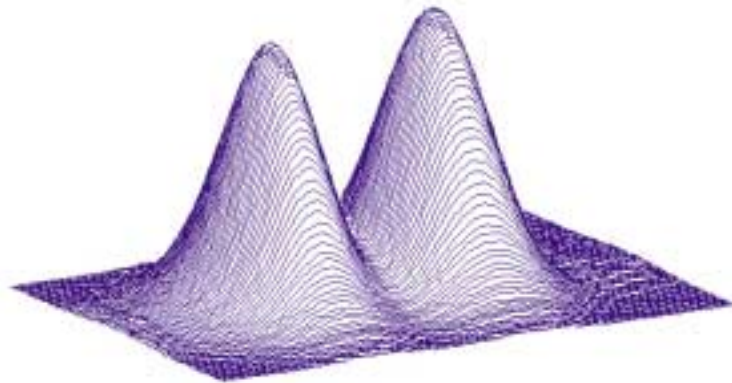


Figure 11.5: Two dimensional intensity distribution of the light on the split photodiode with the interferometer locked to a dark fringe.

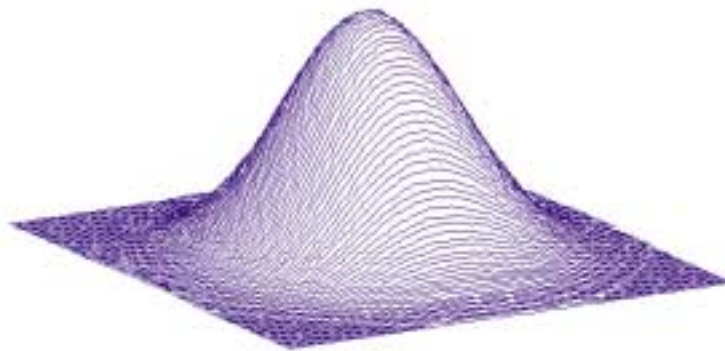


Figure 11.6: Two dimensional intensity distribution of the light at the bright fringe port with the interferometer locked to a dark fringe via tilt locking.

readout of signals at the dark fringe involves complex internal modulation and signal extraction algorithms. Tilt locking has the potential to remove much of this complexity, as it is ideally suited to dark fringe operation.

We have constructed a Sagnac delay line with a round trip length of 19.1 m as shown in figure 11.8. A tracking generator is used to inject a 15 dBm signal into a single phase modulator positioned directly after the beam splitter. A split photodiode at the dark fringe is used to measure the signal. By driving the phase modulator via the tracking generator of a spectrum analyser we were able map out the frequency response of the system.

We have constructed the Sagnac interferometer so that there is a waist in its center (mirror M1) and a waist at the output where the split photodiode is situated. In this situation any tilt introduced by mirror M1 will also appear as tilt on the photodetector. If it not possible to organise the interferometer in such a way then the TEM_{10} mode at the output may have some component of the offset TEM_{10} mode. This can be corrected by placing a lens in front of the photodetector. As the beam propagates away from the lens

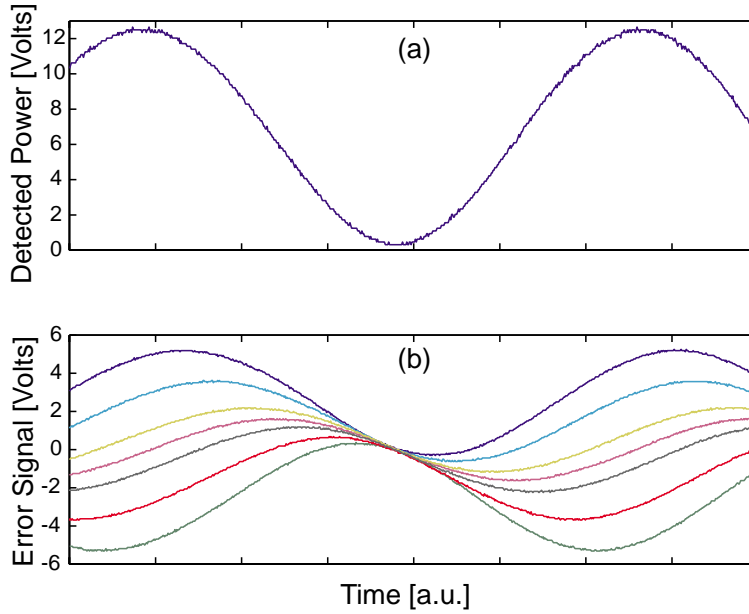


Figure 11.7: (a) Power and (b) error signals as the Mach-Zehnder phase is scanned. The different error signals were obtained for different transverse displacements of the photodetector. Note the zero crossing point at the dark fringe remains basically unchanged.

the Gouy phase shift will ensure that in some plane the TEM_{10} is $\pi/2$ out of phase with the carrier. This is the plane where the photodetector should be situated.

Figure 11.9(a) shows the Sagnac interferometer response from DC to 35 MHz (lower trace) and the frequency response of the photodetector (upper trace). The low frequency spikes on the Sagnac response are due to resonances of the phase modulator (the same ones observed in section 6.5). The frequency response of the photodetector was independently measured by driving the amplitude modulation input of a diode laser with the tracking generator and observing the transfer of the signal to the detector photocurrent [86]. Figure 11.9(b) shows the true Sagnac response recovered by normalising to the photodetector response. A comparison with figure 6.3 shows that the form of the frequency response is indeed what we expect from a delay line Sagnac interferometer.

11.5 Summary

In this chapter, we have discussed the application of tilt locking to two beam interferometers. We have demonstrated tilt locking as a read out system for both Mach-Zehnder and Sagnac interferometers. The tilt locking error signal was shown to be well isolated from changes in the photodetector position due to the high fringe visibilities commonly achieved with two beam interferometers. The implementation of tilt locking into fibre optic Sagnac interferometers is currently underway.

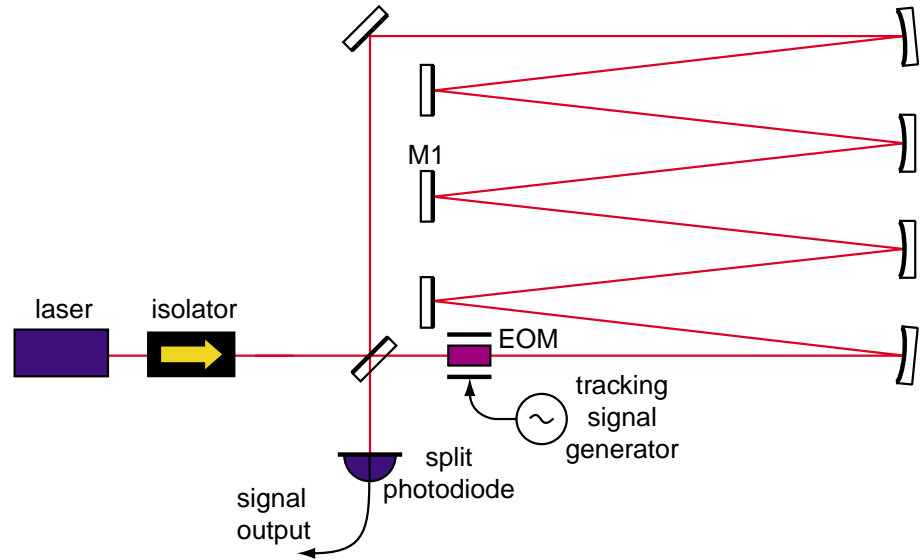


Figure 11.8: Experimental layout for a 19.1 m Sagnac interferometer with a tilt locking signal readout. Mirror M1 is tilted to introduce a TEM_{10} mode at the photodetector.

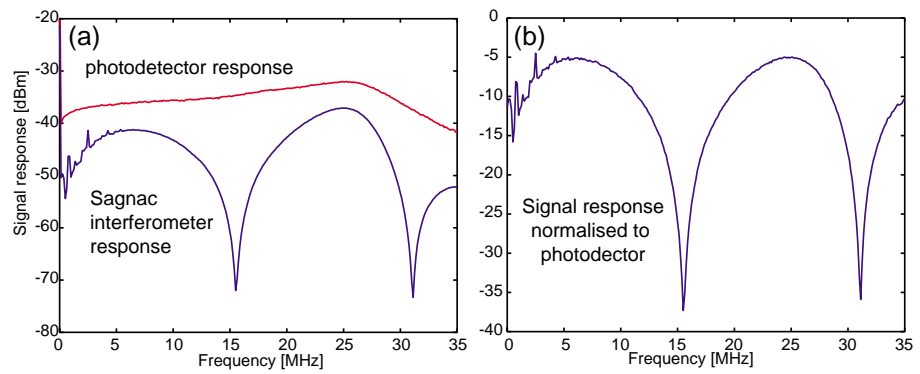


Figure 11.9: (a) Lower trace: Sagnac interferometer frequency response with a tilt locking readout. Upper trace: Photodetector response. (b) The response of the Sagnac interferometer normalised to the photodetector response.

Conclusions

12.1 Summary of interferometer configurations work

This thesis presented experimental investigations of interferometer configurations for an advanced gravitational wave detector.

We have presented the first experimental demonstration of a Sagnac interferometer with resonant sideband extraction. The frequency response of the system was measured for a variety of signal mirrors and a range of signal cavity detunings. A brief comparison of resonant sideband extraction in Sagnac and Michelson based systems has been performed. We found that many of the advantages of a Sagnac over a Michelson in delay line systems, such as simplicity of control and insensitivity to laser frequency noise, are lost when the systems are complicated with optical cavities. We have no immediate plans for the further investigation of cavity based Sagnac interferometers for gravitational wave detection.

A control system for a power recycled Michelson interferometer with resonant sideband extraction has been presented. The control system employs a frontal modulation scheme requiring phase modulation of the carrier field and a phase modulated subcarrier field. We have discussed the application of single sideband modulation and demodulation to obtain an error signal for an optical cavity and double demodulation for a Michelson interferometer. The single sideband signal extraction scheme has a sensitivity lower than the analogous double sideband technique, however the noise floor is also slightly reduced due to the absence of nonstationary shot noise. The dependence of the single sideband modulation scheme on errors in the demodulation phase was analysed. We found that isolation against changes in the demodulation phase is determined by the impedance matching and fringe visibility of the instrument.

In principle, this control system is capable of locking the first four length degrees of freedom (arm cavity common mode, arm cavity differential mode, Michelson common mode, and Michelson differential mode) to a fixed point with the signal cavity detuned to an arbitrary point. In addition, the control system permits this detuning to be altered whilst the interferometer maintains lock.

The subcarrier field was obtained by offset phase locking a low power laser to the carrier laser. It was found that residual noise in the phase locking is equivalent to errors in the demodulation phase. We have discussed one technique for avoiding this problem which involved using the measured beatnote between the lasers as the electronic local oscillator for all subsequent demodulations. After implementing this revised local oscillator scheme we observed an improvement in the noise floor of the error signal by a factor of 35 dB.

The control system for a power recycled Michelson interferometer with RSE has been

implemented in a benchtop prototype interferometer. In addition to monitoring the optical power at various ports, correct operation of the control system was verified by observing the optical spectra at the input, at the power cavity port and at the transmitted port. The interferometer exhibited stable, continuous locking for periods of several hours. In addition, the interferometer could be locked with the signal cavity detuned to an arbitrary position.

A system for measuring the frequency response of the system was devised. This system relied on a third laser injected through the back of one of the arm cavities and was capable of measuring the frequency response out to very high frequencies with a large signal to noise ratio. The frequency response was measured for a range of signal cavity detunings and was found to be in good agreement with theoretical predictions. Finally, the control system's ability to detune the interferometer without dropping lock was experimentally verified.

12.2 Summary of tilt locking work

We presented a new technique for the readout and control of interferometers. This technique, tilt locking, utilises the interference between the TEM_{00} and TEM_{10} modes. Tilt locking replaces the signal generator, modulator, high speed photodetector and mixer of conventional PDH locking systems with a quadrant photodiode and several low frequency op-amps.

A calculation of the sensitivity with which the position of a beam can be measured was performed using the linearised form of the annihilation operator. We demonstrated how this position uncertainty is responsible for the shot noise limit of tilt locking. Using this result we performed a detailed calculation of the shot noise limited performance of tilt locking. We found that tilt locking has an overall quantum efficiency of $\sqrt{2/\pi} \approx 0.80$, that is, tilt locking will have a signal to noise ratio of 80% for a measurement of phase noise at the quantum noise level. This source of the inefficiency was due to imperfect interference of the TEM_{10} and TEM_{00} modes. This is comparable to the $\sqrt{2/3} \approx 0.82$ quantum efficiency of PDH locking. We also analytically demonstrated how the impedance matching of a system can determine the sensitivity of tilt locking to mechanical vibrations and beam jitter.

Tilt locking was demonstrated in a number of applications including laser frequency stabilisation, continuous-wave second harmonic generation and laser injection locking. By locking two lasers to one cavity (situated in an ordinary lab environment) we were able to obtain a beatnote linewidth of 8 Hz with an Allan deviation of 3.3 Hz at 100 ms. In the remaining demonstrations we compared the performance of the tilt-locked and Pound-Drever-Hall-locked systems. In each case, we found that tilt locking offered comparable performance to the PDH system.

Finally, we investigated the use of tilt locking in two beam interferometers. Using a Mach-Zehnder interferometer we experimentally demonstrated how the zero crossing point of the error signal is well isolated from changes in the photodetector position. In addition, tilt locking was used to readout the signal of a Sagnac interferometer.

Tilt locking in many systems is capable of achieving the same sensitivity as the PDH system. Although it is not applicable to the control or readout of a gravitational wave detector due to its incompatibility with suspended interferometry, it should find use in a wide range of applications.

12.3 Further work

Aside from the length sensing control system, many other systems need development before RSE can be implemented in a long base-line gravitational wave detector. These systems include auto-alignment control, input optics, and signal extraction or output optics. Before the control system presented here can be seriously considered for use in a gravitational wave detector a full analysis of the noise performance is needed. One aspect which will require particular attention is the sensitivity to the demodulation phase error. This is particularly important as it influences the gravitational wave signal readout. The results of such calculations may guide the experimental method of production of the subcarrier field. If the degree of noise coupling is unacceptably high, other techniques may need to be employed such as external modulation [43] or offset locking [128].

Similar demonstrations of resonant sideband extraction in a power recycled Michelson interferometer have also been demonstrated this year by Mason at Caltech and Delker at the University of Florida. Now that all three benchtop experiments are completed the focus of the configurations work will shift to Glasgow where this configuration is to be implemented in a suspended prototype. It is intended that the Glasgow work will be a “scientific” prototype of the LIGO II configuration. In a few years, knowledge and experience gained from this scientific prototype will be used to construct a full “engineering” prototype of LIGO II in the 40 m interferometer at Caltech.

The detuning of the signal extraction mirror in an RSE interferometer affects both the signal bandwidth and peak signal frequency of the device. By replacing the fixed reflectivity signal extraction mirror by a short optical cavity (or a Michelson interferometer) the effective reflectivity of the signal mirror can be altered. This provides a greater level of flexibility with the ability to independently adjust the signal bandwidth and peak frequency of the interferometer. This would be of great benefit to a gravitational wave detector allowing the signal response to be optimised for any given source.

The tilt locking work will receive a high performance test when it is used as the primary readout and control technique for the thermal noise measurement system under development at the ANU [129]. This work is to use tilt locking, to frequency stabilise the laser to a rigid modecleaner suspended in vacuum. The output beam from this modecleaner is then directed onto a test cavity, the subject of the thermal noise measurement. Tilt locking is again to be used to measure the thermal noise of this test cavity by sensing the change in resonance frequency. The ability of tilt locking to measure the changes in length of the cavity is expected to approach the shot noise limit derived in chapter 9, as the output of the modecleaner is expected to have only minimal beam jitter.

Work on tilt locking in two beam interferometers is to continue with development already underway to implement tilt locking in a fibre optic Sagnac.

Construction of optical spectrum analysers

We designed and constructed several fibre-coupled optical spectrum analysers (OSA's) with a variety of values for free spectral range (FSR) and resolution, with an aim to have these units as self contained, versatile, and robust as possible.

Physically, our OSA's consist of an invar spaced cavity mounted on a solid block. At the front of the block there is an optical fibre connection port. Light entering through the fibre port passes through an angled neutral density filter, then the cavity before reaching a 25 mm lens and photodetector. All these components are bolted rigidly to a base making the apparatus both robust and transportable. Side on and top down schematics are shown below.

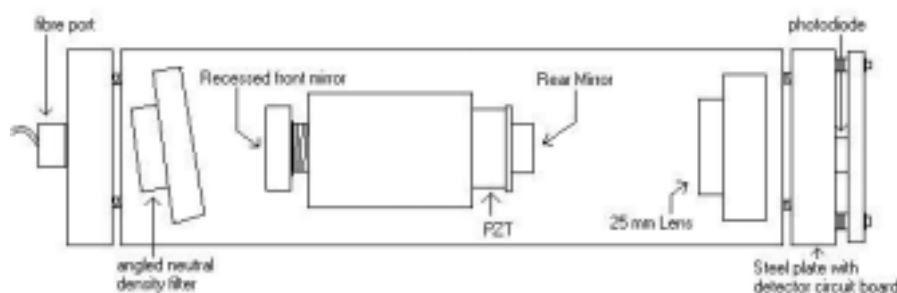


Figure A.1: Top down schematic view of the OSA.

When the OSA's were designed, emphasis was placed on ease and flexibility of use. A solid base was used so that all the necessary components could be transported without need for re-alignment. An angled neutral density filter was used to reduce parasitic etalons between the input fibre port and the front mirror of the cavity. The fibre port had inadequate AR coating, making this measure necessary. The OSA itself was an invar spacer cavity with mirrors from Rimkevicius and Gintautas. Invar has an extremely low coefficient of expansion at 0.9×10^{-6} per Kelvin, more than an order of magnitude below most metals and alloys - this means there is minimal temperature based length change. To allow geometrical length adjustment, the front mirror's holder had a fine thread which screwed into the cavity. The holder was held in the right position by a nylon grub screw. By adjusting the front mirror distance, the cavity could be set quite precisely to confocality. Scanning of the optical length was by a piezo-mechanical device glued between the

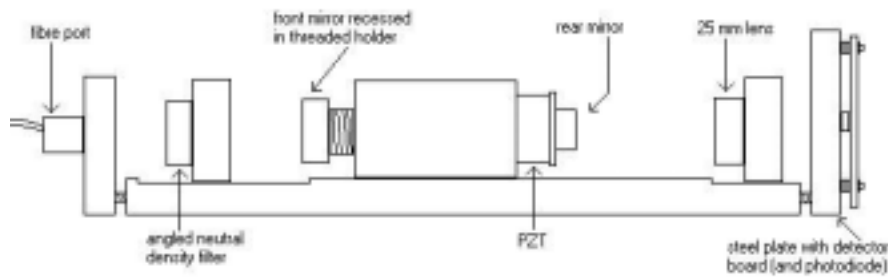


Figure A.2: Side-on schematic view of the OSA.

rear mirror and the cavity.

At the back of the base a perpendicular plate with a half inch hole was bolted on. A photodiode, mounted in its signal amplification board, was bolted directly onto this plate, with the diode centred at the beam focus. With the detector board fixed in front of the 25 mm lens there was no need for either alignment or external components.

The component most important for transportability and versatility were the fibre ports. By having them fixed on the front of the cavity, any fibre input could be coupled into the cavity without need for re-alignment. Also, having a fibre port as input was experimentally practical - anywhere a fibre tap-off can be placed, an OSA can be used. In addition to this, OSA's could be interchanged at will depending on whether large FSR or higher resolution was needed.

Circuit Diagrams

In this appendix we present the circuit diagrams for the tilt photodetector, PZT servo and the laser frequency servo. Details of all other photodetectors used in this work can be found in [86].

B.1 Split photodiode

The circuit diagram for the split photodiodes is shown below. The pictured circuit utilises AD829 amplifiers; however, the AD708 can also be used in the same circuit to obtain higher DC precision at the expense of bandwidth.

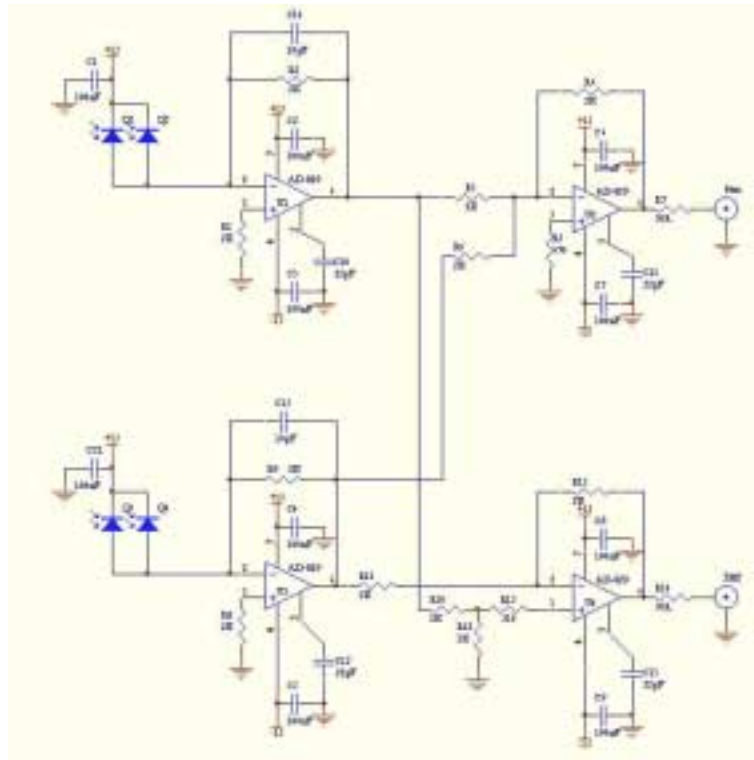


Figure B.1: Circuit diagram used with the split photodiode.

B.2 PZT Servo

The circuit diagram for the PZT servo is shown in figure B.2. The circuit contains a third order elliptic filter which can be tuned to coincide with the resonance of the PZT. More details on the the design and implementation of this filter can be found in [88].

B.3 Laser Frequency Servo

The laser frequency servo (see figure B.3) provides feedback to the laser crystal temperature at low frequencies and the laser crystal PZT at high frequencies. The circuit also contains a third order elliptic filter which can be tuned to coincide the resonance of the laser crystal PZT.

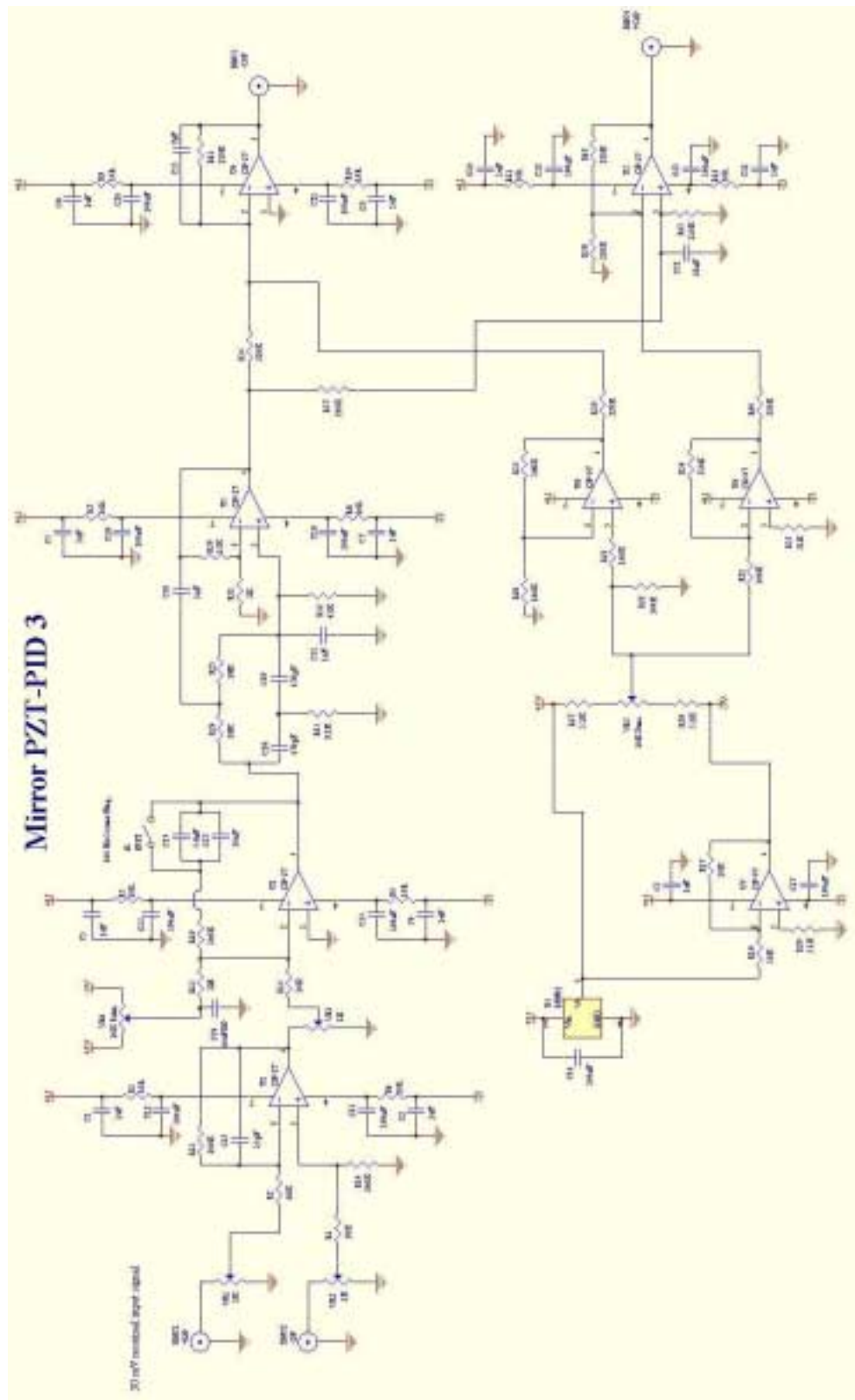


Figure B.2: PZT servo circuit diagram

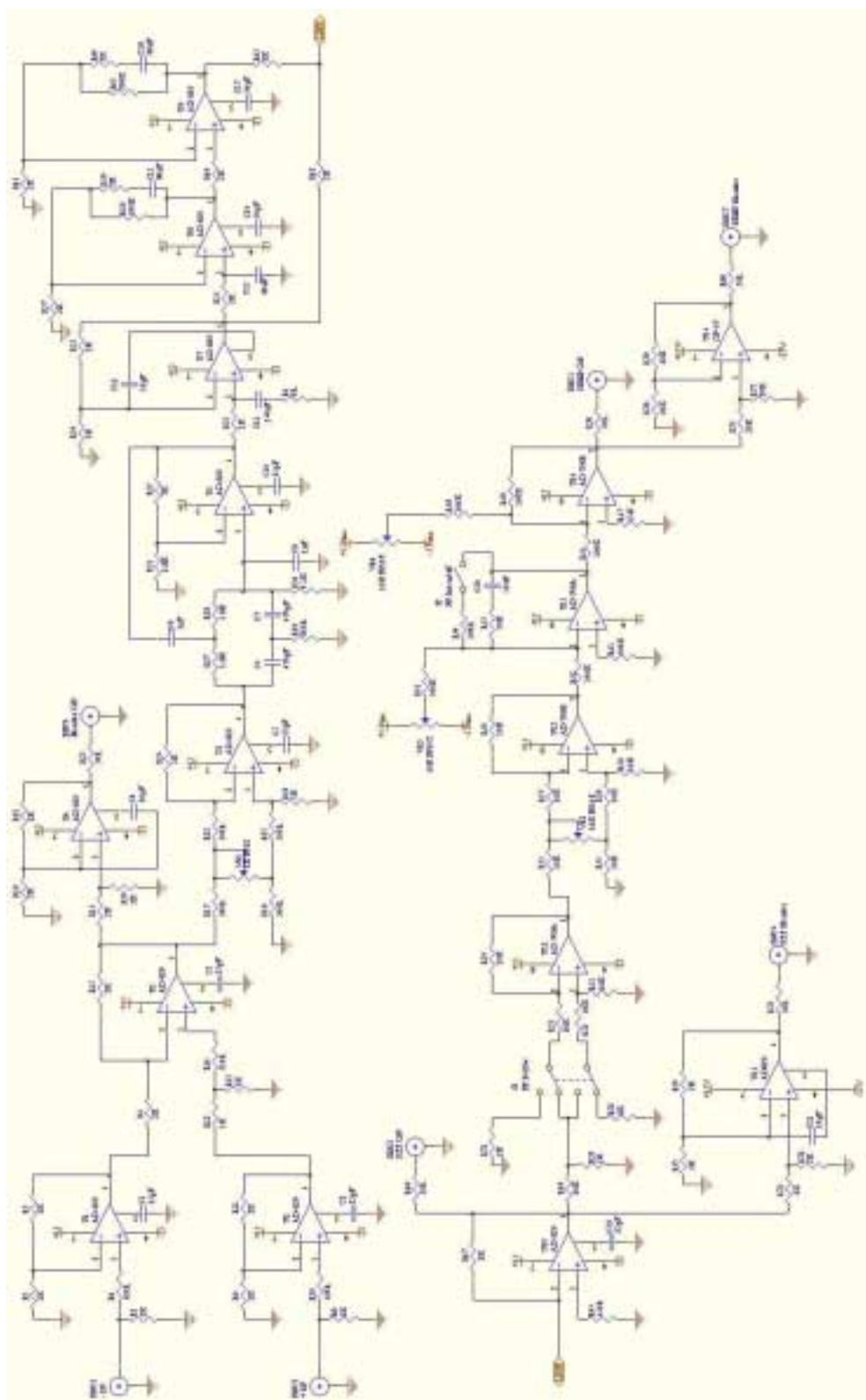


Figure B.3: Laser frequency servo circuit diagram.

Matlab files to model DC error signals

The DC error signals and the look-up table for the subcarrier offset frequency required for a given detuning were calculated using the programs `rsecontrol.m` and `rseinterf.m`.

The program `rsecontrol` defines the mirror reflectivities, interferometer lengths and modulation frequencies used for the control system. This program is quite repetitious and for brevity only a subsection is included.

```
Ps=0.1; % ratio of subcarrier power to carrier power
P2=Ps*0.1; % ratio of each subcarrier sideband to carrier power

sdet=2*pi/180; % signal cavity detuning (radians)

%%% Look up table for signal cavity detuning %%%
% f = 188.2MHz ==> sdet=0.082+/2 (near RSE)
% f = 186.445MHz sdet = 15/180+/2 (15 degrees detuned from RSE)
% f = 184.315MHz sdet = 30/180+/2 (30 degrees detuned from RSE)
% f = 182.493MHz sdet = 45/180+/2 (45 degrees detuned from RSE)
% f = 180.806MHz sdet = 60/180+/2 (60 degrees detuned from RSE)
% f = 179.12MHz sdet = 75/180+/2 (75 degrees detuned from RSE)
% f = 177.035MHz sdet = 2*pi/180 (2 degrees from DR)

%%% Interferometer mirror parameters %%%

rbs=sqrt(0.53); % beamsplitter reflectivity
tbs=sqrt(0.465); % beamsplitter transmittivity
ril=sqrt(0.975); % in-line AC input coupler reflectivity
til=sqrt(0.0222); % in-line AC input coupler transmittivity
ri2=sqrt(0.9955); % in-line AC output coupler reflectivity
ti2=sqrt(1-ri2.^2); % in-line AC output coupler transmittivity
rpl=sqrt(0.975); % perp AC input coupler reflectivity
tp1=sqrt(0.022); % perp AC input coupler transmittivity
rp2=sqrt(0.9961); % perp AC output coupler reflectivity
tp2=sqrt(0.0039); % perp AC output coupler transmittivity
rs=sqrt(0.688); % signal mirror reflectivity
```

```

ts=sqrt(0.312); % signal mirror transmittivity
rp=sqrt(0.682); % power mirror reflectivity
tp=sqrt(0.318); % power mirror transmittivity

%%% Interferometer lengths %%%

Lp=0.8; % power mirror to beamsplitter
Lmi=c/(4*f1)-Lp; % michelson in-line (bs to AC)
Lmp=3/4*c/f1-Lp; % michelson perp (bs to AC)
Ls=Lp; % signal mirror to beamsplitter
Laci=0.175; % AC in-line
Lacp=0.175; % AC perp

Ldelay=(Lp+Ls)+(Lmp+Lmi); % single pass delay for transmit-
ted beam

%%%%%%%%%%%%%%%%%%%%%%%%%%%%%%%%%%%%%%%%%%%%%%%%%%%%%%%%%%%%%%%%%%%%%%%%

points=501; % number of plotting points
range=0.1; % scanning range in radians
dx=2*range/(points-1); % radians between plotting points
det=linspace(-range,range,points); % detuning vector in radians
freq=linspace(-200e6,200e6,points); % frequency vector in Hz
wscan=2*pi*freq; % frequency vector in radians/sec

%%%%%%%%%%%%%%%%%%%%%%%%%%%%%%%%%%%%%%%%%%%%%%%%%%%%%%%%%%%%%%%%%%%%%%%%
%%% Scanning input frequency %%%

w=wscan; % frequency vector
phiP=pi/2+w*Lp./c; % power cavity phase
phiLI=w*Lmi./c; % michelson in-line phase
phiLP=w*Lmp./c; % michelson perp phase
phiS=w*Ls./c+sdet; % signal cavity phase
phiACI=w*Laci./c; % arm cavity in-line phase
phiACP=w*Lacp./c; % arm cavity perp phase

[Er,Et,Ep]=rseinterf(phiP,phiLI,phiLP,phiS,phiACI,phiACP);

figure(1)
subplot(3,1,1)
plot(freq/1e6,abs(Er).^2)
title('modulation frequency')
ylabel('reflected power')
xlabel('frequency')
axis([-200,200,0,1])
subplot(3,1,2)
plot(freq/1e6,abs(Et).^2)

```

```

ylabel('transmitted power')
xlabel('frequency')
axis([-200,200,0,1])
subplot(3,1,3)
plot(freq/1e6,abs(Ep).^2)
ylabel('circulating power')
xlabel('frequency')
axis([-200,200,0,max(abs(Ep).^2)])

%%%%%%%%%%%%%%%%%%%%%%%%%%%%%%%%%%%%%%%%%%%%%%%%%%%%%%%%%%%%%%%%%%%%%%%%%%%%%%
%% Scanning Arm Cavity (common mode) %%

w=0; % carrier field
phiP=pi/2+w*Lp./c; % power cavity phase
phiLI=w*Lmi./c; % michelson in-line phase
phiLP=w*Lmp./c; % michelson perp phase
phiS=w*Lv./c+sdet; % signal cavity phase
phiACI=w*Laci./c+det; % arm cavity in-line phase
phiACP=w*Lacp./c+det; % arm cavity perp phase

[ErC,EtC,EpC]=rseinterf(phiP,phiLI,phiLP,phiS,phiACI,phiACP);

w=w1; % upper sideband
phiP=pi/2+w*Lp./c; % power cavity phase
phiLI=w*Lmi./c; % michelson in-line phase
phiLP=w*Lmp./c; % michelson perp phase
phiS=w*Lv./c+sdet; % signal cavity phase
phiACI=w*Laci./c+det; % arm cavity in-line phase
phiACP=w*Lacp./c+det; % arm cavity perp phase

[Er1,Et1,Ep1]=rseinterf(phiP,phiLI,phiLP,phiS,phiACI,phiACP);

w=-w1; % lower sideband
phiP=pi/2+w*Lp./c; % power cavity phase
phiLI=w*Lmi./c; % michelson in-line phase
phiLP=w*Lmp./c; % michelson perp phase
phiS=w*Lv./c+sdet; % signal cavity phase
phiACI=w*Laci./c+det; % arm cavity in-line phase
phiACP=w*Lacp./c+det; % arm cavity perp phase

[Er_1,Et_1,Ep_1]=rseinterf(phiP,phiLI,phiLP,phiS,phiACI,phiACP);

w=ws; % subcarrier
phiP=pi/2+w*Lp./c; % power cavity phase
phiLI=w*Lmi./c; % michelson in-line phase
phiLP=w*Lmp./c; % michelson perp phase
phiS=w*Lv./c+sdet; % signal cavity phase
phiACI=w*Laci./c+det; % arm cavity in-line phase

```

```

phiACP=w*Lacp./c+det; % arm cavity perp phase

[Ers,Ets,Eps]=rseinterf(phiP,phiLI,phiLP,phiS,phiACI,phiACP);

w=ws+w2; % upper subcarrier sideband
phiP=pi/2+w*Lp./c; % power cavity phase
phiLI=w*Lmi./c; % michelson in-line phase
phiLP=w*Lmp./c; % michelson perp phase
phiS=w*Lv./c+sdet; % signal cavity phase
phiACI=w*Laci./c+det; % arm cavity in-line phase
phiACP=w*Lacp./c+det; % arm cavity perp phase

[Er2,Et2,Ep2]=rseinterf(phiP,phiLI,phiLP,phiS,phiACI,phiACP);

w=ws-w2; % lower subcarrier sideband
phiP=pi/2+w*Lp./c; % power cavity phase
phiLI=w*Lmi./c; % michelson in-line phase
phiLP=w*Lmp./c; % michelson perp phase
phiS=w*Lv./c+sdet; % signal cavity phase
phiACI=w*Laci./c+det; % arm cavity in-line phase
phiACP=w*Lacp./c+det; % arm cavity perp phase

[Er_2,Et_2,Ep_2]=rseinterf(phiP,phiLI,phiLP,phiS,phiACI,phiACP);

% Calculate total power at each detector %
Pr=(abs(Erc).^2+P1*abs(Er1).^2+P1*abs(Er_1).^2+Ps*abs(Ers).^2+...
    P2*abs(Er2).^2+P2*abs(Er_2).^2)/(1+2*P1+Ps+2*P2);
Pp=(abs(Epc).^2+P1*abs(Ep1).^2+P1*abs(Ep_1).^2+Ps*abs(Eps).^2+...
    P2*abs(Ep2).^2+P2*abs(Ep_2).^2)/(1+2*P1+Ps+2*P2);
Pt=(abs(Etc).^2+P1*abs(Et1).^2+P1*abs(Et_1).^2+Ps*abs(Ets).^2+...
    P2*abs(Et2).^2+P2*abs(Et_2).^2)/(1+2*P1+Ps+2*P2);

%%% demodulation at w1 on power cavity tap off %%%

demod=0; % demodulation phase angle
IPCp=-imag((conj(Epc).*Ep_1-conj(Ep1).*Epc).*exp(i*demod));
% in phase component
QCp=real((conj(Epc).*Ep_1-conj(Ep1).*Epc).*exp(i*demod));
% quadrature component

figure(2)
subplot(3,1,1)
plot(det,Pp)
title('scanning AC common mode')
ylabel('circulating power')
subplot(3,1,2)
plot(det,IPCp)

```

```

ylabel('In Phase')
subplot(3,1,3)
plot(det,QCp)
ylabel('Quadrature')
xlabel('demodulation @ 75.9MHZ')

% caculating slope %
a=diff(IPCp)./dx;
ACcommslope=a((points+1)./2)

```

The program `rseinterf.m` caculates the fields at the three interferometer ports when provided with the phase shifts. The Matlab code is presented below.

```

function [Er,Et,Ep]=rseinterf(phiP,phiLI,phiLP,phiS,phiACI,phiACP);

% This m-file describes the amplitude and phase re-
% sponse of a power recycled
% michelson interferometer with resonant sideband extraction.
% Usage [Er,Et,Ep]=rseinterf(phiP,phiLI,phiLP,phiS,phiACI,phiACP);
%
% The inputs are:
% phiP, the power recycling cavity phase shift (single pass)
% phiLI,the michelson phase shift in line arm (single pass)
% phiLP,the michelson phase shift perpendicular arm (sin-
% gle pass)
% phiS,the signal cavity phase shift (single pass)
% phiACI,the in line arm cavity phase shift (single pass)
% phiACP,the perpendicular arm cavity phase shift (single pass)
%
% The outputs are:
% Er,the field reflected from the power mirror
% Et, the field transmitted through the signal mirror
% Ep, the field measured at the power cavity tap off (di-
% rected towards laser)

global rbs tbs ril ri2 til ti2 rp1 rp2 tp1 tp2 rs ts rp tp

%%% Arm Cavities %%%
raci=ril-(til.^2.*ri2.*exp(i*2*phiACI))./(1-
ril.*ri2.*exp(i*2*phiACI)); % AC in-line reflectivity
racp=rp1-(tp1.^2.*rp2.*exp(i*2*phiACP))./(1-
rp1.*rp2.*exp(i*2*phiACP)); % AC perp reflectivity

%%% Michelson %%%

```

```

rml=rbs.^2.*racp.*exp(i*2*phiLP)+tbs.^2.*raci.*exp(i*2*phiLI);
% mich reflectivity from laser
tml=i*tbs.*rbs.*racp.*exp(i*2*phiLP)-i*tbs.*rbs.*raci.*exp(i*2*phiLI);
% mich transmission (from laser)
rm2=-rbs.^2.*raci.*exp(i*2*phiLI)-tbs.^2.*racp.*exp(i*2*phiLP);
% mich reflectivity from signal mirror
tm2=tml; % mich transmission (from sm)
% note: these expressions for the michelson assume
% that it is locked to a dark fringe for phi=0
% ie, an artificial factor of pi is already included.

%%% Signal Cavity %%%
ri=rml+(tml.*tm2.*rs.*exp(i*2*phiS))./(1-rs.*rm2.*exp(i*2*phiS));
% reflectivity of RSE inter (no PM)
ti=i.*ts.*tml.*exp(i*phiS)./(1-rs.*rm2.*exp(i*2*phiS)); % transmission
% of RSE inter (no PM)

%%% Full power recycled RSE interferometer %%%
Er=rp-(tp.^2.*ri.*exp(i*2*phiP))./(1-ri.*rp.*exp(i*2*phiP));
% reflected port
Et=(i.*tp.*ti.*exp(i.*phiP))./(1-ri.*rp.*exp(i*2*phiP));
% transmitted port
Ep=(i.*tp.*ri.*exp(i*2*phiP))./(1-ri.*rp.*exp(i*2*phiP));
% power cavity port

```

Bibliography

- [1] A. Einstein, *Ann. Phys. Lpz* **49**, 769 (1916).
- [2] A. Einstein, *Preuss. Akad. Wiss. Berlin* , 688 (1916).
- [3] C. W. Misner, K. S. Thorne, and J. L. Wheeler, *Gravitation*, Freeman, San Francisco, 1973.
- [4] P. R. Saulson, *Fundamentals of interferometric gravitational wave detectors*, World Scientific, Singapore, 1 edition, 1994.
- [5] T. Damour, *General relativity and experiment: a brief review*, *Class. Quantum Grav.* **9**, 55 (1992).
- [6] R. A. Hulse and J. H. Taylor, *Discovery of a pulsar in a binary system*, *Astrophys. J. (Letters)* **195**, L51 (1975).
- [7] J. H. Taylor and J. M. Weisberg, *A new test of general relativity: gravitational radiation and the binary pulsar PSR 1913+16*, *Astrophys. J.* **253**, 908 (1982).
- [8] J. H. Taylor and J. M. Weisberg, *Further experimental tests of relativistic gravity using the binary pulsar PSR 1913+16*, *Astrophys. J.* **345**, 434 (1989).
- [9] J. H. Taylor, A. Wolszczan, T. Damour, and J. M. Weisberg, *Experimental constraints on strong-field relativistic gravity*, *Nature* **355**, 132 (1992).
- [10] B. F. Schutz, *Gravitational wave astronomy*, *Class. Quantum Grav.* **16**, A131 (2000).
- [11] N. A. Robertson, *Laser interferometric gravitational wave detectors*, *Class. Quantum Grav.* **17**, R19 (2000).
- [12] J. Weber, *Evidence for discovery of gravitational radiation*, *Phys. Rev. Lett.* **22**, 1320 (1969).
- [13] J. P. Zendri, L. Baggio, M. Bonaldi, M. Cerdonio, L. Conti, V. Crivell Visconti, P. Flferi, P. L. Fortini, V. Martinucci, R. Mezzena, A. Ortolan, G. A. Prodi, G. Soranzo, L. Taffarello, G. Vedovato, A. Vinante, and S. Vitale, *Status report of the gravitational wave detector AURIGA*, *Gravitational Waves: Third Edoardo Amaldi Conference, Pasadena*. ed S. Meshkov , 421 (2000).
- [14] E. Hecht, *Optics*, Addison-Wesley, Reading, 2 edition, 1987.
- [15] C. M. Caves, K. S. Thorne, R. W. P. Drever, V. D. Sandberg, and M. Zimmermann, *On the measurement of a weak classical force coupled to a quantum-mechanical oscillator. I. Issues of principle*, *Rev. Mod. Phys.* **52**, 341 (1980).
- [16] C. M. Caves, *Quantum-mechanical noise in an interferometer*, *Phys. Rev. D.* **23**, 1693 (1981).

-
- [17] P. R. Saulson, *Thermal noise in mechanical experiments*, Phys. Rev. D **42**, 2437 (1990).
 - [18] A. Abramovici, W. E. Althouse, R. W. P. Drever, Y. Gursel, S. Kawamura, F. J. Raab, D. Shoemaker, L. Sievers, R. E. Spero, K. S. Thorne, R. E. Vogt, R. Weiss, S. E. Whitcomb, and M. E. Zucker, *LIGO: the Laser Interferometer Gravitational-Wave Observatory*, Science **256**, 325 (1992).
 - [19] A. Brillet et al., Virgo proposal to CNRS and INFN, unpublished, 1989.
 - [20] H. Lück, P. Aufmuth, O. S. Brozek, K. Danzmann, A. Freise, S. Goßler, A. Grado, H. Grote, K. Mossavi, V. Quetschke, B. Willke, K. Kawabe, A. Rüdiger, R. Schilling, W. Winkler, C. Zhao, K. A. Strain, C. Cagnoli, M. Casey, J. Hough, M. Human, P. McNamara, G. P. Newton, M. V. Plissi, N. A. Robertson, S. Rowan, D. I. Robertson, K. D. Skeldon, C. I. Torrie, H. Ward, B. F. Schutz, I. Taylor, and B. S. Sathyaprakash, *The status of GEO600*, Gravitational Waves: Third Edoardo Amaldi Conference, Pasadena. ed S. Meshkov , 119 (2000).
 - [21] M. Ando, K. Tsubono, and the TAMA collaboration, *TAMA Project: design and current status*, Gravitational Waves: Third Edoardo Amaldi Conference, Pasadena. ed S. Meshkov , 128 (2000).
 - [22] R. J. Sandeman and D. E. McClelland, *Laser interferometer gravitational-wave observatories: an overview*, J. Modern Opt. **37**, 1747 (1990).
 - [23] D. E. McClelland, M. B. Gray, D. A. Shaddock, B. J. Slagmolen, S. M. Scott, P. Charlton, B. J. Whiting, R. J. Sandeman, D. G. Blair, L. Ju, J. Winterflood, D. Greenwood, F. Benabid, M. Baker, Z. Zhou, D. Mudge, D. Ottaway, M. Ostermeyer, P. J. Veitch, J. Munch, M. W. Hamilton, and C. Hollitt, *Status of the Australian Consortium for Interferometric Gravitational Astronomy*, Gravitational Waves: Third Edoardo Amaldi Conference, Pasadena. ed S. Meshkov , 140 (2000).
 - [24] P. Bender et al., *LISA Pre-Phase A Report*, Max Plank Institute for Quantum Optics, 1998.
 - [25] A. Vecchio, *Deep surveys of massive black holes with LISA*, Gravitational Waves: Third Edoardo Amaldi Conference, Pasadena. ed S. Meshkov , 238 (2000).
 - [26] D. F. Walls and G. J. Milburn, *Quantum Optics*, Springer-Verlag, Berlin, 1 edition, 1994.
 - [27] B. Yurke, *Use of cavities in squeezed state generation*, Phys. Rev. A **20**, 408 (1984).
 - [28] S. Reynaud, C. Fabre, E. Giacobino, and A. Heidmann, *Photon noise reduction by passive optical bistable systems*, Phys. Rev. A **40**, 1440 (1989).
 - [29] H. Haken, *"Laser theory"*, in *Encyclopedia of Physics*, Vol. XXV/2c, *Light and Matter 1c*, Springer-Verlag, Berlin, 1 edition, 1970.
 - [30] Amnon Yariv, *Quantum Electronics*, John Wiley & Sons., Singapore, 3 edition, 1989.
 - [31] A. E. Siegman, *Lasers*, University Science Books, Mill Valley, California, 1986.
 - [32] J. F. James, *A student's guide to Fourier transforms*, Cambridge University Press, Cambridge, 1995.

-
- [33] R. W. P. Drever, J. L. Hall, F. V. Kowalski, J. Hough, G. M. Ford, A. J. Munley, and H. Ward, *Laser phase and frequency stabilization using an optical resonator*, Appl. Phys. B **31**, 97 (1983).
 - [34] L. Schnupp, Conference presentation, in *European collaboration Meeting on Interferometric Detection of Gravitational Waves*, 1988.
 - [35] D. E. McClelland, *An overview of recycling in laser interferometric gravitational wave detectors*, Aust. J. Phys. **48**, 953 (1995).
 - [36] J. Mizuno, *Comparison of optical configurations for laser-interferometric gravitational-wave detectors*, PhD thesis, Max-Planck-Institut Fur Quantenoptik, Garching, Germany, 1995.
 - [37] J. Mizuno, A. Rudiger, R. Schilling, W. Winkler, and K. Danzmann, *Frequency response of Michelson- and Sagnac-based interferometers*, Opt. Comm **138**, 383 (1997).
 - [38] W. Winkler, *A Michelson interferometer using delay lines*, in: The detection of gravitational waves, ed D. G. Blair , 269 (1991).
 - [39] G. E. Moss, L. R. Miller, and R. L. Forward, *Photon-noise-limited laser transducer for gravitational antenna*, Appl. Opt. **10**, 2495 (1971).
 - [40] R. Drever, *Interferometric detectors for gravitational radiation*, in Gravitational Radiation, Les Houches 1982 eds. N. Deruelle and T. Piran (North-Holland, Amsterdam) , 321 (1983).
 - [41] B. J. Meers, *Recycling in laser-interferometric gravitational-wave detectors*, Phys. Rev. D **38**, 2317 (1988).
 - [42] K. Maischberger, A. Rüdiger, R. Schilling, L. Schnupp, W. Winkler, and G. Leuchs, *Status of the Garching 30 m prototype for a large gravitational wave detector*, in Proc. Int. Symp. on Experimental gravitational physics, Guangzou, China, eds. P. Michelson, Hu En-ke and G. Pizella (World Scientific, Singapore) , 316 (1988).
 - [43] C. N. Man, D. Shoemaker, M. Pham Tu, and D. Dewey, *External modulation technique for sensitive interferometric detection of displacements*, Phys. Lett. A **148**, 8 (1990).
 - [44] D. Schnier, J. Mizuno, G. Heinzel, H. Lück, A. Rüdiger, R. Schilling, M. Schrempel, W. Winkler, and K. Danzmann, *Power recycling in the Garching 30 m prototype interferometer for gravitational-wave detection*, Phys. Lett. A **225**, 210 (1997).
 - [45] P. Fritschel, G. Gonzalez, B. Lantz, H. Rong, P. Saha, D. Shoemaker, R. Weiss, M. Zucker, and S. Whitcomb, *Recent research with the LIGO phase noise interferometer*, Gravitational Wave Detection: Proceedings of the TAMA International Workshop on Gravitational Wave Detection, Saitama, Japan, 1996. eds K. Tsubono, M.-K. Fujimoto and K. Kuroda (1997).
 - [46] P. Fritschel, D. Shoemaker, and R. Weiss, *Demonstration of light recycling in a Michelson interferometer with Fabry-Perot cavities*, Appl. Opt. **31**, 1412 (1992).
 - [47] M. W. Regehr, F. J. Raab, and S. E. Whitcomb, *Demonstration of a power-recycled Michelson interferometer with Fabry-Perot arms by frontal modulation*, Opt. Lett. **20**, 1507 (1995).

-
- [48] M. W. Regehr, *Signal extraction and control for an interferometric gravitational wave detector*, PhD thesis, California Institute of Technology, Pasadena, California, USA, 1995.
 - [49] R. Flaminio and H. Heitmann, *Longitudinal control of an interferometer for the detection of gravitational waves*, Phys. Lett. A **214**, 112 (1996).
 - [50] D. Sigg, N. Mavalvala, J. Giaime, P. Fritschel, and D. Shoemaker, *Signal extraction in a power-recycled Michelson interferometer with Fabry-Perot arm cavities by use of a multiple-carrier frontal modulation scheme*, Appl. Opt. **37**, 5687 (1998).
 - [51] M. Ando, K. Kawabi, and K. Tsubono, *Signal-separation technique for a power-recycled interferometric gravitational wave detector*, Phys. Lett. A **237**, 13 (1997).
 - [52] M. Ando, K. Arai, K. Kawabe, and K. Tsubono, *Demonstration of power recycling on a Fabry-Perot-type prototype gravitational wave detector*, Phys. Lett. A **248**, 145 (1998).
 - [53] K. Arai, M. Ando, S. Moriwaki, K. Kawabe, and K. Tsubono, *New signal extraction scheme with harmonic demodulation for power-recycled Fabry-Perot-Michelson interferometers*, Phys. Lett. A **273**, 15 (2000).
 - [54] D. E. McClelland, J. B. Camp, J. Mason, W. Kells, and S. E. Whitcomb, *Arm cavity resonant sideband control for laser interferometric gravitational wave detectors*, Opt. Lett. **24**, 1014 (1999).
 - [55] B. J. Meers, *The frequency response of interferometric gravitational wave detectors*, Phys. Lett. A **142**, 465 (1989).
 - [56] K. A. Strain and B. J. Meers, *Experimental demonstration of dual recycling for interferometric gravitational-wave detectors*, Phys. Rev. Lett. **66**, 1391 (1991).
 - [57] M. B. Gray, A. J. Stevenson, H.-A. Bachor, and D. E. McClelland, *Broadband and tuned signal recycling with a simple Michelson interferometer*, Appl. Opt. **37**, 5886 (1998).
 - [58] G. Heinzel, A. Rüdiger, W. Winkler, R. Schilling, K. Strain, J. Mizuno, and K. Danzmann, *Experimental demonstration of a suspended dual recycling interferometer*, Phys. Rev. Lett. **81**, 5493 (1998).
 - [59] P. Hello and J.-Y. Vinet, *Simulation of thermal effects in interferometric gravitational-wave detectors*, Phys. Lett. A **178**, 351 (351).
 - [60] W. Winkler, K. Danzmann, A. Rudiger, and R. Schilling, *Heating by optical absorption and the performance of interferometric gravitational-wave detectors*, Phys. Rev. A **44**, 7022 (1991).
 - [61] K. A. Strain, K. Danzmann, J. Mizuno, P.G. Nelson, A. Rudiger, R. Schilling, and W. Winkler, *Thermal lensing in recycling interferometric gravitational wave detectors*, Phys. Rev. A **194**, 124 (1994).
 - [62] W. Winkler, A. Rudiger, R. Schilling, K. A. Strain, and K. Danzmann, *Birefringence-induced losses in interferometers*, Opt. Comm. **112**, 245 (1994).

-
- [63] J. Mizuno, K. A. Strain, P. G. Nelson, J. M. Chen, R. Schilling, and A. Rudiger, *Resonant sideband extraction: a new configuration for interferometric gravitational wave detectors*, Phys. Lett. A **175**, 273 (1993).
- [64] K. A. Strain and J. Hough, *Experimental demonstration of the use of a Fabry-Perot as a mirror of variable reflectivity*, Rev. Sci. Instrum. **65**, 799 (1994).
- [65] G. Heinzel, J. Mizuno, R. Schilling, W. Winkler, A. Rudiger, and K. Danzmann, *An experimental demonstration of resonant sideband extraction for laser-interferometric gravitational wave detectors*, Phys. Lett. A **217**, 305 (1996).
- [66] M. B. Gray, D. A. Shaddock, and D. E. McCelland, *A power recycled Michelson interferometer with resonant sideband extraction*, Gravitational Waves: Third Edoardo Amaldi Conference, Pasadena. ed S. Meshkov , 193 (2000).
- [67] J. Mason and P. Willems, *Signal extraction and length sensing for LIGO II RSE*, Gravitational Waves: Third Edoardo Amaldi Conference, Pasadena. ed S. Meshkov , 208 (2000).
- [68] Thomas Delker, 2000, Private communication.
- [69] E. Gustafson, D. Shoemaker, K. Strain, and R. Weiss, *LSC White Paper on Detector Research and Development*, LIGO T990080-00-D (1999).
- [70] N. M. Sampas and D. Z. Anderson, *Stabilization of laser beam alignment to an optical resonator by heterodyne detection of off-axis modes*, Appl. Opt. **29**, 394 (1990).
- [71] E. Morrison, B. J. Meers, D. I. Robertson, and H. Ward, *Automatic alignment of optical interferometers*, Appl. Opt. **33**, 5041 (1994).
- [72] E. Morrison, B. J. Meers, D. I. Robertson, and H. Ward, *Experimental demonstration of an automatic alignment system for optical interferometers*, Appl. Opt. **33**, 5037 (1994).
- [73] C. T. Taylor and J. P. Coulon, *Automatic alignment stabilisation for VIRGO frequency prestabilisation system*, Report for the VIRGO group, Orsay (1995), unpublished.
- [74] N. Mavalvala, *Alignment issues in in laser interferometric gravitational-wave detectors*, PhD thesis, Massachusetts Institute of Technology, Cambridge, 1997.
- [75] N. Mavalvala, D. Sigg, and D. Shoemaker, *Experimental test of an alignment sensing scheme for a gravitational-wave interferometer*, Appl. Opt. **37**, 7743 (1998).
- [76] Y. Hefetz, N. Mavalvala, and D. Sigg, *Principles of calculating alignment signals in complex resonant interferometers*, J. Opt. Soc. Am. B **14**, 1597 (1997).
- [77] A. Rudiger G. Heinzel, R. Schilling, K. A. Strain, W. Winkler, J. Mizuno, and K. Danzmann, *Automatic beam alignment in the Garching 30-m prototype of a laser-interferometric gravitational wave detector*, Opt. Comm. **160**, 321 (1999).
- [78] G. Sagnac, *L'éther lumineux démontré par l'effet du vent relatif d'éther dans un interféromètre en rotation uniforme*, C. R. Acad. Sci. **95**, 708 (1913).
- [79] K.-X. Sun, M. M. Fejer, E. K. Gustafson, and R. L. Byer, *Sagnac interferometer for gravitational-wave detection*, Phys. Rev. Lett. **76**, 3053 (1996).

-
- [80] K.-X. Sun, E. K. Gustafson, M. M. Fejer, and R. L. Byer, *Polarization-based balanced heterodyne detection in a Sagnac interferometer for precision phase measurement*, Opt. Lett. **22**, 1359 (1997).
 - [81] K.-X. Sun, M. M. Fejer, E. K. Gustafson, and R. L. Byer, *Balanced heterodyne signal extraction in a postmodulated Sagnac interferometer at low frequency*, Opt. Lett. **22**, 1485 (1997).
 - [82] P. T. Beyersdorf, M. M. Fejer, and R. L. Byer, *Polarization Sagnac interferometer with postmodulation for gravitational-wave detection*, Opt. Lett. **24**, 1112 (1999).
 - [83] P. T. Beyersdorf, M. M. Fejer, and R. L. Byer, *The Polarization Sagnac interferometer as a candidate configuration*, Gravitational Waves: Third Edoardo Amaldi Conference, Pasadena. ed S. Meshkov , 200 (2000).
 - [84] B. Petrovichev, M. B. Gray, and D. E. McClelland, *Simulating the performance of Michelson- and Sagnac-based laser interferometric gravitational wave detectors in the presence of mirror tilt and curvature errors*, Gen. Rel. & Grav. **30**, 1055 (1998).
 - [85] T. W. Hänsch and B. Couillaud, *Laser frequency stabilisation by polarisation spectroscopy of a reflecting reference cavity*, Opt. Comm. **35**, 441 (1980).
 - [86] M. B. Gray, D. A. Shaddock, C. C. Harb, and H.-A. Bachor, *Photodetector designs for low-noise, broadband, and high power applications*, Rev. Sci. Instrum. **69**, 3755 (1998).
 - [87] *LIGO II Conceptual Project Book*, LIGO M990288-A-M (1999).
 - [88] A. B. Williams and F. J. Taylor, *Electronic filter design handbook: LC, active and digital filters*, McGraw-Hill, New York, 2 edition, 1988.
 - [89] P. Horowitz and W. Hill, *The Art of Electronics*, Cambridge University Press, Cambridge, 2 edition, 1991.
 - [90] G. Mueller, 2000, Private communication.
 - [91] A. Brillet, 2000, Private communication.
 - [92] N. Uehara, *Ring mode cleaner for the initial LIGO 10 Watt laser*, Internal report, Ginzton Laboratory, Stanford University (1997).
 - [93] C. N. Man and A. Brillet, *Injection locking of argon-ion lasers*, Opt. Lett. **9**, 333 (1984).
 - [94] F. Bondu, P. Fritschel, C. N. Mann, and A. Brillet, *Ultrahigh-spectral-purity laser for the VIRGO experiment*, Opt. Lett. **21**, 582 (1996).
 - [95] K. Schneider, S. Schiller, J. Mlynek, M. Bode, and I. Freitag, *1.1-W single-frequency 532-nm radiation by second-harmonic generation of a miniature Nd:YAG ring laser*, Opt. Lett. **21**, 1999 (1996).
 - [96] B. C. Young, F. C. Cruz, W. M. Itano, and J. C. Bergquist, *Visible lasers with subhertz linewidths*, Phys. Rev. Lett. **82**, 3799 (1999).
 - [97] D. A. Shaddock, M. B. Gray, and D. E. Mclelland, *Frequency locking a laser to an optical cavity by use of spatial mode interference*, Opt. Lett. **24**, 1499 (1999).

-
- [98] B. Willke, S. Brozek, K. Danzmann, V. Quetchke, and S. Gossler, *Frequency stabilization of a monolithic Nd:YAG ring laser by controlling the power of the laser-diode pump source*, Opt. Lett. **25**, 1019 (2000).
 - [99] T. Day, *Frequency stabilized solid state lasers for coherent optical communication*, PhD thesis, Stanford University, Stanford, California, 1990.
 - [100] R. L. Barger, M. S. Sorem, and J. L. Hall, *Frequency stabilization of a CW dye laser*, Appl. Phys. Lett. **22**, 573 (1973).
 - [101] A. D. White, *Frequency stabilization of gas lasers*, IEEE J. Q. Elect. **1**, 349 (1965).
 - [102] M. S. Taubman and J. L. Hall, *Cancellation of laser dither modulation from optical frequency standards*, Opt. Lett. **25**, 311 (2000).
 - [103] N. C. Wong and J. L. Hall, *Servo control of amplitude modulation in frequency spectroscopy: demonstration of shot noise limited detection*, J. Opt. Soc. Am. B **2**, 1527 (1985).
 - [104] A. Rüdiger, R. Schilling, L. Schnupp, W. Winkler, H. Billing, and K. Maischberger, *A mode selector to suppress fluctuations in laser beam geometry*, Optica Acta **28**, 641 (1981).
 - [105] C. E. Wieman and S. L. Gilbert, *Laser-frequency stabilization using mode interference from a reflecting reference interferometer*, Opt. Lett. **7**, 480 (1982).
 - [106] D. Schnier and A. A. Madej, *Dither-free method for phase-mirror control in optical-feedback stabilized diode laser systems*, Opt. Comm. **105**, 388 (1994).
 - [107] T. Day, E. K. Gustafson, and R. L. Byer, *Sub-Hertz relative frequency stabilization of two diode laser pumped Nd:YAG lasers locked to a Fabry-Perot interferometer*, J. Q. Elect. **28**, 1106 (1992).
 - [108] M. B. Gray, A. J. Stevenson, H.-A. Bachor, and D. E. McClelland, *Harmonic demodulation of nonstationary shot noise*, Opt. Lett. **18**, 759 (1993).
 - [109] A. Huber, Th. Udem, B. Gross, J. Reichert, M. Kourogi, K. Pachucki, M. Weitz, and T. W. Hänsch, *Hydrogen-deuterium 1S-2S isotope shift and the structure of the deuteron*, Phys. Rev. Lett. **80**, 468 (1998).
 - [110] A. Brillet and J. L. Hall, *Improved laser test of the isotropy of space*, Phys. Rev. Lett. **42**, 549 (1979).
 - [111] S. W. Henderson and K. Ota, *Recent improvements in eyesafe, solid-state and coherent laser radar technology*, **25**, 19 (1997).
 - [112] N. M. Sampas, E. K. Gustafson, and R. L. Byer, *Long-term stability of two diode-laser-pumped nonplanar ring lasers independently stabilized to two Fabry-Perot interferometers*, Opt. Lett. **18**, 947 (1993).
 - [113] R. Storz, C. Braxmaier, K. Jäck, O. Pradl, and S. Schiller, *Ultrahigh long-term dimensional stability of a sapphire cryogenic optical resonator*, Opt. Lett. **23**, 1031 (1998).
 - [114] C. T. Taylor, M. Notcutt, and D. G. Blair, *Cryogenic, all-sapphire, Fabry-Perot optical frequency reference*, Rev. Sci. Instrum. **66**, 955 (1995).

-
- [115] T. Day, A. C. Nilsson, M. M. Fejer, A. D. Farinas, E. K. Gustafson, C. D. Nabors, and R. L. Byer, *30 Hz-linewidth, diode-laser-pumped, Nd:GGG nonplanar ring oscillators by active frequency stabilisation*, Electron. Lett. **25**, 810 (1989).
- [116] D. W. Allan, *Statistics of Atomic Frequency Standards*, Proc. IEEE **54**, 221 (1966).
- [117] D. W. Allan, *Time and frequency (time-domain) characterization, estimation, and prediction of precision clocks and oscillators*, IEEE Trans. Ultrason. Ferroelec. & Freq. Contr. **34**, 647 (1987).
- [118] W. J. Kozlovsky, C. D. Nabors, and R. L. Byer, *Efficient Second Harmonic Generation of a Diode-Laser-Pumped Nd:YAG Laser Using Monolithic MgO:LiNbO₃ External Resonant Cavities*, IEEE J. Quant. Elec. **24**, 913 (1988).
- [119] A. Arie, S. Schiller, E. K. Gustafson, and R. L. Byer, *Absolute frequency stabilization of diode-laser-pumped Nd:YAG lasers to hyperfine transitions in molecular iodine*, Opt. Lett. **17**, 1204 (1992).
- [120] H. Matsumoto and T. Honda, *Modulation-free iodine-stabilized green YAG laser with a common-path interferometer*, opt. Commun. **127**, 283 (1996).
- [121] J. Ye, L. Robertsson, S. Picard, L.-S. Ma, and J. L. Hall, *Absolute frequency atlas of molecular I₂ at 532nm*, IEEE Trans. Instrum. Meas. **48**, 544 (1999).
- [122] M. L. Eickhoff and J. L. Hall, *Optical frequency standard at 532 nm*, IEEE Trans. Instrum. Meas. **44**, 155 (1995).
- [123] D. J. Ottaway, P. J. Veitch, M. W. Hamilton, C. Hollitt, D. Mudge, and J. Munch, *A compact injection-locked Nd:YAG laser for gravitational wave detection*, IEEE J. Quant. Elect. **34**, 2006 (1998).
- [124] A. D. Farinas, E. K. Gustafson, and R. L. Byer, *Frequency and intensity noise in an injection-locked, solid state laser*, J. Opt. Am. Soc. B **12**, 328 (1995).
- [125] G. Mueller and K.-I. Ueda, *Stabilization of injection locking using polarization spectroscopic technique*, Jpn. J. Appl. Phys. **37**, 3313 (1998).
- [126] W. K. Burns (ed), *Optical fiber rotation sensing*, Academic Press, San Diego, 1994.
- [127] H. S. Kang, J. H. Lee, and K. S. Lee, *A stabilization method of the Sagnac optical fiber current sensor with twist control*, IEEE Phot. Tech. Lett **10**, 1464 (1998).
- [128] K. A. Strain, 2000, Private communication.
- [129] K. G. Baigent, D. A. Shaddock, M. B. Gray, and D. E. McClelland, *Laser stabilisation for the measurement of thermal noise*, Gen. Rel. & Grav. **32**, 399 (2000).